A novel Adaptive Filtering approach to Drive File Identification for Service Environment Replication

Bharath Balasubramanya

Dissertation submitted to the Faculty of the
Virginia Polytechnic Institute and State University
in partial fulfillment of the requirements for the degree of

Doctor of Philosophy
in
Mechanical Engineering

Steve C. Southward, Chair
Andrew Kurdila
Alexander Leonessa
Craig Woolsey

November 4, 2024
Blacksburg, Virginia

Keywords: Service Environment Replication, Drive File Identification, Adaptive Filtering

A novel Adaptive Filtering approach to Drive File Identification for Service Environment Replication

Bharath Balasubramanya

(ABSTRACT)

Service Environment Replication refers to the process of using test machines to apply controlled dynamic loads to test articles in order to replicate operating conditions that the article was designed for. Such test machines hence require the development of dynamic time series commands that drive the actuators in order to replicate the responses of the actual dynamic system measured separately in its service environment.

A novel adaptive filtering approach, called the Pulse Train Filtered-x Least Mean Square algorithm for waveform generation and drive file identification is proposed in this thesis based on methods developed for Active Noise and Vibration Control. Simulation studies are considered using various test benches with varying degrees of nonlinearity to validate the performance of the proposed algorithm to rapidly converge to a dynamic solution in a small number of iterations. The PT-Fx-LMS algorithm is also shown to enable targeted iteration over isolated time slices within the data set, which challenge conventional iterative DFID techniques. Further modifications to the algorithm are proposed that uses a completely offline workflow using the estimated dynamics of the plant and an empirical termination criteria to improve performance and ensure stability of the adaptive process. The architecture developed is applicable for a wide array of dynamic systems with single or multiple actuators and sensors. Experimental validation of the proposed algorithm is conducted using an acoustic setup to replicate target sound fields for a wide array of configurations.

A novel Adaptive Filtering approach to Drive File Identification for Service Environment Replication

Bharath Balasubramanya

(GENERAL AUDIENCE ABSTRACT)

Testing an article in the environment where it is designed to be operated can be a time-consuming and expensive process without laboratory-based, repeatable testing environments. The goal of these test rigs is hence to replicate the service environment in order to design, develop and validate the article-under-test. Different methods have been developed over the years by manufacturers to replicate such environments within the confines of a laboratory where the most important task is to generate the required control signals to drive the actuators on the test rig to induce the required responses from the dynamic system under test.

The objective of the thesis is to develop a novel time-domain based algorithm that can be used to iteratively derive the control signals required to replicate the responses of the dynamic system on a simulated test bench in as few iterations as possible, thereby saving computation time, experiment time and cost. The proposed algorithm is compared against conventional methods for deriving these control signals and further improvements to the proposed method are suggested in order to improve performance, stability, safety and ease of workflow on the test rig.

Dedication

To my parents, family and friends who have believed in me throughout this journey

Acknowledgments

I would like to acknowledge all my loved ones over the course of this journey without whom this would not have been possible.

First and foremost, I would like to thank my parents for their incredible support and belief throughout my life, their never ending passion to always support my educational and personal pursuits, including moving to a country across the world and for all that they have taught me on how to navigate this world.

I am very fortunate to have had the opportunity to pursue my Ph.D. at Virginia Tech and would like to thank my committee chair Dr. Southward whose support and guidance has been invaluable. The number of times we have overrun our scheduled research meetings because we were just that excited about solving a problem or planning out the research path has forever set a benchmark on how to stay motivated and curious about interesting practical applications. Your feedback and words of appreciation especially during the tough periods has always lifted my spirits and am forever grateful for your insights on building out a career. I would also like to thank my committee members for their guidance and appreciation during the pre-defense. Dr. Leonessa and Dr. Kurdila, I am also grateful for the control theory courses I took with you that I still end up flipping through my notes because of how relevant and useful they were.

I am also grateful to Virginia Tech to have given me the opportunity for 6 continuous years to be a teaching assistant and all the amazing faculty members that I got to interact

and develop courses with along the way. All of my thanks to Dr. Wicks and Dr. Diller for their years of wisdom and encouragement, Dr. Benning, Dr. McGinnis and Dr. Nowinski for teaching me the perspective required in a classroom setting to give back to the students and how best to allow them to succeed.

Special thanks to my partner Maggie who has been the source of my strength through the last years of being a graduate student, for your love, faith and support. I am also grateful to all my friends I've made over the years here in Blacksburg, a tiny town in the mountains that I will dearly miss, the ones back home in India, all your love, support and belief is what has kept me going.

Finally, I also want to thank the amazing team I have found myself with at Ford in the next chapter of my career, who have been incredibly supportive over the last few months as I complete this dissertation to make the many years of effort and focus worthwhile.

Contents

List of Figures

List of Tables

Chapter 1

Introduction

The testing of mechanical systems to study the dynamic behavior of the test specimen, its durability during operation through its service time, develop system models to aid in design of control strategies and optimize its vibrational characteristics has been a major part of the design process in product development. Validating complex mechanical and mechatronic systems only in its service environment is a time-consuming and expensive process, which has prompted manufacturers to test these systems on hardware-in-the-loop (HiL) test benches, that provide major savings in time and cost while also allowing repeatable results in a controlled environment. With the advancements in sensor technology and signal processing tools, the field of research focused on improving the efficiency, in terms of accuracy, reliability, speed and cost of such testing procedures has seen many advancements in the last decades. For testing procedures that require the dynamical system to follow a certain trajectory, a large number of industrial mechanical test machines require some method for synthesizing a set of command input signals that cause multiple system outputs to closely match a set of desired target responses. This dissertation is focused on developing a novel time domain based algorithm that improves the identification of these input command signals for a specific class of dynamical systems and applications that provides certain advantages over the current state-of-the-art. It is also the objective of this work to investigate the questions of existence and uniqueness as applied to the derivation of said command input signals for mechanical test-rigs in order to guide the user through the testing process.

The remainder of this chapter is devoted to briefly describing the problem of Service Environment Replication (section 1.1), the current solutions and their limitations, which leads to the motivation for this work and the problem statement. The contributions of the author to this work and the road map to the rest of this thesis is provided at the end of the chapter.

1.1 Service Environment Replication

Mechanical fatigue occurs in components that do not always sustain damage when a force is applied just once, but rather when variable stresses are repeatedly applied over its service lifetime. In many cases, such stress levels are less than the yield strength of the material and the damage that occurs in the internal structure of the material that could lead to formation of cracks and fractures, and eventually failure. Research into fatigue began in the early 19^{th} century and was quickly adopted by the ground vehicle industry after catastrophic accidents due to wagon axle failures [75]. Subsequent research in and analysis of various accidents across industries due to stress concentration factors, fatigue limits of metals, metallurgy, corrosion and temperature effects have reinforced the importance of fatigue testing in the design cycle of every mechanical structure, especially considering the dynamic loads that the structure will endure through its service life in its service environment.

Another important application of vibration testing is in the field of seismology, where large-scale models of critical infrastructure like tall buildings, bridges, nuclear reactors etc. are tested on periodic actuators or shakers for the design and development of earthquake-proof structures [38, 59]. Combined with sensing of the deformations and acceleration of these structures during actual earthquakes, such testing methods on shaker tables can be used to further analyze and optimize building designs using much more repeatable tests using

scaled-models.

In the vehicle industry, durability tests, both on physical structural components or in computer aided simulations form a critical phase of the design process during the validation of components for ground vehicles such as automobiles, motorcycles, trucks, agricultural vehicles, trains etc. [24, 60] and aerospace vehicles such as planes, helicopters [65, 84] and even satellites and space stations [80, 83]. Aside from safety considerations, testing of components play a huge role in the characterization, optimization and performance enhancement of various subsystems. Indoor laboratory testing of suspension components and sub-assemblies, wheels, brakes, steering systems, seats, engine parts etc. are commonplace in the modern automotive industry [36, 60] and more recently, full-scale dynamic testing of an entire vehicle is used to analyze dynamic motions of the vehicle and/or suspension components for ride, handling and durability studies [5, 8, 48, 82].

Many of the testing applications presented above require a test specimen to be excited by actuators in a controlled laboratory environment that apply a pre-defined excitation sequence such that it replicates the motions and forces experienced by the test specimen in its actual service environment. This process is called "Service Environment Replication", or SER. A successful SER scheme allows accurate, repeatable, safe, fast and a cost-effective method for various design and optimization requirements of the dynamical system-under-test.

1.1.1 Hydraulic Test Rigs in the Automotive Industry

Since the motivation for this thesis was based out of the challenges faced with SER in the automotive industry, this section gives a brief background of the hydraulic test rigs that are most commonly used for the dynamical testing of specimens, from small components to complex assemblies or entire vehicles. This section serves to discuss the different types of test

rigs prevalent in the automotive industry used for different applications like durability testing, optimization of performance characteristics like Noise, Vibration and Harshness (NVH), comfort and safety [5, 48, 102]. Understanding the different types of test rigs currently in use in the industry will help to develop the simulation test benches that will be used to test the SER algorithms in this thesis.

The goals and in turn, the complexity of such test benches vary depending on the application and industry in which they are utilized. Automotive manufacturers would be primarily interested in NVH and durability studies of the automobiles they develop, while the racing industry would focus on the durability and performance characterization and tuning of various suspension and chassis components to improve ride and handling. Efficient SER testing of the components would require predefined control inputs to be fed to the actuators on the test rig in order to measure the responses as desired on the test specimen for further analysis.

Hydraulic actuators are commonly used for such applications because of their excellent power density, precise control, and the large forces they can develop. The test rigs are usually classified based on the degrees-of-freedom of actuation or the specific subsystem they serve to test.

1.1.1.1 Complex Shaker Rigs

Some of the most complex test benches are 4-post, 7-post and 8-post shaker rigs that are designed to test using the entire automobile instead of a representative scaled-model. These full-scale test benches overcome the difficulty of modeling highly complex, nonlinear dynamic systems and allow engineers to validate simpler models developed during the initial design phases of the product development, test high-risk, edge-case conditions in the safety of a laboratory environment and provide the ability to produce repeatable test conditions to

refine various mechatronic components and iterative versions of hardware components, while incurring lesser penalty of cost and time through field-testing.

Servo-hydraulic 4-post systems are usually tire-coupled test benches that can apply vertical forces to the 4 wheels of the vehicle independently. Each actuator supports the vehicle on a platform under each tire. Such test rigs are usually the simplest forms of these complex shaker rigs and are useful for durability, comfort and NVH applications. An example of such a test bench is the MTS Systems' Model 320 Tire-coupled simulator shown in Figure 1.1. Modern test benches like MTS Systems' Model 329i Spindle-coupled Road simulators can provide up to an 80 Hz frequency road input [87], and it is noted that the bandwidth of most servo-hydraulic test systems is 100 Hz or less [94].

Figure 1.1: MTS Systems' Model 320 Tire-coupled Road Simulator [89]

Kinematic and Compliance (K&C) deflections of an automotive suspension can also be measured using 4-post test benches, like the MTS K&C System shown in Figure 1.2. These can be used to analyze the ride and handling characteristics of a vehicle in response to precisely controlled displacements and forces applied to the four tires. As an improvement on the vertical actuation of the test bench in Figure 1.1, a K&C test bench can also apply moments in all three directions and has the capability of providing steering inputs to analyze

axle and suspension behavior in almost any road condition. While the test bench shown in Figure 1.1 and Figure 1.2 are tire coupled road simulators, spindle coupled simulators also exist that can be used to serve similar applications.

Figure 1.2: MTS Systems' K&C Deflection Measurement System [88]

The most advanced shaker rigs currently used in the industry are the 7-post test rigs which offer immense capability in terms of exactly replicating the conditions required to test advanced vehicles like race cars and high performance road cars that experience high aerodynamic loads in their service environment. The three additional electromagnetic, pneumatic or hydraulic actuators in addition to the 4-post test rigs are usually attached to the chassis of the test vehicle to simulate the aerodynamic and inertial loading of the chassis. Consequently, these test rigs are extremely complex Multi-input/Multi-Output (MIMO) systems that require specialized algorithms to replicate the target responses for full-scale dynamic testing of these vehicles [5, 8, 48, 82]. Since these test rigs are usually used by major automotive manufacturers for in-house testing, race teams, an example of which is shown in Figure 1.3 and developed by a handful of suppliers, very little literature exists that dis-

cuss the specific algorithms used by such test systems in order to protect their intellectual properties and competitive advantage.

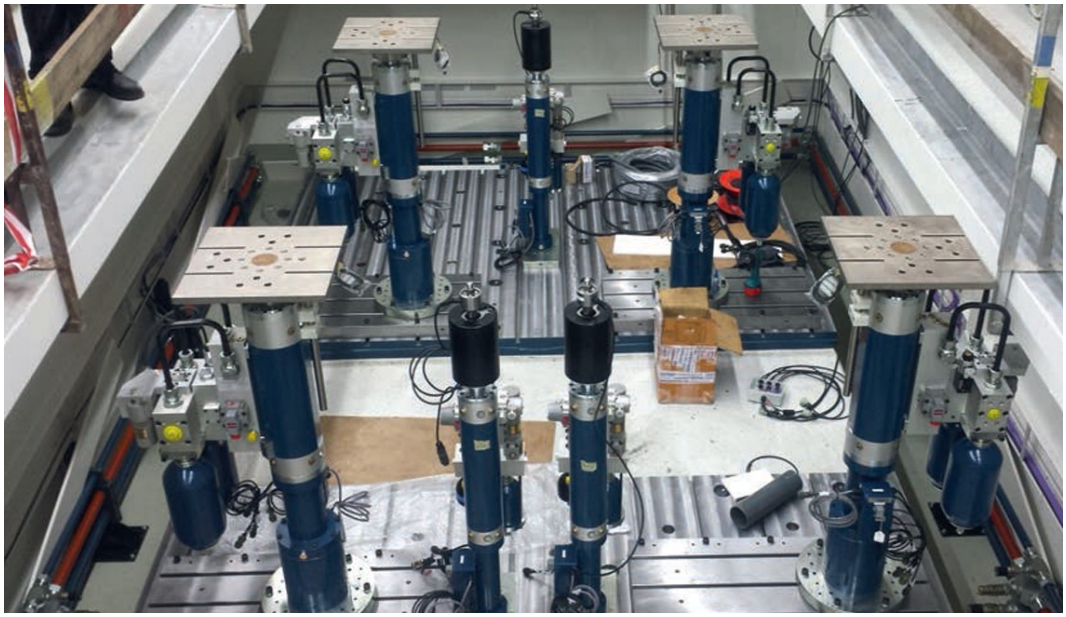

Figure 1.3: The Servotest 7-post Vehicle Ride Simulator used by TRE [40]

While the test benches mentioned above are some of the most complex examples of the test rigs used in the industry, they are also significantly expensive to build and maintain, require fully built prototypes of vehicles and require skilled engineers with controls knowledge to operate the equipment and interpret the results. The test benches for specific subsystems that are much smaller in scale are also used very commonly during the design process and are much more ideal for prototyping and fine-tuning these subsystems.

1.1.1.2 Suspension Test Rigs

Instead of considering the entire dynamic system of the vehicle, it is often more convenient to model and test just one quarter end of the vehicle dynamics using a suspension test rig, often called a quarter-car rig. This greatly reduces the complexity and computational time and can also be more easily modeled for hardware-in-the-loop simulation purposes. Depending

on the application, the test rig can accommodate the exact vehicle suspension prototype or could be built as a representative dynamic model. Figure 1.4 shows a proof-of-concept quarter-car rig that integrates an actual vehicle suspension with the sprung mass modeled using metal plates mounted on linear sliders. The actuation is provided by an electronically controlled servo-hydraulic system with the tire resting on a platform. Such test benches are very useful for rapid prototyping of suspension components, dynamic and K&C analysis of just one quarter-end of a vehicle.

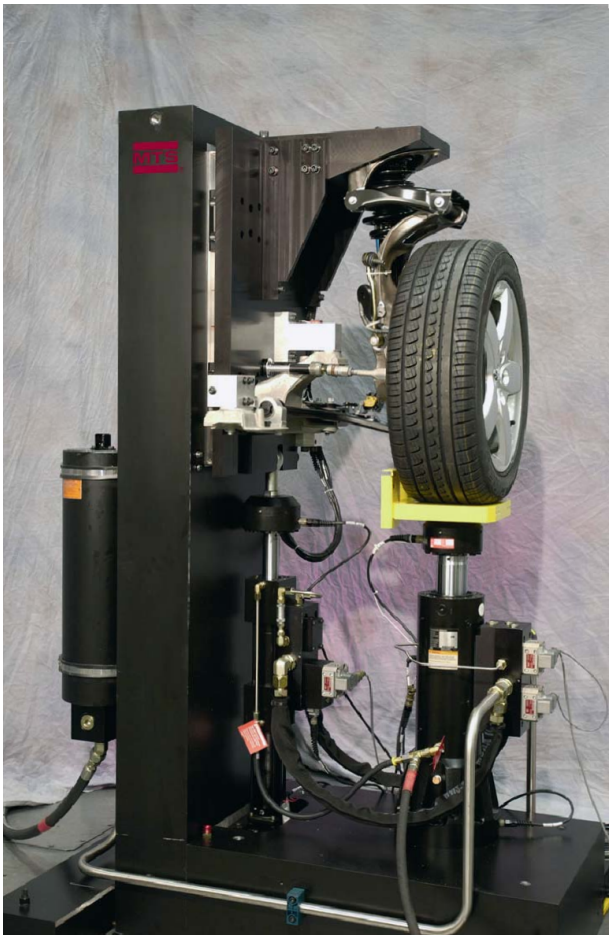

Figure 1.4: MTS Systems' Mechatronics Development and Validation Bench [52]

Just as for the 4-post test rigs presented previously, additional actuators, or degrees-of-freedom can be introduced to suspension test rigs in order to further replicate the service

environment when testing suspension components. These are more common in the racing industry where track-specific loads need to be simulated to fine-tune setup changes for just the suspension components. The additional degrees-of-freedom are introduced by allowing not only vertical forces acting on the spindle, but also the lateral and longitudinal forces along with all three moments. Such actuation can be introduced using different concepts, the easiest of which is by simply adding more actuators that impose individual degrees-of-freedom or by using a hexapod test-rig [49]. An example of the former as used by Formula 1 teams is shown in Figure 1.5.

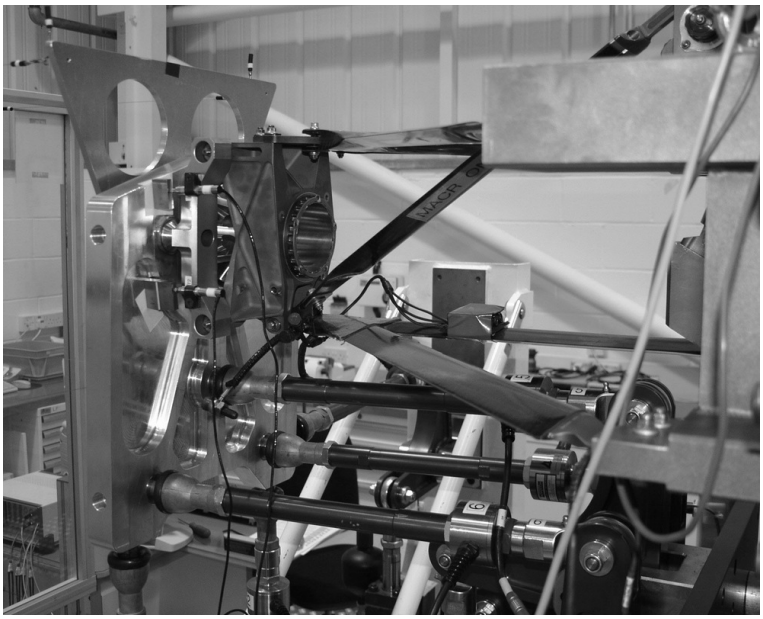

Figure 1.5: Multi-DOF Suspension Test rig used by Formula 1 Teams [73]

1.1.1.3 Shaker tables

Multi-axis shaker tables are widely used not just in the automotive industry, but also in the aerospace and civil engineering industries to evaluate the behavior of components under a diverse array of real-world vibration phenomena. Automotive subsystems like seats, dashboards, body components, exhaust systems, fuel and storage tanks and more recently,

lithium-ion battery packs are tested on such tables for durability, NVH, ride comfort and modal evaluation before being integrated into the full vehicle. Modern shaker tables can apply forces and motions with six degrees-of-freedom using a hydraulically actuated hexapod systems that can simulate a vide range of forces and motions up to a frequency of 100-150 Hz, an example of which is shown in Figure 1.6. Such hexapod design simulation tables are also used for many driver-in-the-loop virtual simulators for testing of active safety systems, driver characterization and performance enhancement [96].

Figure 1.6: MTS Systems' Multi-Axial Simulation Table (MAST) system [90]

Outside the automotive industry, shaker tables also find extensive usage for similar durability and vibration analysis and much larger structures than the one shown in Figure 1.6 are used in the civil engineering industry for seismic studies of critical infrastructure.

1.1.2 The SER testing procedure

As has been described using various examples in section 1.1.1, the SER testing procedure can be used for various applications like durability testing, system characterization, performance optimization of components etc. The specifics of each testing procedure differ slightly but

also have many commonalities with respect to the replication of the service environment on the test rig. The key difference would be the "drive files" that need to be fed to the actuators. A drive file is simply a synchronized batch sequence of dynamic time-series commands that are sent to each actuator defining what forces or displacements should be achieved by the actuators (posts). For example, for modal testing and specimen characterization, sine-sweeps or white-pink noise drive files are commonly used that would excite all the modes of interest on the specimen within the bandwidth capabilities of the actuators. Certain durability studies can also use standardized, artificial road profiles, for examples those defined by ISO 8608 for different classes of road roughness which defines the spectral characteristics of the road profiles for testing purposes [36, 93]. In such cases, the identification of the drive files is a straightforward process and can be designed irrespective of the responses of the specimen in its service environment.

Of more interest to this thesis are the cases where the drive files need to be identified such that they replicate the target responses of the dynamic system on the test rig, which is the case for many durability studies and track testing. In the case of durability test programs, vehicles are often tested on special test tracks that include specific classes of potholes, road roughness, impact loading profiles or off-road tracks [104]. These special tracks are designed based on rainflow counting matrices that allow equivalent fatigue loading in a much shorter time than running the vehicle on public roads for hundreds of thousands of kilometers and significantly reduce the testing time required [4, 37]. The exact description of the development of such durability test programs is outside the scope of this thesis. For comfort optimization studies in vehicles, the test program is developed similarly, but instead of fatigue loading, the displacement and acceleration levels of the driver, chassis or the suspension subsystems are of more interest.

The SER testing procedure for vehicle testing can hence be broken down into a few key

stages. An overview of the SER testing procedure is shown in Figure 1.7.

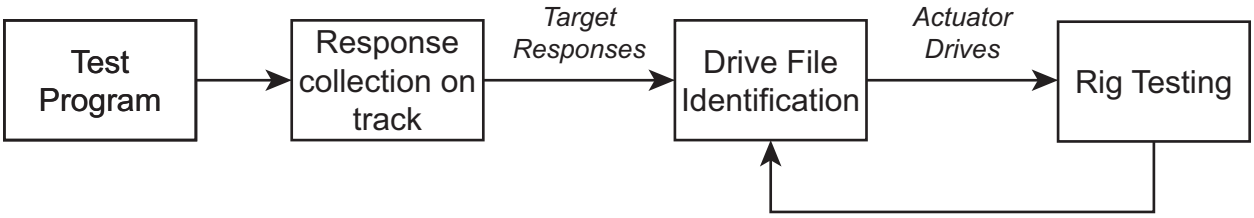

Figure 1.7: Overview of the SER Testing procedure

Design of the test program Based on the application, a test program should be designed that will be appropriate to be replicated on the test rig. In the case of a durability test program, as previously mentioned, the vehicle could be driven over a special track that is best suited for fatigue loading of the components of interest. Based on the rainflow counting matrices [4, 37], the actual loading caused by these specific tracks are higher than normal roads but accumulate to the representative fatigue loading in a significantly reduced time.

In the motorsport industry, restrictive rules often govern the amount of track testing that any team can perform per season, meaning that instrumented track testing for iterative tuning is almost impossible. Hence, teams often have to always rely on track models and complex shaker rigs to fine tune the performance characteristics of the car prior to even arriving at the track. The design of the test program in such cases, which are usually track-specific, becomes extremely crucial in a competitive and cost intensive environment. Teams usually have access to very detailed track maps, road profiles and historical telemetry data to design these test programs for testing their current racecars on the test rigs.

Response Collection on track Prior to generating a drive file, the test vehicle must be instrumented with a set of sensors such as wheel force transducers, shock potentiometers,

wheel hub accelerometers, spring load cells, and/or laser ride height sensors. Typically, only a few sensors are used for each corner of the vehicle. Once instrumented, data is collected from all sensors while the vehicle is driven on a track or test course. This data and the instrumented vehicle would then be brought back to the shaker rig for testing. The measured loads and responses of just one loop can be applied over a number of repetitions as required by the test program on the test-rig in a test laboratory for durability analysis or performance optimizations [24]. This was a novel idea first proposed by Cryer et al. [13] who termed this stage as "Response Simulation".

Drive File Identification The measured data set, which constitute the reference signals, is called the "target data", since the primary objective of drive file identification (DFID) is to find a set of commands to send to each actuator such that the sensor response measured on the test rig matches the target data that was recorded during the road or track test. In general, it is not possible to perfectly match the target response data, but it is often possible to match very closely, for which different error measures are typically used to quantify the performance of the DFID process. The ability to closely match the target response using a test rig will largely depend on how well correlated the test rig actuation inputs are to the real vehicle inputs during the road or track test [82].

Figure 1.8 gives a schematic representation of the DFID process and the different components of the same are listed below which will be used throughout the thesis.

- *Control Inputs ("drives"):* the control inputs are the signals sent to the dynamic system, which in this case is the test rig with the vehicle/test specimen mounted on it. The number of control inputs depend on the type of test rig which could have one or many actuators.
- *Dynamic System:* the dynamic system consists of the test rig with the hydraulic

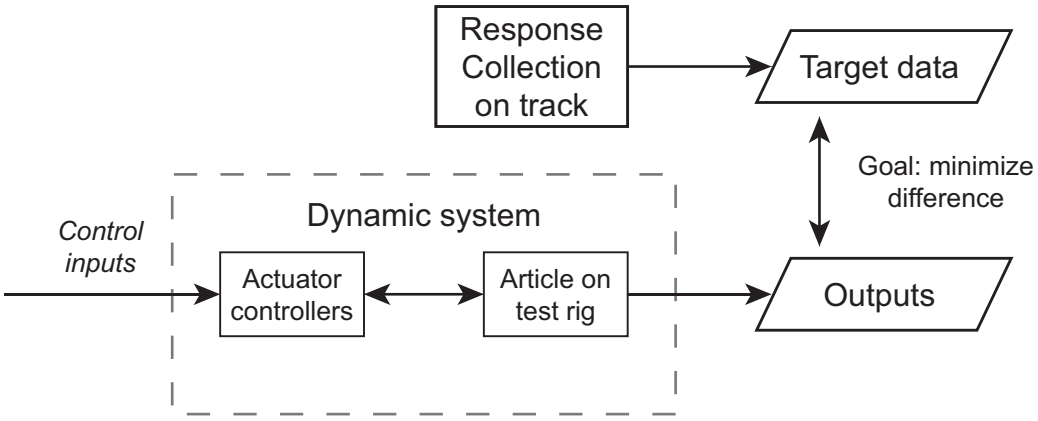

Figure 1.8: Schematic representation of the Drive File Identification process

actuators, a set of controllers that control each actuator and the vehicle/test specimen mounted on the rig. For real world test rigs and test specimen, the dynamic system constitutes a highly nonlinear dynamic system which makes the multi-variable problem of DFID very complex. The performance of the actuator controllers are bound to affect the outputs measured on the test specimen, but many strategies have been developed over the years that have optimized performance such that their effect on the SER testing procedure is minimal. While there could exist some bandwidth limitations, for most test rigs, a conventional PID controller is usually sufficient [9, 19, 86]. More advanced control strategies for the actuators in cases of large cross-coupling between actuators or nonlinear dynamics have been discussed in [10, 30, 67, 76, 81] that improve reference tracking, allow for compensation of nonlinear effects and increase the bandwidth of the closed-loop system.

- *Outputs:* the outputs of the system are the displacements, forces or accelerations measured on the specimen on the rig. They are measured using different sensors usually mounted on the spindles, chassis, shocks etc. For the case of DFID, these sensors are attached in the same way as the instrumented vehicle on the test

track.

- *Reference signals ("target"):* these are the signals that have been measured by the instrumented vehicle during the response collection stage of the SER testing procedure that need to be reproduced on the test rig, i.e. the outputs should match the target data.

Rig testing Once a suitable drive file is generated, it is played out many times on the test rig as required by the designed test program. Additional sensors are usually attached to the test specimen to monitor all critical locations, especially for durability studies. Different physical setup combinations can also be tested while recording all the pertinent vehicle dynamic motions that engineers can analyze to select or design an optimal setup based on performance requirements.

1.2 Drive File Identification methods

This thesis focuses on one specific stage of the SER testing procedure, namely the Drive File Identification process. This section will focus on a brief summary of the different methods that have been developed over the years for DFID.

1.2.1 Iterative Learning Control

The first iterative frequency domain based road replication method was developed by Dodds [26]. While this method focused on replicating the spectral characteristics of the road, an Iterative Learning Control (ILC) scheme to accurately replicate road vibrations on test vehicles for service environment replication was first presented by Cryer et al. [13] because road profile replication using standard Power Spectral Density (PSD) profiles were insufficient to

replicate edge case loads and accelerations on test vehicles that were nonlinearly coupled. Instead, the sole objective for this development was to replicate the measured responses, which is the crucial element for durability testing, and not the road profile itself. The developed method allowed for computing the required drive files to match both the response time history for test-critical events and also a statistical domain validation to study the vehicle response for a broader class of road profiles and excitations. The DFID using the method presented by Cryer et al. [13] was completely off-line using frequency domain based system identification methods followed by a regular inversion of the model. An initial estimate of the required drive file was derived by filtering the required response through the identified inverse model and then an iterative process is used to update the drives until the response error is reduced to an acceptable level.

This process is represented in Figure 1.9 and the iterative process is considered off-line here because the computation of the modified drives is not performed until after the response, and consequently the error, has been measured on the test rig. A more thorough discussion of the conventional ILC method, including its formulation and convergence criteria will be presented in Chapter 2.

Many commercial packages from servo-hydraulic test bench manufacturers have been developed based on this scheme, for examples, MTS Systems' widely reputed "Remote Parameter Control" RPC® was initially developed in 1977, [2], Spectral Dynamics' JAGUAR MIMO waveform replication [99] and "Time Waveform Replication" TWR® by LMS International [15]. These solutions all use the same fundamental approach to derive the drive files, but they differ slightly in algorithmic detail and over the years, with extensive research and improvement in computational capabilities, the performances of these methods have been improved for the specific applications they cater to.

The simplicity of the approach offers many advantages. The use of the Fast Fourier

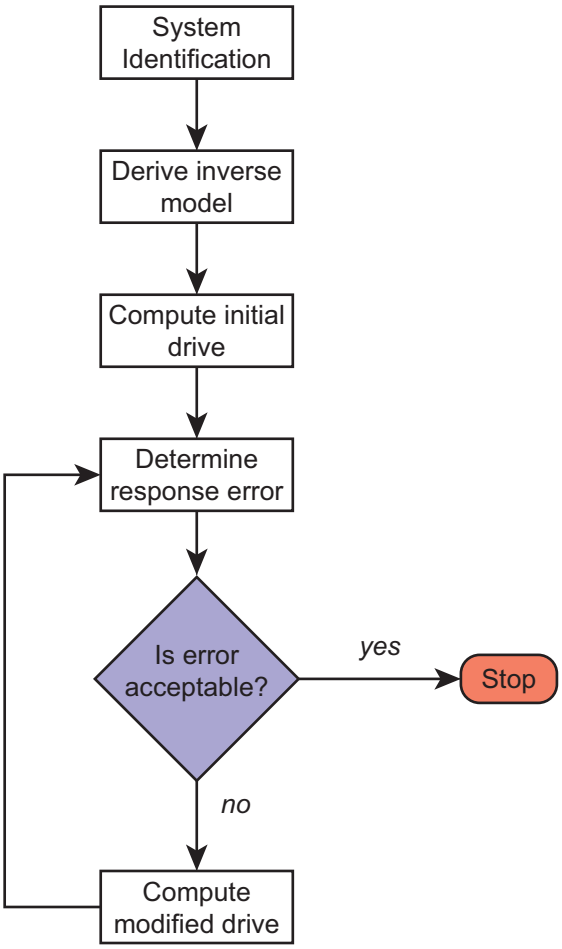

Figure 1.9: Schematic representation of the Iterative Learning Control scheme

Transform (FFT) algorithm enables fast computation of the drive files in the frequency domain. Each iteration of the scheme starts and ends in a steady-state condition, and this scheme can be used for controlling multi-axis systems, like the ones presented in section 1.1.1 where controlling four to six actuators are common. It also has the distinct advantage that the target signals need not be the targets of the closed-loop variables, i.e. they may be targets for sensors placed elsewhere on the dynamic setup [67]. The frequency domain based identification of the forward linear model can lead to the identification of a non-minimum phase plant, but since the off-line approach can compensate for non-causal controllers with delays and since the reference signal is completely known a priori, this is not a limitation

[21, 79]. The requirement of a global linear model identification means that it forms the basis for the main limitation of the ILC scheme because the linear model identified would only be an estimate of the generally nonlinear test rig. To ensure stability of the iterative process, a conservative iterative process is required that significantly slows down the time required until an acceptable error is achieved in the responses.

1.2.2 Advances to the Iterative Learning Control scheme

Many variations to the ILC scheme have been suggested in literature to compensate for the deficiencies encountered in the control of the hydraulic actuators, plant modeling and the iterative process.

1.2.2.1 Frequency domain methods

The first method of improving the ILC scheme is with the system identification phase of the process. The most convenient method, and the one most commonly used in commercial DFID software, is to identify the Frequency Response Function (FRF) using the H_1 estimator technique [3], which is appropriate here since the input drives sent to the actuators are known exactly, and it is assumed that there is no noise present in the inputs. This is, by definition, a linear model estimate of the dynamic system which usually shows many nonlinear behaviors especially at higher amplitudes. A "good" identification of the forward system model hence requires uncorrelated inputs with higher amplitudes, or at the correct excitation levels that produce such nonlinear behavior across the frequency band of interest. This might not always be possible since the actuators may be limited in the magnitude of displacements or excitations they can produce especially at higher frequencies or the specimen could be damaged during the identification phase due to larger sustained excitations which then yields

a "poorer" linear model of the nonlinear dynamic system [66]. The poor identification of the nonlinear behavior can lead to slower convergence during the iterative scheme or even divergence in the case of harsh nonlinearities. For displacement-controlled actuators, "white-pink noise" drives with constant magnitude spectrum at the lower frequencies, a decreasing amplitude spectrum at higher frequencies and uniformly distributed random phase for all the frequencies of interest is suitable for initial system identification, since this is uncorrelated in nature and also prevents large amplitudes at higher frequencies from endangering the specimen or the equipment [19].

As shown in Figure 1.9, the purpose of an improved forward model identification is the computation of the inverse model that is consequently used for the derivation of the drive files. Cornelis et al. describe an adaptive modeling technique that improves the TWR convergence for nonlinear systems by updating the identified inverse model based on the difference between the predicted (produced by the identified forward linear model using the H_1 estimator technique) and measured responses on the test rig. Updating the inverse model between each off-line iteration was shown to produce improved convergence rates and also prevent divergence in some cases of harsher nonlinearities. Manabe and Miyazaki also suggested a similar tuning of the inverse model in the frequency domain based on a local linearization approach.

While improving the H_1 estimation technique can yield good results, other methods of system identification have been described in detail in the literature. The Recursive Least Squares (RLS) or the Recursive Extended Least Squares (RELS) algorithms are used for parameter estimation of closed loop dynamics [78], which can lead to identification of a system with unstable zeroes, i.e. a non-minimum phase (NMP) system. Tomizuka presented the Zero Phase Error Tracking Algorithm for NMP systems that was further discussed by Butterworth et al. for DFID applications to derive stable inverse feed-forward controllers

that can be used in the ILC scheme.

An extension to the frequency domain based ILC scheme was presented by Cuyper et al. that describes an augmented, real-time, mixed sensitivity $\mathcal{H}_\infty$ optimization based feedback controller that reduces the tracking error in the frequency band of interest. While this formulation can reduce the number of iterations required to achieve an acceptable level of error for the ILC scheme, the author states that the feedback controller has limited performance in cases where the identified dynamic system contains delays or NMP zeroes. Tang et al. proposed a DFID method that combined the identification of a system using the RELS algorithm, an internal model control scheme to compensate for the modeling errors due to nonlinearities present in servo control systems and the real-time feedback controller proposed in [16].

1.2.2.2 Time domain and online methods

Despite frequency domain iterative techniques being widely used in the industry, time domain methods have also been developed over the years. With increasing computation capabilities in modern signal processing tools, time domain methods have found increasing potential for using nonlinear techniques for the DFID problem. Raath and Waveren introduced a DFID method that makes use of state-space models instead of the typical frequency domain transfer function models that replace the use of FFT analysis. The authors describe a method of formulating a state space model using Autoregressive Moving Average models with exogenous inputs (ARMAX) that also allows direct inversion to derive the inverse required for determining the required drive files. Cuyper and Verhaegen also presented a novel approach for DFID by using a developed class of "MOESP Subspace Identification Method" [101] to identify a state-space model for which the computation cost is comparable to conventional FRF techniques and the inversion of the state-space model is performed using the Stable

Dynamic Inversion procedure [35]. The determination of the required control inputs using this method then becomes a state reconstruction problem which can be solved using the Kalman filtering framework.

System identification of the forward model and the inverse model can also be performed using adaptive techniques such as the Least Mean Square (LMS) algorithm. The gradient descent LMS algorithm was first introduced by Widrow and Stearns and can be used for system identification of dynamic systems as Finite Impulse Response (FIR) filters. This thesis will use the LMS algorithm as the basis for system identification procedures for DFID and will be discussed further in Chapter 2.

Roberts and Hay recast the DFID problem as a system of algebraic equations for which numerical solutions exist in the form of iterative Newton's method. The authors describe that derivation of the ideal solution requires knowledge of the explicit form of the nonlinearity to compute the Jacobian of the vector-valued function which is not known in most practical applications. Hence, a "quasi-Newton" method is considered where an initial estimate of the Jacobian is considered, usually the circulant matrix constructed using the FIR filter of the identified nonlinear system that is then updated iteratively. While the algorithm presented is computationally efficient, care must be taken in choosing the initial estimates and the step-sizes used for the iterative procedure to ensure global convergence even in the cases where a unique solution exists.

Many of the methods described previously in this section have focused on off-line iterative methods, i.e. the system identification phase and the update of the drive files based on the results of the previous iteration are computed away from the test rig and the responses from the dynamic system are measured in batches. Off-line methods have the distinct advantage that linear NMP plants or plants with delays do not affect the adaptation process and can be accurately controlled. But, this requires accurate estimation of the dynamic system model

and the inverse function for accurate response replication and the dynamic system has to undergo repetitive excitations which can break the specimen [98]. Additionally, the assumption is that the dynamic system and its inverse model, especially in the case of nonlinear systems are time-invariant through the course of the testing procedure which need not be true [67]. Inverse frequency response functions also may not satisfy the real-time requirements of these test rigs due to the computational burdens of the FFT and inverse FFT algorithms that form the basis for many of the frequency domain iterative controllers. Online adaptive controllers such as the gradient descent based LMS algorithm and its derivatives for system identification [105], the Adaptive Inverse Controller (AIC) [106] for direct identification of the inverse model of the dynamic system and the Minimal Control Synthesis (MCS) algorithm developed as an extension to the Model Reference Adaptive Control algorithm [85] have been investigated for DFID applications to remedy these shortcomings [20, 34, 45, 77].

1.3 Problem Statement

The main challenge in the Service Environment Replication problem for dynamic system testing in a lab is the Drive File Identification phase, which is a practical control problem with the requirement of achieving accurate tracking results of responses on test rigs in the shortest amount of time. Drawing inspiration from the many solutions presented in literature and using the signal processing tools available, it is the objective of this dissertation to develop a novel algorithm for DFID with the ability to synthesize arbitrary time domain waveforms. In addition to the primary DFID objective of achieving accurate tracking of responses, there is a fundamental need for a mathematical foundation to quantify the achievable performance, both in terms of the final responses achieved by the system-under-test and the amount of time required to converge to those results. The latter is a non-trivial problem considering

that in real-world test rig experiments, the time spent is dependent on operator skill and experience, software packages available to process data and the ability to tune the DFID algorithms for a range of dynamic systems and target responses. In this thesis, for the iterative solutions that will be investigated, the number of iterations required to achieve an acceptable error in the target response will be the quantitative measure for the time spent.

Frequency domain based methods, as discussed in section 1.2.1, inherently assume linearity and salvage performance for nonlinear dynamic systems using iterative algorithms or complicated compensators. The use of adaptive time domain algorithms is hypothesized to be more robust to a wider class of nonlinearities with improved modeling performance, better control over inversion algorithms and faster convergence of the drives that produce acceptable target responses on test rigs. A time domain based DFID method would also serve the requirement to select unique convergence rates over different time intervals in a test sequence for which the conventional frequency domain iterative methods show poor performance.

While many solutions have been developed for the DFID problem, the question of existence and uniqueness of a solution, in this case, the drive files that replicate the target responses on a test rig, has not been thoroughly investigated in literature. When a "perfect" solution does not exist, it is still possible to derive drive files that reduce the tracking error of the responses to a certain degree, but this usually takes a large amount of time and resources. The lack of guidelines, based on the dynamic system-under-test and the set of target responses to be achieved, in order to identify the method of DFID that would best provide the solution to the DFID problem is a research gap.

1.4 Contributions

The first novel step in the development of the proposed approach to this problem was to recognize the DFID block diagram of Figure 1.8 as a representation of the Active Noise and Vibration Control (ANVC) dynamics associated with using secondary path inputs to cancel noise and/or vibration caused by the primary path. Although the diagram is essentially the same for both ANVC and DFID, the nomenclature, objectives, causality, and the known solution approaches have significant differences. More importantly, there are no known control solutions from ANVC, which can directly be applied to the DFID problem.

The first main contribution of this thesis is the development of a novel DFID algorithm, called the "Pulse Train Filtered-x Least Mean Square (PT-Fx-LMS) algorithm for DFID", leverages existing structures from ANVC, where possible, to build the foundation of a general methodology for the DFID problem with the ability to synthesize arbitrary time domain waveforms. The design of the controller is discrete-time oriented and hence does not require any discretization of continuous-time models and the system models exclusively use Finite Impulse Response (FIR) models to enforce stability and safety of actuator limits during tests. The architecture of this method is consistent with the online adaptive methods discussed in section 1.2.2. Since off-line iterative methods also offer specific advantages related to ease of computation and independence from time delays and effects of NMP systems, the novel DFID method is extended using an estimation based approach that can further reduce the number of actual test runs on the test rig that constitutes the bulk of the time-consuming DFID process. A termination criterion for the adaptive process is presented here that also makes it more robust to harsh nonlinearities in the dynamic system and simulation results show that divergence in the tracking error can be avoided. The performance of the novel approach to DFID is benchmarked against a conventional ILC approach for DFID using simulation tests

for a simple Single-Input Single-Output (SISO) dynamic system that is still representative of certain automotive rig testing scenarios considered for this thesis. The dynamics considered for these systems are a simple linear spring, mass and damper system, a piece-wise linear model and also cubic nonlinear models that show varying degrees of nonlinearities.

The Multi-Input Multi-Output (MIMO) implementation of the PT-Fx-LMS algorithm beginning with the construction of generic MIMO, Linear Time Invariant (LTI) systems that have a desired range of FIR filter lengths, are causal, minimum phase and fully controllable is presented. Similar to the benchmarking considered for the SISO dynamic systems, the performance of the PT-Fx-LMS method is compared against a conventional ILC implementation that uses adaptive inverse based methods. Simulation study for a quarter-car model that more closely represents the requirements in industrial automotive testing that considers linear and nonlinear dynamic system models is conducted. Specific attention is paid to cases where there exist more sensors than actuators, that is more target signals need to be matched than the number of actuators that can control the dynamic system.

An acoustic experimental study is conducted to validate the proposed DFID algorithm for an SER testing procedure for a range of configurations considering multiple sensors (microphones) and actuators (loudspeakers) in an anechoic chamber. The testing procedure includes the initial measurement of the target response as a stand-in for the service environment response, identification of the dynamic plant and iteratively deriving the drive files. Considerations were made for different bandwidths of the target signals and the effect of shifted dynamics during the replication step compared to the initial reference measurement step.

This research work has resulted in the following accepted and planned peer-review journal publications:

- Balasubramanya B, Southward S C. Pulse Train Fx-LMS Algorithm for Drive File Identification. *Published: Machines. 2024; 12(5):286. https://doi.org/10.3390/machines12050286*

- Balasubramanya B, Southward S C. Estimation-based approach and advancements to the Pulse Train Fx-LMS Algorithm for Drive File Identification *Minor revisions recommended before publication*

- Balasubramanya B, Southward S C. MIMO architecture for Drive File Identification using the PT-Fx-LMS algorithm *Under preparation for submission*

1.5 Thesis Outline

The rest of this dissertation is organized as follows:

Chapter 2 discusses in detail the system identification and inverse model identification methods employed for the development of the proposed DFID algorithm and its comparative methods. This chapter also discusses in more detail the conventional Iterative Learning Control scheme that is widely used in the industry.

Chapter 3 presents the dynamic system test benches under consideration for the validation of these DFID methods, the example target response and discusses in detail the results of the forward system and inverse model identification procedures.

Chapter 4 presents the novel DFID algorithm and a series of case studies demonstrating the performance of the proposed algorithm for the dynamic system test benches under consideration and compares it against the conventional DFID methods. Two particular case studies that closely resemble certain difficult procedures in the SER testing procedure are considered in this chapter that demonstrate the effectiveness of the proposed algorithm.

Chapter 5 improves upon the previously presented novel DFID algorithm using the estimated linear model to run completely offline iterative updates of the drive files in a simulation domain to further reduce the number of batch iterations required to arrive at a suitable drive file to replicate target responses. A termination criterion is also presented that can be used to reduce the number of batch iterations in the simulation domain and ensure stability of the iterative process for harsher nonlinearities of the test bench or deficiencies in the model estimation.

Chapter 6 introduces the architecture for the MIMO implementation of the PT-Fx-LMS algorithm. The novel method for direct control synthesis is demonstrated using a simple, linear, discrete-time test bench and the performance is characterized against a conventional DFID method. An additional case study using a quarter-car dynamic system test bench is also presented considering both square and non-square system functions.

Chapter 7 details the set up of a series of acoustic experiments in various configurations conducted to validate the proposed DFID algorithm.

Chapter 8 concludes this thesis document by providing a summary of the research study and recommendations for future work.

Chapter 2

Background

2.1 Introduction

This chapter will focus on detailing the different signal processing tools that form the basis for the formulation and analysis of the DFID process that will be described in this thesis. The methods described in this chapter are prior art material and is only meant for the reader to be introduced to these tools that will be leveraged for building the architecture of the novel PT-Fx-LMS algorithm for DFID and for setting up a state-of-the-art method used for benchmarking the former.

Section 1.2.1 briefly introduced the workflow used by ILC approaches, which begins with first identifying the forward system model. Section 2.2 will discuss in more detail the system identification phase of the DFID process, for which a frequency domain based approach and a time domain based adaptive method will be presented. The next phase in the DFID process is the identification of the inverse model of the plot which will be discussed in section 2.3. The inverse model can be identified using conventional frequency domain methods, as is used in many industrial solutions, and an adaptive inverse identification method from an identified FIR model will also be presented. The formulation for the Filtered-x LMS algorithm that forms the basis for an adaptive inverse modeling method and the novel algorithm developed in this thesis is introduced in section 2.3.2.2. Section 2.4 discusses in more detail the conventionally used frequency domain implementation of ILC and a similar

implementation using digital filters without loss of generality. Finally, section 2.5 introduces the concept of Normalized Error Energy (NEE) that will be used throughout the thesis to assess iteration quality for adaptive methods.

2.2 System Identification Methods

Different types of hydraulic test rigs have been shown in section 1.1.1 that were classified based on the design of the test rig, the components to be tested, number of actuators, degrees of freedom of control and the sensors used on such test rigs. This section focuses on the identification algorithms that can be used that forms the first step of the DFID process.

2.2.1 Components of a hydraulic test rig

To properly understand the importance of the identification of a "good" system model, it is first necessary to describe the system that is being identified in this process. The purpose of the system identification phase for DFID is not to identify the individual parameters of the system, but the overall dynamics of the plant, denoted in Figure 2.1 by G, between the control inputs (or "drives") and the measured output responses from the test rig. The main components of the test rig that form the dynamic system to be identified are shown in the schematic in Figure 2.1 and are listed below:

Test specimen: This would be the same specimen that has already been tested in its service environment and the objective of the SER process is to replicate the target responses on the test rig. It could be an instrumented vehicle, a component or a subassembly, such as a suspension system.

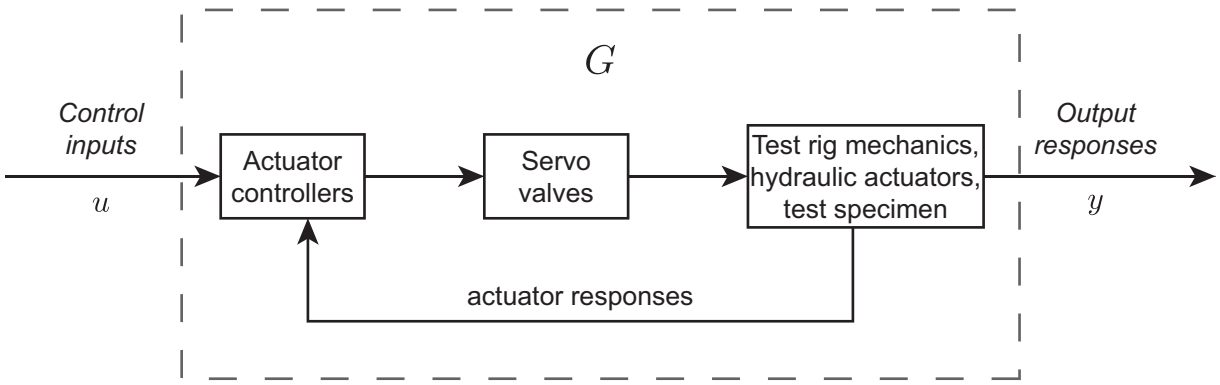

Figure 2.1: Schematic representation of a hydraulic test rig

Mechanical components on the test rig: These form the mounting points, levers, rods and joints that interface the test specimen with the hydraulic actuators. In order to minimize its impact on the overall dynamic system, they are designed to be lightweight and have high stiffness.

Hydraulic actuators: These are the actuators that induce the motions to and forces on the test specimen. The actuators are regulated by servo-valves that control the oil flow rates to the actuators. Actuators in modern test rigs are capable of motions that range from ± 200 mm and can apply forces up to 50–80 kN in the vertical direction at operating frequencies of 50–80 Hz [87], depending on the application.

Actuator controllers: As mentioned in section 1.1.2 on p. 14, the actuator controller can be a PID controller or other forms of feedback controllers that have been developed to control hydraulic actuators. Based on the designed drive files and the measured actuator responses, they generate the current signals that drive the servo-valves.

Sensors: Two sets of sensors are used on test rigs: one set to measure the internal feedback signals used by the actuator controllers and a different set of sensors on the test specimen used to measure the output response of the system.

- Internal feedback signals are usually the displacement and actuator force sig-

nals measured with a Linear Variable Displacement Transducer (LVDT) and load cells respectively. The choice of feedback signals depends on the design of the controller.

- Output responses being measured on the test specimen are usually the displacements and accelerations on different parts of the test specimen that are of interest for the SER testing procedure. These are the responses that need to track the target responses measured on the specimen in its service environment.

The DFID process is aimed at deriving the drive signals u that produces a response y from the overall dynamics of the test rig, G. It does not constitute the tuning of the actuator controllers or make use of the internal feedback signals. Deriving a model, say $\widehat{G}$, of the dynamic system is necessary for the next phase of the conventional DFID method, which is the inversion of the dynamic system model to derive the drive files which will be discussed further in sections 2.3 and 2.4 respectively.

2.2.2 Frequency domain approach

A frequency domain based, iterative approach to the multi-variable tracking problem of DFID was first suggested by Dodds and has been used extensively since on many industrial test rig implementations. A linear, frequency domain model of the dynamic system, the Frequency Response Function (FRF) is first identified using the H_1 estimator technique [3] over a frequency range that covers the spectral energy in the target data, typically from DC to some finite bandwidth.

2.2.2.1 H_1 Estimator technique

The drive signals used for system identification here are distinct from the drives to be derived using the DFID process, and consequently so are the responses of the system during the identification process and the target responses of the SER process. This estimation can be accomplished with a random band limited noise excitation or a swept sine excitation; specific choices about excitation drives will be discussed in section 2.2.2.3. Independent random excitations can be applied to each actuator simultaneously, or alternatively, the excitation can be applied to one actuator at a time. For SISO or for MIMO systems, given the Discrete Fourier Transform (DFT) of the designed input and measured output signals, u and y respectively are given by U_k and Y_k, and are related to the FRF model $\widehat{G}$ at each spectral line ω_k as

$$Y(\omega_k) = \widehat{G}(\omega_k)U(\omega_k) \tag{2.1}$$

From 2.1, a relationship between the cross power spectrum S_{yu} and the input auto power spectrum S_{uu} can be determined as

$$S_{yu}(\omega_k) = \widehat{G}(\omega_k)S_{uu}(\omega_k) \tag{2.2}$$

Hence, the H_1 technique identifies the FRF model, $\widehat{G}$ of the dynamic system G, at each spectral line ω_k as

$$\widehat{G}(\omega_k) = [S_{yu}(\omega_k)][S_{uu}(\omega_k)]^{-1} \tag{2.3}$$

The coherence function is used to validate the identified model since it gives a measure as to what extent the output behavior is explained by the identified linear model excited by

the designed inputs, defined as the ratio of the predicted to the measured output auto power spectra:

$$C(\omega_k) = [\widehat{S}_{yy}(\omega_k)][S_{yy}(\omega_k)]^{-1} \tag{2.4}$$

From 2.1, the predicted auto power spectrum is given by

$$\widehat{S}_{yy}(\omega_k) = \widehat{G}(\omega_k)S_{uy}(\omega_k) \tag{2.5}$$

Substituting 2.3 and 2.5 into 2.4, the coherence function for a SISO system is given by

$$C(\omega_k) = \frac{|S_{uy}(\omega_k)|^2}{S_{uu}(\omega_k)S_{yy}(\omega_k)} \tag{2.6}$$

For MIMO systems with M input channels, the multiple coherence function for the i^{th} output is given by [46]

$$C_{Uy_i}(\omega_k) = \frac{S^*_{Uy_i}(\omega_k)S^{-1}_{UU}(\omega_k)S_{Uy_i}(\omega_k)}{S_{y_iy_i}(\omega_k)} \tag{2.7}$$

where:

- U corresponds to the matrix of M inputs
- S_{Uy_i} is the M-dimensional vector of cross power spectral densities between the array of inputs and output y_i
- S_{UU} is the $M \times M$ matrix of power spectral densities and cross power spectral densities of the inputs
- $S_{y_iy_i}$ is the auto power spectral density of the output y_i

- The $*$ stands for the complex conjugate transpose, also called the Hermitian transpose.

Relatively high coherence (i.e. > 0.75) is required between each sensor and at least one actuator and poor coherence is usually indicative of poor excitation or nonlinearities [24]. An identified linear model will only be able to estimate the nonlinear dynamics of the plant up to a certain extent and is one of the deficiencies of this method, which is compensated during the DFID process by an iterative approach with a conservative iterative step size. It is also common practice to hence limit the frequency range of model inversion to frequencies that correspond with high coherence values. The system identification results can be slightly improved by proper choice of the excitation drives in the identification phase which will depend on the degree of nonlinearity in the dynamic system.

2.2.2.2 Sources of nonlinearities in hydraulic test rigs

A linear model, be it the one developed in section 2.2.2.1 or the time domain FIR filter model that will be developed in section 2.2.3 will only be estimates of the usually nonlinear dynamics that are the components of the hydraulic test rig. Different approaches can be implemented to improve the estimation that will make the DFID process more stable and allow for faster computation of the required drive files using iterative methods. The nonlinear effects of the different components of the test rig appear at different frequencies and amplitudes which determine the ideal choices to be made in the design of excitation inputs of the system identification phase.

In the case of suspension test rigs, which are the primary focus of this thesis, the DFID process primarily focuses on the frequency range from 0 to 50 Hz, with the nonlinear effects most apparent between 0 and 20 Hz due to the dynamic system and convergence issues above 20 Hz due to poor coherence and modeling deficiencies in the identification phase

caused by insufficient excitation levels [19]. In the test specimen itself, the shock absorbers contribute to the majority of the nonlinear characteristics of the plant. This is usually by design to provide adequate comfort to passengers in the vehicle and to limit excessive displacements of the shock absorbers by the use of rubber "bump-stops". While the spring rates are usually fairly linear in the operating range of the suspension, at higher amplitudes closer to full compression of the springs, the bump-stops induce a much higher spring rate limiting vertical deflections despite increased loading [70]. Another nonlinear effect that feature in most suspension springs is the effect of hysteresis, caused by material properties in compression springs [33], frictional (in the case of leaf springs [108]) or thermodynamic (in the case of air springs [55]) dissipation of energy in loading and unloading cycles of the spring. Figure 2.2 shows a representative spring force profile of the vertical force to the vertical displacement of a suspension shock absorber that shows both the bump-stop and hysteretic nonlinear behavior. Beyond the binding point of -50 mm of spring compression, the stiffness of the spring shows a nonlinear increase to almost 10 times the value in the rest of its operating range.

These nonlinear effects only play a significant role for large vertical compressions of the spring and hence their effect is predominantly at the lower frequency ranges from 0 to 10 Hz because higher frequency excitations do not reach such large amplitudes, both in real world testing and on the test rig where the actuators cannot sustain that level of energies. Lateral and longitudinal dynamics are not considered in this thesis, but it is important to note that in real world quart-car suspension test rigs and full vehicle test rigs, bushings in the suspension elements and coupling between horizontal and vertical displacements due to suspension geometry also impart nonlinear dynamics in the lateral and longitudinal directions.

In addition to the test specimen itself, the test rig itself exhibits nonlinear behavior due to the fluid flow in the hydraulic actuators. But these nonlinear effects are slightly

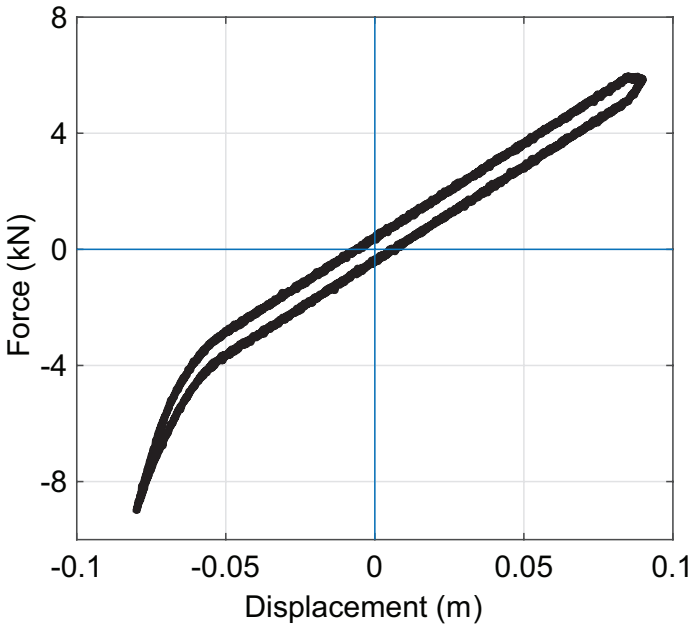

Figure 2.2: Representative nonlinear behavior of a suspension shock absorber in the vertical direction

relaxed by the linearizing effect of the feedback actuator controllers. While PID controllers have limited bandwidth, other controllers like Three-Variable Controllers can increase this bandwidth and the linearizing effect is most strong within this bandwidth [19].

2.2.2.3 Design of excitation drives for system identification

Since the objective of SER is most importantly to reproduce conditions that cause failures in the test specimen, such conditions often involve high-amplitude loading which can lead to the test specimen to behave nonlinearly as described in section 2.2.2.2. The design of the drive files that include correct excitation levels producing good estimation of these nonlinear characteristics is hence critical.

The ideal amplitude spectrum for excitation drives for system identification would be an all-pass, white noise spectrum and the phase is uniformly distributed, random sequence

over the entire frequency bandwidth of interest. This is because equation 2.3 requires that the matrix $S_{uu}(\omega_k)$ be full rank at each frequency for inversion, i.e. the excitation drives for system identification need to be uncorrelated. The amplitude of the excitation drives also need to be at an operating level comparable to the actual service environment where the nonlinear dynamics come into play for the best possible linear approximation. These requirements are often not possible to be met on the test rig because of actuator limitations where it is not possible for the hydraulic actuators with limited bandwidth to provide such high energy (high frequency and high amplitude) excitations to the test specimen. Additionally, repeated high level excitations during the identification phase can often break specimen even before the SER process which undermines the whole durability testing objective. Uncorrelated drives also require no phase relationship between different actuators which is often not possible without causing damage to the test rig components where fixtures and movements are coupled.

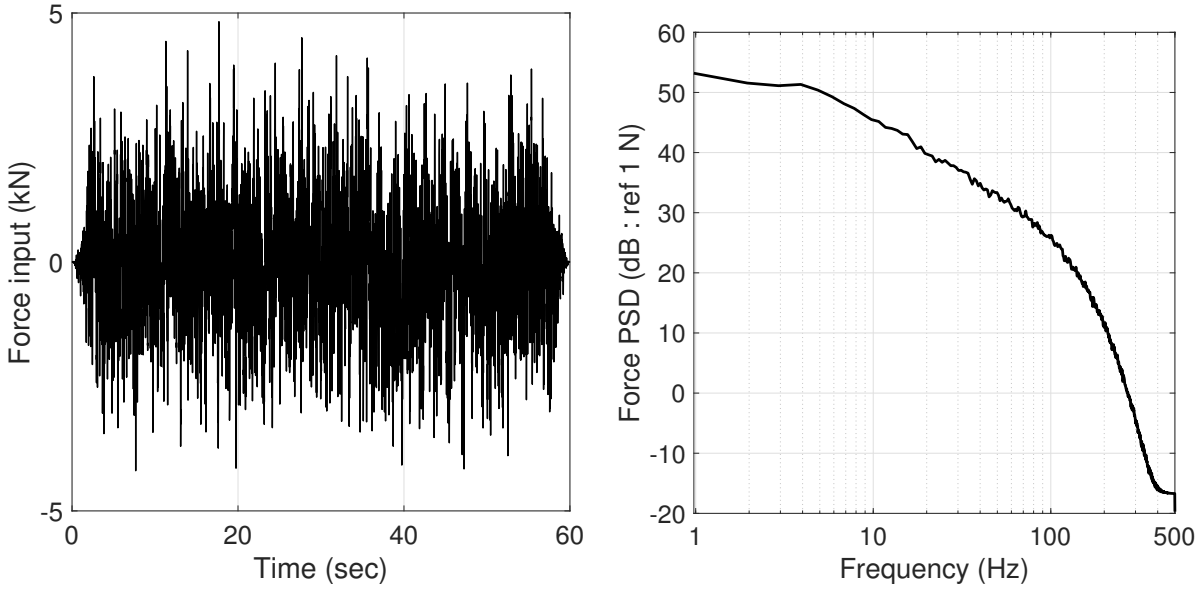

(a) Time domain representation (b) Frequency domain representation

Figure 2.3: Typical identification drive for a test rig with force controlled actuators

Nevertheless, identification drives are designed to approximate the operational conditions

as closely as possible for both the frequency and amplitude requirements without endangering the test specimen. "White-pink noise" drives are hence most commonly used such that high and constant amplitude spectrum is designed for low frequencies with a decreasing amplitude spectrum at higher frequencies to excite the specimen at a sufficient but safe level for "good" identification results. A typical representative identification drive for a force controlled actuator is shown in Figure 2.3 where the uncorrelated, random nature of the drive is evident in Figure 2.3a and the power spectrum that incorporates the requirements of typical force controlled actuators discussed previously is shown in Figure 2.3b where the spectrum shows a constant amplitude from 0 to 5 Hz and the amplitude spectrum decreases at a slope of approximately 20 dB/decade up to 150 Hz and then at a faster rate beyond the typical limits of force controlled actuators for suspension test rigs. To improve model accuracy even further, the identification can be performed with different sets of identification drives, maybe with different excitation spectra, and an average FRF model can be calculated with the coherence function used as a weighting factors for different frequency bandwidths.

2.2.3 Adaptive modeling using the LMS algorithm

Adaptive filters can be used to be model a dynamic system to imitate the input-output characteristic of a plant. The dynamic system is considered as a "black box" with one or more inputs and outputs and both the plant and the adaptive filter are driven by the same excitations and the filter is allowed to adjust, based on different strategies until it converges such that the output of the adaptive model matches the output of the plant. The adaptive filter must contain enough "degrees of freedom", or adjustable weights in order to achieve a close fit or even a perfect fit of the plant response. Even if the structure of the adaptive model may or may not match the dynamic system, the input-output relationship can be replicated to a high level of accuracy [105].

This section will focus on introducing the basic concepts of the adaptive linear combiner that forms the basis of the adaptive modeling technique that utilizes the Least Mean Square algorithm for gradient estimation.

2.2.3.1 Adaptive Linear Combiner

An adaptive linear combiner is one of the most fundamental structures in adaptive signal processing, that can be defined as a time-varying, non-recursive digital filter [105]. It consists of an input signal vector $\mathbf{x}$, a corresponding time-varying set of adjustable weights $\mathbf{w_k}$ and an output signal vector $\mathbf{y}$. The "linear" characteristic of the combiner comes from the fact that for a particular setting of the weights, the output is a linear combination of the input signal.

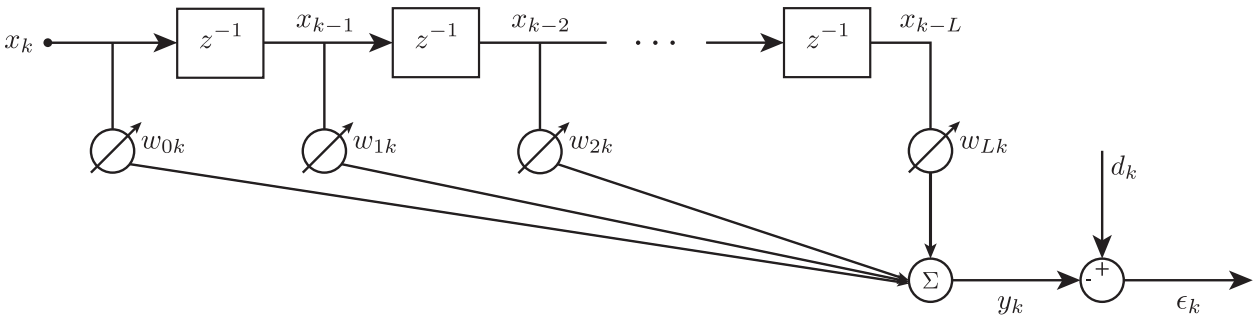

Figure 2.4: Adaptive linear combiner represented as a single input transversal filter with desired response and error signal

The elements of the input signal could be from simultaneous multiple input sources at the k^{th} or described as a sequence of elements collected at time indices $k, k-1, \cdots$. The latter is presented as the temporal form of the adaptive filter, referred to as the adaptive transversal filter, shown in Figure 2.4. The input signal for the single input transversal filter

at the time instant k for an $L+1$ length adaptive filter is given by

$$\mathbf{x}_k = \begin{bmatrix} x_k & x_{k-1} & \cdots & x_{k-L} \end{bmatrix}^T \tag{2.8}$$

The scalar output at the k^{th} time step is hence obtained as

$$y_k = \sum_{l=0}^{L} w_{lk}\, x_{k-l} \tag{2.9}$$

Similar to 2.8, the weight vector is given as

$$\mathbf{w}_k = \begin{bmatrix} w_{0k} & w_{1k} & \cdots & w_{Lk} \end{bmatrix}^T \tag{2.10}$$

With the definitions in 2.8 and 2.10, the output signal in 2.9 can be denoted in vector form as

$$y_k = \mathbf{x}_k^T \mathbf{w}_k = \mathbf{w}_k^T \mathbf{x}_k \tag{2.11}$$

The weight vector typically depends on the output signal and a target signal or desired response in closed-loop, performance feedback systems, where the weight vector is driven towards values such that the output signal closely matches the target signal by minimizing the mean-square value of the error signal. The desired response and the error signal are denoted by d_k and ϵ_k respectively in Figure 2.4. The error signal at the k^{th} time step is simply given as follows

$$\epsilon_k = d_k - y_k = d_k - \mathbf{x}_k^T \mathbf{w}_k = d_k - \mathbf{w}_k^T \mathbf{x}_k \tag{2.12}$$

2.2.3.2 Gradient descent and the Wiener solution

An adaptive algorithm seeks to minimize a cost function by various methods. In the case of the adaptive linear combiner, the cost function is usually the Mean-Square Error (MSE) and the final weight vector upon convergence is the solution that minimizes said cost function. The subscript k is dropped for the weight vector for this analysis since they are not yet being adjusted and the instantaneous squared error can be obtained by squaring 2.12

$$\epsilon_k^2 = d_k^2 + \mathbf{w}^T \mathbf{x}_k \mathbf{x}_k^T \mathbf{w} - 2 d_k \mathbf{x}_k^T \mathbf{w} \tag{2.13}$$

Making the assumptions that $\epsilon_k, d_k, \mathbf{x}_k$ are statistically stationary, the expected value of 2.13 is considered

$$E[\epsilon_k^2] = E[d_k^2] + \mathbf{w}^T E[\mathbf{x}_k \mathbf{x}_k^T] \mathbf{w} - 2E[d_k \mathbf{x}_k^T] \mathbf{w} \tag{2.14}$$

Let $\mathbf{R}$ be the square, input correlation matrix, with the diagonal elements are the mean squares of the input signal elements and the off-diagonal terms are the cross correlations among the input components.

$$\mathbf{R} = E[\mathbf{x}_k \mathbf{x}_k^T] = E \begin{bmatrix} x_k^2 & x_k x_{k-1} & x_k x_{k-2} & \cdots & x_k x_{k-L} \\ x_{k-1} x_k & x_{k-1}^2 & x_{k-1} x_{k-2} & \cdots & x_{k-1} x_{k-L} \\ \vdots & \vdots & \vdots & \ddots & \vdots \\ x_{k-L} x_k & x_{k-L} x_{k-1} & x_{k-L} x_{k-2} & \cdots & x_{k-L}^2 \end{bmatrix} \tag{2.15}$$

Similarly, defining $\mathbf{P}$ as the column vector of cross correlations between the desired response

and the input signal as

$$\mathbf{P} = E[d_k \mathbf{x}_k] = E\begin{bmatrix} d_k x_k & d_k x_{k-1} & \cdots & d_k x_{k-L} \end{bmatrix} \tag{2.16}$$

Note that $\mathbf{R}$ and $\mathbf{P}$ have been defined in 2.15 and 2.16 respectively for the single input signal case and can be defined similarly for the multiple input case for the k^{th} time instant. Using 2.15 and 2.16 in 2.14, the MSE, designated as ξ can be expressed in matrix form as

$$\text{MSE} \triangleq \xi = E[\epsilon_k^2] = E[d_k^2] + \mathbf{w}^T \mathbf{R} \mathbf{w} - 2\mathbf{P}^T \mathbf{w} \tag{2.17}$$

The expression in 2.17 clearly shows that the MSE is a quadratic function of the given weights under the assumption that the input signal and the desired response components are stationary stochastic variables. The "performance surface" for example, for a single weight, say w_0, the MSE function would be a parabola and for an adaptive filter with exactly two weights, the performance surface would be a paraboloid (and a hyper-paraboloid for >2 weights), with a single global minimum value, which is the optimum weight vector.

Gradient descent methods seek to adapt the weight vector to the minimum of the performance surface and the gradient, $\nabla(\xi)$ of the mean-square error performance surface can be calculated by differentiating the expression for ξ derived in 2.17 as

$$\nabla(\xi) \triangleq \frac{\partial \xi}{\partial \mathbf{w}} = \begin{bmatrix} \frac{\partial \xi}{\partial w_0} & \frac{\partial \xi}{\partial w_1} & \cdots & \frac{\partial \xi}{\partial w_L} \end{bmatrix}^T \tag{2.18}$$

$$= 2\mathbf{R}\mathbf{w} - 2\mathbf{P} \tag{2.19}$$

Considering that at the minima of the performance surface, the weight vector $\mathbf{w}$ is at its

optimal value $\mathbf{w}^*$ and the gradient is zero

$$\nabla(\xi_{min}) = \mathbf{0} = 2\mathbf{R}\mathbf{w}^* - 2\mathbf{P} \tag{2.20}$$

the Wiener solution for the optimal weight vector can be given by the Wiener-Hopf equation as

$$\mathbf{w}^* = \mathbf{R}^{-1}\mathbf{P} \tag{2.21}$$

The minimum mean-square error can hence be derived from 2.17 by plugging in the optimal value of the weight vector as follows. Detailed derivation of this expression is shown in [105, pp. 22].

$$\xi_{min} = E[d_k^2] - \mathbf{P}^T\mathbf{w}^* \tag{2.22}$$

2.2.3.3 The LMS algorithm

While an exact solution to the optimal weight vector is numerically ideal, in many practical applications, the performance surface is not known and needs to be measured or estimated, and a slow adaptation process is desired for stability, improved performance and robustness. Different gradient search methods have been proposed in literature, discussed by Widrow and Stearns. An iterative gradient search algorithm can be represented generally as

$$\mathbf{w}_{k+1} = \mathbf{w}_k + \mu(-\nabla_k) \tag{2.23}$$

Note that here, the subscript k is the step or iteration number and rather than the time index used previously. The parameter μ is the iteration constant that is tuned to ensure

stability and maintain a good rate of convergence of the iterative process and ∇_k is the gradient measured for the iteration number k when the weight vector is given by $\mathbf{w} = \mathbf{w}_k$.

Even 2.23 assumes the existence of an exact measurement of the gradient ∇_k at each iteration step for the adaptive process which is usually not available in many practical applications. The estimation of the gradient and its effect on the adaptive process has been thoroughly discussed in [105, ch. 5], but this section is focused on one such estimate of the gradient that forms the basis of the LMS algorithm for the adaptive linear combiner discussed in section 2.2.3.1.

The LMS algorithm considers the square of the error, ϵ_k^2 itself, and not its expected values as an estimate of the MSE, ξ. Using 2.18 and 2.12, the gradient estimate at each iteration step k is hence given by

$$\widehat{\nabla}_k = \begin{bmatrix} \frac{\partial \epsilon_k^2}{\partial w_0} \\ \vdots \\ \frac{\partial \epsilon_k^2}{\partial w_L} \end{bmatrix} = 2\epsilon_k \begin{bmatrix} \frac{\partial \epsilon_k}{\partial w_0} \\ \vdots \\ \frac{\partial \epsilon_k}{\partial w_L} \end{bmatrix} = -2\epsilon_k \mathbf{x}_k \tag{2.24}$$

Substituting 2.24 in to 2.23, the LMS algorithm is hence given by

$$\mathbf{w}_{k+1} = \mathbf{w}_k + 2\mu\epsilon_k \mathbf{x}_k \tag{2.25}$$

The gradient estimate used in the LMS algorithm is convenient since it is obtained from a single sample of the error without any squaring, averaging or differentiation. The adaptive process can be noisy, i.e. does not follow the path of steepest descent on the performance surface due to the imperfect estimate of the gradient, the noise is attenuated by the adaptive process and its convergence characteristic can be investigated for the case when the input signal is considered statistically stationary. Considering that the weight vector is

held constant for this analysis, taking the expected value of 2.24

$$\begin{aligned} E[\widehat{\nabla}_k] &= -2E[\epsilon_k \mathbf{x}_k] \\ &= -2E[d_k \mathbf{x}_k - \mathbf{x}_k \mathbf{x}_k^T \mathbf{w}] \\ &= 2(\mathbf{R}\mathbf{w} - \mathbf{P}) = \nabla \end{aligned} \tag{2.26}$$

The mean value of the gradient estimate is hence shown to be equal to the true gradient derived in 2.19, hence $\widehat{\nabla}_k$ is an unbiased estimate of the gradient. The weight vector $\mathbf{w}_k$ is also shown to be a function of the past input vectors, and if successive input vectors are independent over time, it can be shown that the expected value of the weight vector $E[\mathbf{w}_k]$ also converges to the Wiener solution given in 2.21 [105, pp. 102].

The above described convergence is guaranteed, as given by Widrow and Stearns, only if the iteration constant is bound by the maximum eigen value of the input correlation matrix, $\mathbf{R}$

$$\frac{1}{\lambda_{\max}} > \mu > 0 \tag{2.27}$$

It is also noted that $\lambda_{\max}$ cannot be grater than the trace of $\mathbf{R}$ and hence, for a transversal filter as given in Figure 2.4

$$0 < \mu < \frac{1}{(L+1)(\text{signal power})} \tag{2.28}$$

The above methods and conditions for convergence have been described considering the stationarity of the input vector. This is necessary for analytic convenience to derive necessary conditions for convergence, but in practical applications, this condition can be relaxed to utilize the LMS algorithm, but in those cases, the analysis becomes much more complex with

no known unconditional proofs of convergence in the literature.

2.2.3.4 System Identification

With the structure of the adaptive transversal filter presented in Figure 2.4, plant modeling or system identification of an unknown dynamic system follows naturally from the developed LMS algorithm in section 2.2.3.3. A basic block diagram for the modeling of a SISO plant is shown in Figure 2.5 and its similarity to the structure in Figure 2.4 can be easily seen. The same input signal is played out to both the unknown dynamic plant to record the desired response signal and to the adaptive transversal filter that estimates an FIR filter model of the unknown plant such that the output of the filter closely matches the desired signal by minimizing the mean-square error.

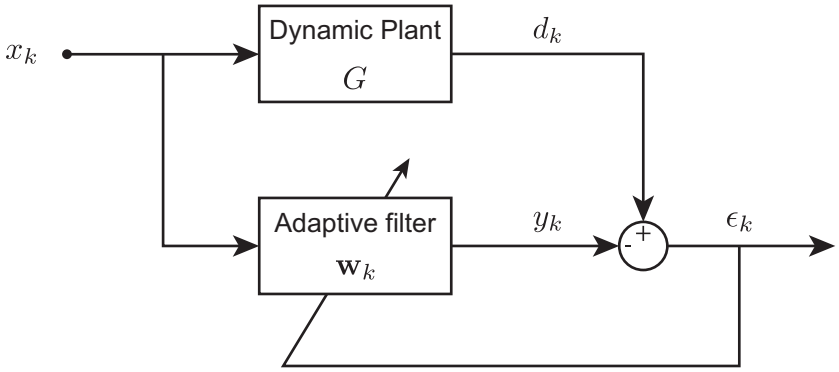

Figure 2.5: System identification of a SISO noise-free plant using an adaptive filter

While the block diagram and the LMS methods presented previously have been for the noise-free case, in real-world test rigs and sensor measurements, the dynamic plant to be modeled and the output responses measured will have a component of noise that will be added to it. This noise is usually uncorrelated with the plant input and the adaptive process will be unaffected by the presence of plant noise, in the sense that upon convergence to a level of MSE determined by the signal power of the noise, the expected weight vector of the

adaptive model will remain unaffected as long as the adaptive filter has sufficient degrees of freedom to model the dynamic system.

The requirements of the excitation input signal are similar for this time domain adaptive system identification method as the ones mentioned in section 2.2.2.3. While the conditions for convergence described in section 2.2.3.3 require uncorrelated input signals, the LMS algorithm can still be used for system identification with correlated drives, although this is known to affect the rate of convergence as a consequence. It is still necessary for the input drives to excite the dynamic system similar to its service environment and to a sufficient level so that any nonlinear dynamics are reproduced on the test rig during the identification procedure in order to estimate a reasonably accurate linear FIR model. Hence, similar drives as in Figure 2.3 can be used for the method described in this section as well.

While the derived FIR filter form of the model will be sufficient for most of the algorithms used in this thesis, it is quite straightforward to derive the equivalent frequency domain transfer function from the derived FIR model by taking the z-transform of the impulse response filter or Discrete Fourier Transform of the impulse response as follows

$$\widehat{G}(z) \triangleq \sum_{l=-\infty}^{\infty} w_{lK}\, z^{-l} = \sum_{l=0}^{L} w_{lK}\, z^{-l} \tag{2.29}$$

$$\widehat{G}(\omega) = \widehat{G}(z)\,\big|_{z=e^{j\omega}} = \sum_{l=0}^{L} w_{lK}(e^{j\omega})^{-l} \tag{2.30}$$

where:

- ω represents the frequency in normalized units (*radians/sample*) and the substitution $\omega = 2\pi f/f_s$ can be made to change the units of frequency to *cycles/second*, where f_s is the sampling rate of the input signal in *samples/second*.
- The summation only ranges from 0 to L, because for a causal filter, the value of the

filter coefficients for $l < 0$ are zero and the filter has a finite length L.

- The subscript K in w_{lK} denotes that this transfer function is calculated for the weights or the FIR filter at the end of the adaptation process where each iteration step is denoted by the smaller-case k.

2.3 Inverse model identification

The next phase of the DFID procedure is the identification of an inverse model of the identified plant. As in section 2.2, two methods of inverse model identification are presented here: the conventional frequency domain method that is most commonly used in the current state-of-the-art applications and an adaptive filtering method to identify an FIR model of the plant inverse using a modification of the previously presented LMS algorithm, called the Filtered-x LMS algorithm.

2.3.1 Frequency domain approach

In the conventional frequency domain approach, the identified transfer function, $\widehat{G}(\omega_k)$ derived in equation 2.3 is inverted at each frequency ω_k. In the case of MIMO systems, the derived transfer function matrix is inverted at each frequency and in practical applications, it is usually the case that this matrix is not a square matrix because most test rig setups are over-determined systems with more sensors (or targets) than actuators. It is also possible to have under-determined systems, but this situation almost never happens in real world applications. In either case, direct inversion is not possible and a pseudo-inverse of the transfer function matrix is calculated in a least-squares sense. Using the pseudo-inverse, the

left inverse of the derived FRF matrix is hence given by

$$\widehat{G}^{+}(\omega_k) = [\widehat{G}^{*}(\omega_k)\widehat{G}(\omega_k)]^{-1}\,\widehat{G}^{*}(\omega_k) \tag{2.31}$$

More recently, the pseudo-inverse can be derived based on singular value decomposition (SVD) [18] to ensure numerical stability in the case where the derived FRF matrix is close to singular by leaving out the singular values that are close to zero. Given the decomposition of the FRF matrix at each frequency ω_k as

$$\widehat{G}(\omega_k) = U\Sigma V^{*} \tag{2.32}$$

where U and V are the left and right singular vectors respectively and Σ is the diagonal matrix of singular values, the pseudo inverse is given as

$$\widehat{G}^{+}(\omega_k) = V\Sigma^{+}U^{*} \tag{2.33}$$

While the above inverse models can be directly used in the cases where the identified model $\widehat{G}_{\omega_k}$ is minimum phase, i.e. all the zeroes are stable and inside the unit circle, the inverse derived from this model cannot be used directly in the cases where the identified forward model is non-minimum phase (NMP), since the inverse would then have unstable poles and make the ILC scheme unstable. In such cases, the inverse model poles need to be stabilized before its use in the DFID algorithms for which different methods have been proposed in literature [6, 71]. Most of these methods depend on introducing delays to the transfer function that can be a detriment to real-time DFID techniques, but since the conventional methods are usually off-line iterative methods, this is not a limitation.

2.3.2 Adaptive inversion techniques

2.3.2.1 Adaptive inverse modeling using the LMS algorithm

The foundation for inverse modeling using adaptive technique follows from the development of the LMS algorithm developed in section 2.2.3.3. In its simplest form, adaptive inverse modeling can be represented by the block diagram shown in Figure 2.6a with an input x_k to the actual plant to be inverted, plant noise n_k considered here for generality and an adaptive transversal filter used to represent the inverse model that is driven by the error between the inverse model output and the input to the plant. In the absence of the plant noise, a low enough value of the adaptation step size μ and with enough weights included in the adaptive filter, the transfer function of the inverse model filter would be the reciprocal of the transfer function of the plant, and when cascaded, their combined transfer function would ideally be close to unity upon convergence with a low enough value of the error, ϵ_k [105].

The presence of plant noise will affect the performance of the adaptive LMS algorithm, raising the minimum mean-square error that can be achieved once the adaptation is converged while simultaneously rejecting the noise and identifying an inverse model of the plant. Additionally, real-world dynamic plants are causal in nature and the to ensure the inverse is also a causal adaptive filter, it is often necessary to include a delay in the identification of the inverse to avoid the need for a predictive adaptive filter. This scheme is shown in Figure 2.6b with Δ samples of delay. This enables the adaptive process to achieve a lower minimum value of the mean-square error. Such a delay is also advantageous in the many cases where the dynamic plant to be inverted is NMP, which would allow the inverse plant model to be two-sided and also remain causal. In the applications of interest for this thesis, an identified delayed inverse is perfectly applicable since the iterative algorithms are mostly computed off-line.

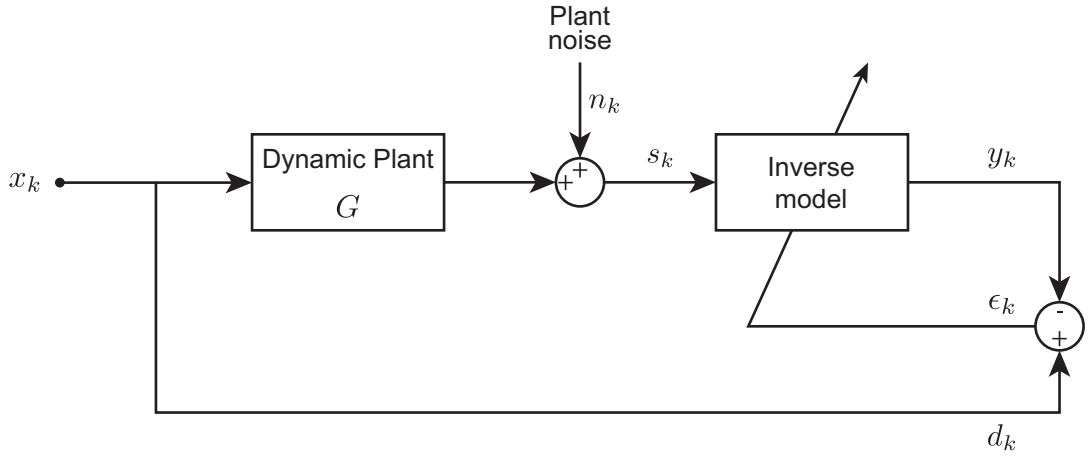

(a) Modeling scheme when no delay is considered

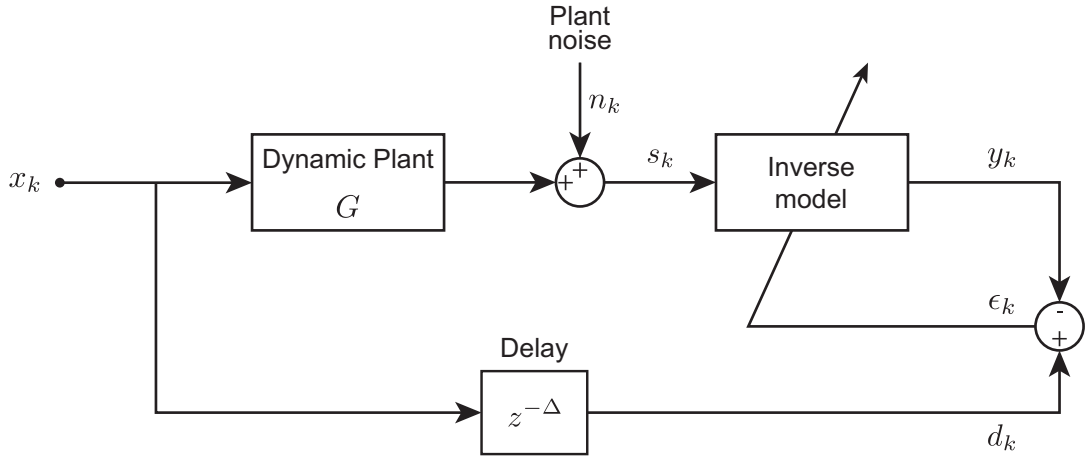

(b) Modeling scheme when Δ samples of delay is considered

Figure 2.6: Adaptive inverse modeling schemes

The choice of the number of samples of delay required depends on the length of the adaptive filter that models the inverse of the plant, with a good rule-of-thumb being a delay equal to half the number of samples of the filter. This choice also depends on the magnitude of noise present in the system since distortion of the inverse solution can result in such cases. Once the adaptation has converged, the convolution of the FIR filter that models the dynamic plant and the adaptive filter of the delayed inverse would ideally result in a single impulse with a delay of Δ. Although such a method of inverse modeling can yield

good results, the least-squares solution is sensitive to noise and can result in ineffective plant inverses being modeled that cannot be used for many practical implementations.

While a significant amplitude of plant noise is disadvantageous to the overall performance of the adaptation in terms of the final achievable minimum MSE, a small amount of random dither added to the reference signal of the adaptive process, in this case the estimated control signal u_k is known to promote smooth and constant adaptation, especially in cases where the reference signal activity is insufficient to sustain the adaptive process [105]. An adaptive inverse model based control system, as is required for the DFID process is shown in Figure 2.7 which combines the inverse model identification blocks of Figure 2.6 and the control problem of deriving the drive file to replicate a target response. This method of DFID is similar to the methods discussed in this thesis except that this method only gives an initial estimate of the drive files for the iterative methods described, especially the conventional methods that will be described in more detail in section 2.4.

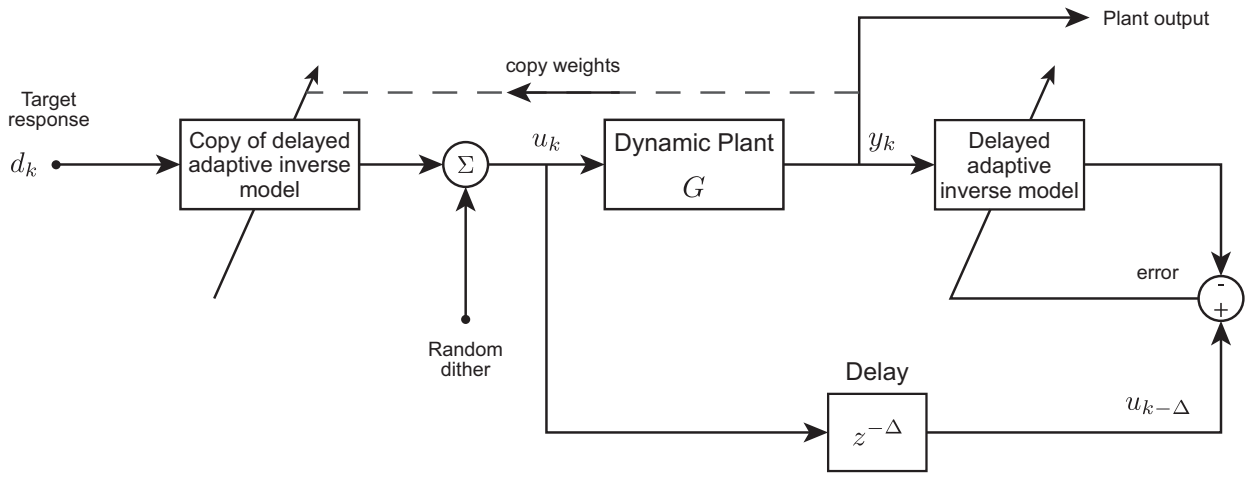

Figure 2.7: Adaptive inverse model based control system

2.3.2.2 Filtered-x LMS algorithm

Looking back at Figure 2.6, it can be seen that the input to the adaptive filter model is directly affected by the plant noise and hence, the output and the error signals are also corrupted by the noise, with the latter driving the LMS algorithm. This was the motivation for the development of the Filtered-x LMS algorithm. The primary difference is the commutation of the adaptive inverse filter and the plant model in the cascaded sequence because of which the plant noise does not appear in the adaptive filter input. Considering that the goal of an LMS algorithm is the minimization of the MSE, if the error signal, ϵ_k, i.e. the difference between the plant output and the desired target response is to be used, commuting the filter blocks consequently requires the derivation of the correct input to the adaptive filter since d_k and ϵ_k in this scheme would be the target response and error signal of the plant output and not the filter output as in Figure 2.6. Widrow and Stearns suggested filtering the reference input x_k through a model of the dynamic plant, $\widehat{G}(z)$ which can be derived using the system identification procedure discussed in section 2.2.3.4, as shown in Figure 2.8, which is why this method is called the Filtered-x LMS algorithm.

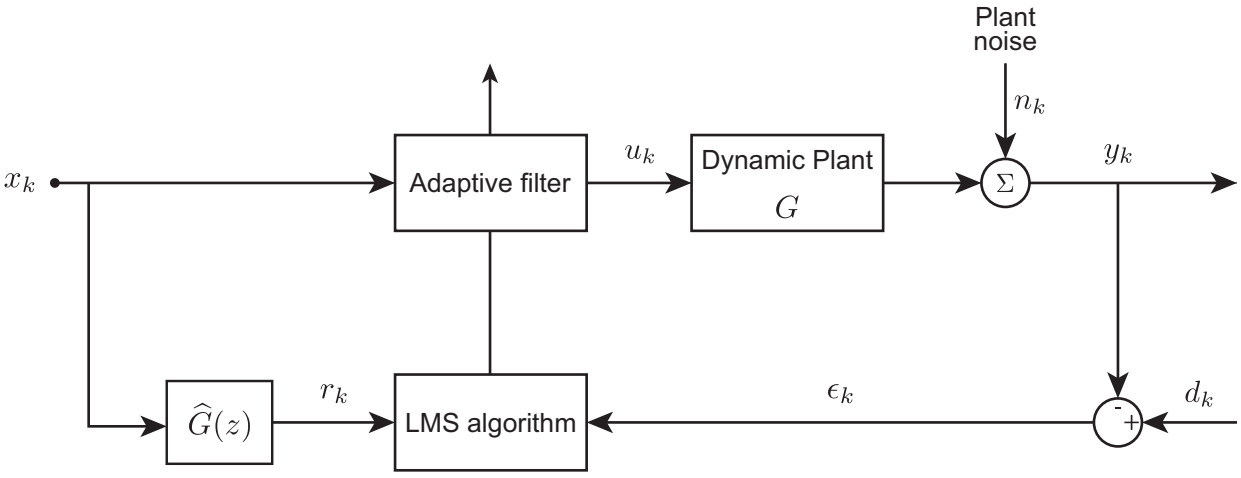

Figure 2.8: Block diagram of the Filtered-x LMS algorithm

This adaptation scheme works under the assumption that the plant and the adaptive

filter blocks can even be commuted as has been presented above. This is valid when the filter blocks are linear and time-invariant. But, the adaptive filter block is neither linear nor time invariant. Despite this fact, the plant and filter blocks are commutable to a good approximation if the plant is linear and if the time constants of the plant and filter FIR were long compared to the combined time constant, which is usually the case for slow adaptation rates. In practice, rapid adaptation has been achieved using the filtered-x algorithm, with performance and convergence conditions similar to the LMS algorithm [105].

Figure 2.9: Block diagram of adaptive inverse control using the Filtered-x LMS algorithm combined with the system identification process

The use of the plant model to filter the reference input instead of the plant itself has also been shown to be robust, and the model does not need to be very precise in order for the filtered-x algorithm to drive the adaptive weights to a delayed inverse of the plant, as shown by the adaptive inverse model control scheme presented in Figure 2.9. Note that the system identification process can be performed separately if there is a requirement for separate identification drives as discussed in section 2.2.2.3.

Without considering the random dither mixed with the reference input and the additive plant noise in Figure 2.9, the adaptive algorithm for the inverse model weights at each time instant is given as follows

$$\mathbf{w}_{k+1} = \mathbf{w}_k + \mu\epsilon_k\mathbf{r}_k \tag{2.34}$$

where $\mathbf{w}_k$ is the entire FIR filter that models the inverse of the dynamic plant at time step k with enough weights to model the dynamic inverse, ϵ_k is the instantaneous scalar output error (in the case of a SISO plant) for the k^{th} iteration at the time instant being evaluated

and is given as

$$\epsilon_k = d_{k-\Delta} - y_k \tag{2.35}$$

Given the plant model $\widehat{G}$ is represented by an $L+1$ length FIR filter with coefficients $\widehat{G}(z) = \begin{bmatrix} \hat{g}_0 & \hat{g}_1 & \cdots & \hat{g}_L \end{bmatrix}^T$, the filtered reference signal r_k is given by

$$r_k = \sum_{l=0}^{L} \hat{g}_l \, d_{k-l} \tag{2.36}$$

Upon convergence of the adaptive algorithm, the filter weights represent the delayed adaptive inverse of the dynamic plant and can henceforth be used for the iterative DFID procedure discussed in the next section.

2.4 Conventional Iterative Learning Control scheme

Upon the identification of the forward linear model of the dynamic system and the inverse model as discussed in the previous sections, the conventional ILC scheme, as used most commonly in industrial test rigs, is the next phase of the DFID process which involves an iterative process to derive the required drive files for target simulation. While the specifics of the solutions offered by industrial manufacturers of servo-hydraulic test rigs are not readily available in order to protect their intellectual property and competitive advantage, information gleaned from filed patents [2, 31, 54] and available literature [13, 15, 19, 25, 26] about this conventional method give enough details to analyze the DFID method and use as a benchmark for the novel algorithms presented in this thesis.

2.4.1 General frequency domain procedure

The conventional ILC method for DFID is a frequency domain based method because the identified system is a frequency domain FRF as described in section 2.2.2.1, specifically equation 2.3. The Discrete Fourier Transform (DFT) and its inverse (IDFT) are used to make the necessary transformations of the signals from the time domain to the frequency domain and vice versa respectively. Similar to the identification drives in Figure 2.3a, the target response $\mathbf{d}$ is considered to be one period of a periodic signal, because the signal is windowed at the beginning and end of the signal such that the target reference signal in one period begins and ends at zero.

For a real-valued periodic signal of length N given by $\mathbf{x} = \begin{bmatrix} x_0 & x_1 & \cdots & x_{N-1} \end{bmatrix}^T \in \mathbb{R}^N$, the DFT, $\mathbf{X} = \mathcal{F}(\mathbf{x})$ is defined by

$$X_k = \sum_{n=0}^{N-1} x_n \cdot e^{-j\frac{2\pi}{N}kn} \tag{2.37}$$

Similarly, the inverse DFT $\mathbf{x} = \mathcal{F}^{-1}(\mathbf{X})$ for the complex valued sequence $\mathbf{X}$ is given by

$$x_n = \frac{1}{N} \sum_{k=0}^{N-1} X_k \cdot e^{j\frac{2\pi}{N}kn} \tag{2.38}$$

The above defined transforms are used to transform the time domain measured signals of the drive signal $\mathbf{u}$, the target response $\mathbf{d}$, the sensor output $\mathbf{y}$ and the error signal $\mathbf{e} = \mathbf{d} - \mathbf{y}$ into the frequency domain representations given by $\mathbf{U}, \mathbf{D}, \mathbf{Y}$ and $\mathbf{E}$ respectively. The conventional iterative method is shown in Figure 2.10 and described in equations 2.39 - 2.42 below. The dotted lines in the figure below are used to show the operations and signals that are processed off-line and away from the test rig and the subscript i refers to the iteration number, i.e. $i = 1, 2, \cdots$.

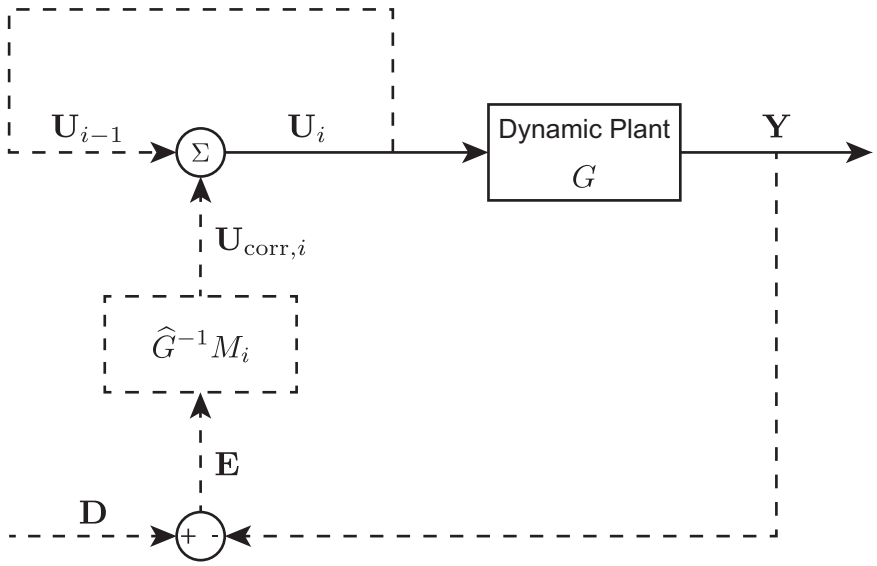

Figure 2.10: Block diagram of the conventional ILC scheme for DFID in the frequency domain

In the presence of large nonlinearities in the dynamic system G and consequently poor estimates of the forward linear model $\widehat{G}$ and its inverse $\widehat{G}^{-1}$, a conservative approach is followed where the iteration is relaxed by an iteration constant with values between 0 and 1. In the case of a single response to be tracked, a single iteration constant μ is considered, whereas Figure 2.10 presents the more general case with multiple target responses being tracked requiring a diagonal matrix M of iteration constants for each channel of the output. The iteration constants can also be iteration-dependent such that faster adaptation rates can be set in the beginning and the iteration constant can be relaxed to smaller values to allow for more stable and accurate adaptation results. The iterative algorithm has two main steps:

1. Off-line calculation of a new drive signal, equations 2.39 - 2.41

2. Output acquisition on the test rig based on the derived drive file, equation 2.42

With the drive and output signals initialized at $\mathbf{u}_{i=0} = \mathbf{y}_{i=0} = \mathbf{0}$, an iterative algorithm is

used to calculate the drive correction, $\mathbf{U}_{\text{corr}}$ and the updated drive based on the response error in the frequency domain as follows for $i = 1, 2, \cdots$ until convergence or an acceptable level of error is achieved.

$$\mathbf{E}_i = \mathbf{D} - \mathbf{Y}_i \tag{2.39}$$

$$\mathbf{U}_{\text{corr},i} = \widehat{G}^{-1} M_i \mathbf{E}_{i-1} \tag{2.40}$$

$$\mathbf{U}_i = \mathbf{U}_{i-1} + \mathbf{U}_{\text{corr},i} \tag{2.41}$$

$$\mathbf{Y}_i = G \cdot \mathbf{U}_i \tag{2.42}$$

Note that the i^{th} drive file is calculated based on the error measured by the application of the drive file calculated during the iteration number $i - 1$. Once an acceptable level of error has been achieved, the iterative adaptation of the drive files is stopped and the final drive file $\mathbf{U}_{\text{final}}$ can be transformed back to the time domain signal $\mathbf{u}_{\text{final}}$ that can be used to drive the test rig for the designed durability test program.

Since this is an off-line process and because the signals shown in Figure 2.10 are in the frequency domain, the measurement of the output needs to be known completely in order to be transformed to the frequency domain using the inverse DFT given in 2.38. Hence, the signals are acquired, and then the drive correction is computed completely off-line. In the presence of a perfectly identified model and a determined inverse, the iterative scheme will show a reducing tracking error until the output perfectly tracks the target signal, limited only by the presence of measurement noise. In practice, since the derived model is never perfectly accurate and the dynamic plant is usually nonlinear, a safe approach is used for the iterative scheme by using smaller values of μ in the matrix of iteration step size constants, M. This will slow down the iterative process, requiring more number of iterations until the desired error is achieved, but will ensure robustness to the model inaccuracies and provide

stability to the process.

2.4.2 Convergence analysis of the ILC scheme

As has been described previously, with the objective of the ILC scheme being the reduction of the MSE of the output response with respect to the desired target response, it is evident that the stability and convergence of this iterative scheme depends on the identified model, the uncertainty in the model with respect to the plant and the choice of the iterative constants. De Cuyper presented a convergence and robustness analysis of this conventional scheme based on the above factors which will be briefly described in this section. The analysis requires an initial assumption to be made about the plant model uncertainty in order to describe the convergence rate of the iterative process based on the method described in section 2.4.1. The multiplicative output uncertainty in the plant model is shown in the frequency domain blocks of Figure 2.11 and defined by

$$G = (I + \Delta G)\,\widehat{G} \tag{2.43}$$

where G is the actual plant dynamics, ΔG describes the model uncertainty of the plant dynamics from the identified plant model $\widehat{G}$.

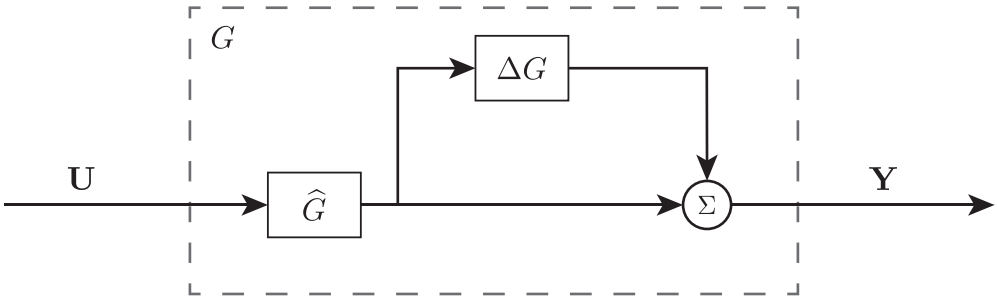

Figure 2.11: Block diagram of the plant with a multiplicative model output uncertainty

Based on the iterative scheme described by equations 2.39 - 2.42 and the model uncer-

tainty defined by 2.43, the error at iteration i can be described as a difference equation as a function of the error at iteration number $i-1$ as follows

$$\mathbf{E}_i = (I - (I + \Delta G)\, M_i)\mathbf{E}_{i-1} \tag{2.44}$$

For the iterative algorithm to descend the performance surface, it is evident that the error must reduce over each iteration in order to converge to a minimum MSE. For frequency domain signals, in this application of interest, it is often sufficient to consider a truncated 2-norm within a limited frequency band. For example, for the error signal $\mathbf{E}$, the truncated 2-norm is given by

$$\|\mathbf{E}(j\omega)\|_{2,t} = \sqrt{\int_{\omega_{min}}^{\omega_{max}} |E(j\omega)|^2\, d\omega} \tag{2.45}$$

To ensure convergence of the iterative process, it is hence required that the truncated 2-norm of the output error reduce over iterations, that is

$$\|\mathbf{E}_i\|_{2,t} < \|\mathbf{E}_{i-1}\|_{2,t} \tag{2.46}$$

Based on 2.46, it can hence be deduced from 2.44 that

$$\|I - (I + \Delta G)\, M_i\|_{2,t} < 1 \tag{2.47}$$

In the case of a SISO system and considering a constant step-size $0 \leq \mu \leq 1$ across iterations,

2.47 reduces to

$$|1 - (1 + \Delta G)\,\mu| < 1 \tag{2.48}$$

$$\Rightarrow \left| \left(\frac{1}{\mu} - 1 \right) - \Delta G \right| < \frac{1}{\mu} \tag{2.49}$$

2.49 can be interpreted as follows [100]: the iterative method will converge if the model uncertainty ΔG lies within a circle centered at $\left(\frac{1}{\mu} - 1, 0\right)$ and a radius of $\frac{1}{\mu}$ on the complex plane. While this provides a theoretical understanding for the convergence of the ILC scheme, in practice, the iteration step-size is usually chosen by trial and error, beginning with a safe approach and slowly tuned such that rapid adaptation and stability are maintained since the multiplicative model error ΔG is never explicitly known.

2.4.3 Alternative time domain ILC scheme

When the identified system model and the inverse are time domain FIR filters as shown using adaptive methods in sections 2.2.3 and 2.3.2, the ILC scheme described previously for the frequency domain implementation can be applied in the time domain with no loss of generality. The drive correction would hence be calculated as

$$\mathbf{u}_{\text{corr},i} = \widehat{G}^{-1}(z) * (\mathbf{d} - \mathbf{y}_{i-1}) \tag{2.50}$$

where $\widehat{G}^{-1}(z)$ is the FIR filter inverse of the dynamic plant as derived by the adaptive process given in 2.34, $*$ represents the convolution operation and the error is computed in the time domain unlike in 2.39. Despite 2.34 yielding a delayed inverse of the plant, since this calculation of the drive is performed off-line, the delay can be easily compensated for during post-processing before being played out to the dynamic system to measure the output

responses.

Beyond the possible estimation of better system and inverse models using the adaptive methods in the time domain that can improve the ILC scheme for DFID, time domain ILC also provides the benefit of selectively choosing, when necessary, different convergence rates for different time sections of the responses which can be crucial to avoid divergence of the adaptive process when those time sections simulation highly nonlinear events like a suspension on a vehicle hitting a curb or a pot-hole that can compress suspension springs to its binding point or hit its bump stops. The ability to use different step sizes for different time sections can prevent such a single event that is part of the durability testing program from disrupting the rest of the time signal that can iteratively adapt using larger iteration constants.

2.5 Quantification of iteration quality for adaptive methods

Various iterative and adaptive methods have been presented previously for identification of the system model and the inverse and for the iterative control of the DFID process in this chapter and a novel adaptive method will also be presented in this thesis. While overlaid spectrums of the target and the obtained outputs at the end of each iteration can give an initial qualitative assessment of the DFID process, quantification of the time domain MSE is the most common method used in these applications. Widrow and Stearns define the term misadjustment as a dimensionless measure of the excess mean-square error caused by gradient estimation noise relative to the minimum mean-square error produced by an optimal Wiener filter. A lower minimum MSE achieved by an adaptive method hence has a lower

misadjustment since it converges to the optimal Wiener filter.

For tracking controllers, the relative mean-square error with respect to the desired target response hence provides an easily quantifiable measure of the performance. The Normalized Error Energy (NEE) at the end of each iteration is hence defined as

$$NEE_i = \frac{\mathbf{e}_i^T \mathbf{e}_i}{\mathbf{d}^T \mathbf{d}} \tag{2.51}$$

where $\mathbf{e}_i$ is the entire error signal vector at the end of each batch loop iteration i. NEE is a normalized measure of the mean-square error averaged over the entire batch of data, and usually expressed on a decibel scale. NEE essentially measures how close the SER test rig response data is to the desired target data. As with most real-world DFID processes, the adaptive algorithm is terminated when the error is smaller than a predefined threshold. Since this quantity only depends on the output measurements of any identification or adaptive process, a similar quantification of the performance can also be considered for non-adaptive methods like the frequency domain based system model and inverse model identification methods described in sections 2.2.2.1 and 2.3.1.

For the adaptive delayed inverse identification method discussed in section 2.3.2, another useful visualization of the performance of the inversion process is the cascade of the plant model and delayed inverse model FIR filters which is plotted as the convolution of the two filters. In the ideal scenario of the perfect identification of the inverse when the inverse model filter has enough degrees of freedom and an appropriate amount of delay to generate a causal inverse model, the convolution plot would show a single impulse with a value of 1 with a delay equal to number of samples of delay in the inverse model filter, Δ.

An example for a SISO FIR filter model, its identified delayed inverse and the convolution of the two filters is shown in Figures 2.12a - 2.12c. Figures 2.12d - 2.12f presents an example

of an imperfect inverse identification which shows the convolution of the two filter models not having a perfect unitary impulse at Δ and small side-lobes around the sample number Δ. As discussed previously, such results are more common in the situations where the inverse filter does not have enough weights to model the inverse of the dynamic plant, when the plant shows strong nonlinearities or when the excitation drives for the inverse identification process is not spectrally rich enough.

In the case of MIMO dynamic plants with M inputs and N outputs, the dynamic plant model is an $N \times M$ matrix of FIR filters, the identified inverse model will consequently be an $M \times N$ matrix and the cascade of the two will yield an $N \times N$ matrix of impulse responses. In the case of the "perfect" identification of the inverse FIR filter model, the convolved impulse response on the diagonal of this square matrix would have a unitary pulse at Δ and all the other convolved impulse responses will be zero.

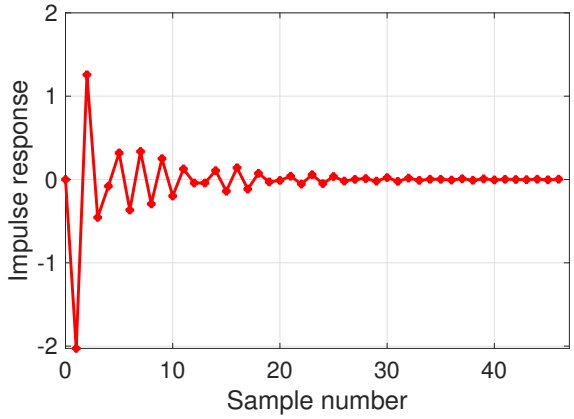

(a) Impulse response of the forward plant model with $L = 47$

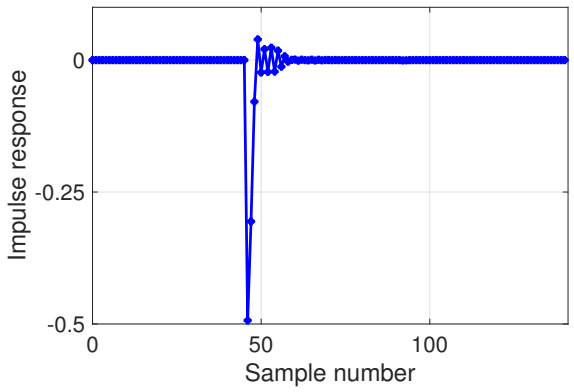

(b) Impulse response of the identified inverse plant model with $L = 141$ and $\Delta = 47$

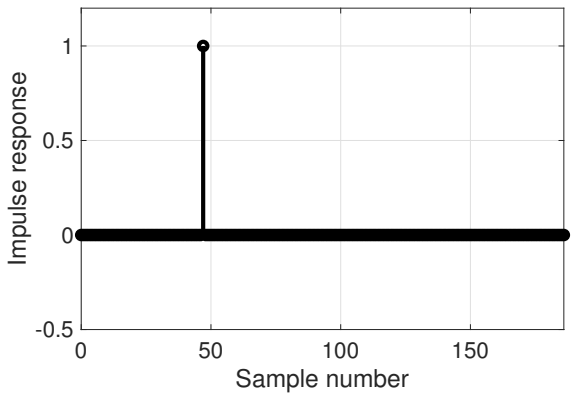

(c) Impulse response of the cascaded plant and inverse models

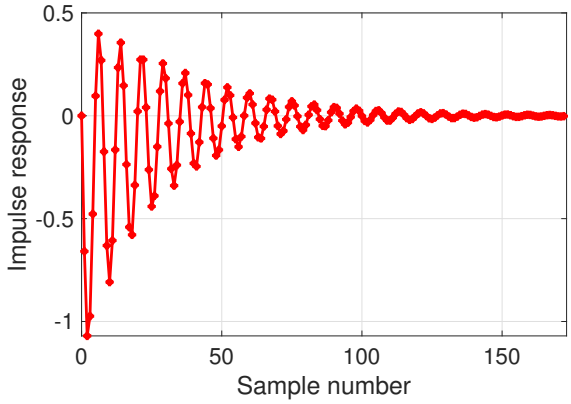

(d) Impulse response of the forward plant model with $L = 173$

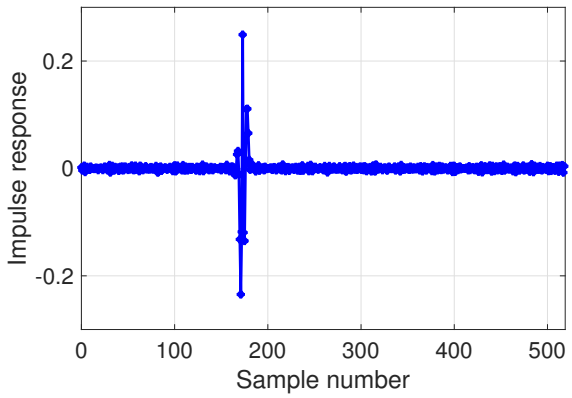

(e) Impulse response of the identified inverse plant model with $L = 519$ and $\Delta = 173$

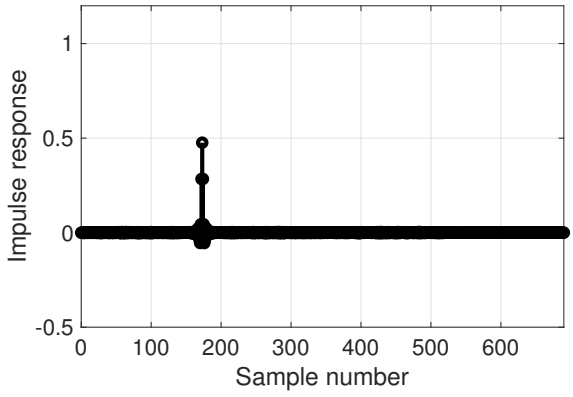

(f) Impulse response of the cascaded plant and inverse models

Figure 2.12: Two examples of an FIR plant model with *perfect* (on the left) and *imperfect* (on the right) identification of the inverse model

Chapter 3

Simulation Test Benches and Target Responses

3.1 Introduction

In this thesis, the novel DFID algorithm that will be developed will be demonstrated on a set of simulated dynamic systems and the same dynamic systems will be used to benchmark the proposed method against the state-of-the-art DFID methods. This chapter will focus on setting up these dynamic system test benches that will be used as a "black-box" with a set of inputs and outputs. Currently, the dynamic system considered is a SISO mass-spring-damper system that is considered as a very basic model of the quarter-car setup of a vehicle. Complexity is introduced to this system by considering different force profiles of the compression spring by introducing forms of nonlinearity that is representative of real-world suspension systems on automobiles.

Section 3.2 will introduce the SISO mass-spring-damper systems considered for the case studies presented in this thesis, considering four different test benches: a purely linear dynamic system, a piece-wise linear spring model and two cubic on-linear spring force profiles. Section 3.3 discusses the target responses that will be considered for the simulation case studies for the specific models being considered in line with the vehicle test rig applications of interest in this thesis. The results of the forward model identification methods as discussed

in section 2.2 and the inverse model identification as discussed in section 2.3 for the considered dynamic systems will be discussed in section 3.4. The time-domain implementation of the novel DFID method also requires a specific representation of the nonlinear dynamic system block for the purpose of deriving the output from the plant for simulation purposes, which will be discussed in section 3.5.

3.2 Dynamic system test benches

For the purposes of representing a dynamic system such as a suspension test rig in a simple manner, a SISO mass-spring-damper is considered with varying forms and degrees of nonlinearities for the spring force. Unlike Figure 2.2 which shows nonlinear behavior of the spring rate and its hysteretic effects for a representative suspension system, the dynamic systems considered here do not include hysteretic nonlinearities. Similarly, the damper in real-world dynamic systems is an inherently nonlinear element in a suspension system with both hysteretic effects that are dependent on the frequency and magnitude of operation and the mean value of the damper force is also never a linear function of the velocity. However, in this thesis only a linear viscous damping model, i.e. the damping force is proportional to the velocity, is considered for simplicity.

For all the plants discussed in this section, the force input, $F(t)$ is the single input to the dynamic system and the vertical displacement of the point mass, $y(t)$ is the only sensor output. Unlike real-world automobiles and test rig setups, the mass has a single degree-of-freedom and hence horizontal displacements or rotational dynamics are not considered.

3.2.1 Linear dynamic system

In its simplest form, the dynamic system considered is a purely linear time-invariant system with a constant spring rate and a linear viscous damper with a constant damping coefficient. The schematic diagram of the dynamic plant is shown in Figure 3.1 and the specific parameter values that are listed in Table 3.1 used to design this plant are representative of actual quarter-car rigs and typical spring and damper rates used in automobiles.

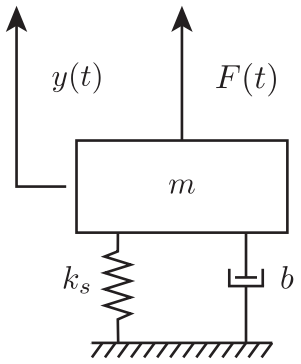

Figure 3.1: Illustration of the simple primary suspension system used as a black-box dynamic plant with one input $F(t)$ and one output $y(t)$

Table 3.1: Parameters for the linear dynamic system used for simulation

Parameter	Details	Units
m	200	kg
k_s	$6.5e4$	N/m
b	$3e3$	Ns/m

From first principles and the free-body diagram of the dynamic system shown in Figure 3.1, the dynamics of the plant are governed by the following second order equation

$$m\ddot{y} + b\dot{y} + k_s y = F(t) \tag{3.1}$$

The same equation can be represented in the conventional state-space form using a pair of first-order ordinary differential equations, with the assignment of the input as $u = F(t)$ and

the vector of state variables defined as $\mathbf{x} = \begin{bmatrix} x_1 & x_2 \end{bmatrix}^T = \begin{bmatrix} y & \dot{y} \end{bmatrix}^T$

$$\dot{\mathbf{x}} = \begin{bmatrix} 0 & 1 \\ -\frac{k_s}{m} & -\frac{b}{m} \end{bmatrix} \mathbf{x} + \begin{bmatrix} 0 \\ \frac{1}{m} \end{bmatrix} u \tag{3.2}$$

$$y = \begin{bmatrix} 1 & 0 \end{bmatrix} \mathbf{x} \tag{3.3}$$

3.2.2 Piece-wise linear dynamic system

Nonlinear dynamic plants are first introduced by considering a piece-wise linear system shown by the illustration in Figure 3.2. The dynamic system is a primary suspension with a stiffness that enters a binding condition after a displacement of $-y_B$. Albeit a simple example, this is actually a very realistic dynamic occurrence for a broad class of vehicles in the motorsports industry.

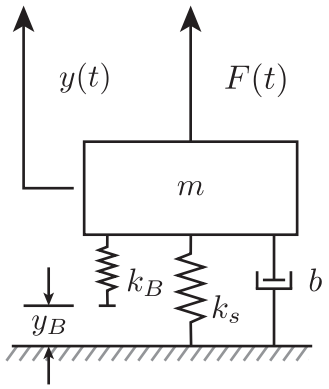

Figure 3.2: Illustration of the SISO piece-wise linear primary suspension system that enters a binding condition

The dynamical equations are stated as follows, with the conditional nature of the effective spring force being the nonlinear component of this plant. The parameters for the considered plant are given in Table 3.2. Additionally, the force profile of the spring for this plant, and

all the others presented in this section are shown in Figure 3.3.

$$m\ddot{y} + b\dot{y} + F_{eq} = F(t) \tag{3.4}$$

where the equivalent spring force is given by

$$F_{eq} = \begin{cases} k_s y, & \text{if } y \geq -y_B \\ k_s y + k_B(y + y_B), & \text{if } y < -y_B \end{cases} \tag{3.5}$$

Table 3.2: Parameters for the piece-wise linear dynamic system used for simulation

Parameter	Details	Units
m	200	kg
k_s	$6.5e4$	N/m
k_B	$3e4$	N/m
y_B	0.05	m
b	$3e3$	Ns/m

As with the other nonlinear plants considered in this section, the exact form of the nonlinearity will not be used explicitly in the formulation of the problem or the solution. The representation of the nonlinear dynamics will be used only for computing the actual response from the plant for simulation purposes as will be discussed in section 3.5 which is replaced in the real-world by the measurement of actual responses on the test rig.

3.2.3 Cubic nonlinear dynamic systems

While the nonlinearity defined by the piece-wise linear system in section 3.2.2 is fairly simple in-terms of its algebraic formulation, the stiffening characteristic in real-world springs is rarely discontinuous. Such spring profiles are more accurately represented by cubic equations,

such as the Duffing oscillator [42] where the stiffness of the spring increases with amplitude. Since the spring force is no longer given by Hooke's law as in equations 3.1 and 3.4 and Figure 3.1, and considering the spring force is denoted by the function $F_s(y)$, the equation of motion is given as

$$m\ddot{y} + b\dot{y} + F_s(y) = F(t) \tag{3.6}$$

$$F_s(y) = a_1 y^3 + a_2 y^2 + a_3 y \tag{3.7}$$

Two dynamic systems are considered for this form of nonlinearity: the first, given by $F_s(y)$ in Table 3.3 is a mild cubic nonlinearity because it deviates from the linear spring profile less than the second plant which has a harsher cubic nonlinearity defined by $F_s^{'}(y)$ as can be seen in Figure 3.3 which shows the spring force profiles of all the dynamic systems considered in this section.

Table 3.3: Parameters for the cubic nonlinear dynamic systems used for simulation

Parameter	Details	Units
m	200	kg
b	$3e3$	Ns/m
$F_s(y)$	$1.2e7y^3 + 1.2e6y^2 + 9.5e4y$	N
$F_s^{'}(y)$	$2.5e7y^3 + 3e5y^2 + 6.5e4y$	N

The compression spring defined by the force profile $F_s(y)$ shows very little deviation from the linear spring defined by the spring constant k_s from section 3.2.1 when the spring is compressed from zero to the binding point y_B and then the stiffness increases continuously as a cubic function. The harsh cubic spring defined by the force profile $F_s^{'}(y)$ shows a fairly linear characteristic around zero but the stiffness increases in both tension and compression at higher deflections to almost eight times the stiffness at lower deflections.

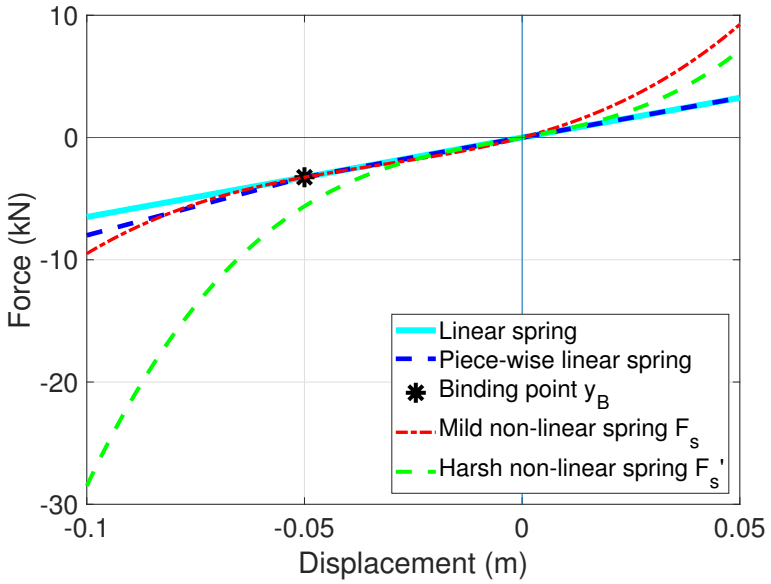

Figure 3.3: Spring force profiles of the different linear and nonlinear dynamic plants considered

3.3 Target responses for simulation case studies

The target data used for the simulation case studies for the SISO dynamic systems is the chassis displacement measured on an actual vehicle relative to the track surface during a 25-second lap around a test track as shown in Figure 3.4. Displacement of the chassis is usually measured using a laser ride height sensor, and it is the objective of the DFID process to replicate this response on the test rig to a reasonably accurate degree. The signal is sampled at a rate f_s of 1000 Hz. For the simulation case studies presented for the SISO implementation of the current state-of-the-art and the novel algorithm, this same target response will be used, with the aero-loader force $F(t)$, as shown in Figures 3.1 and 3.2 being the control input to the test rig to be derived by the DFID process.

While Figure 3.4 provides a description of a measured signal, for simulation purposes it is also useful to define a more generalized scheme for designing target responses. Standardized, artificial road profiles such as the ISO 8608 [93] road profile characterizations are

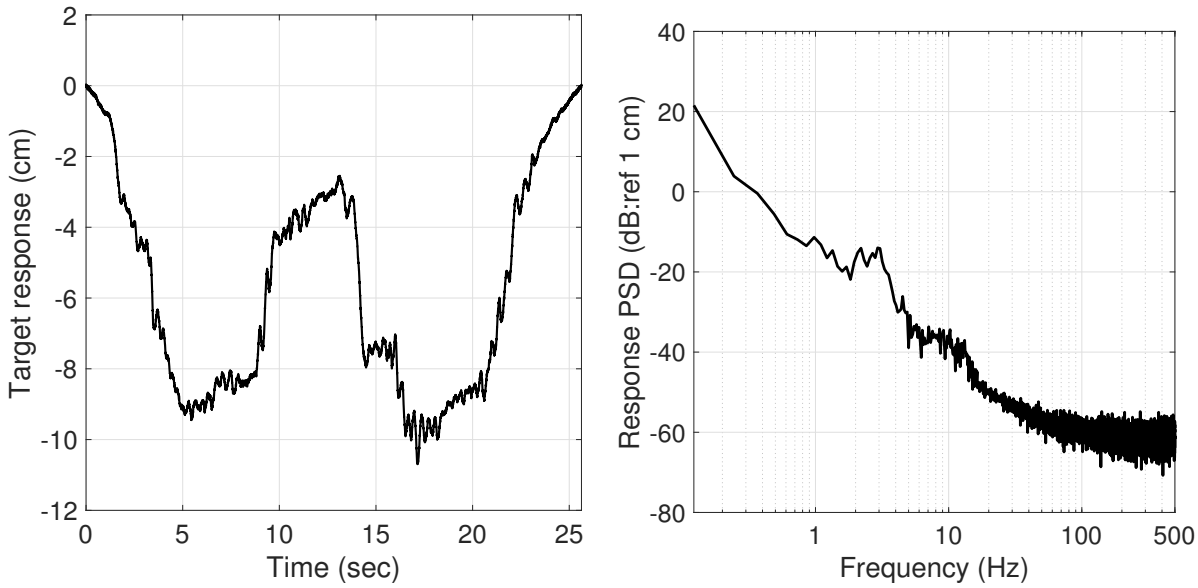

(a) Target response signal (b) PSD of the target response signal

Figure 3.4: Target response measured on an actual vehicle around a test track used for simulation case studies

very common in the testing industry in order to synthesize the required excitations to a test specimen which can be used to derive the target responses for simulation purposes in this thesis.

3.4 System model and inverse model identification results

3.4.1 System model identification

As has been discussed previously in section 2.2, "good" identification of the dynamic plant requires an input which induces a response that is able to sufficiently excite the nonlinear dynamics of the plant and is representative of the target response for the durability case study discussed in section 3.3. In this case, since the displacement is all in the negative direction,

i.e. the spring is always in compression and considering that the maximum displacement is approximately 10 cm with the binding point for the nonlinear dynamic systems defined in section 3.2 is at a spring compression of 5 cm, an appropriate identification drive is designed that matches the capabilities of real-world test rigs described in section 1.1.1. Such an identification drive is presented in Figure 3.5 which shows the time domain input signal and its PSD.

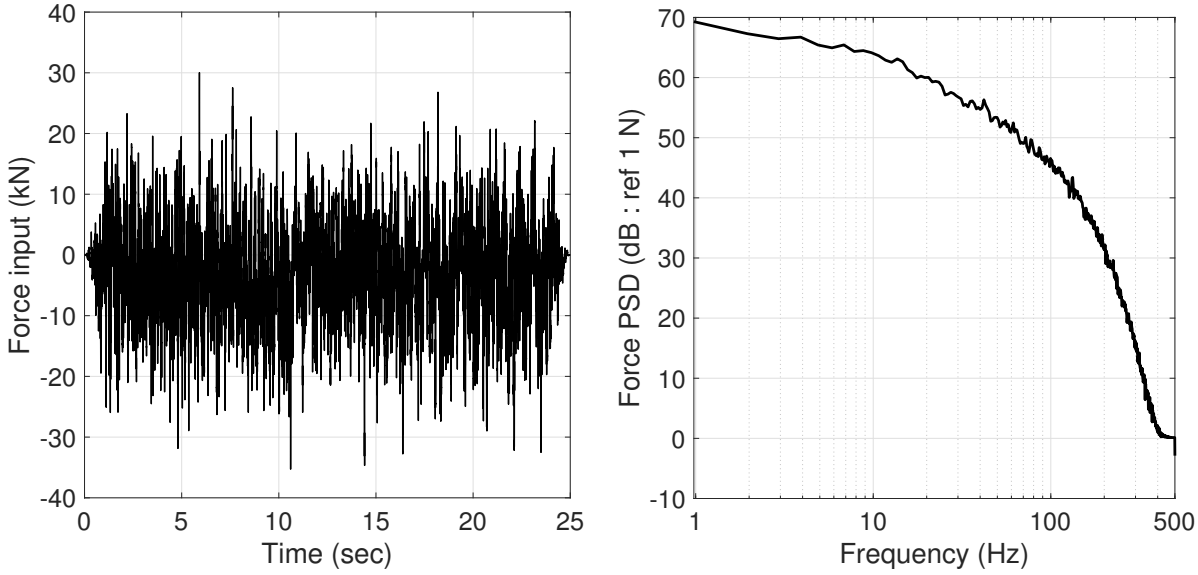

(a) Time domain representation (b) Frequency domain representation

Figure 3.5: Control inputs used for system identification of defined plants on a simulated SER test rig

As discussed in section 2.2.2, the H_1 estimator method is used to identify the forward system model in the frequency domain using 100 batches of the identification drive in Figure 3.5. Figure 3.6 presents the coherence function and the FRF of all four dynamic systems presented in section 3.2 for the H_1 estimation procedure for each of the plants.

For the results shown in Figure 3.6, the model obtained from each batch of 25 seconds of identification drive is weighted by its corresponding coherence function to derive a weighted average model of the plant. The coherence function shown in the figure is the average

value of the function across all batches of identification. It is clear from Figure 3.6 that for all the dynamic plants considered, the coherence function drops off significantly beyond approximately 25 Hz. In such cases, when deriving the inverse plant model for the DFID process, only the frequencies with a relatively high coherence (> 0.75) is considered.

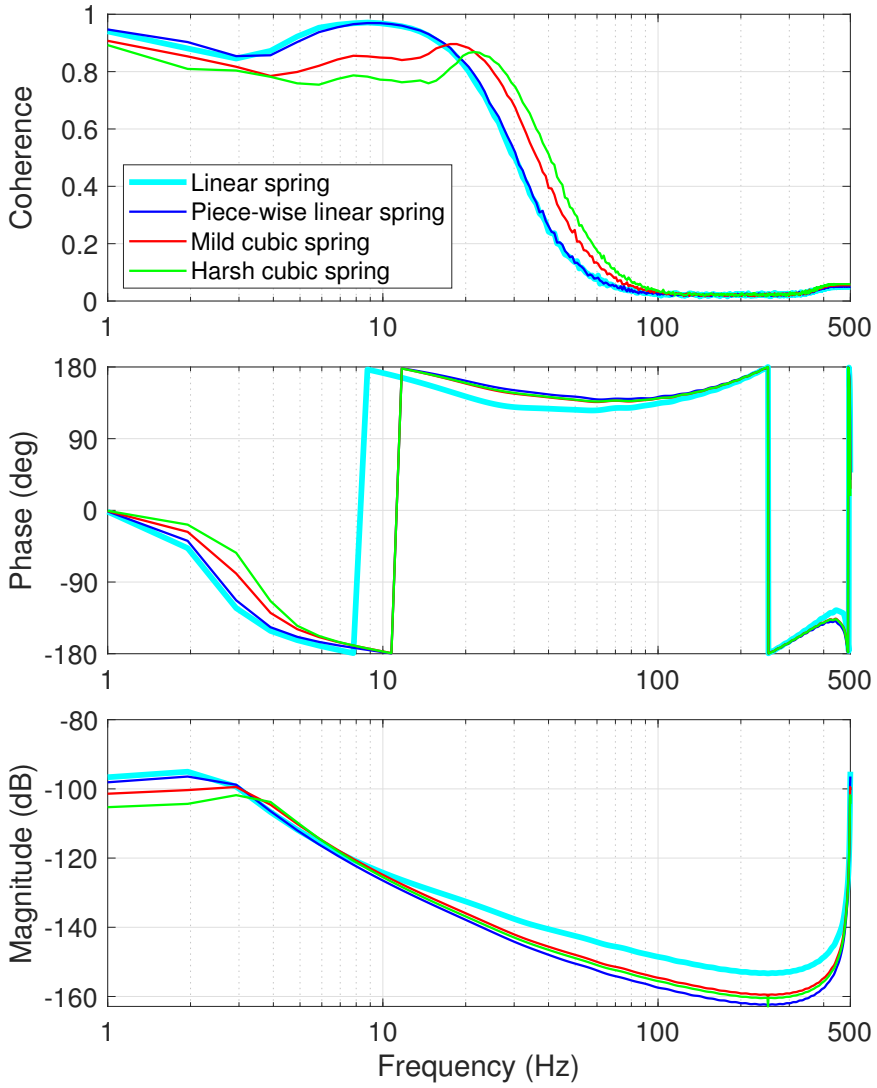

Figure 3.6: Frequency Response Function of the considered plants derived using the H_1 estimation method

System models can be analyzed and compared in the time domain through their FIR filters or in the frequency domain as their FRF. In this case, the FIR of the identified fre-

quency domain model can be derived by first estimating a transfer function model using the inverse z-transform of the FRF (`invfreqz` function is used on MATLAB with an appropriate number of numerator and denominator coefficients for each model) and computing a 1000-coefficient impulse response using the `impz` function on MATLAB. This is compared in Figure 3.7 against the identified 1000-coefficient FIR models of the dynamic plants derived using the LMS System identification process discussed in section 2.2.3.

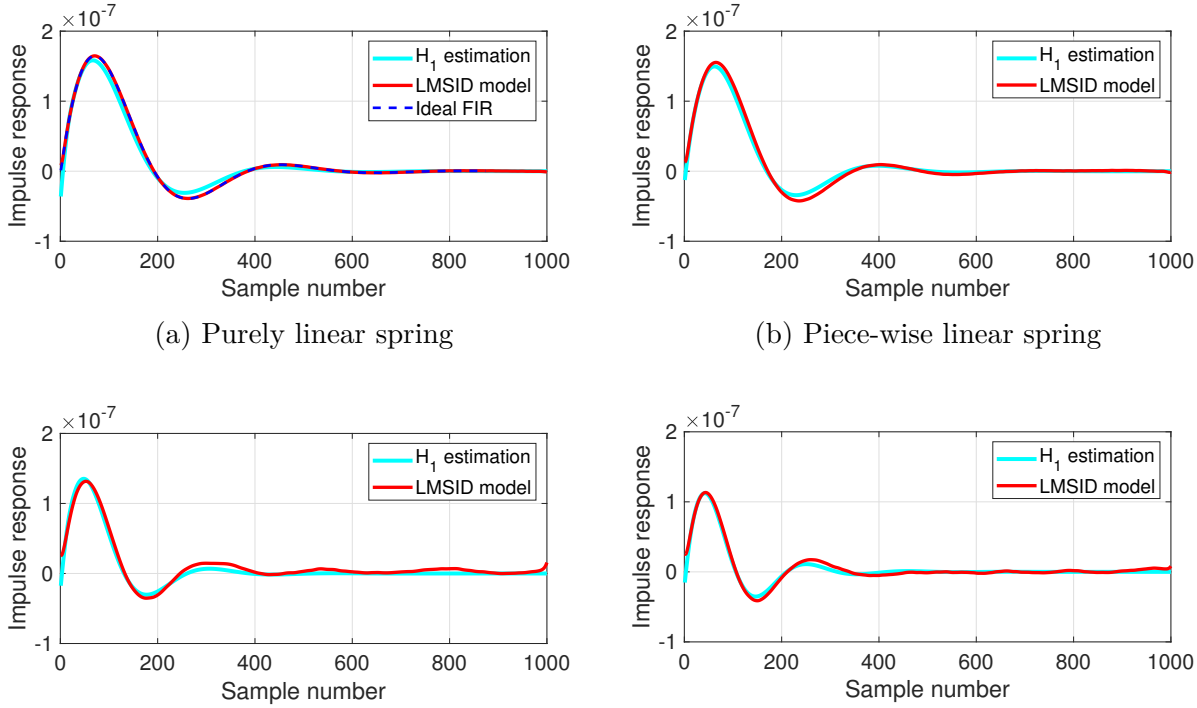

(a) Purely linear spring

(b) Piece-wise linear spring

(c) Mild cubic spring, $F_s(y)$

(d) Harsh cubic spring, $F_s'(y)$

Figure 3.7: Finite Impulse Response of models derived from the H_1 estimation method and the Least Mean Square system identification method

It can be seen from Figure 3.7 that both the H_1 estimation method and the LMS identification method yield fairly similar results for all four plants. In the case of Figure 3.7a, it can be seen that the LMSID model perfectly matches the ideal impulse response of the purely linear plant. The accuracy of the identification methods can be more quantitatively compared using the NEE of the output of the dynamic plant. Figure 3.8 shows the conver-

gence of the adaptive method in terms of the output NEE as described in section 2.5 through the iterations along with the final NEE achieved using the frequency domain model.

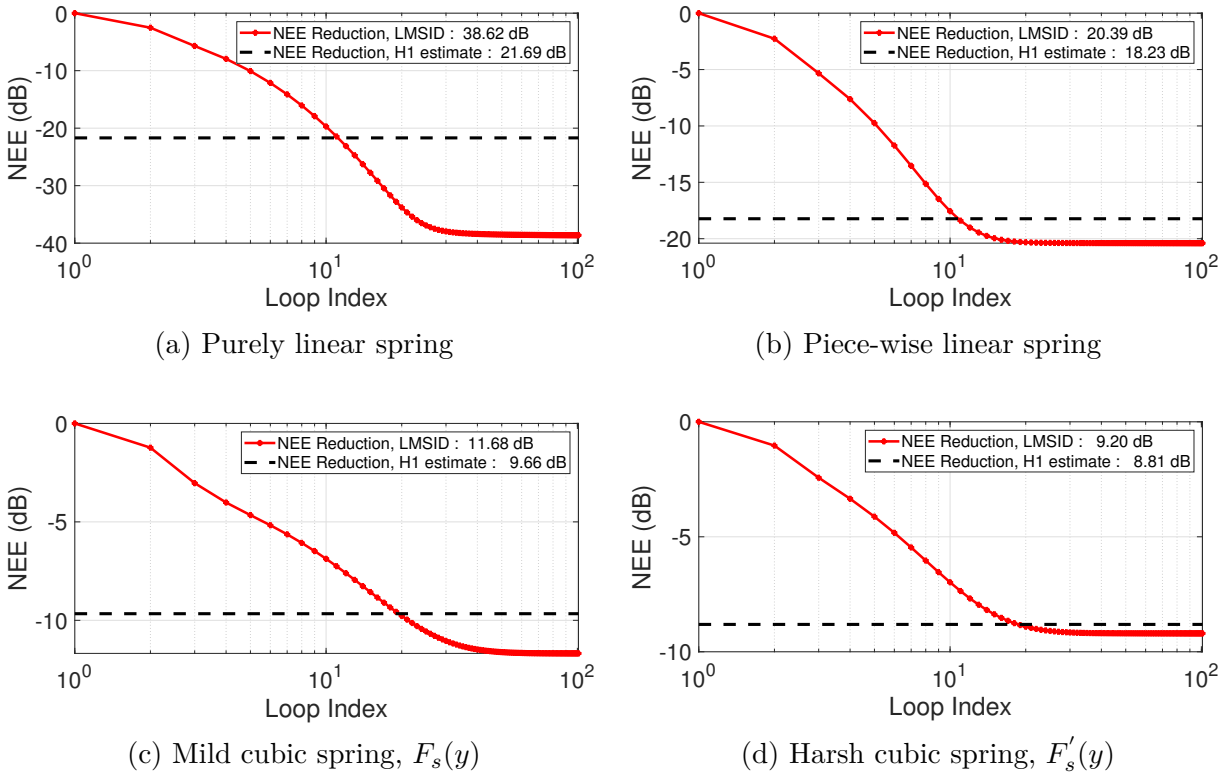

(a) Purely linear spring

(b) Piece-wise linear spring

(c) Mild cubic spring, $F_s(y)$

(d) Harsh cubic spring, $F_s'(y)$

Figure 3.8: NEE reduction through the 100 iterations of the LMS system identification process and the final output NEE achieved by the H_1 estimation model

The NEE results show that despite a higher degree of control with the adaptive identification process, the models identified do not show significant improvements compared to the frequency domain H_1 estimation method even for the harsher nonlinear plants. The difference in model accuracy is much more significant for the purely linear plant as can be seen in Figure 3.8a. Attempts were made to improve the performance of the adaptive method by reducing the step-size to allow very slow convergence of the process through a larger number of iterations and by increasing the degrees-of-freedom of the model, i.e. the number of coefficients of the FIR filter. Neither method showed any significant reductions

in the output NEE from the model, but this is to be expected since both the identification methods seek to model a nonlinear plant using a linear model.

3.4.2 Inverse model identification

As discussed in section 2.3.1, the identification of the inverse model from the identified FRF can be a straightforward process for SISO systems by simply taking the inverse of the derived FRF at each frequency ω_k. The inversion process is often limited to those frequencies that have a high coherence value (> 0.75) as in Figure 3.6 in order to prevent model inaccuracies from corrupting the inverse model. Only a narrow band of frequencies satisfies this condition and this method also does not account for the presence of any NMP zeroes in the forward linear model that could render the inverse model unstable. Hence, a more analytical approach is considered here to derive the inverse model in the frequency domain. The Zero Magnitude Error Tracking controller (ZMETC) is an appropriate candidate strategy to stabilize the NMP zeroes with poles added to the identified model [6, 92]. For the implementation of this algorithm, the identified FRF is first used to derive a discrete-time transfer function of the form

$$\widehat{G}(z) = \frac{B_m(z)\, B_n(z)}{A(z)} \tag{3.8}$$

where $B_m(z)$ and $B_n(z)$ denote the numerator polynomials containing all the minimum phase and non-minimum phase zeroes respectively and $A(z)$ is the denominator polynomial of poles. The $B_n(z)$ polynomial can be expressed as

$$B_n(z) = b_{n_n} z^{n_n} + b_{n_{n-1}} z^{n_{n-1}} + \cdots + b_{n_0} \tag{3.9}$$

where n_n is the number of NMP zeroes. For the ZMETC method, all the n_n NMP zeroes are stabilized by adding an equivalent number of poles to ensure causality and an updated denominator polynomial is derived containing all the zeroes inside the unit circle by inverting the corresponding coefficients of 3.9. The stable inverse model of the plant is hence given by

$$\widehat{G}^{-1}(z) = \frac{A(z)}{z^{n_n} B_m(z) \left(b_{n_0} z^{n_n} + b_{n_1} z^{n_{n-1}} + \cdots + b_{n_n}\right)} \tag{3.10}$$

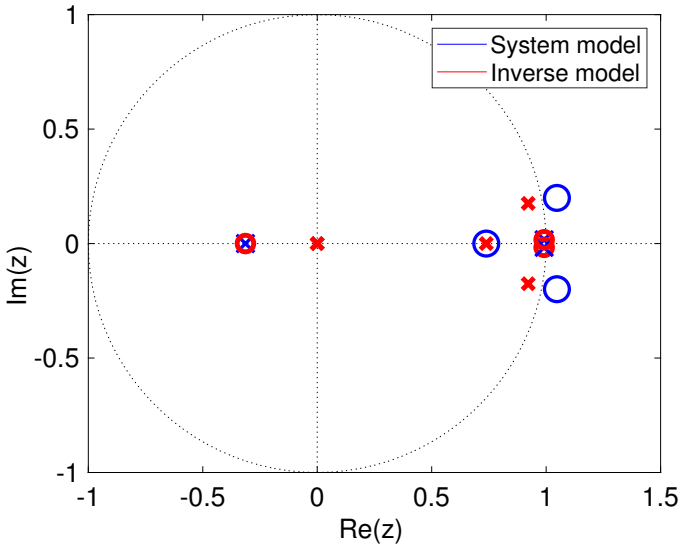

Figure 3.9: Pole-Zero maps of the forward system model $\widehat{G}(z)$ and the inverse model $\widehat{G}^{-1}(z)$ derived using the ZMETC method for the dynamic system with a purely linear spring

Figure 3.9 shows an example of the ZMETC inversion method for the dynamic system with a purely linear spring for which a discrete time transfer function $\widehat{G}(z)$ with three poles and zeroes was identified based on the FRF shown in Figure 3.6. This identified model had two zeroes outside the unit-circle (NMP zeroes) which have been stabilized for the inverse model $\widehat{G}^{-1}(z)$ by the introduction of two poles at the origin. Consistent with the results in Figure 3.6 which do not show large differences in the estimated linear models for all the plants, only the results for the purely linear spring have been shown in Figure 3.9 to avoid repetition but have been included in Appendix A.1.

The easiest method to quantify the performance of this inversion method, which also forms the first step of the ILC procedure is to use the inverse model and the known target data shown in Figure 3.4 and derive an initial estimate of the required drive file. This drive file can then be applied to the actual dynamic system to measure its response and compare against the target signal using the NEE defined in equation 2.51. Based on the H_1 estimation results shown in Figure 3.6 and the ZMETC method described above, the output NEE obtained from the initial estimate of the drive file for all the dynamic plants considered are listed in Table 3.4. The actual simulated response and the error signals obtained from this initial estimation of the drive file is presented in Appendix A.1.

Table 3.4: Output responses derived using the ZMETC inverse model identification method

Plant	NEE reduction (dB)	Magnitude of maximum error (mm)
Purely linear	30.22	4.7
Piece-wise linear	21.48	10.9
Mild cubic, F_s	10.88	28.3
Harsh cubic, $F_s^{'}$	8.14	33.4

Alternatively, the inverse model can also be computed using the time domain adaptive method described in section 2.3.2.2 using the Filtered-x LMS algorithm. The inversion scheme aims to generate a delayed inverse of the plant modeled as an FIR filter, as in Figure 3.7 and the number of filter coefficients in the inverse model L_{inv}, the number of samples of delay Δ, the reference excitation for the adaptive process and the number of batch iterations are all individually controlled for each dynamic plant.

Since the FIR system models derived in the previous section and shown in Figure 3.7 are 1000-coefficient filters and are much more lightly damped than the examples shown in Figure 2.12, very long filters are considered for the inverse models of the considered plants. The reference excitation considered for these simulated test benches is the target response

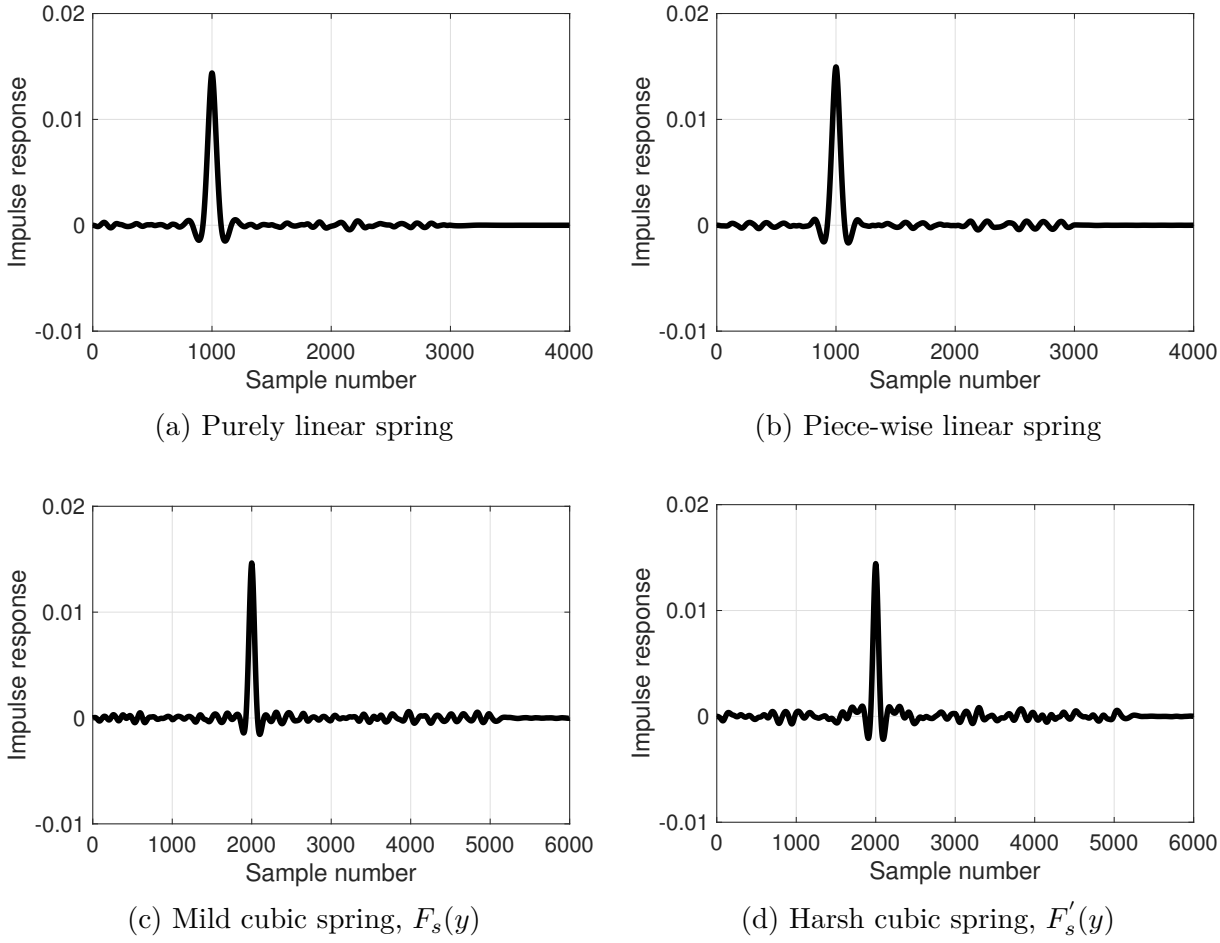

(a) Purely linear spring

(b) Piece-wise linear spring

(c) Mild cubic spring, $F_s(y)$

(d) Harsh cubic spring, $F_s^{'}(y)$

Figure 3.10: Impulse response of the cascaded FIR filters of the system model and the delayed adaptive inverse model for the considered dynamic systems

itself with an added dither at a signal-to-noise ratio (SNR) of 1 dB. The impulse response of the cascaded plant and inverse models also do not show a single impulse of magnitude 1, but are many orders of magnitude smaller as can be seen from the results in Figure 3.10. The actual inverse model FIR filters and the output response from the derived drive files are shown in Appendix A.2. Despite this fact, an initial estimate of the drive file can be calculated which produces comparable or even better results, as shown in Table 3.5, than the frequency domain based results shown in Table 3.4.

Table 3.5: Output responses derived using the Filtered-x LMS based adaptive inverse identification method

Plant	L_{inv}	Δ	$\left(\widehat{G}(z) * \widehat{G}^{-1}(z)\right)_{z=\Delta}$	NEE reduction (dB)	Magnitude of maximum error (mm)
Purely linear	3000	1000	0.0144	47.11	1.9
Piece-wise linear	3000	1000	0.0150	20.64	12.1
Mild cubic, F_s	5000	2000	0.0146	18.00	21.2
Harsh cubic, $F_s^{'}$	5000	2000	0.0144	14.68	24.4

In comparison to the frequency domain based ZMETC inverse identification method, the output responses yielded from the adaptive inverse identification are comparable for the piece-wise linear and harsh cubic nonlinear dynamic plants but significantly improved for the purely linear and mild cubic nonlinear dynamic plants in terms of the reduction in NEE using the initial estimate of the drive file. These inverse models will henceforth be used for the iterative DFID algorithms as discussed in section 2.4 and their results will be discussed directly in comparison to the novel DFID methods introduced in the next chapter.

3.5 Nonlinear test bench representation

The state-of-the-art Iterative Learning Control scheme for DFID, as illustrated in Figure 2.10 and discussed in detail in section 2.4 performs all the iterative computations of the error and drive file updates completely off-line. The output response is measured by providing the entire drive file as a batch to the actual test rig in the real world and the simulation test bench in this thesis. On the other hand, time domain adaptive DFID techniques that will be discussed in the next chapters can adapt the filter weights online, which requires the computation of the output response on the simulation test bench in a real-time sense or with very minimal delay.

This motivates the development of a block-oriented representation of the nonlinear dynamic system purely for simulation purposes that is able to replicate the real-world practice of measuring the output response in real-time. The specific nature of the nonlinearity will not be explicitly or implicitly used for the adaptive algorithms developed but is considered known for the simulated test benches based on the design of these as discussed in section 3.2.

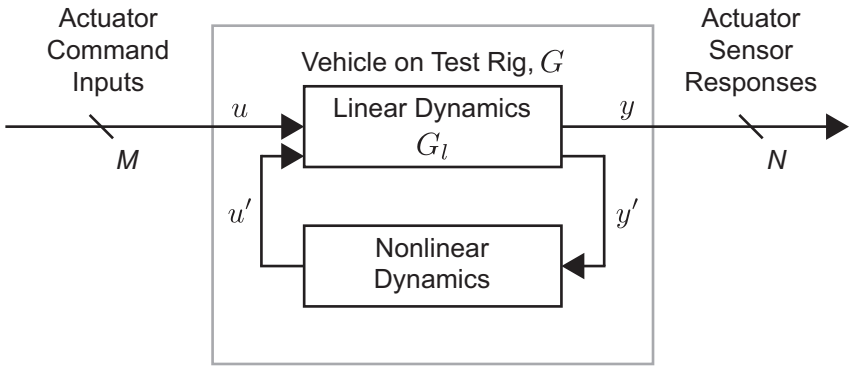

Figure 3.11: Simple feedback block-oriented representation of a nonlinear dynamic system

The representation of nonlinear dynamic systems does not typically have a universal approach and depends on the prior knowledge of the kind of nonlinearity of the dynamical system. Different block-oriented representations have been suggested in literature such as the Wiener, Hammerstein, Wiener-Hammerstein or simple feedback blocks [69, 74]. The model for G is represented here as a set of linear dynamics G_l interconnected with a nonlinear positive feedback path. There are many possible representations for nonlinear systems; however, the representation in Figure 3.11 reflects the common engineering practice and desire to develop linear models of the nonlinear system while still acknowledging the fact that nonlinearities are present in the dynamics. As indicated by the state-space formulation of 3.11, the block diagram structure in Figure 3.11 is quite general and can be used to represent a wide range of nonlinear time-invariant dynamic systems.

$$\dot{\mathbf{z}} = \mathbf{A}\mathbf{z} + \mathbf{B}\mathbf{u} + \begin{bmatrix} \mathbf{I} & \mathbf{0} \end{bmatrix} \mathbf{u}' \tag{3.11}$$

Notice that the block diagram for G in Figure 3.11 is actually a generalization of the Lur'e problem, where the functions $\mathbf{f}$ and $\mathbf{g}$ are memoryless sector-bounded nonlinear vector-valued functions [47, 103].

$$\dot{\mathbf{z}} = \mathbf{A}\mathbf{z} + \mathbf{B}\mathbf{u} + \mathbf{f}(\mathbf{z}, \mathbf{u}) \tag{3.12}$$

$$\mathbf{y} = \mathbf{C}\mathbf{z} + \mathbf{D}\mathbf{u} + \mathbf{g}(\mathbf{z}, \mathbf{u}) \tag{3.13}$$

$$\Leftrightarrow \underbrace{\begin{bmatrix}\mathbf{y}\\ \mathbf{y}'\end{bmatrix} = \begin{bmatrix}\mathbf{C}\\ \mathbf{I}\\ \mathbf{0}\end{bmatrix}\mathbf{z} + \begin{bmatrix}\mathbf{D}\\ \mathbf{0}\\ \mathbf{I}\end{bmatrix}\mathbf{u} + \begin{bmatrix}\begin{bmatrix}\mathbf{0} & \mathbf{I}\end{bmatrix}\\ \mathbf{0}\\ \mathbf{0}\end{bmatrix}\mathbf{u}'}_{\text{Linear dynamics}} \quad \text{and} \quad \underbrace{\mathbf{u}' = \begin{bmatrix}\mathbf{f}(\mathbf{z},\mathbf{u})\\ \mathbf{g}(\mathbf{z},\mathbf{u})\end{bmatrix} = \begin{bmatrix}\mathbf{f}(\mathbf{y}')\\ \mathbf{g}(\mathbf{y}')\end{bmatrix}}_{\text{nonlinear dynamics}} \tag{3.14}$$

For the nonlinear dynamic plant test benches defined in sections 3.2.2 and 3.2.3, the block-oriented simple feedback representations are shown in Figure 3.12, where the linear dynamics G_l are given by the purely linear plant defined in section 3.2.1.

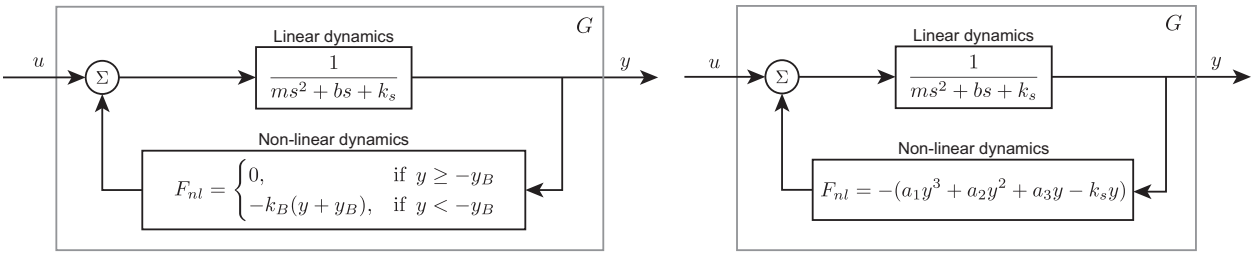

(a) Piece-wise linear plant (b) Cubic nonlinear plant

Figure 3.12: Simple feedback block-oriented representation of the nonlinear dynamic test benches considered in this thesis

For the case studies presented in the next chapters, output responses from the test benches when simulated off-line from the adaptation process, is computed as a single batch using the constitutive second-order dynamic equations described in section 3.2 whereas the

simulated response of the test bench is computed with a single-sample delay using the representation in Figure 3.12 for the nonlinear dynamic plants when required during the adaptive process at each time instant.

Chapter 4

Pulse Train Filtered-x LMS algorithm for DFID

4.1 Introduction

This chapter introduces a novel method, referred by the author here as the Pulse Train Filtered-x LMS (PT-Fx-LMS) algorithm, for the iterative estimation of drive files based on methods developed for Active Noise and Vibration Control (ANVC). The initial driving factor for this approach was the recognition of the DFID block diagram as a representation of the ANVC dynamics associated with using secondary path inputs to cancel noise and/or vibration caused by a primary path [27, 105].

Section 4.2 describes the ANVC architecture and how its nomenclatures, objectives, causality and solution approaches relate to the requirements of the DFID process. The signal definitions and the update algorithm of the proposed general-purpose DFID solution is presented in section 4.3. To establish proof-of-concept, the performance of the PT-Fx-LMS algorithm is demonstrated in section 4.4 using the dynamic test benches defined in Chapter 3 and illustrated through several case studies to benchmark it against the state-of-the-art DFID methods presented in section 2.4.

4.2 Background

4.2.1 The Active Noise and Vibration Control architecture

Active Noise control is based on the property of superposition to cancel primary unwanted noise, which could be acoustic or unwanted vibrations, using an electro-acoustic or electromechanical system to generate an anti-noise signal that combines with the primary signal to hence cancel both [32, 50, 51, 62]. Unlike passive noise control techniques such as barriers and silencers which are very effective over a broad frequency range but largely ineffective or bulky and expensive at low frequency ranges, active noise control techniques have been developed and largely successful in being compact and inexpensive to attenuate low frequency noises. Modern signal processing hardware has enabled the development of adaptive algorithms and cost-effective implementations of ANC systems that allow real-time attenuation of often non-stationary noise.

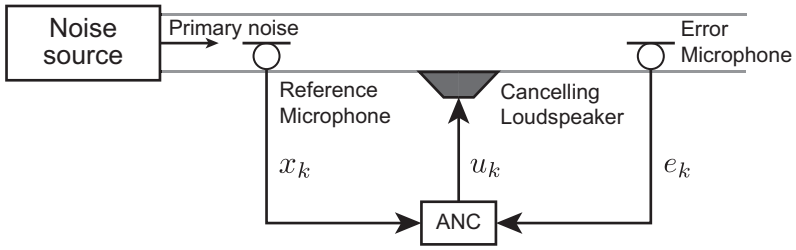

Figure 4.1: Schematic of a single-channel, broad-band, feed-forward, duct-acoustic ANC system

ANC systems have been designed over the years to meet performance requirements of efficiency across the largest possible frequency ranges, adaptability to changes in parameters of the dynamic system, robustness and reliability of the control system and ease of installation of the control system in terms of complexity of algorithm, manufacturing and cost. To illustrate the general technique of ANVC for a wide variety of acoustic and vibration applications, a schematic [51] of a general single-channel, broad-band, duct-acoustic ANC

system is shown in Figure 4.1.

4.2.1.1 Primary and secondary path effects in an ANVC system

For ANVC applications, the adaptation process is typically some form of gradient descent algorithm such as Least-Mean-Squares (LMS), as discussed previously in Chapter 2.

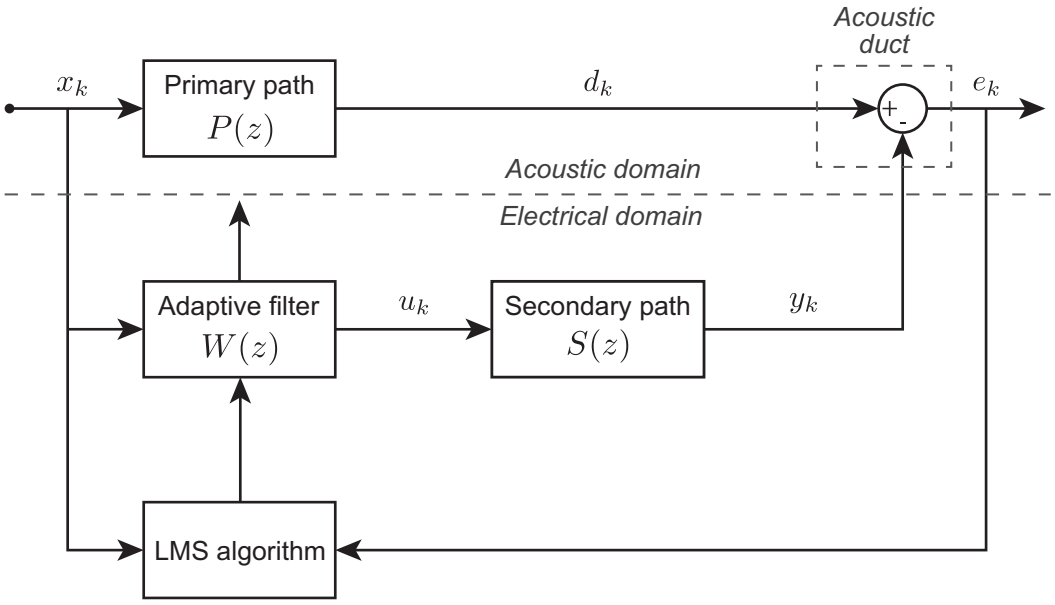

Figure 4.2: Simplified block diagram of a single-channel, feedforward, duct-acoustic ANC system

Figure 4.1 shows that the objective of the ANC system is the acoustic superposition of the primary noise with the output of the adaptive filter from the canceling loudspeaker in order to eliminate the combined noise measured at the error microphones. It is hence necessary to compensate for the secondary path from the adaptive filter to the error microphone through the acoustic duct and all the relevant measurement and signal processing equipment. When including the secondary path transfer function, $S(z)$, a simplified block diagram of the ANC system is shown in Figure 4.2. Considering the objective of the ANC system is to drive the

error to zero, the z-transform of the error signal is

$$E(z) = [P(z) - S(z)W(z)]X(z) \tag{4.1}$$

and the auto-power spectrum of e_k, given by

$$S_{ee}(\omega) = [1 - C_{dx}(\omega)]S_{dd}(\omega) \tag{4.2}$$

where $C_{dx}(\omega)$ is the magnitude-squared coherence function between the two wide-sense stationary random processes, the primary path noise d_k and the reference signal x_k and $S_{dd}(\omega)$ is the auto-power spectrum of the primary path noise. This indicates that the performance of the ANC system is limited by the coherence function, similar to the result discussed in section 2.2.2.1. Making the assumption of ideal convergence of the adaptive filter and assuming the residual error converges to zero, the optimal transfer function of the adaptive filter, $W^*(z)$ can hence be derived following from 4.1 as

$$W^*(z) = \frac{P(z)}{S(z)} \tag{4.3}$$

which shows that the filter must simultaneously model the primary path and the inverse of the secondary path. It is often difficult to compensate for the inherent delay due to the modeling of the inverse secondary path $1/S(z)$ if the primary path also does not contain an equal amount of delay, in order to ensure causality of the filter.

4.2.1.2 Relating the ANVC architecture to the DFID problem

Although both ANVC and DFID seek to drive the output error to zero (or to the theoretical lower bound) ANVC applications require real-time determination of the control inputs

whereas the command inputs resulting from DFID can be synthesized offline and played out in real-time as a batch that is synchronized with the target data. The signals and blocks given in Figure 4.2 can be related to the DFID problem as follows:

- For ANVC applications, the signal d_k or an array of signals $\mathbf{D}$ in the case of a MIMO system represents the primary disturbance noise and/or vibration field measured by N sensors. In the case of the DFID application of interest for this thesis, this signal is the desired target response of the dynamic system, measured in its service environment.

- The signal y_k or the array of N signals $\mathbf{Y}$ for MIMO systems represents the secondary noise and/or vibration field created by M control actuators to cancel the primary disturbance in an ANVC system. These would be the actual sensor responses of the dynamic system on a test rig during an SER testing procedure.

- The error signal e_k or an array of N signals $\mathbf{E}$ for MIMO systems represents the acoustic or vibrational superposition of the primary and secondary disturbance signals which is to be driven to zero by the ANVC system. In the case of DFID applications, this is the error measured between the desired target responses and the actual sensor responses of the dynamic system on the test rig.

- The x_k signal, or an array of P signals $\mathbf{X}$ for MIMO systems represents the set of reference inputs which for ANVC applications must be mutually independent and highly correlated to the primary disturbance signal $\mathbf{D}$ [27, 32, 50, 62, 105].

- The symbol W in Figure 4.2 represents a dynamic filter or $\mathbf{W}$ for MIMO systems as a bank of typically Finite Impulse Response (FIR) filters, whose coefficients are updated in response to the measured error signals.

- The control signal u_k or an array of M control signals $\mathbf{U}$ for MIMO systems contains the outputs from the bank of adaptive filters in response to the reference inputs $\mathbf{X}$.
- The primary path transfer function in the ANVC block diagram, $P(z)$ represents the unknown dynamics of the acoustical system from the reference microphones to the error microphones where the noise attenuation is to be achieved. In the DFID equivalent system, this primary path represents the unknown dynamics of the dynamical system under test in its service environment which generates the target response required to be replicated on the test rig.
- The secondary path transfer function $S(z)$ for ANVC systems includes the dynamics of the signal processing, measurement and actuator apparatus and the dynamics of the system from the noise or vibration cancelling equipment, like loudspeakers for an acoustic duct to the error sensors. For DFID applications of interest, this secondary path represents the dynamical system under test installed on the test rig, G with all the dynamics of the actuators and measurement sensors.

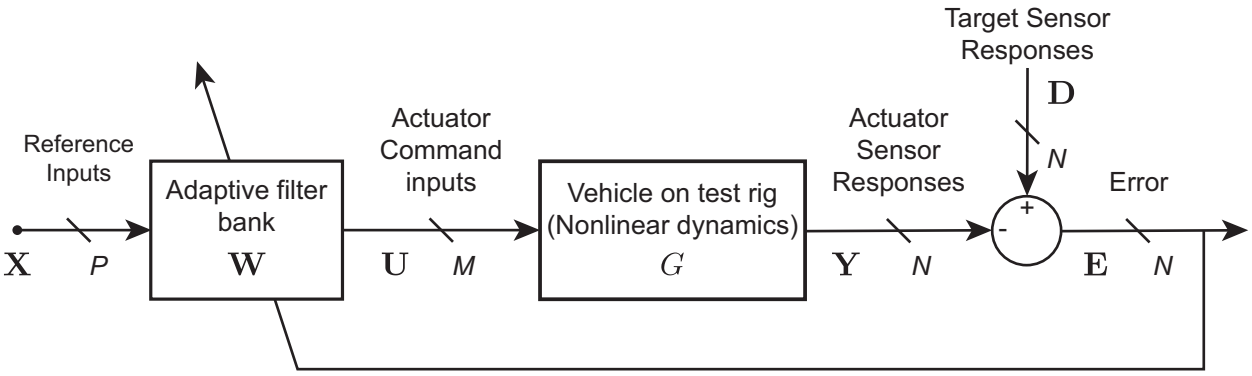

Figure 4.3: Adaptive filter architecture from ANVC applied to the general MIMO DFID problem

The time-invariant dynamics of the vehicle on the test rig, given by the symbol G in Figure 4.3 can be represented as a set of linear dynamics interconnected with a nonlinear

feedback path as discussed in section 3.5. It hence follows from Figure 4.3 and as previously presented for the conventional frequency domain ILC scheme in 2.4.1 that the dynamic equation governing the overall block diagram is given by

$$\mathbf{E}_k = \mathbf{D}_k - G\mathbf{U}_k \tag{4.4}$$

where the subscript k is a discrete time index and G is considered here to be an $N \times M$ operator that represents the nonlinear time-invariant dynamic system, with the primary objective of the DFID solution being to find a finite sequence $\mathbf{U}_k$ such that $\mathbf{E}_k$ is zero (or as close to zero as possible) for the entire batch of recorded target data $\mathbf{D}_k$ and a secondary objective being mathematically determining the theoretical lower bound of the error.

For ANVC applications, the adaptation process is typically some form of gradient descent algorithm such as Least Mean Squares (LMS). One common adaptation solution developed for the block diagram structure in Figure 4.3 is the Filtered-x LMS algorithm [27, 29, 50, 105], previously discussed in section 2.3.2.2 for inverse model identification. Most commercially available ANVC systems today only operate on periodic or narrowband waveforms. Even though the structure of Figure 4.3 with Filtered-x adaptation can theoretically be used with broadband signals, such configurations have had very limited success largely because broadband ANVC problems have a number of severe physical restrictions such as: high modal density, existence of sufficiently correlated upstream reference signals, high computational burden, and zones of silence with limited spatial extent [11, 27, 32, 39, 62]. For the DFID problem, virtually all responses generated from complex excitations will result in target signals that have broadband spectral content, thus making DFID a technically challenging problem.

4.2.2 DFID solution using inversion of the plant dynamics

Inspection of the block diagram of Figure 3.11 along with 4.4 leads to one potential solution for DFID. In the special case where the dynamics G are dynamically invertible, and because $\mathbf{D}_k$ is assumed to be known *apriori*, the multiple input command sequence $\mathbf{U}_k$ can be synthesized by simply pre-filtering the target data through an inverse or pseudo-inverse model:

$$\mathbf{U}_k = \begin{cases} G^{-1}\mathbf{D}_k, & \text{if } M = N \text{ and } G \text{ full rank} \\ G^{+}\mathbf{D}_k, & \text{if } M \neq N \text{ or } G \text{ not full rank} \end{cases} \tag{4.5}$$

Unfortunately, G is rarely invertible in practice, for example, if G has elements that are multi-valued functions. Even if G is restricted to be linear, then several physical requirements must still be met for an exact inverse solution to exist, as has been demonstrated for the dynamic systems under consideration in 3.4.2. The basic adaptation procedure of a conventional frequency domain DFID technique has been discussed previously [18, 19] in section 2.4.1, the following requirements are well known for LTI dynamic systems; however, it is anticipated that similar requirements will exist for nonlinear dynamic systems:

Case 1: When the dynamic system is square ($M = N$, same number of actuators and sensors), then G must be minimum phase and full rank in order to be invertible. Even if G is not minimum phase, then a delayed inverse may exist for some finite delay time [106, 107]. For the broad class of problems of interest in this research, a delayed inverse solution would be perfectly acceptable since absolute timing of the signals is not important; however, relative timing is critical.

Case 2: When the dynamic system is not square ($M > N$, fewer sensors than actuators), then a pseudo-inverse solution must be used (G^{+} in 4.5). In this case, the error $\mathbf{E}$

will only be zero if the target data **D** is in the column space of the dynamic system G. This case results in an under-determined solution that can lead to additional but manageable problems since there can be an infinite number of possible solutions that result in the same error.

Case 3: When the dynamic system is not square ($M < N$, more sensors than actuators), a pseudo-inverse solution must also be used. Again, the error **E** will only be zero if the target data **D** is in the column space of the dynamic system matrix G. This case results in an over-determined solution, which generally leads to a single unique solution.

In practice, it is difficult or impossible to obtain a time-domain inverse model of G for any of the three cases above. The digital architecture of Figure 4.3 and the adaptive inverse model identification procedure discussed in section 2.3.2.2 using the Filtered-x LMS method shows that if the reference inputs **X** are chosen to be the target sensor responses **D**, or a time-advanced version of them, then the converged filters **W** would represent an approximation to the dynamic pseudo-inverse of the nonlinear system G. But the results in section 3.4.2 have shown that this can be a computationally expensive method or the obtained response can be lacking in performance for certain applications. This is a likely justification for the prevalence of frequency domain DFID solutions, as discussed in section 2.4 since it is relatively straightforward to compute the inverse models in the frequency domain one frequency at a time using singular value decomposition. Frequency domain techniques necessarily assume linearity in the dynamic system, which is frequently a poor assumption that will either lead to divergence of the iterative process or exceptionally large amounts of iteration time. This unfortunate condition generally requires skilled engineers to manually "steer" the iteration process. Time domain inverse models are usually only required to have sufficient accuracy over a restricted bandwidth. It is sometimes possible to take advantage of selectively inverting the dynamics only over the frequency range of the

target data. A deeper study of the existence and uniqueness of solutions for MIMO dynamic systems presented in this section is planned for the final dissertation of this research.

4.3 PT-Fx-LMS algorithm for DFID

The primary inspiration for the proposed PT-Fx-LMS algorithm for DFID comes from a solution for narrowband ANC systems, originally conceived for removing harmonic synchronously sampled interferences from signals using a generated signal to synthesize the reference input $\mathbf{x}$ in Figure 4.3. Elliott and Darlington [28] showed that setting the sample rate of the adaptive canceler to be an integer multiple of the fundamental frequency of the interference such that it is synchronously sampled an integer number of times significantly improves the efficiency of the noise cancellation. This technique is also known to have several other advantages [44]: (1) preventing acoustic interference from secondary path sources, such as secondary loudspeakers in acoustic ANC systems back to the reference signal, (2) a synthesized reference signal prevents nonlinearities and hysteretic problems, (3) relaxes causality constraints as delays can be more easily implemented, (4) makes the control of individual harmonics easier, and (5) makes the modeling of dynamic plants easier since it is only necessary to model plants in the frequency range of the harmonics of interest, thus making FIR filter models of lower order sufficient. For narrowband ANC systems, two types of synthesized reference signals can be used: an impulse train with a period equal to the inverse of the fundamental frequency of the periodic interference to be canceled, and a single or a summation of sine waves at frequencies that match the harmonics required to be canceled.

A thorough review of the literature indicates that this particular algorithm and choice of reference signals has not been extended to generate control inputs for MIMO dynamic

systems, nor has it ever been applied to broadband signals. The strength of the proposed algorithm is derived from its ability to synthesize arbitrary time-domain waveforms and using the newly proposed formulation, this synchronous harmonic algorithm provides the basis for a new candidate general-purpose time-domain DFID solution.

For a SISO dynamic system, and with reference to Figure 4.3, we have $M = N = 1$. Similar to the original development for harmonic synchronous interferences by Elliott and Darlington [28], the novel aspect of the proposed formulation is to select the reference input $\mathbf{x_k}$ to be a unitary pulse train (PT) sequence. Assuming that the entire target data of K samples is considered as a single period T_0, sampled at a period of T such that $T_0 = KT$, the reference signal is a synthesized pulse train sequence of period T_0, such that

$$\begin{aligned} \mathbf{x_k} &= \begin{bmatrix} x_1 & \cdots & x_q & \cdots & x_K \end{bmatrix}^T \\ x_q &= \begin{cases} 1 & \text{if } q = k \\ 0 & \text{if } q \neq k \end{cases} \end{aligned} \tag{4.6}$$

This unique choice of reference input enables interpretation of the target response vector $\mathbf{d}$ as an FIR filter whose coefficients are identical to the measured set of target data. Clearly, the output of this FIR filter excited by the unitary pulse train sequence is the target response $\mathbf{d_k} = \begin{bmatrix} d_1 & \cdots & d_k & \cdots & d_K \end{bmatrix}^T$. Referring to Figure 4.4, a second FIR filter $\mathbf{w_k} = \begin{bmatrix} w_1 & \cdots & w_k & \cdots & w_K \end{bmatrix}^T$ is defined, exactly the same length as the target data set. After convergence, and by construction, the coefficients of $\mathbf{w}$ will be the final drive file.

An adaptive process is used to dynamically update the FIR filter coefficients in $\mathbf{w}$. Following the practice from ANVC [105], a scalar quadratic cost function, J of the output

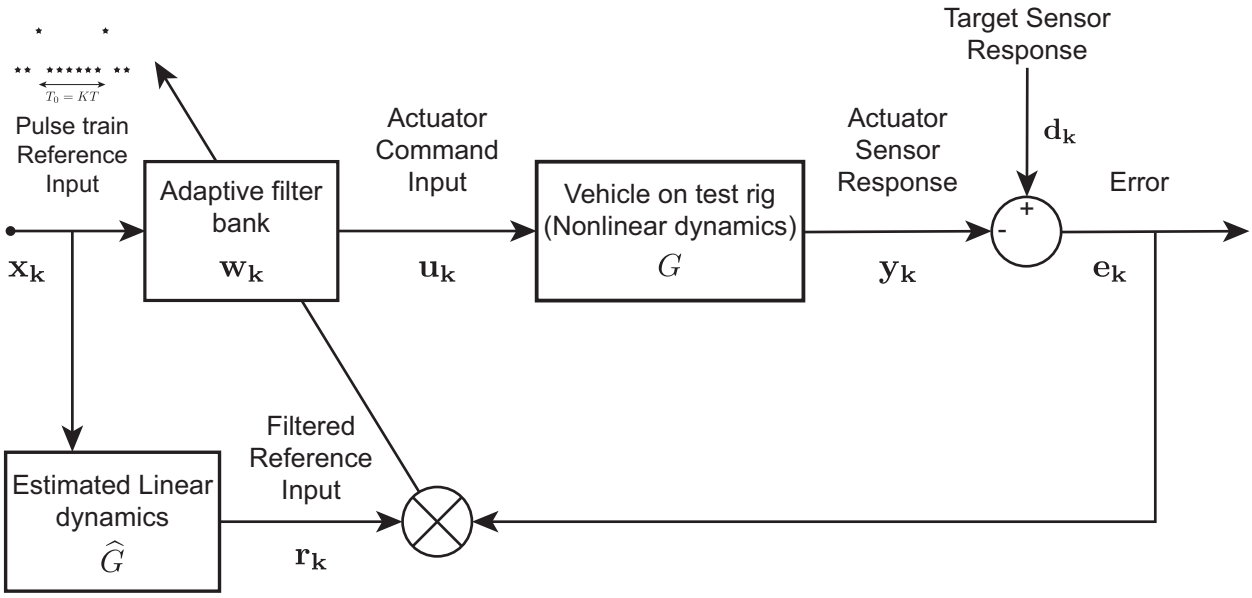

Figure 4.4: Adaptive filter architecture from ANVC using the Filtered-x LMS algorithm applied to the general SISO DFID problem with the pulse train reference input

error is established, which is to be minimized over time.

$$\mathbf{e_k} = \mathbf{d_k} - \mathbf{y_k} = \begin{bmatrix} e_1 & \cdots & e_k & \cdots & e_K \end{bmatrix}^T \tag{4.7}$$

$$J = E\left\{ \sum_{k=1}^{K} {e_k}^2 \right\} \tag{4.8}$$

where $E\{\bullet\}$ is the expectation operator and $\mathbf{y_k} = \begin{bmatrix} y_1 & \cdots & y_k & \cdots & y_K \end{bmatrix}^T$ is the response vector obtained from the dynamic plant to control input $\mathbf{u_k} = \begin{bmatrix} u_1 & \cdots & u_k & \cdots & u_K \end{bmatrix}^T$. A fundamental assumption in the Fx-LMS algorithm derivation is that the FIR filter $\mathbf{w_k}$ can be commuted with the plant dynamics, which of course requires linearity in the plant [105]. In general, commutability will not generally be possible for nonlinear systems. Disregarding this fact for the moment and ignoring the nonlinear portion of the dynamics, a Q-coefficient linear FIR filter $\widehat{G} = \begin{bmatrix} \hat{g}_0 & \hat{g}_1 & \cdots & \hat{g}_{Q-1} \end{bmatrix}^T$ can be constructed to model the dynamic plant

around an operating point. Application of the conventional Fx-LMS algorithm in Figure 4.4 and as discussed previously in section 2.3.2.2 yields the gradient descent method for updating the FIR filter coefficients [105]:

$$\mathbf{w}_{k+1} = \mathbf{w}_k + \mu e_k \mathbf{r}_k \tag{4.9}$$

where $\mathbf{w}_k$ is the entire K-coefficient FIR filter at time step k, μ is a small positive constant known as the step size, which controls the convergence rate, e_k is the instantaneous scalar output error, and $\mathbf{r_k}$ is a vector of length K constructed as the buffered output of the linear impulse response model $\widehat{G}$ due to the reference input $\mathbf{x_k}$. It has been shown that the step size μ depends on the inverse of the signal power [105]; however, it is also known that these relationships do not yield precise constraints. The simplicity of the unitary pulse sequence, combined with the novel structure of the $\mathbf{w_k}$ vector representing the actual drive file and the linear FIR model $\widehat{G}$, can now be exploited to yield a remarkable simplification of the adaptation law given by:

$$\begin{bmatrix} w_q \\ w_{q-1} \\ \vdots \\ w_{q-Q+1} \end{bmatrix}_{k+1} = \begin{bmatrix} w_q \\ w_{q-1} \\ \vdots \\ w_{q-Q+1} \end{bmatrix}_{k} + \mu e_k \begin{bmatrix} \hat{g}_0 \\ \hat{g}_1 \\ \vdots \\ \hat{g}_{Q-1} \end{bmatrix} \tag{4.10}$$

$$\text{where } q = k \bmod K$$

where q is an index into the $\mathbf{w_k}$ vector at the current time step k. It can be seen from the equation that at any given time step, only a subset (Q coefficients) of the overall weight vector $\mathbf{w_k}$ is required to be updated, and the gradient is simply the FIR filter $\widehat{G}$ multiplied by the instantaneous error. This update law makes physical sense in that the input action at

any time step will influence the response that lasts for the duration of the impulse response of the plant. By construction, each weight w_q represents an input action at the q^{th} time step.

4.4 Performance evaluation case studies

This new formulation is demonstrated using multiple simulation case studies with simple Single-Input Single-Output (SISO) linear and nonlinear dynamic systems presented in section 3.2. The required estimated linear dynamics of the test bench of interest as described in the previous section has been presented in section 3.4.1 and based on the results in Figures 3.7 and 3.8, the $Q = 1000$ coefficient FIR models derived using the LMSID method will be used for the simulation case studies. Similarly, the output response signal at each time instant k required for the adaptation law described in equations 4.7 - 4.10 are calculated using the nonlinear test bench representation discussed in section 3.5. Similarly, the target response considered for the case studies has been presented in section 3.3 and one of the case studies presented in this section will be a slight modification of the target response shown in Figure 3.4 to demonstrate an edge case often found in practical applications.

The performance of the proposed PT-Fx-LMS method is compared against an existing DFID formulation based on the Iterative Learning scheme previously discussed in section 2.4. For the case studies presented in this section, the time domain version of the ILC scheme, presented in section 2.4.3 is primarily considered with the delayed inverse models identified for the various test benches considered in this thesis using the adaptive inverse Filtered-x LMS method presented in section 3.4.2 and the results of the delayed FIR inverse models shown in Table 3.5 and in more detail in Appendix A.2.

Additionally, the quantification of the iteration quality and progression of the adaptation performance using misadjustment and Normalized Error Energy (NEE) is described in

section 2.5 that was also used to describe the performance of the LMSID system identification and the Filtered-x LMS adaptive inversion procedures presented in section 3.4.1 for the various test benches under consideration. For an appropriate comparison of performance of the methods of DFID considered, the step sizes for the adaptation methods were tuned to balance rapid reduction in NEE and stability, such that the NEE does not show divergence and a 'ringing' phenomenon is not observed on the adapted drive files or the output response being generated.

4.4.1 Case Study 1: Drive files initialized at zero

The primary case study considers the simplest case of initializing the adaptive filter, and consequently the drive file at zero and allowing the adaptive process converge to the required drive file that produces the desired target response. At the end of each batch loop, the final drive signal is used as the initial drive signal for the next batch loop. For all the simulations presented in this case study, 100 batch loop iterations have been considered, while in practice, the adaptation process is generally stopped when the error is smaller than a set threshold. In the presence of sensor and actuator noise which is not considered in these simulations, an NEE reduction of approximately 40–50 dB would be considered appropriate for the applications of interest in this thesis.

The parameters used for these simulations for this case study are presented in Table 4.1 for the four test benches considered using: (1) the conventional frequency domain ILC method discussed in section 2.4.1 for which the inverse model derived using the ZMETC method presented in section 3.4.2 is used, (2) the conventional time domain ILC method that uses the delayed inverse FIR models presented in Table 3.5 are used and, (3) the proposed PT-Fx-LMS method.

Table 4.1: Iteration step size parameter and the NEE reduction results at the end of 100 batch loops for the iterative DFID methods used for each of the considered dynamic test benches for Case Study 1

(a) Purely linear spring

Method	Iteration step size μ	NEE reduction (dB)
Conventional frequency-domain ILC	0.025	49.29
Conventional time-domain ILC	0.2	56.93
PT-Fx-LMS method	4e9	52.62

(b) Piece-wise linear spring

Method	Iteration step size μ	NEE reduction (dB)
Conventional frequency-domain ILC	0.033	46.72
Conventional time-domain ILC	0.2	58.45
PT-Fx-LMS method	4.6e9	53.10

(c) Mild cubic spring, $F_s(y)$

Method	Iteration step size μ	NEE reduction (dB)
Conventional frequency-domain ILC	0.031	31.70
Conventional time-domain ILC	0.2	56.18
PT-Fx-LMS method	4.4e9	53.15

(d) Harsh cubic spring, $F_s^{'}(y)$

Method	Iteration step size μ	NEE reduction (dB)
Conventional frequency-domain ILC	0.038	35.94
Conventional time-domain ILC	0.2	57.13
PT-Fx-LMS method	4.6e9	53.75

As has been mentioned previously for the adaptive processes in Chapter 3, the iteration step size depends on the method of iterative process used. For the conventional ILC methods used to derive the drive files, a conservative step size < 1 has been chosen after trials to balance stability in order to prevent divergence or large 'ringing' phenomena in the derived drive files, performance in terms of fast reduction of output NEE in a reasonable number of batch loops and convergence of the iterative process where possible. For the PT-Fx-LMS

based methods, the step sizes are chosen with similar considerations, but owing to the pulse-train nature of the reference inputs, the iteration constants depend on the length of the adaptive filters and the power of the required drive files or actuator forces.

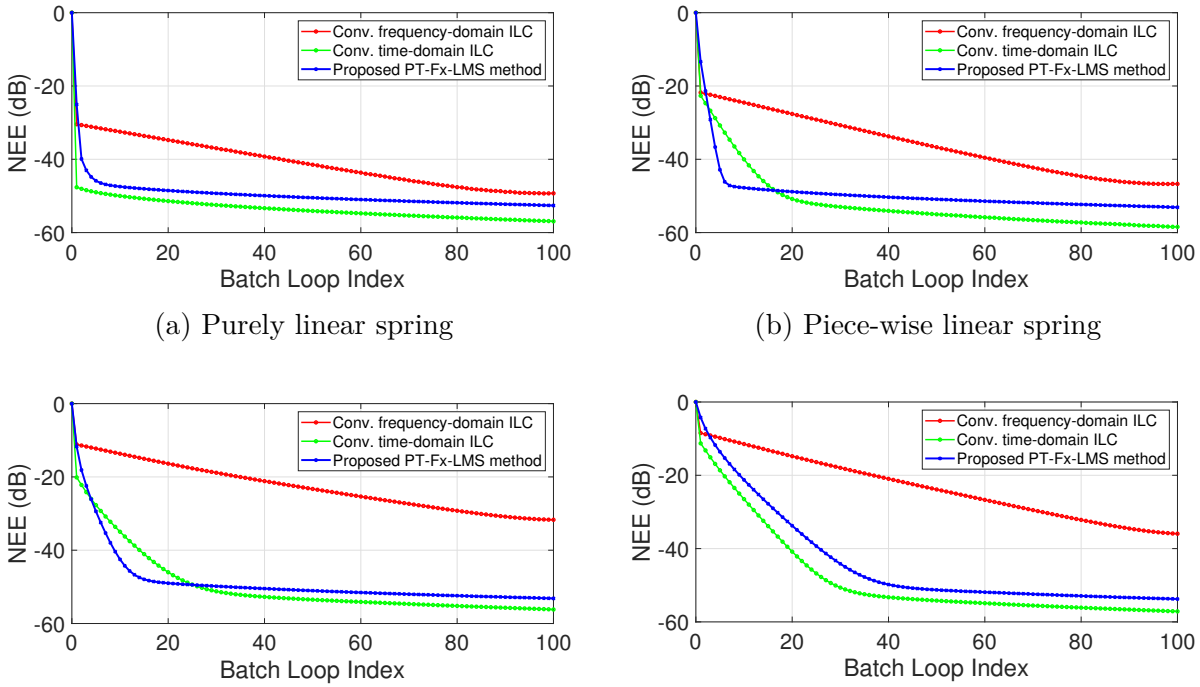

(a) Purely linear spring

(b) Piece-wise linear spring

(c) Mild cubic spring, $F_s(y)$

(d) Harsh cubic spring, $F_s^{'}(y)$

Figure 4.5: NEE reductions through the 100 batch loop iterations for the simulation test benches in Case Study 1

In addition to the final results of the simulations presented in Table 4.1, it is also useful to observe the convergence process of the adaptive process and the rate at which the NEE reduction is achieved through the batch iterations. Figure 4.5 shows the NEE reduction through the 100 batch loops considered for this case study for the four test benches of interest, and it can be seen that the proposed PT-Fx-LMS method for DFID achieves a low misadjustment that is often viable enough for practical applications at a very similar rate as the conventional time-domain ILC method. For these set of simulations, it is seen that both these methods have a very fast rate of NEE reduction initially and with the constant

iteration step-sizes used for these adaptive processes, the rate of NEE reduction slows down significantly. Since the purpose of the DFID process is only to synthesize control inputs that would generate a response as close to the desired response as possible, convergence of the algorithm is not shown in Figure 4.5 for the conventional time-domain ILC method or the proposed PT-Fx-LMS method. Simulations were nevertheless carried out to check for stability and convergence of the algorithm and was found that for the systems under test and choice of step size used here, the NEE reduction converges to -70 dB after approximately 2000 iterations which is far greater than what would be feasible due to time and cost constraints on a real-world test rig for the DFID process.

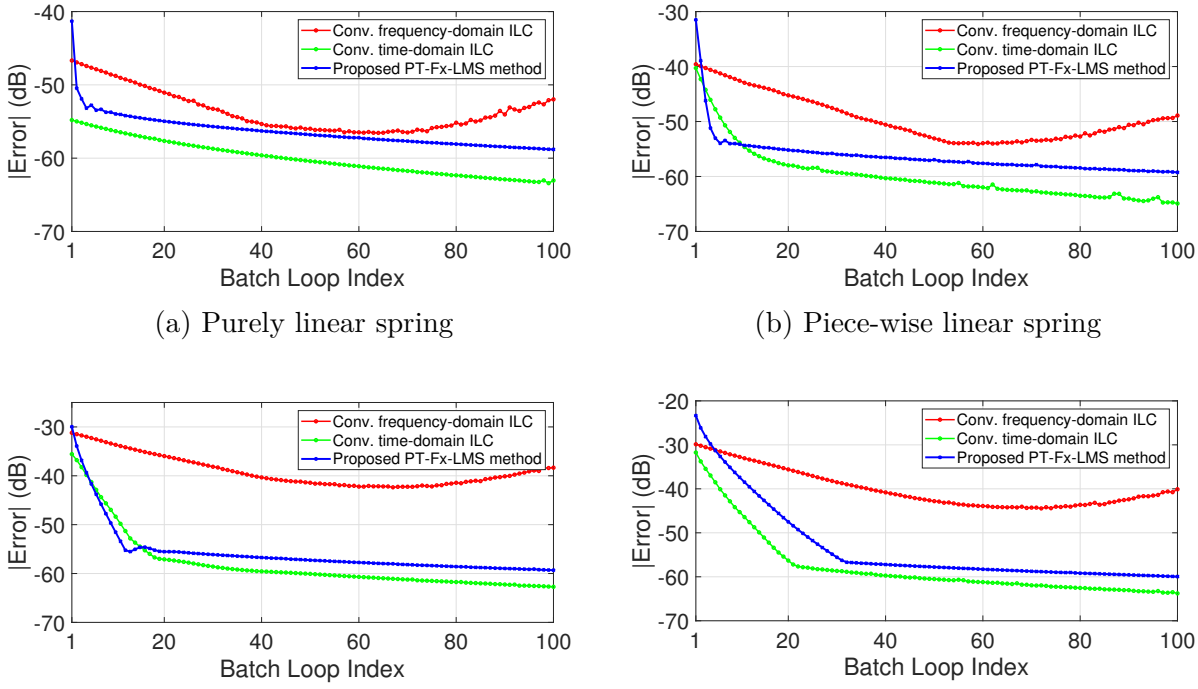

(a) Purely linear spring

(b) Piece-wise linear spring

(c) Mild cubic spring, $F_s(y)$

(d) Harsh cubic spring, $F_s^{'}(y)$

Figure 4.6: Maximum output error in dB through the 100 batch loop iterations for the simulation test benches in Case Study 1

For this case study, it can also be seen that these two methods perform significantly better than the conventional frequency-domain ILC method, which has been tuned for these

simulations to achieve the minimum misadjustment at the end of the 100 batch loop iterations. Further iterations or a higher but constant step size for this method actually increase the misadjustment and the adaptive process diverges. This can also be observed in Figure 4.6 which shows the maximum amplitude of the output error (in dB) at the end of each iteration.

It is also necessary to note that the conventional time-domain ILC method requires the identification of both a forward system model, identified here using the LMS system identification procedure presented in section 2.2.3 followed by the identification of a good delayed inverse FIR model, as given in section 2.3.2.2 using the Filtered-x LMS algorithm. This requires the selection of appropriate reference inputs and the tuning of these algorithms to achieve the performance presented here. In contrast, the proposed PT-Fx-LMS method is more robust to the accuracy of the identified forward system models and does not require the identification of any FIR inverse models.

While the final output error is of most concern for the objectives of the DFID process alongside the necessity to reduce the number of iterations and consequently testing time to achieve this performance, many SER testing procedures also require the spectral accuracy of the output response in comparison to the target response and the necessity to make sure the derived drive files do not overwhelm the capabilities of the actuators.

Figure 4.7 compares the power spectrum density of the final output responses at the end of 100 batch loop iterations of the three methods used in this case study in comparison to the PSD of the target response previously presented in Figure 3.4b. It is observed that the maximum deviation of the output responses from the target response occurs in the 6–80 Hz bandwidth and hence only this frequency range is shown in Figure 4.7. From these spectra, it can be observed for all the test benches, the output response obtained from the final drive derived using the PT-Fx-LMS method deviates the most from the target response in the 8–15 Hz range, with the results from the conventional time-domain ILC method being slightly

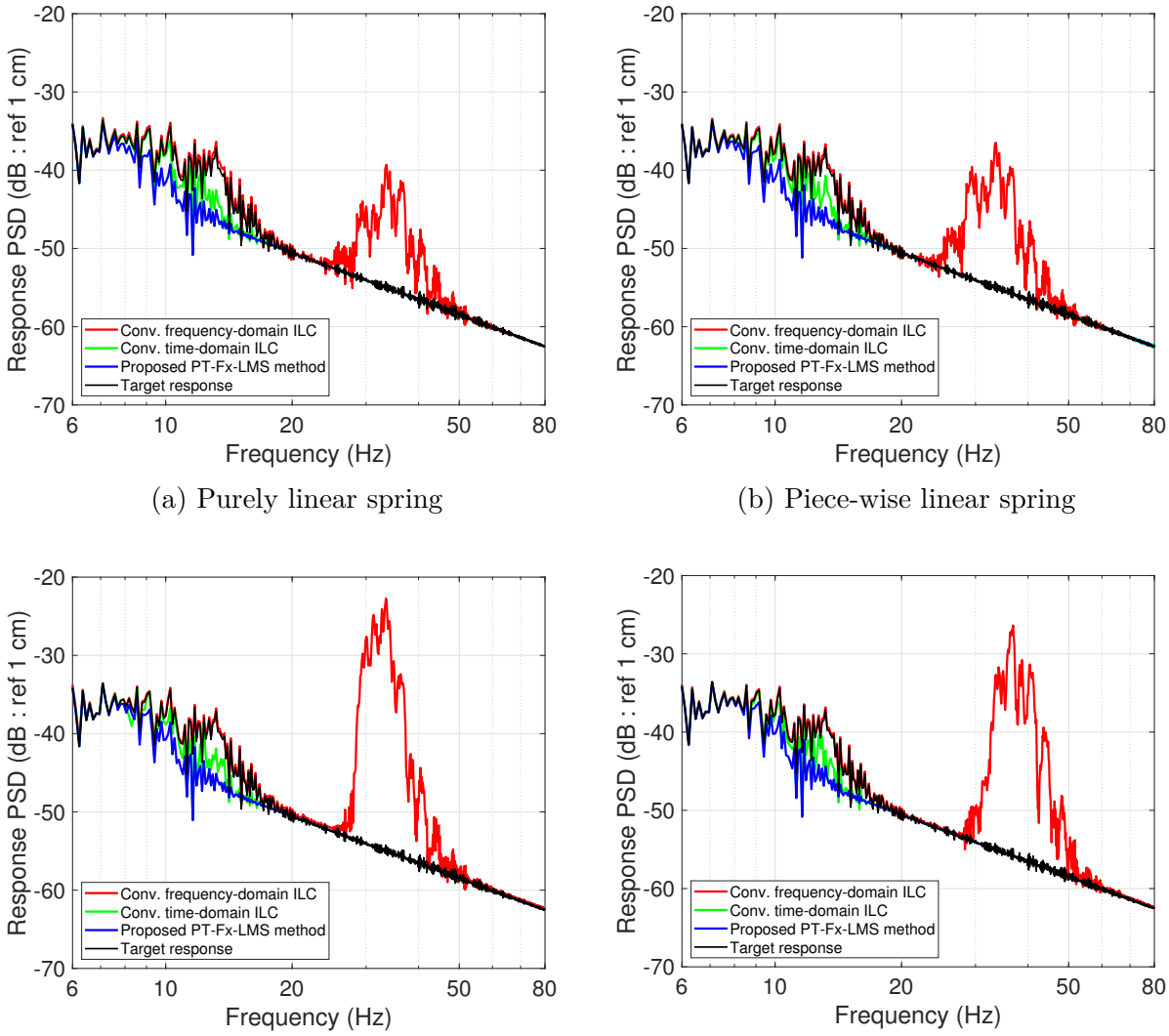

(a) Purely linear spring

(b) Piece-wise linear spring

(c) Mild cubic spring, $F_s(y)$

(d) Harsh cubic spring, $F_s^{'}(y)$

Figure 4.7: Final output response PSD in comparison to the target response **d** for the simulation test benches in Case Study 1

closer to the ideal target spectrum in this frequency range. It could be hypothesized that this performance could be improved by adjusting the identification drive shown in Figure 3.5 in order to further excite the system in this frequency range to improve these results. When the iterative process is continued beyond the 100 iterations presented in this case study, it is nevertheless seen that the output response achieved from both of these methods eventually

approaches the target response. On the other hand, the output response obtained through the conventional frequency-domain ILC method shows much larger deviations in the 20–60 Hz frequency range that contributes to the overall poorer results of this method as can be seen in the final NEE reduction presented in Table 4.1. This outcome can be attributed to the drop in the coherence function of the H_1 estimation at 25 Hz as shown in Figure 3.6, which would consequently also affect the inverse models identified using the ZMETC models, since the inverse model identification is also weighted by the respective coherence functions for each of the test benches.

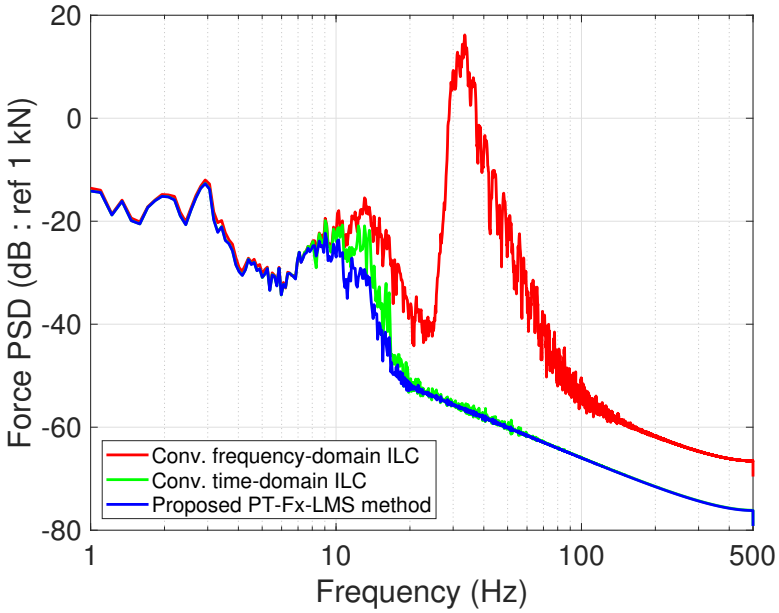

Figure 4.8: PSD of the derived final drive file using different methods for the mild cubic spring model test bench in Case Study 1

While the output responses obtained for the conventional frequency-domain ILC method could still be acceptable for most SER applications, since for all the test benches considered the overall NEE reduction obtained is in the 30–50 dB range, see Table 4.1, the actual drive files derived to produce these responses have extremely large actuator forces, especially at higher frequencies (for example, up to 70 dB higher power at 33 dB in this simulated test bench) which can overwhelm the actuator authority of many SER test rigs. This is shown

through the actuator force PSD plot for the mild cubic spring test bench in Figure 4.8. The time series final drive files and the final output responses for all the test benches are attached in Appendix B.1 which shows that the drive files obtained using the conventional frequency-domain ILC method produce actuator forces in excess of 20 kN and much more high frequency deviations than the drive files produced by the other two DFID methods. Such results in the DFID procedure often requires the operator to implement additional filtering of the drive files in order to maintain safety of the SER testing equipment for certain conventional methods and sometimes compromise on the final output responses that can be achieved on these test rigs.

4.4.2 Case Study 2: Perturbed drive signals in time slices

In many practical DFID applications, it is often useful or necessary to have the ability to fine-tune sections of the drive file by focusing on specific intervals in time. Frequency-domain techniques typically have difficulty focusing on select time intervals without perturbing the response outside those intervals, since the entire batch of data is required to be adapted. To illustrate the ability of the PT-Fx-LMS DFID method to focus on specific time intervals, another series of case studies are performed.

In this first time-slice study, the optimal drive signal from the previous evaluation derived using the PT-Fx-LMS method was artificially perturbed by zeroing out the drive signal over two time intervals: from 5–7 seconds and 15–20 seconds; such a modified drive for the purely linear model test bench is shown in Figure 4.9. The duration of these perturbations, 2 and 5 seconds respectively, were also considered such that they are longer than the period of the FIR filters of the estimated linear models considered. This perturbed drive signal was then used as the initial control sequence, and the adaptation process was iterated to observe if the

drive file would return to the original solution. Partially zeroing out the control sequence in intervals is an extreme test to evaluate how well the algorithm works within time slices while also not affecting the converged drive file outside these regions. In order to avoid sharp discontinuities in the initial drive file that could lead to large spikes in actuator authority, the transition at the intervals were smoothed. While the conventional frequency-domain ILC implementation for DFID remains the same as set up in the previous case study where the entire batch of data is updated for every batch loop as is required for a frequency domain adaptive structure, the time-domain implementations of the DFID algorithms used here, i.e., the conventional time-domain ILC scheme and the proposed PT-Fx-LMS method only update the drive files in the neighborhood in order to isolate the adaptive process to the time intervals of interest, hence saving computational resources and demonstrate the abilities of such time-domain adaptive filtering processes.

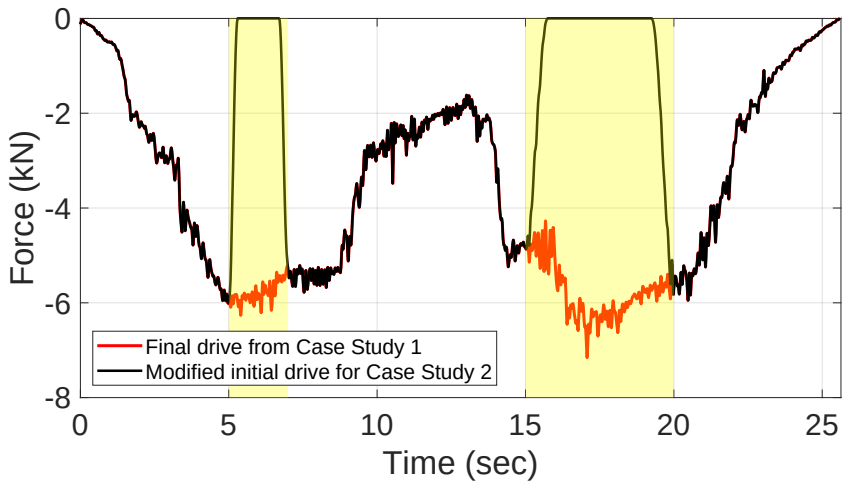

Figure 4.9: Modified initial drive for the purely linear model test bench for Case Study 2

Considering that only certain intervals of the drive needs to be updated in this case study, fewer batch loops, in comparison to the 100 in the first case study were required to achieve convergence or for the iterative process to achieve the minimum output misadjustment, especially in the case of the frequency-domain DFID method which begins to diverge with

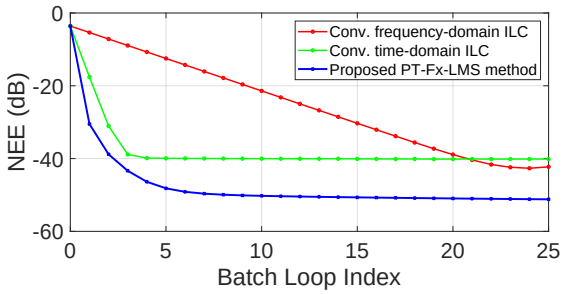

(a) Purely linear spring

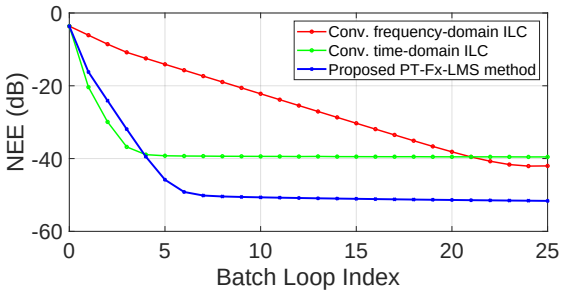

(b) Piece-wise linear spring

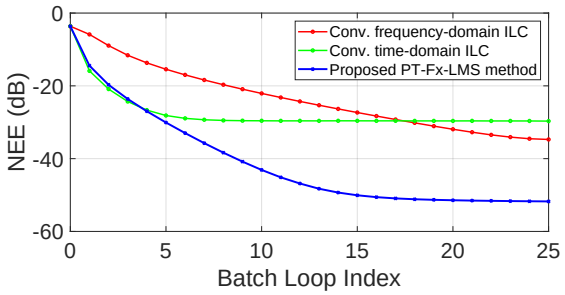

(c) Mild cubic spring, $F_s(y)$

(d) Harsh cubic spring, $F_s^{'}(y)$

Figure 4.10: NEE reductions through the batch loop iterations for the simulation test benches in Case Study 2

more iterations with this specific choice of the iteration step size. Similar to the previous case study, the simulation parameters and final NEE reduction results are presented in Table 4.2. Of most interest in this case study is the ability of the adaptive algorithm to achieve a low output misadjustment, shown in Figure 4.10 for the test benches of interest and the three DFID methods considered, and also not affect the response outside the perturbed intervals because of the adaptation of the drive files within those specified time slices. This latter aspect is more clearly visualized by observing the final error at the end of the batch loops as shown in Figure 4.11.

In terms of the NEE reduction achieved through the iterative processes, the conventional frequency-domain method required much more iterations than the other two methods, espe-

Table 4.2: Iteration step size parameter and the NEE reduction results at the end of the batch loops for the iterative DFID methods used for each of the considered dynamic test benches for Case Study 2

(a) Purely linear spring

Method	Iteration step size μ	NEE reduction (dB)
Conventional frequency-domain ILC	0.18	38.69
Conventional time-domain ILC	0.8	36.55
PT-Fx-LMS method	4e9	47.61

(b) Piece-wise linear spring

Method	Iteration step size μ	NEE reduction (dB)
Conventional frequency-domain ILC	0.2	38.40
Conventional time-domain ILC	0.8	35.92
PT-Fx-LMS method	4.6e9	48.01

(c) Mild cubic spring, $F_s(y)$

Method	Iteration step size μ	NEE reduction (dB)
Conventional frequency-domain ILC	0.15	31.11
Conventional time-domain ILC	0.6	26.07
PT-Fx-LMS method	4.4e9	48.13

(d) Harsh cubic spring, $F_s^{'}(y)$, *50 batch loops

Method	Iteration step size μ	NEE reduction (dB)
Conventional frequency-domain ILC	0.09	35.98
Conventional time-domain ILC	0.5	34.81
PT-Fx-LMS method	5e9	49.55

cially in the cases of the purely linear, piece-wise linear and the mild cubic nonlinear model test benches. Despite this method achieving a slightly lower misadjustment than the conventional time-domain ILC alternative, it was observed to be more sensitive to the choice of iteration step size and a stable convergence is not achieved since performing more batch loop iterations leads to an increase in the output error for the choice of a constant step size. The conventional time-domain ILC method is able to very quickly (with a few batch loops)

reach its minimum misadjustment, but converges to an output misadjustment higher than the proposed PT-Fx-LMS method. This is because the simulation is directed to only use the error in the specified time-intervals to update the drive file, and not the entire batch of data as in the previous case study. This is visualized clearly in the time-series of the final output error in Figure 4.11 which shows good performance within the time slices, but shows large deviations in the neighborhood of these time intervals. The proposed PT-Fx-LMS method does not demonstrate such deviations and hence shows that the proposed method is able to isolate adaptation to specific time slices without disturbing the previously converged sections of the drive file. Such a feature is extremely useful in the industry when certain time slices need to be isolated for changing SER testing requirements or for fine-tuning the drive in a particular time interval without the need to run the whole batch of data through the adaptive process, which is often extremely time-consuming.

The final drive files from these simulations similarly reveal the deviations obtained just in the neighborhood of the specified time slices, despite the gentler zeroing of the initial drive to prevent large discontinuities. Figure 4.12 shows the final drives achieved for the mild cubic model test bench, which exhibited the largest magnitude error immediately after the specified time intervals. From the results in Figure 4.11 and 4.12, it is also clear that in the case of the adaptive inverse based conventional time-domain ILC method, the larger errors outside the time intervals of interest last the length of the inverse FIR filters used in the adaptive process. For example, in the case of the mild cubic model test bench, the larger errors preceding the specified time intervals span the samples of delay, Δ for the inverse model given in Table 3.5, and lasts for the duration given by $L_{inv} - \Delta$ immediately after the time slices. In contrast, the proposed PT-Fx-LMS method is able to generate a drive file that does not affect the drive file outside the time intervals of interest, i.e., it perfectly tracks the modified initial drive in those time intervals. The final drive obtained through the

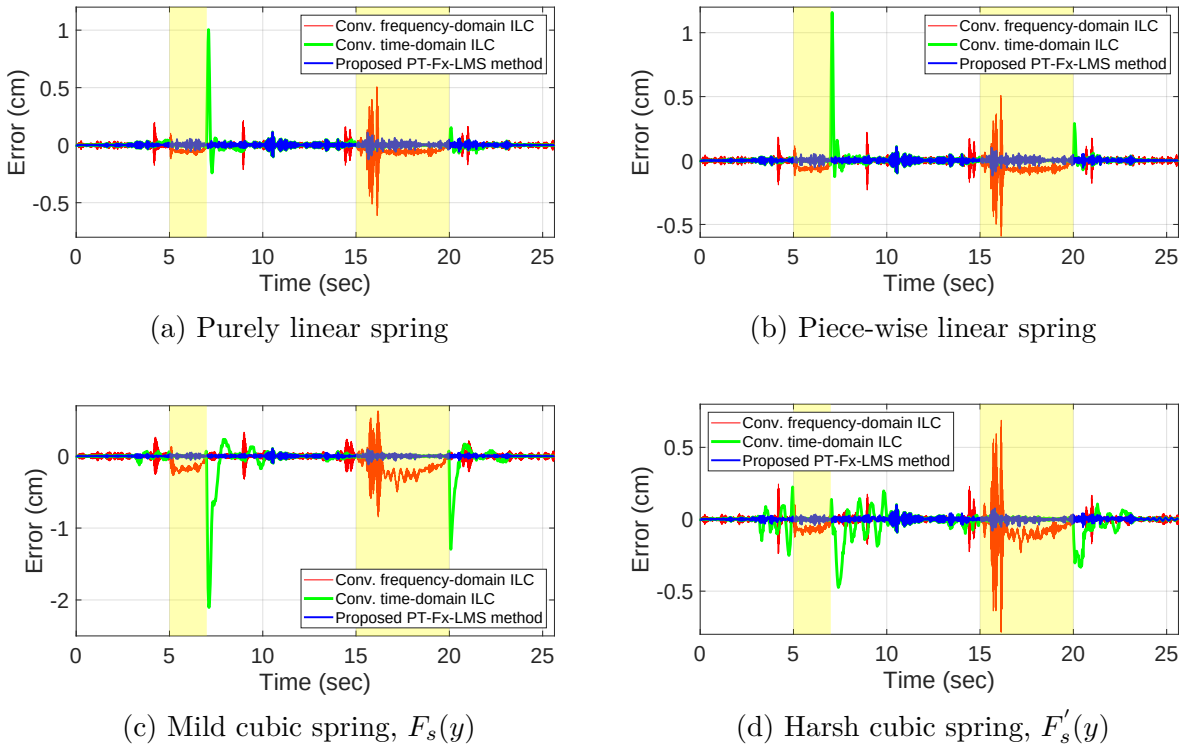

(a) Purely linear spring

(b) Piece-wise linear spring

(c) Mild cubic spring, $F_s(y)$

(d) Harsh cubic spring, $F_s'(y)$

Figure 4.11: Final output error for the simulation test benches in Case Study 2

conventional frequency-domain method is not shown here since the derived drive file showed very high actuator authorities in excess of 40 kN and much higher frequency content, similar to the results in the previous case study, as shown by the results in Appendix B.1.

4.4.3 Case Study 3: Modified target data in time slices

Just as it is useful to update or fine-tune the drive files in specified time intervals, the SER testing procedure sometimes also requires changes to the target data in such time slices and derive the required drive files for the test rig without needing to re-equip the test specimen and record the entire batch of target data again. An example of such target data changes could be the simulation of a suspension system hitting a pot-hole or a curb on the road that

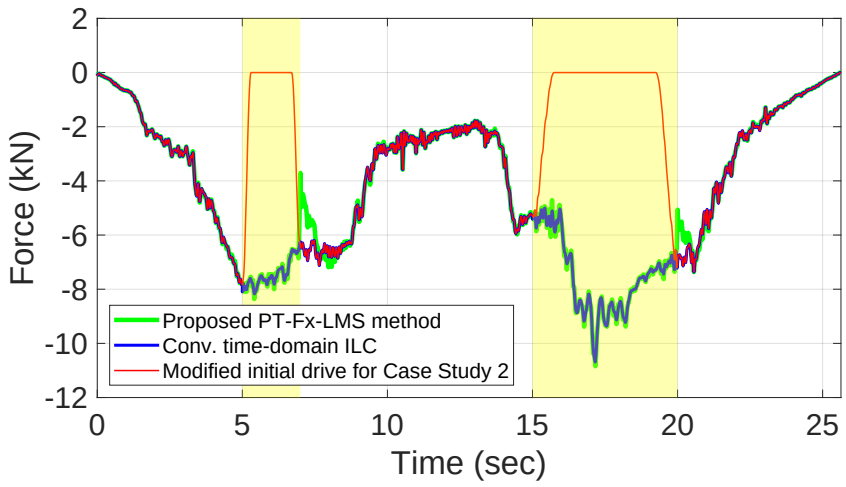

Figure 4.12: Final drive files for the mild cubic model test bench for Case Study 2

leads to a large discontinuous event in a short time interval.

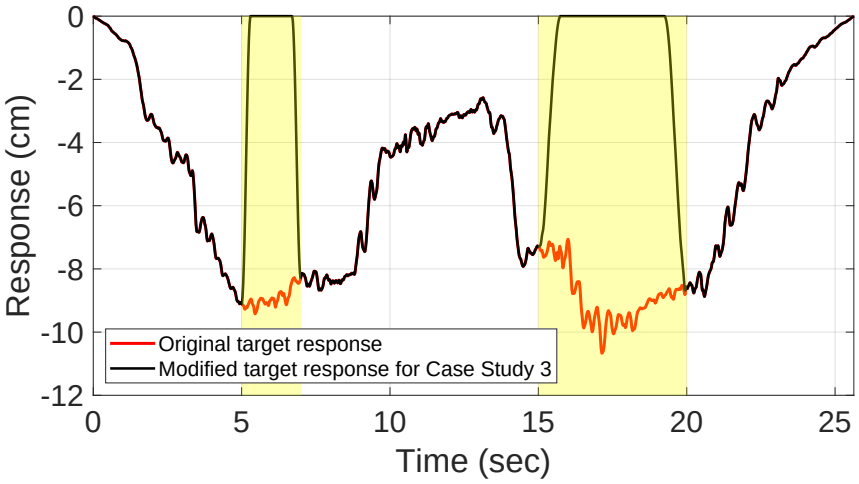

Figure 4.13: Modified target response for Case Study 3

As an extension of the previous case study in 4.4.2, a more extreme perturbation test was performed in which the original optimal final drive from Case Study 1 in 4.4.1 obtained using the PT-Fx-LMS method for the corresponding test bench was chosen to be the initial drive signal, but for this study the target response was zeroed out over the same two time intervals: from 5–7 seconds and 15–20 seconds. As in Case Study 2, the transition in the interval was smoothed as shown in Figure 4.13 to prevent large spikes in the response or actuator

authority. This is an intentionally contrived example whose sole purpose is to illustrate the capability of the method to adapt to the modified drive signals without affecting the drive or response in other sections of the specified time intervals.

Table 4.3: Iteration step size parameter and the NEE reduction results at the end of the batch loops for the iterative DFID methods used for each of the considered dynamic test benches for Case Study 3

(a) Purely linear spring

Method	Iteration step size μ	NEE reduction (dB)
Conventional frequency-domain ILC	0.19	42.41
Conventional time-domain ILC	0.8	48.66
PT-Fx-LMS method	4e9	49.05

(b) Piece-wise linear spring

Method	Iteration step size μ	NEE reduction (dB)
Conventional frequency-domain ILC	0.18	46.97
Conventional time-domain ILC	0.8	42.25
PT-Fx-LMS method	4.6e9	49.47

(c) Mild cubic spring, $F_s(y)$

Method	Iteration step size μ	NEE reduction (dB)
Conventional frequency-domain ILC	0.14	41.02
Conventional time-domain ILC	0.6	28.56
PT-Fx-LMS method	4.4e9	49.57

(d) Harsh cubic spring, $F_s'(y)$, *50 batch loops

Method	Iteration step size μ	NEE reduction (dB)
Conventional frequency-domain ILC	0.09	40.60
Conventional time-domain ILC	0.06	34.04
PT-Fx-LMS method	3e9	49.69

Figure 4.14 shows the adaptation curves for the three methods of DFID and the test benches considered for this case study. It shows that with reducing accuracy of the models used for the adaptive algorithms, the number of batch loops required to achieve its minimum

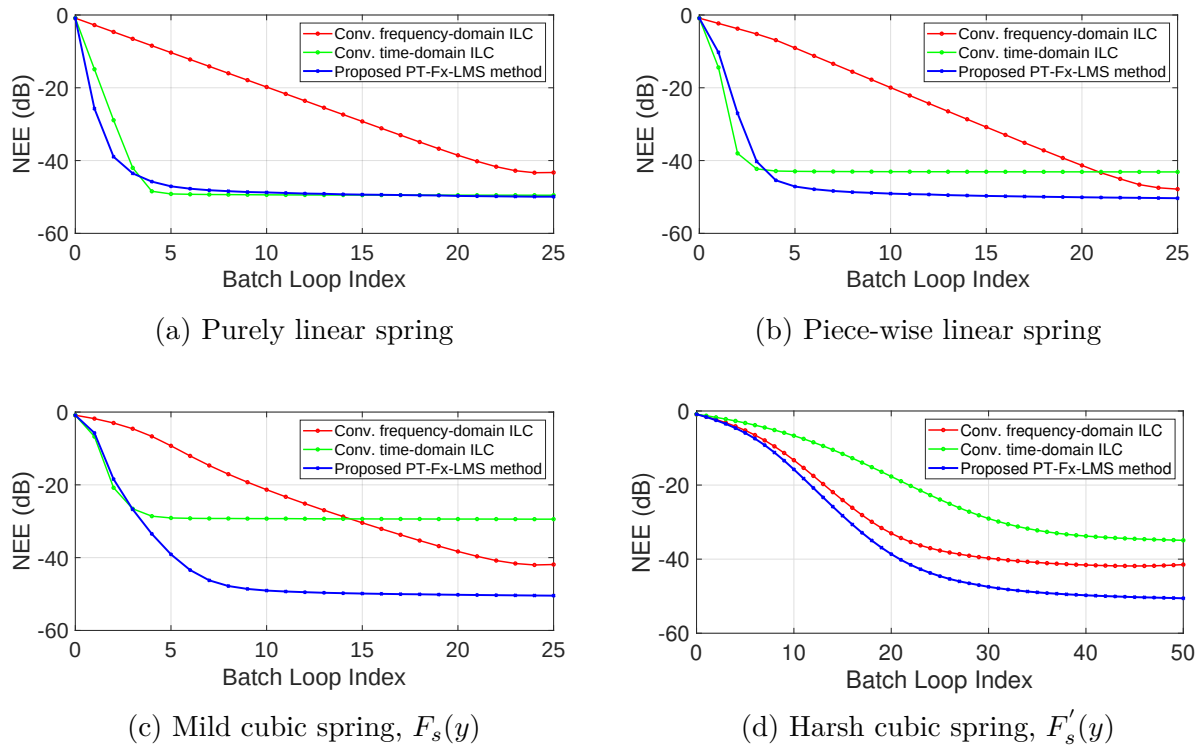

(a) Purely linear spring

(b) Piece-wise linear spring

(c) Mild cubic spring, $F_s(y)$

(d) Harsh cubic spring, $F_s^{'}(y)$

Figure 4.14: NEE reductions through the batch loop iterations for the simulation test benches in Case Study 3

misadjustment increases. The adaptive inverse based conventional time-domain ILC method also shows poorer performance, similar to the results in Case Study 2 when only certain time-slices of the target response is to be adapted. The frequency-domain based method shows better misadjustment (except in the case of the purely linear model test bench) in terms of the overall NEE performance than the conventional time-domain ILC method, but this can be attributed to the fact that the entire batch of data is used in the adaptive process. The proposed PT-Fx-LMS performs the best in this case study across all the considered test bench for the selection of iteration parameters presented in Table 4.3. The final output error time series for these tests are presented in Figure 4.15 which similarly shows the improved performance of the proposed DFID method without affecting the response outside the specified time slices.

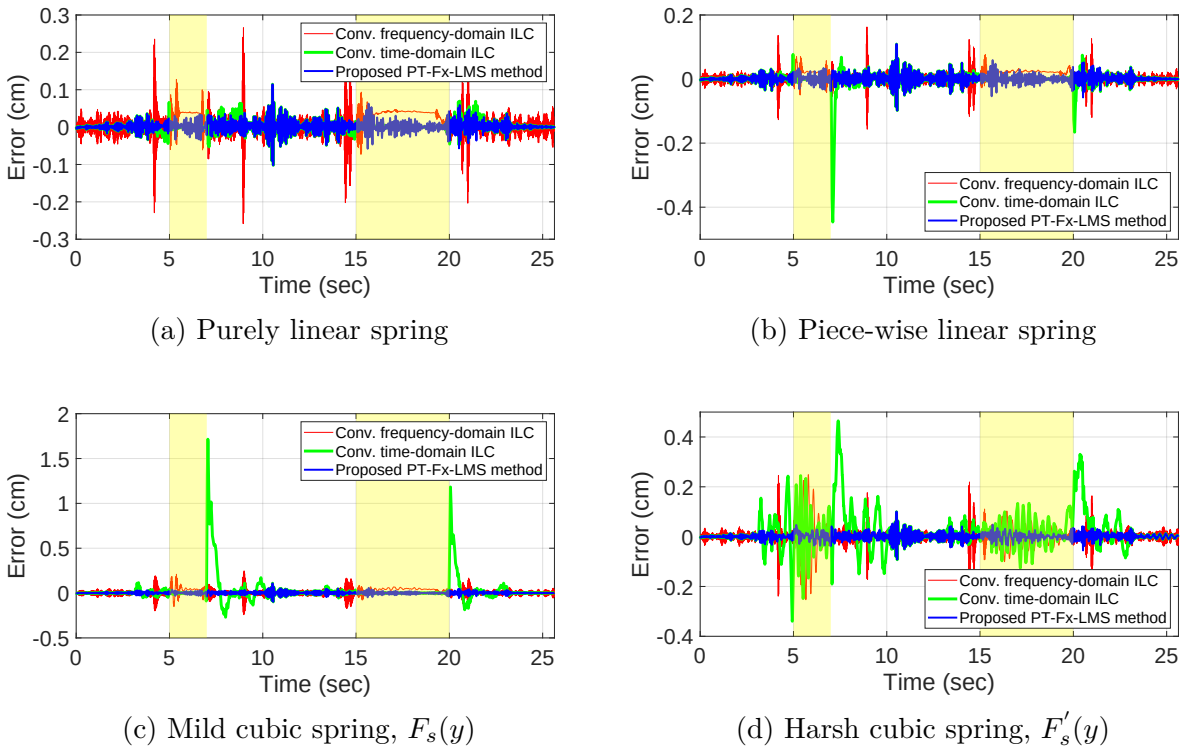

(a) Purely linear spring

(b) Piece-wise linear spring

(c) Mild cubic spring, $F_s(y)$

(d) Harsh cubic spring, $F_s^{'}(y)$

Figure 4.15: Final output error for the simulation test benches in Case Study 3

Similar to the discussion in the previous case study, the frequency-domain ILC method shows deviations outside the time slices of interest, despite the entire batch of data being used to update the drive files. Comparing the conventional time-domain ILC method and the proposed PT-Fx-LMS method, it is similarly observed that while the former produces smaller output errors within the time slices for the selected choice of iteration parameters, except in the case of the harsh cubic nonlinear spring, the long adaptive inverse filters with the included delay affect the performance of this DFID method outside these specified time intervals. While this can be improved by updating the drive file using the entire batch of data or include the time interval as long as the adaptive inverse FIR filter on either side of the perturbed target response, this is not the purpose of this case study which is meant to demonstrate the ability of the proposed algorithm to isolate the drive file update within

these intervals without affecting the response elsewhere. Similarly, it was surmised that the time slices as considered here need to be atleast as long as the length of the forward FIR filter models used for the proposed DFID method, or in the case they are shorter (in this case $Q = 1000$ coefficients), the adaptive algorithm needs to be "allowed" to update the weight filter for atleast that many coefficients.

In the case of the harsh cubic nonlinear spring, it can be seen in Figure 4.15d that the conventional methods fail to effectively converge to the modified target response. It is hypothesized that the poorer quality of the forward and inverse model identification, along with the discontinuous nature of the modified target response, despite the gentle ramp provided at the beginning and end of the time intervals. The iteration parameters for both the conventional methods presented here needed to be significantly relaxed to ensure viable performance and also maintain stability within the batch loops considered for this test case.

4.5 Conclusion

A new algorithm has been proposed for the identification of drive files for Service Environment Replication applications. The proposed Pulse Train Fx-LMS algorithm is derived from a synchronous ANVC adaptive filtering algorithm that is modified to handle the broadband drive file identification application for dynamic systems. The two key modifications that enable PT-Fx-LMS to be useful for DFID applications are: (1) the use of a unitary pulse train reference input of the same length as the batch target data set, which results in (2) a simplified adaptation methodology.

The PT-Fx-LMS algorithm was validated on simple but representative SISO linear and nonlinear suspension test benches using actual suspension displacement time series data from a race car. In addition to demonstrating the iterative operation of the proposed algorithm,

its performance was evaluated and compared against conventional drive file identification methods. The estimated linear model used by the PT-Fx-LMS algorithm for the gradient estimate is shown to work quite well for even nonlinear test bench examples. As is common for conventional Fx-LMS algorithms, linear models used in the gradient estimate are often more than sufficient for nonlinear systems due to the iterative nature of the algorithm.

In order to more thoroughly evaluate the PT-Fx-LMS algorithm, several extreme tests were performed. These tests were created specifically to highlight a common problem that conventional frequency-domain DFID methods have difficulty performing, i.e. focusing the iterative update on isolated time slices in the target data without perturbing the converged response outside those time slices. In one case, the converged control solution was artificially perturbed (set to zero) in two isolated time segments. In the second case, the target data was artificially perturbed (set to zero) in two isolated time segments, and the control solution started from its original converged values. In both cases, the PT-Fx-LMS algorithm was able to converge to the appropriate solution in a small number of iterations without perturbing the existing converged response. The success of the PT-Fx-LMS algorithm in the simulated case studies above clearly establish proof-of-concept for this method.

Chapter 5

An Estimation based approach to the PT-Fx-LMS algorithm for DFID

5.1 Introduction

The performance of the proposed Pulse Train Fx-LMS method for DFID was demonstrated for deriving drive files that reduce tracking error of the target response in as few batch iterations as possible when benchmarked against conventional DFID methods in Chapter 4. The motivation for the developments presented in this chapter to the proposed PT-Fx-LMS algorithm remains to reduce the cycle time through the adaptation workflow.

To establish proof-of-concept, the performance of the new algorithm is demonstrated and compared against the previously proposed DFID method using the same test benches presented in section 3.2 and used in the performance evaluation case studies in section 4.4. A case study exploring the possibilities of a termination criteria are also discussed in the paper that could be used to further speed up the adaptation process or ensure stability of the adaptation process in the case of harsh nonlinear test benches with comparatively deficient identified system models.

5.2 Setup of the EB-PT-Fx-LMS algorithm for DFID

The implementation of the Estimation Based PT-Fx-LMS (EB-PT-Fx-LMS) method for DFID follows the basic structure of the PT-Fx-LMS algorithm presented in Chapter 4. The adaptive filter architecture can be divided into two domains as shown in the filter architecture block diagram shown in Figure 5.1, with the physical domain (above the red dashed line) represents the data collection and processing on the test rig while the simulation domain (below the red dashed line) is where the offline adaptation algorithm is confined to. A similar structure for conventional ILC methods was presented by Müller and Endisch for cross-coupled vehicle test systems.

The same pulse train reference input, $\mathbf{x_k}$ as in 4.6 is used, with a similar period of the pulse train sequence being equal to the length K of the target response. The pulse train sequence $\mathbf{x_n}$ in the physical experiment domain of Figure 5.1 is identical in structure to $\mathbf{x_k}$, with the change in subscript only used to illustrate that the sequences are independent of each other. Similarly, the target response given by $\mathbf{d} = \begin{bmatrix} d_1 & \cdots & d_k & \cdots & d_K \end{bmatrix}^T$ uses the subscripts $\mathbf{k}$ and $\mathbf{n}$ to distinguish the same target responses in the simulation and physical domains respectively. The adaptive filter given by $\mathbf{w_k} = \begin{bmatrix} w_1 & \cdots & w_k & \cdots & w_K \end{bmatrix}^T$ is defined similar to the development of the PT-Fx-LMS algorithm and by construction the coefficients of $\mathbf{w}$ will be the final drive file given by the sequence $\mathbf{u_k} = \begin{bmatrix} u_1 & \cdots & u_k & \cdots & u_K \end{bmatrix}^T$.

The subscript s refers to the simulation iterations (1 through S) conducted between the physical experiments p (1 through P) on the test rig. AT the end of the convergence process and by construction, the FIR filter $\mathbf{w}_{S,P} = \begin{bmatrix} w_1 & \cdots & w_k & \cdots & w_K \end{bmatrix}^T_{S,P}$ will be the final drive file. The objective remains to achieve a low misadjustment [105] with a minimum number of physical experiments on the test rig, p. The key contribution of this method is to carry out a number of simulations in between these physical test runs to adaptively improve the

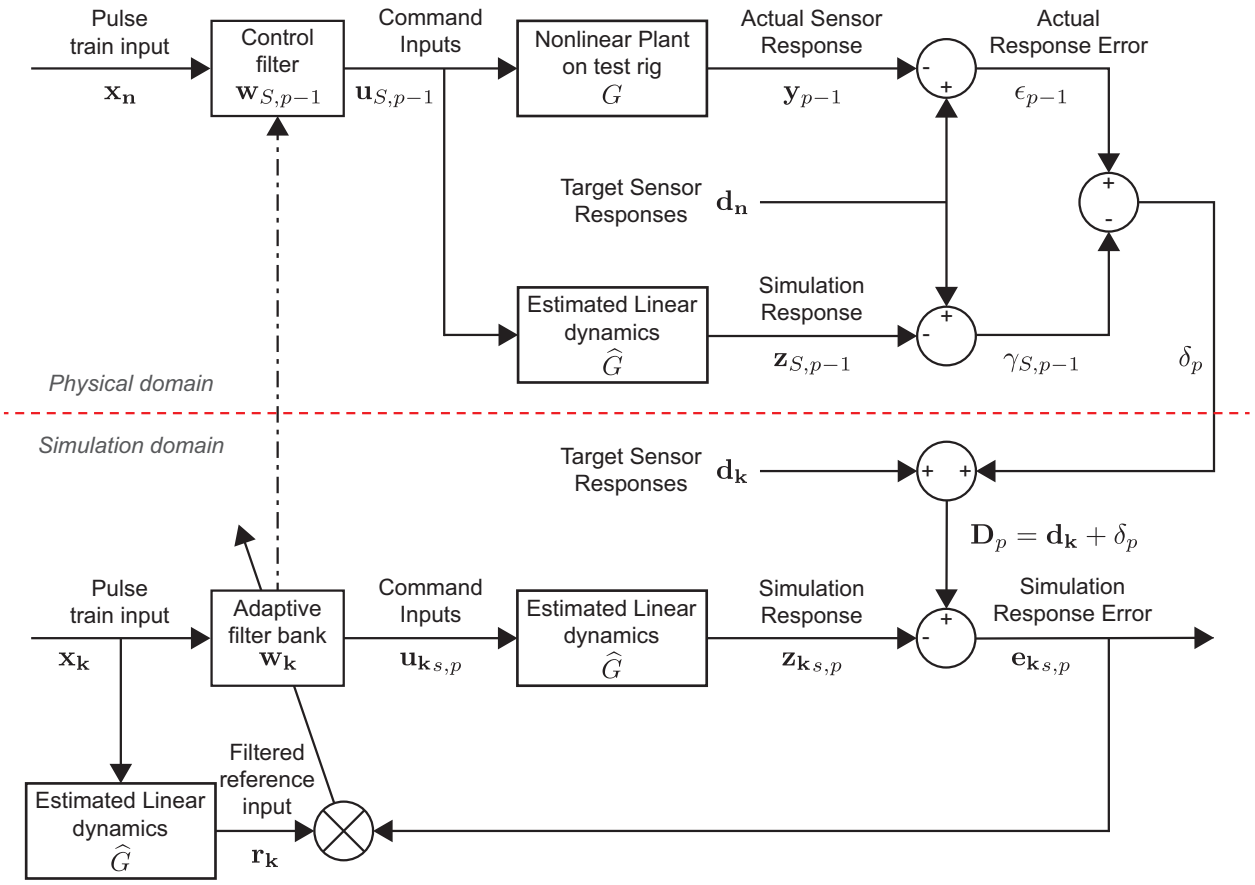

Figure 5.1: Adaptive filter architecture of the Estimation Based PT-Fx-LMS algorithm for DFID

solution before spending the time and resources on a new physical test iteration.

The workflow begins with the estimation of the nonlinear plant as a Q-coefficient linear FIR filter $\widehat{G} = \begin{bmatrix} \hat{g}_0 & \hat{g}_1 & \cdots & \hat{g}_{Q-1} \end{bmatrix}^T$ as presented in section 3.4.1 and previously used for the performance evaluation case studies of section 4.4. The actual sensor response, i.e., the response of the article on the test rig when excited by the command input $\mathbf{u}_{S,p}$ is $\mathbf{y}_p = \begin{bmatrix} y_1 & \cdots & y_k & \cdots & y_K \end{bmatrix}_p^T$. The simulation response $\mathbf{z}_{\mathbf{k}s,p} = \begin{bmatrix} z_1 & \cdots & z_k & \cdots & z_K \end{bmatrix}_{s,p}^T$ is the linear convolution of the command input $\mathbf{u}_{\mathbf{k}s,p}$, constructed after the s^{th} simulation of the p^{th} physical test sequence, and the estimated linear FIR filter $\widehat{G}$. The errors in the above responses $\mathbf{y}_p$ and $\mathbf{z}_{\mathbf{k}s,p}$ w.r.t the appropriate target response is given by

$\epsilon_p = \begin{bmatrix} \epsilon_1 & \cdots & \epsilon_k & \cdots & \epsilon_K \end{bmatrix}_p^T$ and $\mathbf{e}_{\mathbf{k}s,p} = \begin{bmatrix} e_1 & \cdots & e_k & \cdots & e_K \end{bmatrix}_{s,p}^T$ respectively. The subscript $\mathbf{k}$ in the signals $\mathbf{u}_{\mathbf{k}s,p}$, $\mathbf{z}_{\mathbf{k}s,p}$ and $\mathbf{e}_{\mathbf{k}s,p}$ signifies that these signals are computed in the simulation domain and operated on sample-by-sample, instead of the batch processes in the physical domain.

Since the linear FIR filter estimate of a nonlinear plant is never perfect, an iterative method is used to adaptively find the drive file. That concept is extended in this architecture by using the difference $\delta_p = \begin{bmatrix} \delta_1 & \cdots & \delta_k & \cdots & \delta_K \end{bmatrix}_p^T$ between the actual response error when a particular drive file is played out to the real test article, ϵ_p in the physical domain and the response error $\gamma_{s,p} = \begin{bmatrix} \gamma_1 & \cdots & \gamma_k & \cdots & \gamma_K \end{bmatrix}_{s,p}^T$ when the same drive file excites the estimated linear model $\widehat{G}$ as shown in Figure 5.1.

Per the indexing convention used in this chapter, the p^{th} simulation test sequence is preceded by the calculation of δ_p using the drive file generated by the adaptive process at the end of the previous simulation test sequence, $\mathbf{w}_{\mathbf{k}S,p-1}$. The adaptive filter weights are initialized at 0 and hence for the first set of simulation sequences, $\delta_1 = \mathbf{0}$.

$$\delta_p = \epsilon_{p-1} - \gamma_{S,p-1} \tag{5.1}$$

Since the objective of the DFID process is to drive the actual response error, ϵ_p to $\mathbf{0}$, this implies that the error for the PT-Fx-LMS adaptive process during each simulation sequence should converge to $-\delta_p$. Hence, the target response for the p^{th} set of simulation sequences of the adaptive process is augmented by δ_p. This architecture is also significant because the adaptive process is now conducted completely offline and not real-time on a physical test rig. The target response $\mathbf{D}_p$ for the adaptive process is hence given by

$$\mathbf{D}_p = \mathbf{d}_{\mathbf{k}} + \delta_p \tag{5.2}$$

While Figure 5.1 shows the block diagram of the entire architecture for this proposed DFID method at a single instant, the decision tree for this control strategy is presented in Figure 5.2 that shows the sequence of steps to be carried out when transitioning from the physical domain to the simulation domain where the adaptive process is used to derive the drive files.

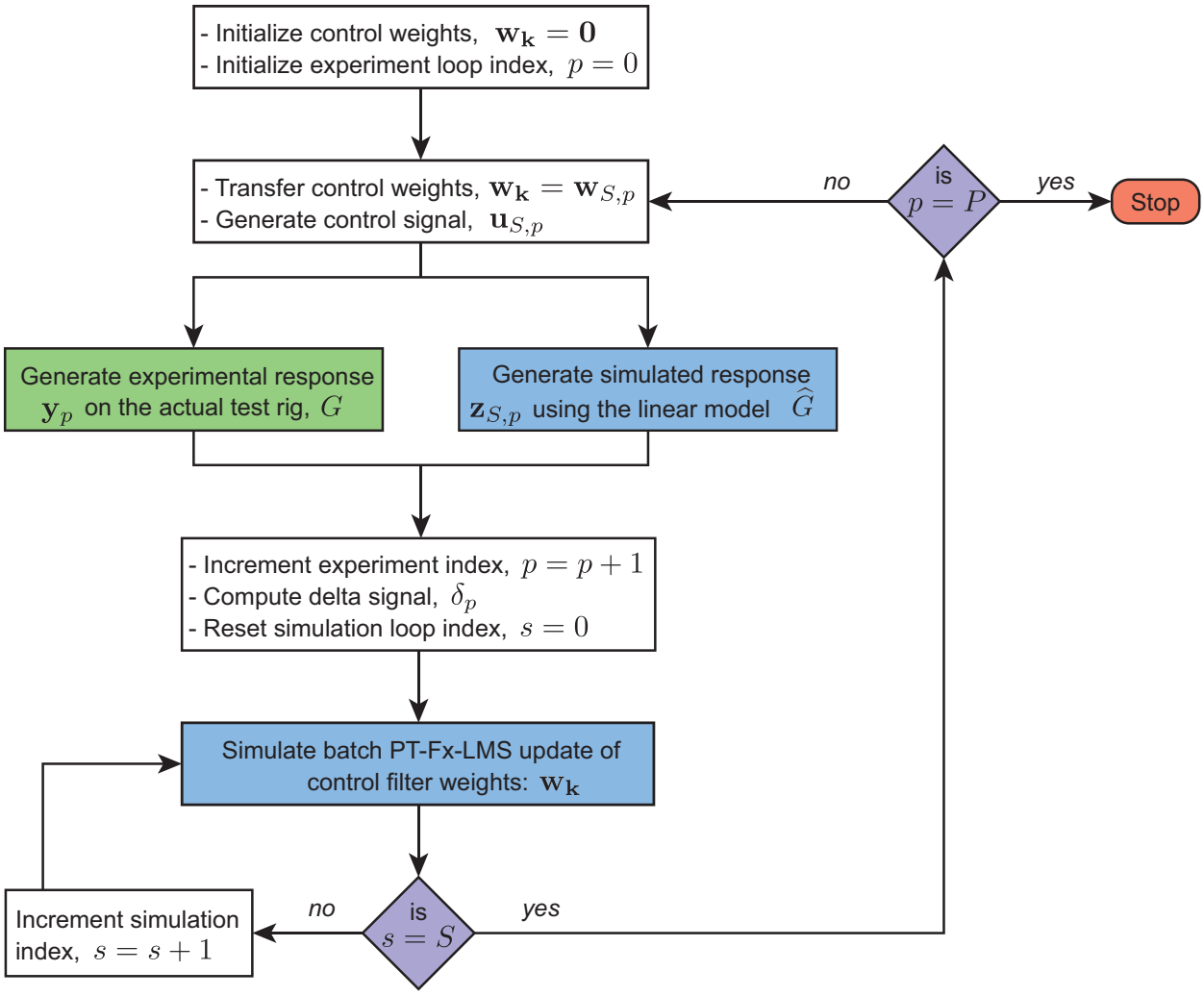

Figure 5.2: Decision flow chart for the Estimation Based PT-Fx-LMS algorithm for DFID

As developed for the ANVC adaptive systems [105], a scalar quadratic cost function J of the output error is established, which is to be minimized over time by the gradient descent

algorithm.

$$\mathbf{e}_{\mathbf{k}s,p} = \mathbf{D}_p - \mathbf{z}_{\mathbf{k}s,p} = \begin{bmatrix} e_1 & \cdots & e_k & \cdots & e_K \end{bmatrix}^T_{s,p} \tag{5.3}$$

$$J = E\left\{ \sum_{k=1}^{K} e^2_{ks,p} \right\} \tag{5.4}$$

where $E\{\bullet\}$ is the expectation operator. Application of the conventional Fx-LMS algorithm in Figure 5.1 yields the gradient descent method for updating the FIR filter coefficients [105]:

$$\mathbf{w}_{\mathbf{k+1}s,p} = \mathbf{w}_{\mathbf{k}s,p} + \mu_s e_{ks,p} \mathbf{r}_{\mathbf{k}s,p} \tag{5.5}$$

where at the simulation index s and physical test index p, $\mathbf{w}_{\mathbf{k}s,p}$ is the entire K-coefficient FIR filter at time step k, μ_s is the positive constant step size, which controls the convergence rate, $e_{ks,p}$ is the instantaneous scalar output error, and $\mathbf{r}_\mathbf{k}$ is a vector of length K constructed as the buffered output of the linear impulse response model $\widehat{G}$ due to the reference input $\mathbf{x}_\mathbf{k}$. Performance of the adaptive process in terms of how fast a low misadjustment can be achieved will depend on the quality of the estimated linear model $\widehat{G}$, the step size μ_s and the amount of uncorrelated noise.

5.3 Performance evaluation simulations and termination criteria

The same test benches presented in section 3.2 and used for the performance evaluation case studies in section 4.4, including the system models used in the adaptive processes to ensure consistency for comparison of the different methods. Similarly, the performance of the adaptation process is evaluated using the Normalized Error Energy (NEE) metric. In

the case of the EB-PT-Fx-LMS method, two different NEE values are computed:

$$\begin{aligned} NEE_p &= \frac{{\epsilon_p}^T \epsilon_p}{\mathbf{d}^T \mathbf{d}} \\ NEE_{s,p} &= \frac{{\mathbf{e}_{s,p}}^T \mathbf{e}_{s,p}}{{\mathbf{D}_p}^T \mathbf{D}_p} \end{aligned} \tag{5.6}$$

where NEE_p is the Normalized Error Energy computed from the actual response error ϵ_p with respect to the required target response $\mathbf{d_k}$ at the end of the p^{th} physical experiment on the test rig and $NEE_{s,p}$ is the Normalized Error Energy computed from the simulation response error $\mathbf{e}_{s,p}$ with respect to the target response for the adaptation process, $\mathbf{D}_p$ at the end of the s^{th} simulation iteration of the p^{th} test sequence.

5.3.1 Case Study 1: Drive files initialized at zero

Similar to the primary case study in section 4.4.1, the drive files are initialized at zero and at the end of each batch loop. Considering the results from the previous chapter, only the conventional time domain ILC method and the previously presented PT-Fx-LMS method are shown here considering the frequency domain ILC method showed consistently poor results for all the test benches. All the simulations in this case are also restricted to 50 batch loop iterations, since the methods of interest here achieve most of their NEE reduction within this range of batch loops.

Table 5.1 presents the parameters used for these simulations for the four test benches considered. In the case of the EB-PT-Fx-LMS method presented on this chapter, the iteration step size is μ_s used for the adaptive process in the simulation domain, the total number of simulation domain batch loops S is given and the total NEE reduction given in Table 5.1 refers to NEE_p as defined in 5.6. Unlike the regular PT-Fx-LMS algorithm, two parameters: (1) the iteration step size, μ_s and (2) number of simulation domain batch loops,

S need to be tuned for in this implementation. The parameters used for the simulations in this study are based on the requirements of maintaining stability, good performance and a feasible duration of computation time.

Table 5.1: Iteration step size parameter and the NEE reduction results at the end of 50 batch loops for the iterative DFID methods for Case Study 1 of the EB-PT-Fx-LMS study

(a) Purely linear spring

Method	Iteration step size μ	NEE reduction (dB)
Conventional time-domain ILC	0.2	54.08
PT-Fx-LMS method	4e9	50.49
EB-PT-Fx-LMS method, $S = 50$	1e9	63.33

(b) Piece-wise linear spring

Method	Iteration step size μ	NEE reduction (dB)
Conventional time-domain ILC	0.2	54.99
PT-Fx-LMS method	4.6e9	50.90
EB-PT-Fx-LMS method, $S = 50$	8e8	61.29

(c) Mild cubic spring, $F_s(y)$

Method	Iteration step size μ	NEE reduction (dB)
Conventional time-domain ILC	0.2	53.49
PT-Fx-LMS method	4.4e9	51.04
EB-PT-Fx-LMS method, $S = 85$	1e8	53.18

(d) Harsh cubic spring, $F_s'(y)$

Method	Iteration step size μ	NEE reduction (dB)
Conventional time-domain ILC	0.2	54.19
PT-Fx-LMS method	4.6e9	51.27
EB-PT-Fx-LMS method, $S = 70$	8e7	52.10

The reduction of NEE through the simulated experimental batch loop iterations and the maximum absolute error in dB for the four test benches and the three DFID methods used in this case study are presented in Figure 5.3 and Figure 5.4 respectively. For the purely linear and piece-wise linear test benches, it can be seen that the EB-PT-Fx-LMS DFID method

is able to achieve very low misadjustment in just the first few experimental tests, at a rate faster than either of the comparative methods. At the end of the 50 batch loops considered here, the proposed method was also able to achieve a lower final misadjustment. It is also interesting to note that while convergence was not achieved within these 50 batch loops, the rate of NEE reduction was still faster than the comparative methods, indicating that further reduction in NEE can be achieved, if necessary.

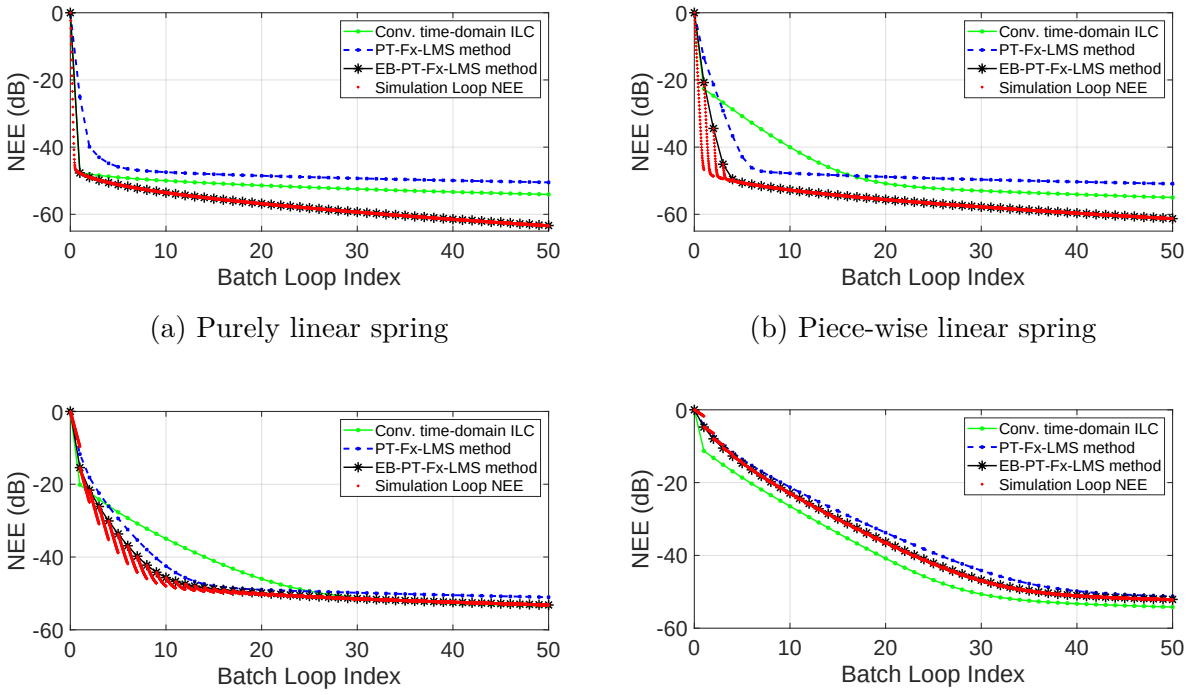

(a) Purely linear spring

(b) Piece-wise linear spring

(c) Mild cubic spring, $F_s(y)$

(d) Harsh cubic spring, $F_s^{'}(y)$

Figure 5.3: NEE reductions through the 50 batch loop iterations for the simulation test benches in Case Study 1 of the EB-PT-Fx-LMS study

It can be seen that as the degree of nonlinearity increases through the four test benches, the number of batch loops required before the NEE levels off close to its respective minimum misadjustment increases. For the mild and harsh cubic spring test benches, the rate of NEE reduction for the EB-PT-Fx-LMS method is comparable to the previously proposed PT-Fx-LMS method, if not slightly improved. All three methods also achieve a similar

misadjustment level at the end of the 50 batch loops considered in this study. To achieve such performance, it can also be seen from Table 5.1 that the constant iteration step sizes for the EB-PT-Fx-LMS method need to be consistently reduced and the number of simulation batch loops tuned appropriately, which is attributed to the deficiencies in the plant model $\widehat{G}$ and the absence of the actual response error from each batch loop used for the adaptive process due to the architecture of the proposed method.

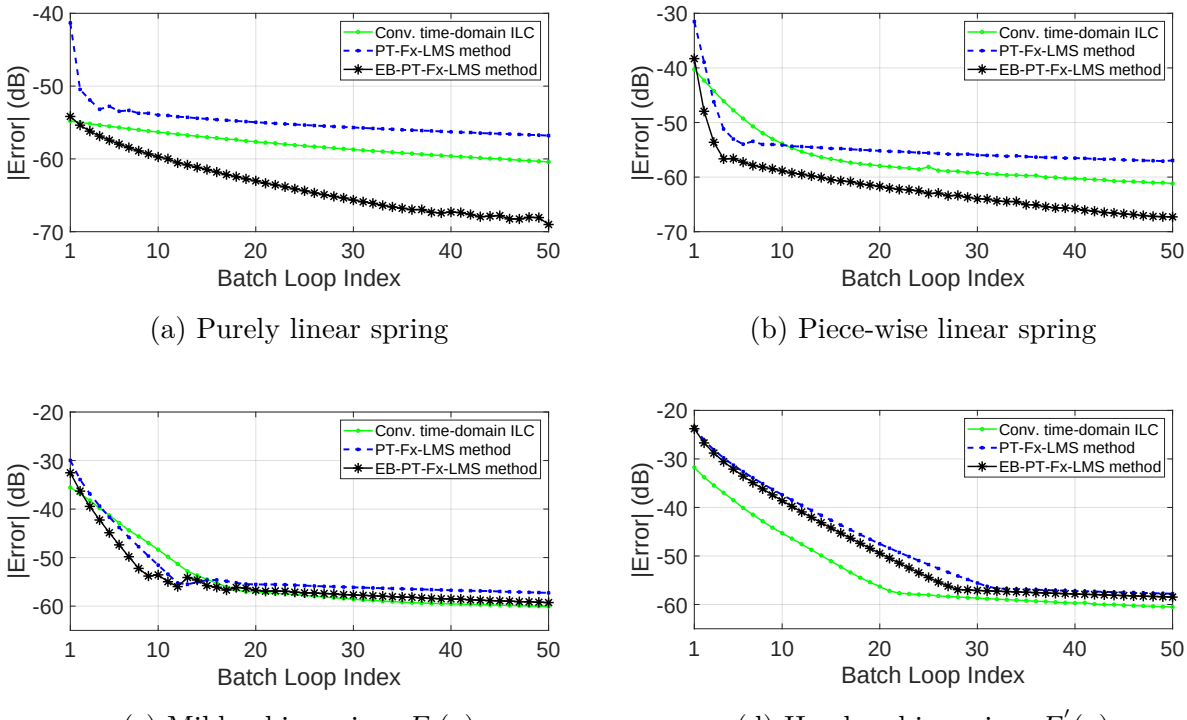

(a) Purely linear spring

(b) Piece-wise linear spring

(c) Mild cubic spring, $F_s(y)$

(d) Harsh cubic spring, $F_s^{'}(y)$

Figure 5.4: Maximum output error in dB through the 50 batch loop iterations for the simulation test benches in Case Study 1 of the EB-PT-Fx-LMS study

5.3.2 Case Study 2: Developing a termination criterion for the EB-PT-Fx-LMS method

As observed from the results in Table 5.1 and Figure 5.3, the tuning of the adaptation parameters for nonlinear systems can be quite challenging while still producing only comparable results to the previously proposed PT-Fx-LMS algorithm for DFID. For example, the 50 simulation batch loops performed for the first few simulated experimental batches for the purely linear and piece-wise linear spring test benches in Figures 5.3a and 5.3b respectively show the simulation loop NEE leveling off, where more simulation loops would not show any significant improvement in performance. On the other hand, for the nonlinear test benches, especially evident in Figure 5.3c for the mild cubic spring test bench, such a leveling off is not achieved with the choice of μ_s and S which were tuned to achieve the best performance in terms of the final output response, and not necessarily to achieve convergence of the individual simulation domain iterative processes.

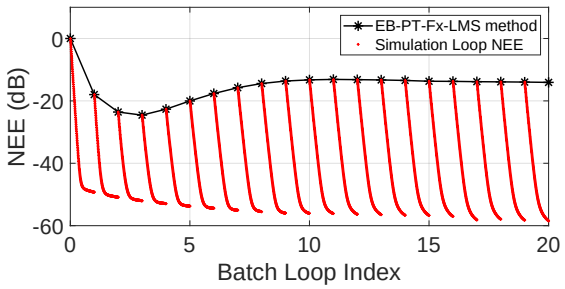

(a) NEE reduction through 20 batch loop iterations with $\mu_s = 5e8$ and $S = 200$ for the simulation domain iterative process

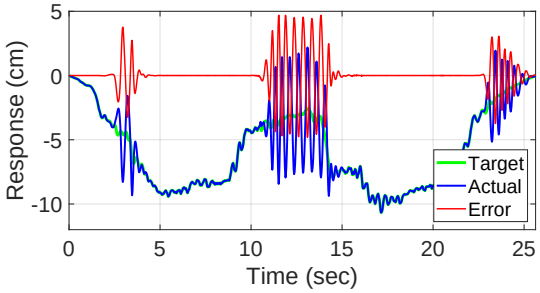

(b) Time series of the final output response, y_{20} and error for the mild cubic spring test bench using the EB-PT-Fx-LMS method

Figure 5.5: Case Study 2 simulation of the failure of the EB-PT-Fx-LMS method due to poor choice of iteration parameters

Conventional rationale would suggest that convergence of the iterative process in the simulation domain where only the estimated linear model $\widehat{G}$ is used for deriving the filtered

reference signal $\mathbf{r_k}$ and generating the simulation response $\mathbf{z_k}$, either through more number of batch loops or through a larger step size would improve performance. Figure 5.5 presents the result of an implementation of the EB-PT-Fx-LMS method for the mild cubic spring test bench with $S = 200$ and $\mu_s = 5e8$, a choice of iteration parameters that drives the simulation domain $NEE_{s,p}$ to converge, or atleast close to leveling off, but the actual response NEE_p shows divergence and much poorer results than the previous case study results. This also exemplifies an initial guess of the iteration parameters which are usually tuned through trial-and-error.

Consider the fifth adaptation sequence conducted in the above case study. While the adaptation in the simulation domain which only uses the estimated linear dynamics is a converging process, the actual NEE_p when the drive file derived at the end of this experiment sequence is played out to the nonlinear dynamic plant actually increases from the previous batch sequence. This can be further understood by conducting a simulated study of the simulation sequence. If the drive file at the end of each iteration s in this simulated sequence were to be applied to the test rig to measure the actual response, the error energy can be clearly seen to be diverging in Figure 5.6. This is a direct consequence of the poor estimation of the nonlinear dynamics of the plant and an incorrect choice of simulation parameters for this nonlinear system.

While one of the methods to prevent such divergences is to unilaterally reduce the constant step size significantly for all the batch loops, this is counter-productive if the objective is to limit the number of simulation runs or reduce the time required to develop the drive file. This suggests that a strategy needs to be developed that allows the termination of the simulation sequence before the actual response begins to diverge. While the ideal termination point would be the minima of the experiment NEE curve in Figure 5.6, for this example at $s = 12$, this curve is presented only as a simulated study and to illustrate the behavior of

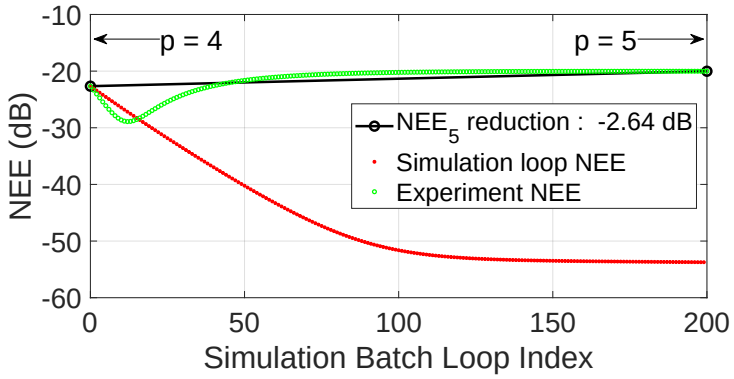

Figure 5.6: Error energy progression for the fifth experiment sequence presented in Case Study 2

the adaptation algorithm in the case of a nonlinear dynamic system and hence is unknown over the course of the simulation sequence.

A termination criterion or a strategy to adjust the iteration step size hence needs to be defined solely based on the information available within the simulation sequence. A novel method to define such a criterion is developed by considering the deviation of the simulation response $\mathbf{z_{s,p}}$ from the actual response measured during the previous physical experiment $\mathbf{y}_{p-1}$ in order to quantify the deviation of the estimated model using the measurable output response. The metric $\Delta_{s,p}$ evaluated for the s^{th} simulation iteration in the p^{th} experiment sequence is defined as

$$\Delta_{s,p} = (\mathbf{z}_{s,p} - \mathbf{y}_{p-1})^T (\mathbf{z}_{s,p} - \mathbf{y}_{p-1}) \tag{5.7}$$

The behavior of this metric in dB for the results presented in Figure 5.5a is given in Figure 5.7a computed for the experiment sequences 2 through 10 along with a marker to indicate the iteration number s at which the experimental error energy of the curve is minimum in the simulated study of playing out every drive file in the simulation sequence to the actual test article, as was done was the fifth experiment sequence in Figure 5.6. As can be seen,

a consistent trend is observed as the adaptation progresses through the simulation indices. Based on the behavior of the curves in Figure 5.7a, for an experiment sequence when $p \neq 1$ and $s > 1$, it can be seen that the slope reduces from an initial value to zero through the adaptation process, as shown in Figure 5.7b. It is important to note that these curves would not be replicated in the case where the simulations would be terminated at the listed simulation batch indices where the NEE curve would be minimum, since that would change the actual output response used to compute the $\Delta_{s,p}$ metric. For this choice of constant iteration step size, most of the simulated NEE curves would achieve their respective minima around 13-17 batch iterations, as indicated in Figure 5.7.

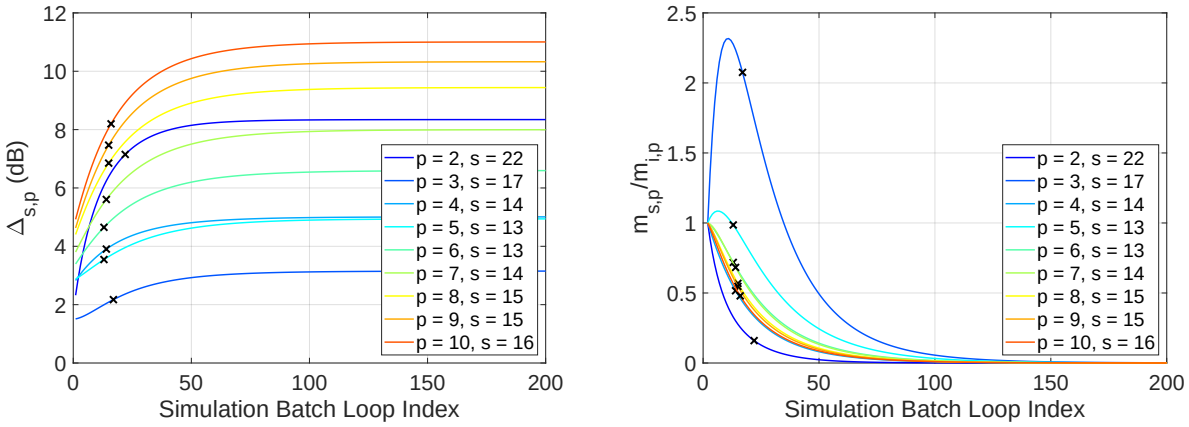

(a) Behavior of the $\Delta_{s,p}$ metric in dB for the experiment sequences 2 through 10

(b) Behavior of the ratio of slopes $m_{s,p}$ and $m_{i,p}$ for experiment sequences 2 through 10

Figure 5.7: Analysis metrics of the failed implementation of the EB-PT-Fx-LMS method due to poor choice of iteration parameters for the mild cubic spring test bench in Case Study 2

An empirical termination strategy is to stop the simulation sequence when the current slope of the curve $m_{s,p}$ is less than a certain threshold ratio $c \in (0, 1)$ of the initial slope $m_{i,p}$

associated with that experiment sequence.

$$\begin{aligned} m_{i,p} &= 10log_{10}\left(\frac{\Delta_{2,p}}{\Delta_{1,p}}\right) \\ m_{s,p} &= 10log_{10}\left(\frac{\Delta_{s,p}}{\Delta_{s-1,p}}\right) \end{aligned} \tag{5.8}$$

$$m_{s,p} < c\, m_{i,p} \rightarrow S_{term,p} = s \tag{5.9}$$

where $S_{term,p}$ is the simulation index of the first occurrence of the event defined by 5.9 in the p^{th} experiment sequence. This can hence be used to terminate the adaptive process if the initial guess of the number of simulation loops S was set too high, hence saving computation time in the simulation domain with no penalty accrued for the required NEE reduction.

This Fast EB-PT-Fx-LMS algorithm hence offers three main advantages: (1) comparable or better performance than the previously proposed PT-Fx-LMS algorithm for deriving the drive files, (2) increased robustness to iteration parameters compared to the regular EB-PT-Fx-LMS algorithm while retaining the ability to fine tune the adaptation performance especially when the estimated linear model is deficient using a single parameter c, and (3) ability to reduce the number of simulation batch iterations required to achieve similar performance saving computation time in the simulation domain without the need for extensive tuning of iteration parameters through trial-and-error. Despite the fact that the conventional time-domain ILC, PT-Fx-LMS and the regular EB-PT-Fx-LMS methods all show very good performances, especially for the purely linear and piece-wise linear spring test benches in Figure 5.3, the performance of Fast EB-PT-Fx-LMS algorithm is demonstrated for the four test benches under consideration and presented in the NEE reduction plots in Figure 5.8, with the iteration parameters for the proposed method given in Table 5.2 and the results for the other methods carried forward from Table 5.1 and Figure 5.3. It is noted that because of the robustness and termination algorithm implemented for the Fast EB-PT-Fx-LMS method,

more aggressive simulation domain step-sizes can be used and only an appropriate guess for the number of simulation batch loops needs to be considered, without leading to instability issues as noted in Figure 5.5, especially for the test benches with deficient estimated linear models.

Table 5.2: Iteration parameters and results for the Fast EB-PT-Fx-LMS algorithm for DFID considering $P = 50$ experiment sequences

Plant	S	μ_s	c	Total S_{actual} (out of $P \times S$)	NEE reduction (dB)
Purely linear	50	3e9	0.1	301/2500	56.29
Piece-wise linear	200	2e9	0.2	544/10000	57.21
Mild cubic, F_s	200	5e8	0.45	598/10000	52.02
Harsh cubic, $F_s^{'}$	200	2e8	0.8	1849/10000	52.28

On further inspection of the parameters used to achieve the results presented in Table 5.2, it can be seen that threshold value c needs to be increased as the degree of nonlinearity increases. Note that a smaller threshold value allows the iterations to progress much further through the simulation loop indices, if required per the termination criteria of 5.9. Despite the very small value of c and the initial guess of S for the purely linear plant, very few simulation iterations are required since the estimated model of the purely linear plant is very close to the actual plant dynamics as discussed in the identification results of section 3.4.1. It is also apparent from Figure 5.8a that most of the NEE reduction is achieved in the first experiment sequence itself, where the simulated sequences are not terminated.

While the NEE curves show similar performances using the methods presented for the purely linear and piece-wise linear spring test benches, the maximum output error plots through the experimental batch loops, presented in Figure 5.9 shows much improved performance when the drive files are derived using the Fast EB-PT-Fx-LMS method. For the mild cubic and harsh cubic spring test benches, the maximum output error curves show similar results as the comparative methods.

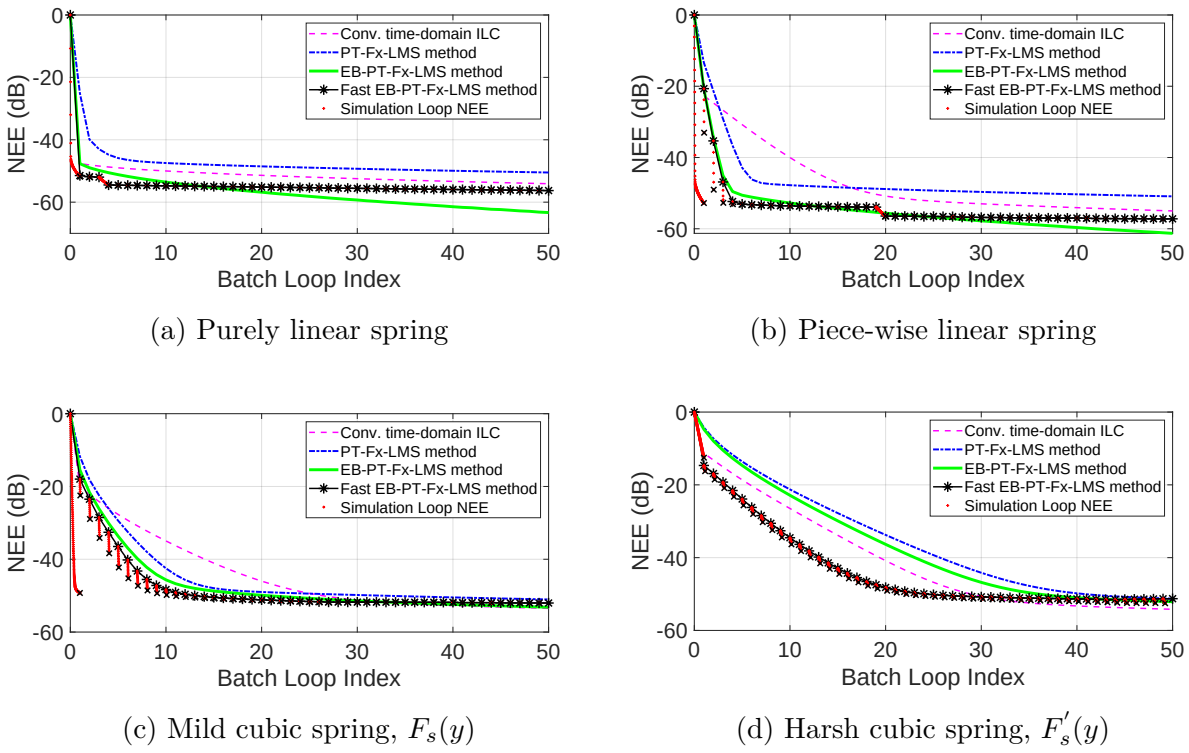

(a) Purely linear spring

(b) Piece-wise linear spring

(c) Mild cubic spring, $F_s(y)$

(d) Harsh cubic spring, $F_s^{'}(y)$

Figure 5.8: NEE reductions through the 50 batch loop iterations for the simulation test benches using the Fast EB-PT-Fx-LMS method for DFID

The simulation index where the iteration is empirically terminated also depends on the step size chosen, which is why the harsh cubic spring test bench required many more batch iterations than the mild cubic spring test bench, despite the choice of a larger threshold value for termination, which would typically terminate the adaptive process much earlier. The results in Figure 5.8 show that the proposed Fast EB-PT-Fx-LMS method shows very similar convergence rate in comparison to the other presented DFID methods for the purely linear, piece-wise linear and mild cubic spring test benches and shows improved performance for the harsh cubic spring test benches despite the more aggressive simulation domain parameters and much fewer simulation batches while also maintaining stability. The decision tree previously presented in Figure 5.2 can hence be updated for the Fast EB-PT-Fx-LMS method as shown in Figure 5.10

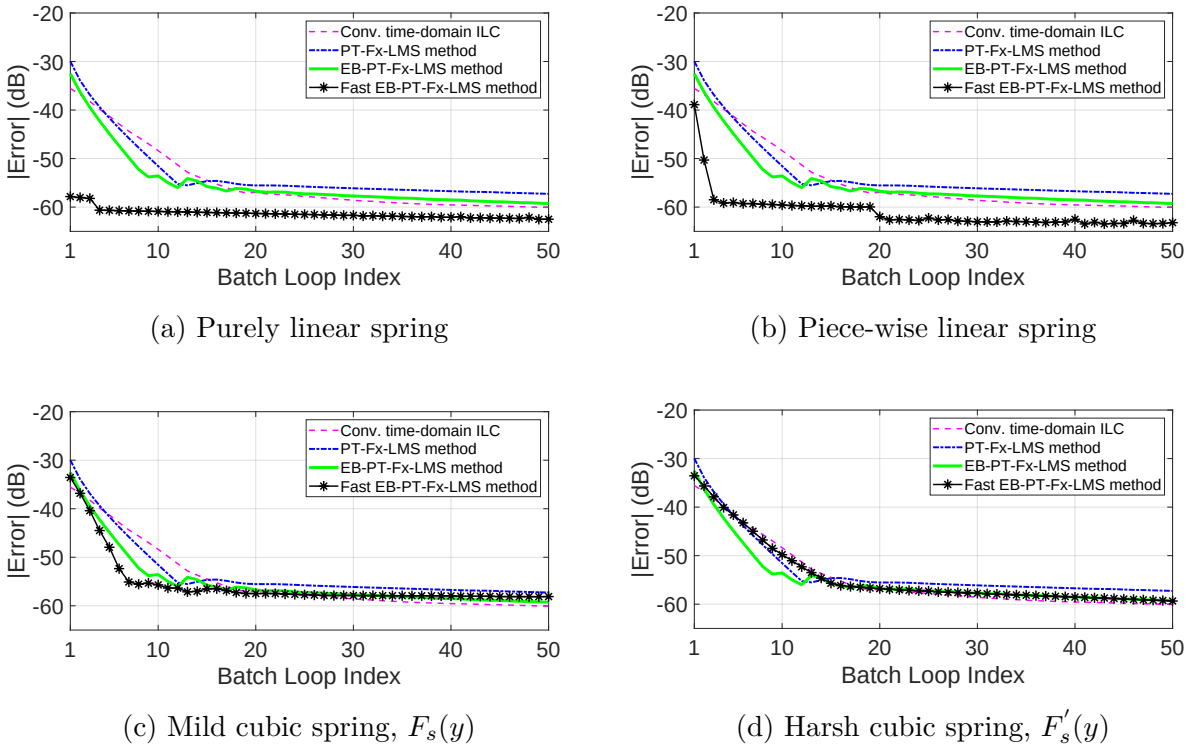

(a) Purely linear spring

(b) Piece-wise linear spring

(c) Mild cubic spring, $F_s(y)$

(d) Harsh cubic spring, $F_s^{'}(y)$

Figure 5.9: Maximum output error in dB through the 50 batch loop iterations for the simulation test benches using the Fast EB-PT-Fx-LMS method for DFID

5.4 Conclusion

A new algorithm has been proposed as an extension and improvement to the Pulse Train Fx-LMS algorithm for DFID applications. As with any DFID procedure, the proposed EB-PT-Fx-LMS method attempts to reduce the number of experiments on a test rig required to complete the adaptation process and identify a drive file that produces a response closely matching the required target response from the dynamic system. The proposed architecture for the implementation of the algorithm uses a unitary pulse train reference input, similar to the PT-Fx-LMS algorithm, but the adaptation process is carried out completely offline using an estimated linear model of the nonlinear plant dynamics. This allows for much finer tuning of the adaptation process, i.e., smaller step sizes and a large number of iterations in

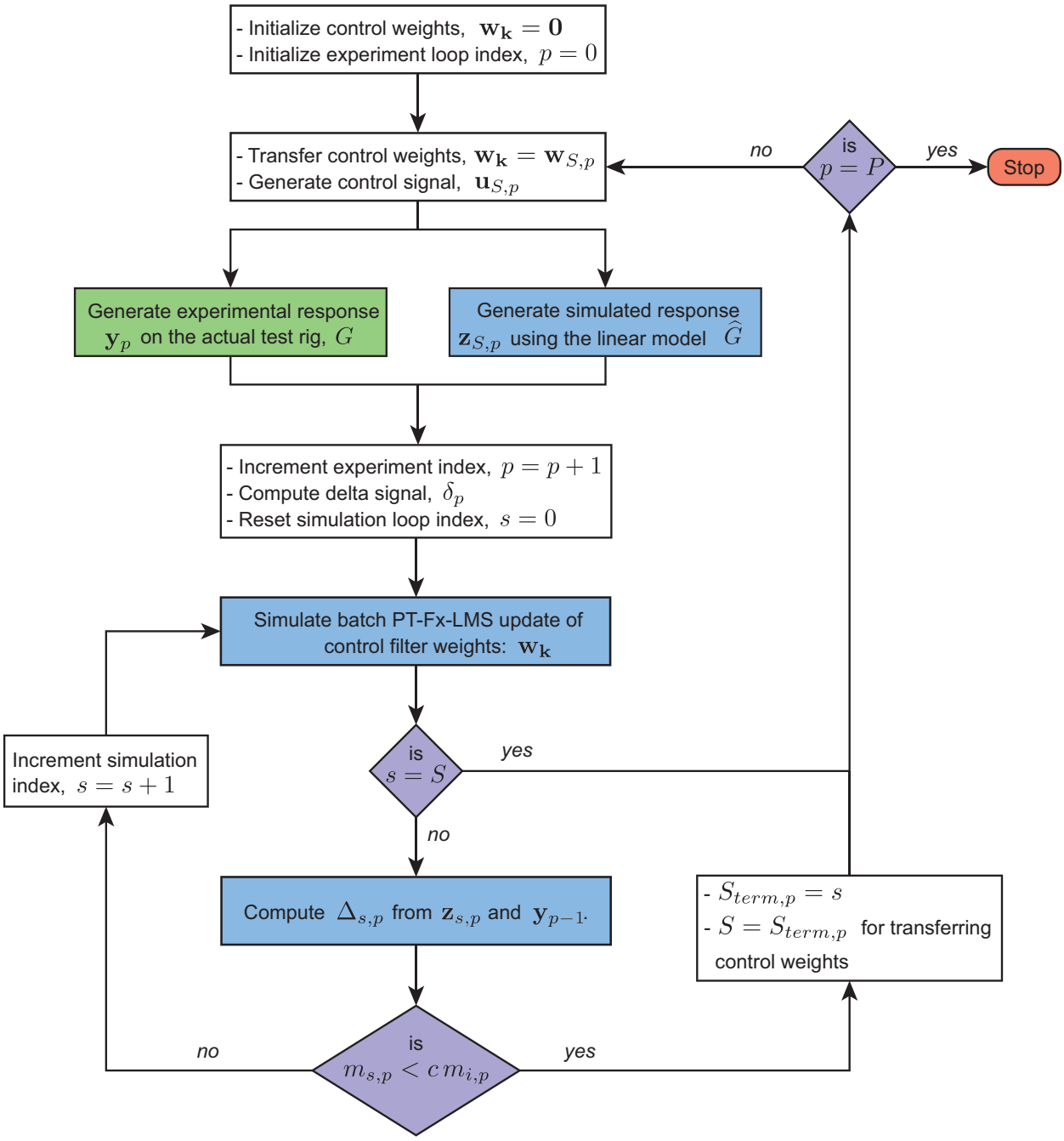

Figure 5.10: Decision flow chart for the Fast EB-PT-Fx-LMS algorithm for DFID

the simulation domain without the need to perform this adaptation process on the experimental test rig itself. This architecture also ensures the safety of the test rig since real-time

adaptation on a test-rig can be dangerous if the process becomes unstable and exceeds the bandwidth and control authority of the actuators.

The proposed EB-PT-Fx-LMS algorithm was validated and compared with the previously proposed PT-Fx-LMS method for four test benches of differing harshness using actual suspension displacement time series data from a race car. The proposed algorithm was able to converge faster, i.e., in lesser number of physical runs on the test rig and also achieve a lower misadjustment as compared to the previously proposed PT-Fx-LMS method. With harsher nonlinearities in the dynamic system, small step sizes and a large number of adaptation iterations in the simulation domain caused the Normalized Error Energy of the response to diverge. This is clearly caused by a deficient estimation of the nonlinear dynamics used for the adaptation process and hence motivated the development of a termination criterion to limit the number of simulation iterations as a function of the difference in responses generated by the actual nonlinear plant and the estimated linear model. It is observed that a termination criterion as presented not only preserves the stability of the adaptation curve but also reduces the number of simulation iterations required for the architecture presented without much loss in performance.

The working of the EB-PT-Fx-LMS method for DFID has been demonstrated in the case studies above and establish a proof-of-concept for this method that can be integrated into the workflow usually used in the DFID process. While it has been validated for the class of nonlinearities relevant to the applications of vehicle testing, it could be expanded further to MIMO systems and other classes of nonlinearities commonly encountered in Service Environment Replication applications.

Chapter 6

Drive File identification for Multi-Input Multi-Output systems

6.1 Introduction

The development of the MIMO implementation of the PT-Fx-LMS algorithm for DFID uses the same pulse-train reference input and the filter weights that will be adapted through the iterative process will be a multidimensional bank of FIR filters. The update algorithm for the filter weights that will be used to generate the drive files will be derived as an extension of the SISO PT-Fx-LMS algorithm derived in chapter 4 considering each error vector and each filtered reference signal due to the multiple paths of a MIMO dynamic system [29]. This chapter focuses on the architecture being expanded to MIMO systems, and the demonstration of the performance of the MIMO PT-Fx-LMS algorithm for DFID will begin with the construction of generic MIMO, Linear Time Invariant (LTI), causal, minimum phase and fully controllable systems that have a desired range of FIR filter lengths. System identification of these dynamic systems also requires a MIMO implementation of the LMS system identification procedures previously presented for the SISO case in section 2.2.3. Similar to the case studies presented in section 4.4, the performance of the proposed DFID algorithm will be benchmarked against conventional DFID methods that iteratively derive the drive files using adaptive inverse models of the dynamic systems.

6.2 Architecture of the MIMO Fx-LMS algorithm

The general Filtered-x LMS architecture remains the same for the updating the filter weights as described previously in section 4.3 and Figure 4.4 for SISO systems. The functional difference is the dimension of the signals and the multidimensional filter banks implemented for the adaptive filter and the plant models used for the adaptive algorithm.

For a generic multidimensional system described by plant dynamics $\mathbf{G}$ with N output sensors and M actuator inputs, and each path in this $N \times M$ system is given as a Q-coefficient Finite Impulse Response filter. Figure 4.3 already describes this multidimensional DFID architecture for SER applications with the appropriate signal dimensions for clarity. Figure 6.1 further expands the block diagram for an example 2×2 MIMO system that shows the signal flow applicable to the implementation of the previously described Filtered-x LMS algorithm, with the pulse train reference input structure that enables the direct generation of command inputs in the adaptive filter bank without the need to first derive an inverse FIR model.

The cross-coupling of signals is evident in the MIMO architecture, and it can be seen that a filtered reference input needs to be generated for each of the $N \times M$ path in the plant model and then used appropriately for each LMS update law. Considering the use of FIR filters to model the plant dynamics, the superposition principle and the unique choice of the pulse-train reference input allows for the direct generation of the control inputs that are then applied to the actual plant to derive the actual response of the system. It is also important to note that each of the N output errors are used in filter update law and hence require N target inputs, $\mathbf{d} \in \mathbb{R}^N$.

Consequently, considering the $N \times M$ filtered reference inputs, each update law also requires its own step-size, or iteration constant. Considering the theoretical limits of the

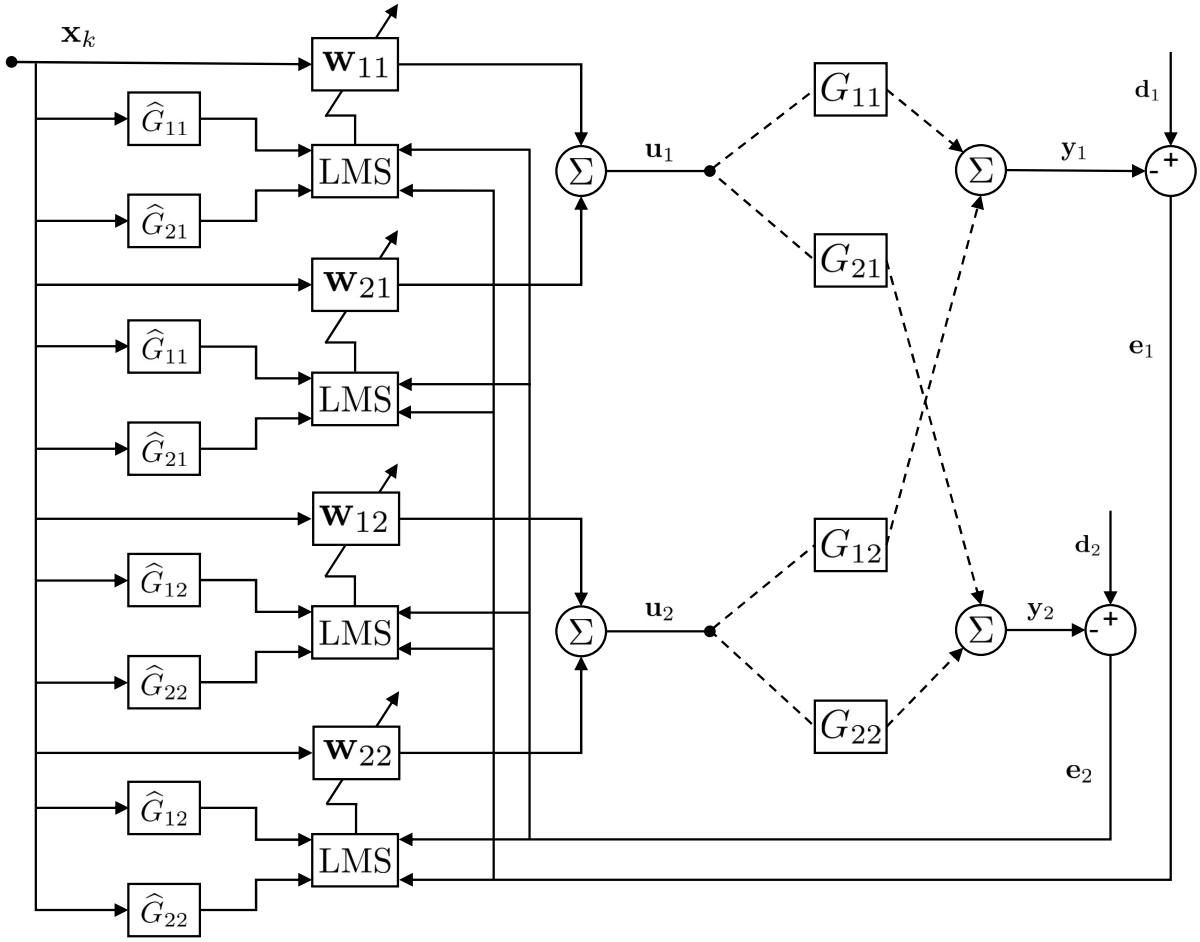

Figure 6.1: Signal flow block diagram for the MIMO DFID architecture for a 2×2 dynamic system

iteration constant for the typical LMS algorithm given in 2.28, the iteration constant for each update law is given as

$$\mu_{nm} = \frac{2}{K \times \mathbf{r}_{nm} \times (fos)} \tag{6.1}$$

where the indices n, m represent the path on the plant model and the respective filtered

reference input $\mathbf{r}$, K is the length of the filtered reference input, and also the total length of the desired target response in this architecture, and fos is a tunable factor-of-safety parameter since the step size often requires to be relaxed from the theoretical limits for practical applications. This tunable parameter can be further investigated to be variable for each path for more targeted adjustments and to refine performance, but that is outside the purview of this work. An alternate solution to relax the overall iteration constant to preserve adaptation stability will be discussed in Chapter 7.

Performance characterization for the adaptive process is consistent with previous presentations of the Normalized Error Energy for each output channel, normalized by the appropriate target response. The following sections in this chapter present the setup of the simulation test benches considered for MIMO dynamic systems and for comparison, a DFID method using a Filtered-x LMS based MIMO adaptive inverse identification step followed by the conventional iterative learning control scheme.

Higher order systems also present significant challenges when it comes to the different classes of systems that can exist. The effect of the relative number of control inputs and response outputs has been described previously in section 4.2. Additionally, from a classical control theory perspective, considerations have to be made regarding the system if they are minimum or non-minimum phase when an inverse problem such as DFID is concerned, if the system is controllable or output-controllable. In this chapter, MIMO systems that are minimum-phase (i.e., a stable inverse exists) and fully controllable are first considered, to validate the presented MIMO PT-Fx-LMS algorithm for DFID on simulated test benches.

6.3 Setup of a simple MIMO test bench for simulation validation case study

While the SISO test benches presented in Chapter 3 was a simplified mass-spring-damper dynamic system, when constructing MIMO test benches for simulation validation, it has to be made sure that each of the plant dynamic paths share the same set of poles, as required for a real system. Hence, to make the dynamic systems under test to be as modular as possible in terms of the number of inputs and outputs, pole-zero locations, controllability of the system, MATLAB's `drss`, or Discrete Random State Space command is used to generate random dynamic systems and an iterative search is conducted to find systems that match the conditions required.

For the first system considered in this section to demonstrate the DFID algorithm, a system with $M = 2$ inputs and $N = 2$ outputs that is minimum phase and fully controllable is considered. For computational simplicity, plant dynamics with higher damping ratios are chosen such that the number of coefficients in the FIR filter model is limited to 20–30 coefficients. Similarly, since these are constructed test cases, the designed target waveform is also limited to a one-second sequence in order to aid rapid prototyping of test cases.

The discrete linear state space system considered is of the form

$$\mathbf{x}_{k+1} = \mathbf{A}_d\mathbf{x}_k + \mathbf{B}_d\mathbf{u}_k \tag{6.2}$$

$$\mathbf{y}_k = \mathbf{C}_d\mathbf{x}_k + \mathbf{D}_d\mathbf{u}_k \tag{6.3}$$

with a sample rate of 1000 Hz. The order of the system is 4, and the pole-zero map is shown in Figure 6.2 and since all the zeroes are inside the unit-circle, this is a minimum phase system. The first step in the DFID procedure is the identification of a plant model as

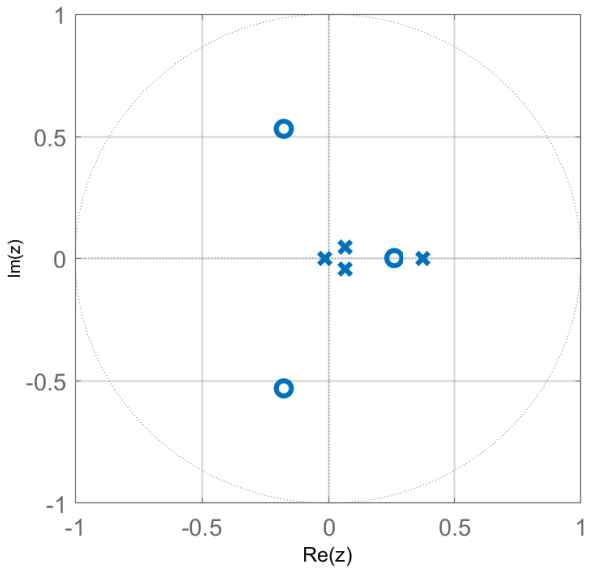

Figure 6.2: Pole-Zero map of the MIMO 2×2 dynamic plant of order 4 generated using MATLAB's `drss` function considered for the simulated test bench

an FIR filter. In the case of a MIMO dynamic plant, each input-output path is identified separately using the LMS algorithm described previously in section 2.2.3. A similar control input as previously described in section 3.4.1 is used for the identification of the MIMO plant model using the adaptive LMS system identification method, with the FIR filter and the adaptation performance of each input-output path shown in Figure 6.3. Considering that this is a very simple, noise-free, linear plant being considered for the simulated test bench, perfect identification of the plant is achieved, both in terms of the output response for the system identification procedure and the actual coefficients computed using the previously described NEE metric. As discussed previously, the quality of the identified model affects all the succeeding steps in the DFID procedure.

For comparing the PT-Fx-LMS DFID method against the conventional ILC scheme, the adaptive inverse method described previously in section 3.4.2 is used to derive the inverse FIR model of the plant. Since the modeled plant has $Q = 21$ coefficients, the inverse model

is initialized with $L = 3Q$ coefficients, with a delay of $\Delta = Q$ coefficients, as shown in Figure 6.4, despite the knowledge that the plant is minimum-phase. This is a standard operating procedure and follows the practice from previous case studies where the actual plant dynamics are assumed to be unknown for the DFID algorithm except to obtain the actual responses.

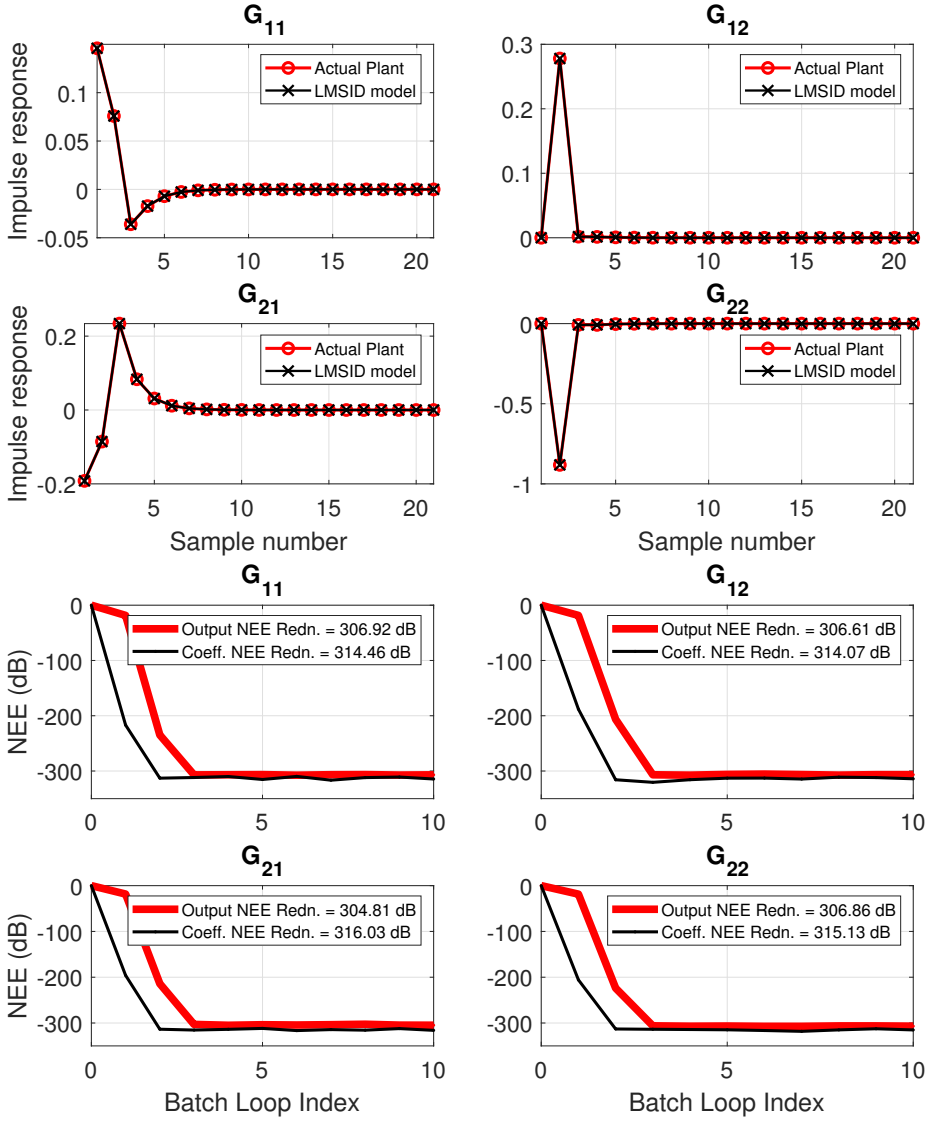

Figure 6.3: Identified FIR filter model and the performance of the adaptive LMS system identification procedure for the considered 2×2 dynamic system

Performance of the inverse identification procedure is characterized as previously by

cascading the plant model with the identified inverse FIR model. In the case of this MIMO system, the cascaded convolution of the FIR filters yields an $N \times N$ matrix of convolutions, with an ideal spike of 1 at sample number Δ along the main diagonal as shown in Figure 6.5. This characterization can be best understood as an extension of the standard linear algebra result for a matrix A, where $AA^{-1} = I$, which when extended to a SISO FIR filter yields results as in Figure 3.10 and for a matrix of FIR filters, the diagonal convolutions should have a single peak of 1 at Δ sample number. For the dynamic system considered and the derived inverse FIR model, it can be seen in Figure 6.5 that the diagonal convolutions do not peak to one and the off-diagonal convolutions also are not perfectly zero.

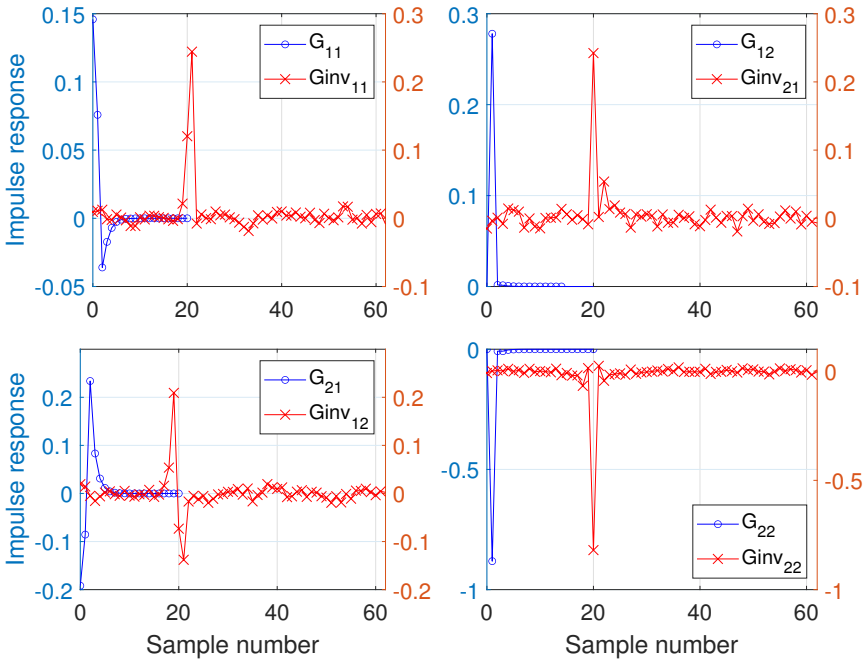

Figure 6.4: FIR plant models of the identified inverse using the Fx-LMS based adaptive inverse method

A simulated case study such as this gives the ability to design known ground truths for the input waveform along with the targt output responses that allows improved analysis of the adaptive process, especially understanding the uniqueness of the derived control sequences in the case of MIMO systems. The designed control inputs and the target output waveforms

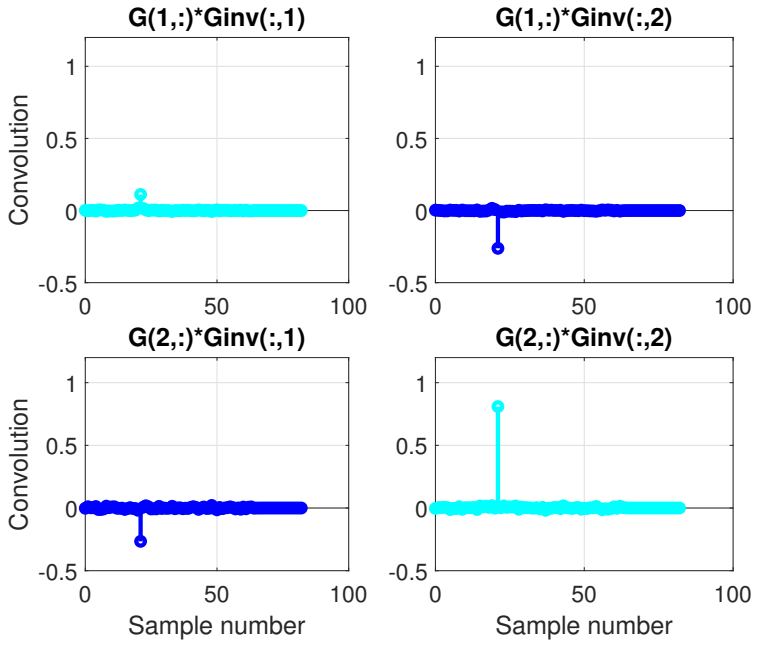

Figure 6.5: Convolution matrix of each path of the cascaded FIR models of the plant model and inverse model

with the considered dynamic plant is shown in Figure 6.6.

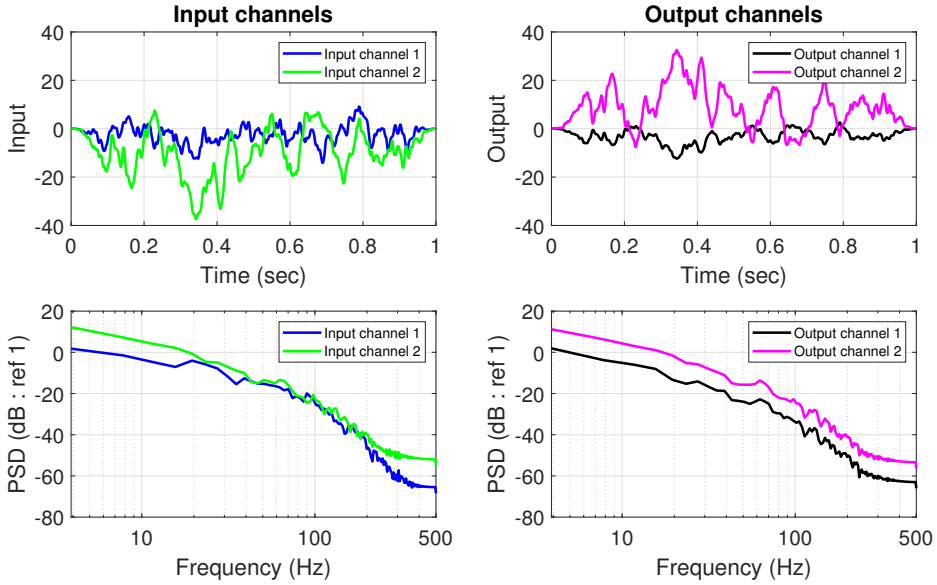

Figure 6.6: Known ground truth input signals and the target responses for the considered 2×2 MIMO dynamic plant

The adaptive DFID procedure for both the conventional and proposed PT-Fx-LMS methods follow the same procedures as the first case study in section 4.4.1. The drive files are initialized at zero, the step sizes for both channels using the conventional adaptive inverse based ILC method was set to 0.15 to balance performance and stability and for the MIMO PT-Fx-LMS DFID method, the iteration constant per path was relaxed with a factor-of-safety (fos in equation 6.1) of 50.

Figure 6.7 presents the results of this simulated case study, with only the trace errors shown for the output and input channels with respect to the target response and known ground truth control presented in Figure 6.6. The second row of plots in Figure 6.7 shows the NEE reduction curves for each channel using both the conventional ILC method and the PT-Fx-LMS method for the output response. The legend in the input channel plots also presents the final NEE of the control input sequences with respect to the known ground truth.

Both channels of the control sequence derived from the PT-Fx-LMS method are seen to converge more closely to the known ground truth, seeing 16 dB and 33 dB of NEE reduction on the input channels. It is hence evident that the output response also very closely matches the respective target responses. Considering the quality of the inverse model and that the plant has a dominant path more dependent on the adaptation performance of one of the input channels because of the unbalanced magnitude of the $\widehat{G}_{22}$ channel as shown in Figure C.1, it is also seen that in such cases, a subset of the input channels can individually generate output responses on both channels that match the target. Conditions like these can result in non-unique solutions to the DFID problem, even if the final performance of the SER procedure is lacking.

It can also be seen clearly in the NEE reduction curve of the PT-Fx-LMS method that the adaptation curve operates in multiple modes, which can be attributed to the fact that

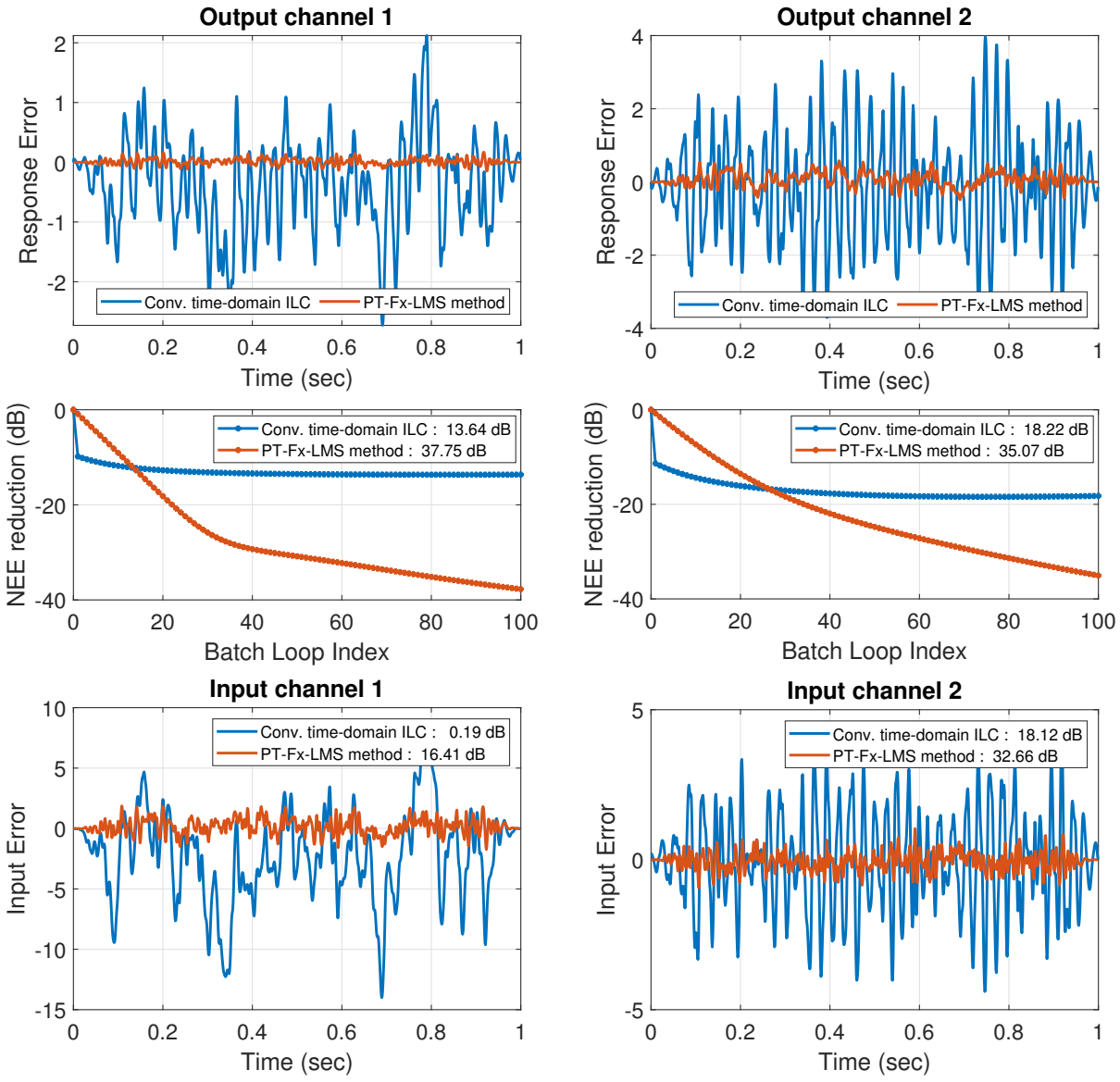

Figure 6.7: Response error, NEE reduction plots and the control input sequence error for both channels of the input and output derived using the conventional time-domain ILC and the proposed PT-Fx-LMS method for the considered MIMO 2×2 dynamic plant.

the plant dynamics has a dominant pole and the adaptive algorithm initially targets the most dominant response and then the less-dominant modes are adapted to at a slower rate. It is also important to note that in this DFID architecture, the initial weights of the adaptive filter, $\mathbf{w}$ are initialized at zero. While the adaptive inverse based ILC method shows poorer

performance in the current configuration, a combination of the adaptive inverse and the proposed PT-Fx-LMS based DFID methods can be setup to derive an initial estimate of the control sequence using the inverse model of the plant, followed by the proposed algorithm for further fine-tuning of the adaptive SER procedure.

While this case study presents an example where the proposed PT-Fx-LMS based DFID method performs significantly better than the conventional ILC based method, this is not necessarily the case for every dynamic system. Improved inverse models, such that the convolution matrix of the cascaded model and inverse model in Figure 6.5 is very close to identity, could result in better results being obtained with the conventional ILC based method for such linear, controllable, minimum-phase systems.

6.4 MIMO DFID for a Quarter-car dynamic system

In the previous case study, the considered dynamic plant was constructed using the MATLAB `drss` function and with poles that have very high damping ratios, with all poles having damping ratios > 0.8. It has been observed that the adaptive inverse identification procedure performs better for such cases and when the FIR filter of the forward model has a low number of coefficients. While the `drss` method can be used with the iterative search algorithm to select plants with longer FIR filter lengths, this section develops a quarter car model since the motivation of this thesis and the application of Service Environment Replication in vehicle dynamic test rigs is an active field of interest, following on from the SISO spring-mass-damper system considered in previous chapters.

The model development for the quarter test bench to establish ground truth and target responses in the absence of actual hardware requires special attention. In order to retain simplicity in the model, the parameter values of the dynamic system are considered such

that they are representative of actual suspension subsystem characteristics and only linear dynamics are modeled. Nonlinear dynamics in the springs, dampers, tire, multi-body interactions from full-vehicle models and vehicle and measurement instrument delays and noise are not considered and is left for future work to develop more sophisticated Simulation-in-the-Loop or Hardware-in-the-Loop test benches with real-time processing hardware.

A simple two mass, spring and damper configuration is considered to model the vertical dynamics of a quarter-car suspension setup, the schematic is shown in Figure 6.8.

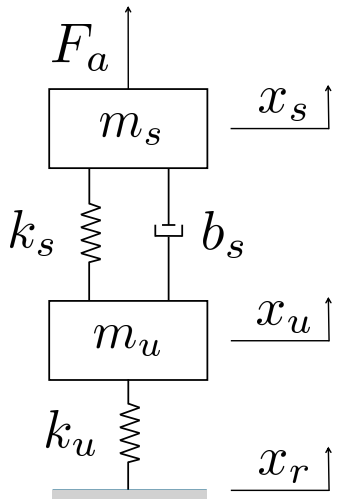

Figure 6.8: Illustration of the simple quarter-car suspension system with two inputs: the aero-loader force $F_a(t)$ and road input x_r and multiple outputs

To define the multiple inputs to the system, the road input x_r and a forcing load F_a on the sprung mass body m_s is considered. The springs k_s and k_u are both linear springs that follow Hooke's Law. No damping is considered on the unsprung mass m_u, which is a regular assumption in the literature considering the very low damping provided by stiff tires. Only linear viscous damping is considered for the suspension damper with a coefficient b_s. The state space formulation considering 4 states is hence given as follows:

$$\begin{bmatrix} \dot{x}_s \\ \ddot{x}_s \\ \dot{x}_u \\ \ddot{x}_u \end{bmatrix} = \begin{bmatrix} 0 & 1 & 0 & 0 \\ -k_s/m_s & -b_s/m_s & k_s/m_s & b_s/m_s \\ 0 & 0 & 0 & 1 \\ k_s/m_u & b_s/m_u & -\frac{(k_s+k_u)}{m_u} & -b_s/m_u \end{bmatrix} \begin{bmatrix} x_s \\ \dot{x}_s \\ x_u \\ \dot{x}_u \end{bmatrix} + \begin{bmatrix} 0 & 0 \\ 1/m_s & 0 \\ 0 & 0 \\ 0 & k_u/m_u \end{bmatrix} \begin{bmatrix} F_a \\ x_r \end{bmatrix} \tag{6.4}$$

The list of parameters considered for this model formulation are given in Table 6.1. These parameter values are representative of the magnitude and ratios of mass, spring rates and damper coefficients based on a survey of published literature related to quarter-car system models.

Table 6.1: Parameters for the linear dynamic system used for simulation

Parameter	Details	Units
m_s	1000	kg
m_u	75	kg
k_s	31.65	kN/m
k_u	326.5	kN/m
b_s	3000	Ns/m

With the choice of the above parameters, the damping ratio and natural frequencies of the system are also modeled to be very close to real vehicle and suspension subsystem ranges, with 4 stable poles very close to the unit circle with frequencies 5.4 Hz, 68.4 Hz and damping ratios 0.234, 0.296 respectively. Since a square 2×2 was already demonstrated in section 6.3, this dynamic plant chooses three outputs that are commonly instrumented on suspensions under test on test rigs, namely the sprung mass displacement x_s, the spring deflection $x_s - x_u$ and sprung mass acceleration $\ddot{x}_s$.

$$\mathbf{y} = \begin{bmatrix} 1 & 0 & 0 & 0 \\ 1 & 0 & -1 & 0 \\ -k_s/m_s & -b_s/m_s & k_s/m_s & b_s/m_s \end{bmatrix} \begin{bmatrix} x_s \\ \dot{x}_s \\ x_u \\ \dot{x}_u \end{bmatrix} + \begin{bmatrix} 0 & 0 \\ 0 & 0 \\ 1/m_s & 0 \end{bmatrix} \begin{bmatrix} F_a \\ x_r \end{bmatrix} \tag{6.5}$$

The aero-loader force input on real test rigs is used to simulate the effect of aerodynamic downforce at high speeds that a shaker rig would not produce in its longitudinal and lateral movements without a wind tunnel, while in this simulated test bench, F_a provides a disturbance input to the system. The designed ground truth for the road displacement excitation is designed based on the ISO 8608 Class D road profile standard [93]. The road profile is designed for a forward velocity of 20 m/s or 65 mph and the time sequence is windowed to begin and end the "lap" at zero deflection. The time series and spectrum of the designed ground truth for the input channels and the target responses for the output channels are presented in section C.1.2.

Similar to the previous test bench simulations, the actual dynamics of the plant are considered unknown, a "black-box" presented only to simulate the actual hardware system-under-test in test rigs and a plant model is separately identified as a bank of FIR filters for simulation validation as shown in Figure 6.9. In this case, even with uncorrelated white Gaussian noise at a signal-to-noise ratio (SNR) of 40 dB injected to the target response, because the plant models are completely linear, the plant model is perfectly identified using the LMS system identification procedure. As can be seen easily from the magnitude of the FIR channels and further evidenced by the very poor conditioning of each time-slice of the 3×2 matrix of coefficients shown in Figure 6.10, this already indicates that the response is sensitive to one of the inputs, in this case the second input, x_r, especially considering the

actuator limits on the aero-loader force actuator.

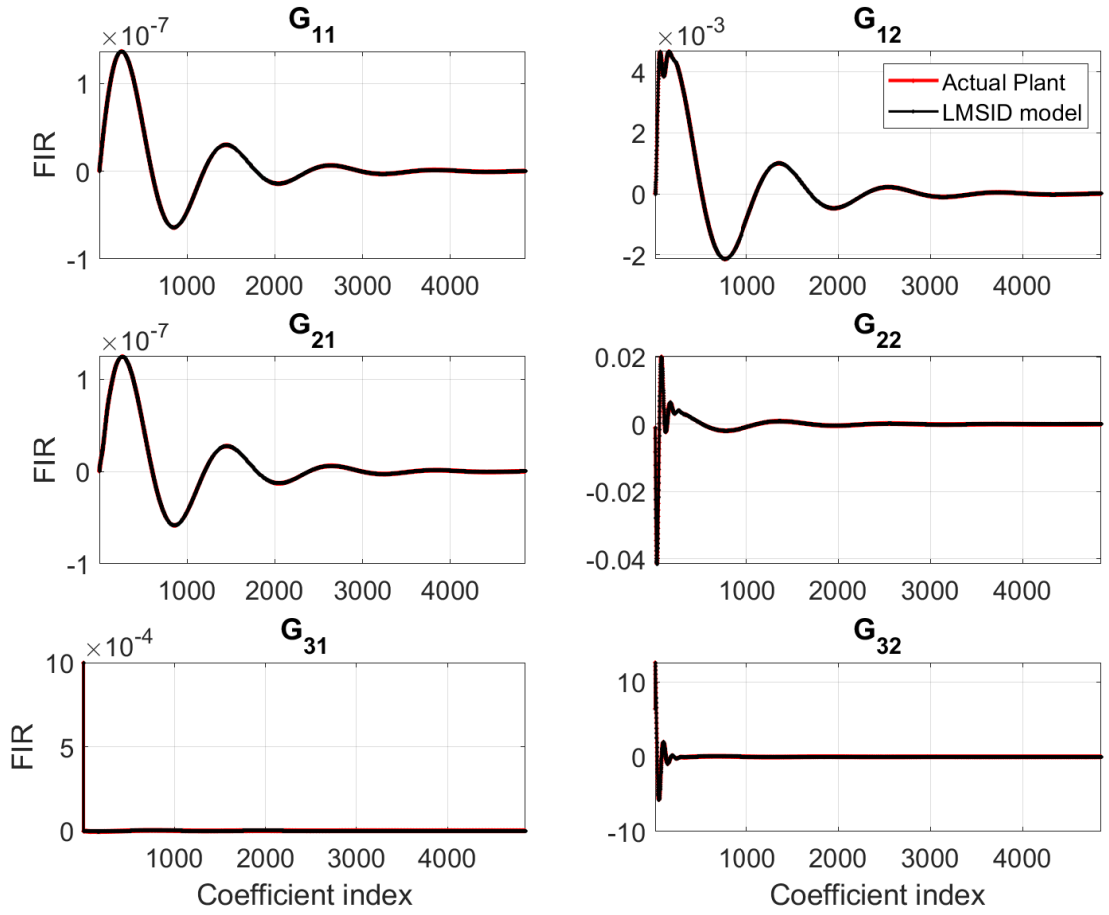

Figure 6.9: Finite impulse response matrix of the 3×2 quarter-car model simulation test bench identified using the LMS system identification method

In real world applications, the identified plant FIR model can be used to derive a state-space realization using the Eigen Realization Algorithm (ERA) introduced by Juang and Pappa. The implementation of the ERA used in this study is described in section. This transformation also allows conventional linear system analysis to identify controllability and allow for model reduction to simply complex dynamic systems, especially in the cases of ill-conditioned plant models. For this designed quarter car system, the threshold on the singular values was set to 10^{-10}, a very small value that can be explained by the conditioning of the system in Figure 6.10 to realize a stable, matching dynamic system.

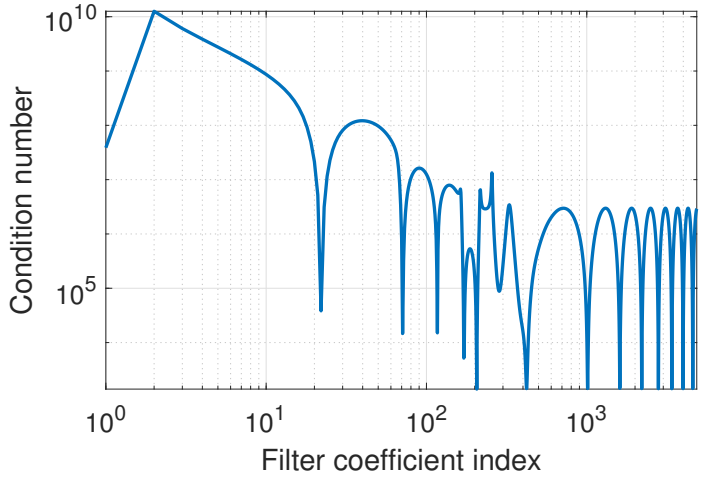

Figure 6.10: Condition number of each 3×2 matrix of the FIR filter bank for the quarter-car model simulation test bench.

The conventional model-inverse based ILC method for control synthesis performs very poorly in this case because of the quality of the model inverse that can be derived for such an ill-conditioned dynamic system. This is analogous to the pseudo-inverse derivation procedure using singular value decomposition. In literature, for the applications of blind-equalization, one of the standard assumptions made to define existence and uniqueness conditions is that each $N \times M$ frame of the Q-coefficient FIR filter must be full rank [41, 53, 56, 97]. While the blind equalization architecture is more aligned with signal reconstructions in the signal processing community, the various mathematical formulations and methods could be valuable to the analogous question for DFID applications. Further study of these methods is outside the scope of this thesis.

With the formulation of the PT-Fx-LMS method for DFID, there is no explicit step to first derive an inverse and allows for direct synthesis of the control inputs. Figures 6.11 and C.5 show the derived input and output signal time series and the NEE reduction through the 200 batch iterations of the DFID procedure. Further performance improvements are possible with targeted adjustments to the step-size of each channel, initializing with an approximate

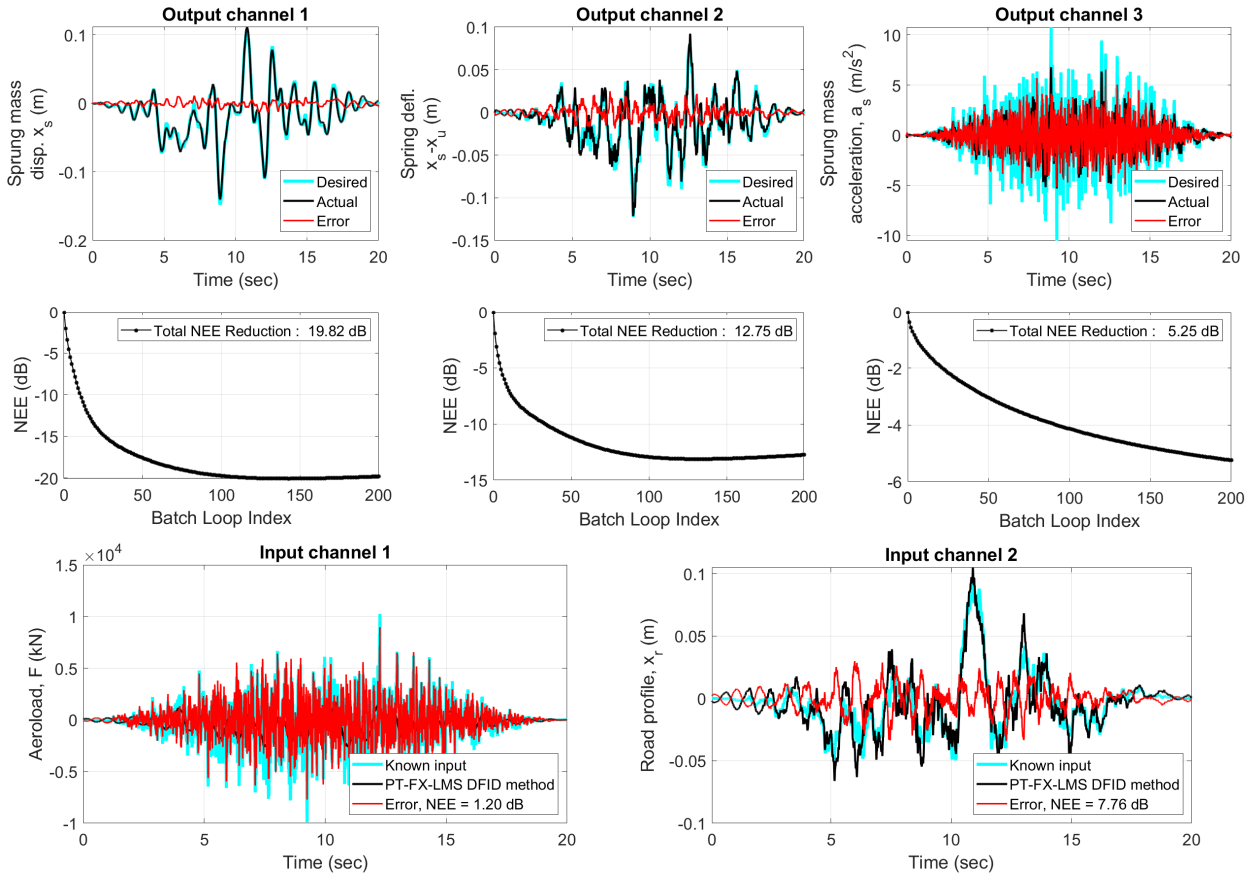

Figure 6.11: Response error, NEE reduction plots and the control input sequence for the 3×2 quarter-car simulation test bench DFID procedure.

drive file using any model inversion method, other estimation-based algorithms to improve performance as discussed in section 5. In HiL configurations, the conditioning of such FIR models should be paid special attention to when designing input-output mappings for signal replication.

6.5 Conclusion

The Pulse Train Fx-LMS algorithm is demonstrated for a simple class of MIMO dynamic systems that often form part of the SER testing applications in the automotive industry.

The novel algorithm is applied for direct control synthesis for linear, controllable and minimum phase systems including a representative model of a quarter-car vehicle suspension subsystem. In real-world applications, the number of inputs and outputs are often much bigger than the considered case studies, but the simulation test benches in this study illustrates the architecture of the algorithm for MIMO systems. The modeling considerations and comparisons against the conventional inverse-based ILC methods for this test bench show the advantages of the novel method in terms of performance and simpler modeling conditions.

Further learning from adjacent scientific areas should be leveraged to develop a more comprehensive mathematical framework to derive the required conditions for existence and uniqueness of solutions. This chapter presents a proof-of-concept for the novel algorithm to be applied and scaled up as necessary for MIMO dynamic systems and such test benches can be developed to prove out a wider class of systems with non-linear dynamics, time-slice adaptation, non-minimum phase plants, combinations and evolutions of presented methods etc. In real world applications, performance characterization of SER algorithms is still a very subjective and is dependent on the nature of testing requirements, hardware limitations and the signals of interest.

Chapter 7

Validation of proposed algorithm through acoustical experiments

7.1 Introduction

The test benches presented in previous chapters are all simulated systems designed to either demonstrate the capabilities of the algorithm or to match common applications in the vehicle industry like suspension subsystems of varying complexity. Certain inherent limitations encountered in real-world applications like uncertain dynamics, data acquisition systems used, hardware limitations, environmental conditions etc. have not been investigated through these simulation test benches despite the modeling of such systemic and environmental factors.

Section 7.2 discusses the hardware setup for the experiment used for validation of the DFID method, the experimental layout to present the SER scenario and the data acquisition and processing methods used. With the defined experimental setup, many different versions of the SER experiment is run, considering different input-output layouts, the audio signal considered for the ground truth input and target response, time or frequency-domain driven adaptation sequences and performance characterization methods. The results and follow-up discussions for the chosen experiment sequences is described in detail in section 7.3.

7.2 Design of the experimental setup

This validation experiment is designed to demonstrate the SER testing procedure, where initially the target responses are measured, the dynamics of the system are identified and a set of control inputs need to be derived to replicate the responses on a set of measurement sensors. Since the development of the PT-Fx-LMS algorithm was motivated by initial advancements in the Active Noise and Vibration cancellation (ANVC) community, an acoustical experiment was considered to be an ideal and cost-effective candidate for experimental validation of the developed algorithms as part of this thesis. This section describes the chosen hardware components, the layout of the speakers (actuators) and microphones (sensors) and the data acquisition tools used for automated batch sequences that are required for the adaptive process.

7.2.1 Hardware resources to set up the experiment

The main considerations when selecting the hardware for the experiment conducted were based on the available data acquisition devices, the frequency bandwidth of the audio signals considered for the tests, cost-effectiveness and the ability to produce and record clean audio signals. In the absence of dedicated hardware to process the high frequency signals associated with audio waveforms for real-time control, the experimental tests in this thesis are restricted to offline, batch processing of the signals and the derivation of a control sequence in a separate, sequential process to the playing out of the control signals and measurement of response waveforms. Figure 7.1 shows a general schematic of the components used in the experimental setup.

As shown in the schematic, the speakers and microphones, multiples of each in the case of a MIMO setup, are placed in an anechoic chamber for the best signal clarity, avoid

environmental noise factors and maintain a consistent signal-to-noise ratio throughout the duration of the adaptive learning procedure. A single USB Data acquisition device, with two waveform generator channels to drive the control signals to the speakers and two scope channels to measure the response from the microphones, is connected to a computer that batch processes the signals during the iterative algorithm. The voltage signals sent to the speakers are first amplified using a dedicated audio amplifier and the microphone output is first conditioned before being digitized by the data acquisition device.

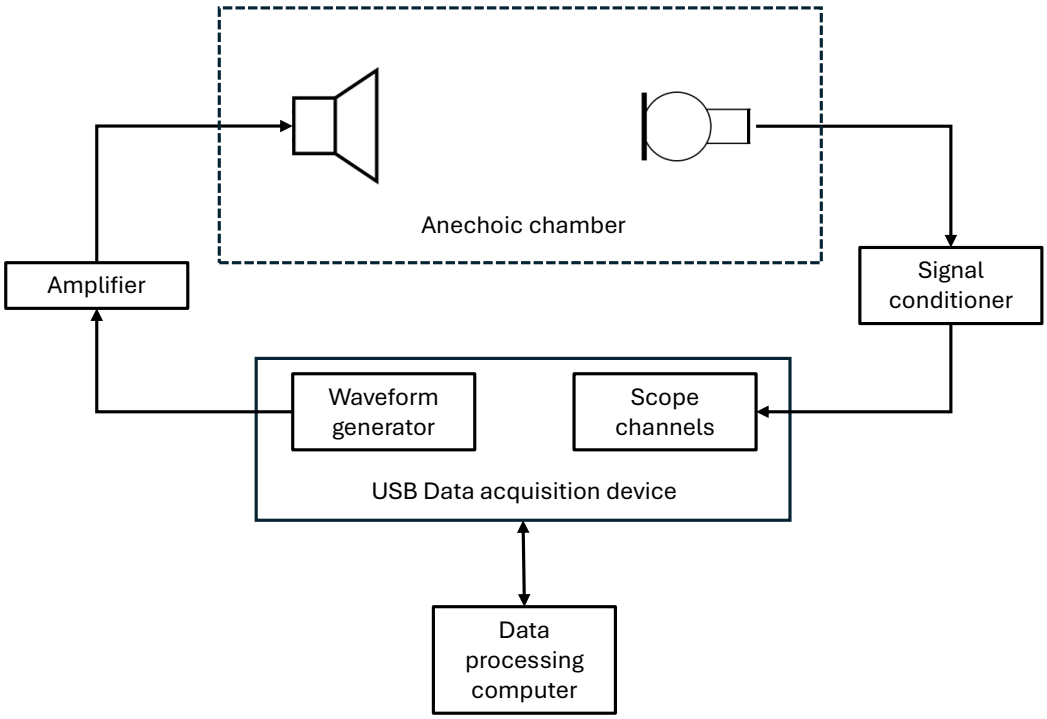

Figure 7.1: Schematic of the hardware devices used in the acoustic experiment

The specific details of the components used in the experiment are listed below:

Anechoic Chamber Following from the simulated test benches in previous chapters, the demonstration of the DFID algorithm in an experimental setting requires controlled environments where as a starting point, characterization of the dynamics of the actu-

ators and the data acquisition are not significantly affected by external noise factors, preserve the linear dynamics and ensure harsh nonlinearities are not introduced. Access to an anechoic chamber allows the mitigation of all of these external noise factors, since disturbances from outside the chamber are heavily isolated, the primary path between the speakers and microphones are not heavily corrupted by reflections from the chamber's foam wedge walls and precise measurements can be made about the sound sources' and microphones' locations with reference to their boundaries. With the measurement devices and data acquisition system, the sound pressure level in the chamber with the necessary devices in the chamber was measured at 15.5 dB SPL.

Speakers Considering the intended audio signal chosen as the target response is a speech signal, and the human voice covers a wide bandwidth with dominant frequencies in the 100-500 Hz range for average men and women [7], mid-range woofer drivers were considered the best performing for good fidelity in sound replication. Different speakers with good low-frequency performance and a flat frequency profile up to the desired frequency range based on the manufacturer's provided Sound Pressure Level (SPL) frequency response specifications were considered.

Figure 7.2: Pair of woofer drivers used as speakers secured in their enclosures

The Dayton Audio DC160S-8 61/2" aperture, 8Ω impedance shielded woofer [17],

capable of delivering 50 W of RMS power, was chosen considering its effectiveness as a high-quality, affordable woofer driver. The specifications state a flat frequency response up to 2 kHz under the manufacturer's testing conditions and this is validated in the lab during this experiment, and the resonance of the speaker is lower than the frequency band of interest at 32 Hz. Such woofer drivers also require a sealed enclosure, carpeted with sound absorbing material to achieve the cleanest acoustical outputs without rattles and distortions, and hence an enclosure with the required recommended volume is used to mount the speaker drivers as shown in Figure 7.2. Use of suitable audio cables, soldered joints at the speaker terminals and high quality BNC cables and connectors are used to supply the speaker signals in order to preserve signal integrity and achieve a high signal-to-noise ratio.

Amplifier Since a USB DAQ device based waveform generator does not output enough wattage to drive the speakers on its own, an amplifier is required to operate the speakers at a reasonable SPL. The chosen amplifier is an ART SLA-4 that is capable of delivering about 100 W/channel RMS when driving an 8Ω impedance speaker. The specifications list [1] a flat frequency response through the entire range of human hearing and extremely low noise amplification with hum and noise being measured $>$ 100 dB below clipping.

Microphones Considering the speech signals under consideration which will be described in section 7.2.2, a free-field directional microphone that performs with a flat frequency response in the frequency range of interest is desired. The PCB Piezotronics 130D20 is chosen for the purpose since the specifications [63] state a ±1 dB bandwidth in the 100–4000 Hz range, and an even extended -2 to 5 dB bandwidth in the 20 to 15000 kHz range. It has a sensitivity of 45 mV/Pa at 1 kHz, and a sound pressure of 1 Pa is equal to an SPL of 94 dB. The inherent signal-to-noise ratio at 1 kHz is >15 dB and

is designed to be powered by simple, inexpensive, constant current signal conditioners. The free-field type microphones are direction sensitive and hence executing the experiment in a noise-absorbing chamber is necessary to avoid non-linear effects due to reverberations from the boundaries. In order to keep the units consistent between microphone measurements and speaker inputs, the spectral analysis of measured sound is retained in units of dBV, and given the sensitivity of the microphone and the constant gain applied on the amplifiers throughout all the experiments, the sound pressure level in dB SPL can be calculated.

The design of these microphones make them suitable for building a 2D array of microphones for complex measurements, but in this case, a pair of such microphones will be used in the experiment. In order to further isolate rattles and nonlinear effects in the primary path, these microphones are fixed securely on vibration dampening mounting mechanisms that are 3D printed and mounted on steady tripod ball-heads as shown in Figure 7.3.

Figure 7.3: PCB Piezeotronics Model 130D20 microphone mounted top tripod ball-head

Signal Conditioner The microphones are paired with a matching constant current signal conditioner from the same manufacturer, which is a PCP Piezotronics Model 482A22 [64]. Signal from the microphones are conditioned and the output of the conditioner is digitized and scoped using the data acquisition device. The constant current excitation of the conditioner is kept at the default 4 mA as specified by the manufacturer for the length of cables being run, and the signal conditioner is designed to produce minimal distortions, voltage offsets or spectral noise.

Analog Discovery USB DAQ With the available computational and equipment resources, the data acquisition platform of choice is a USB-based test and measurement device called Analog Discovery 2 shown in Figure 7.4, designed and manufactured by Digilent [22].

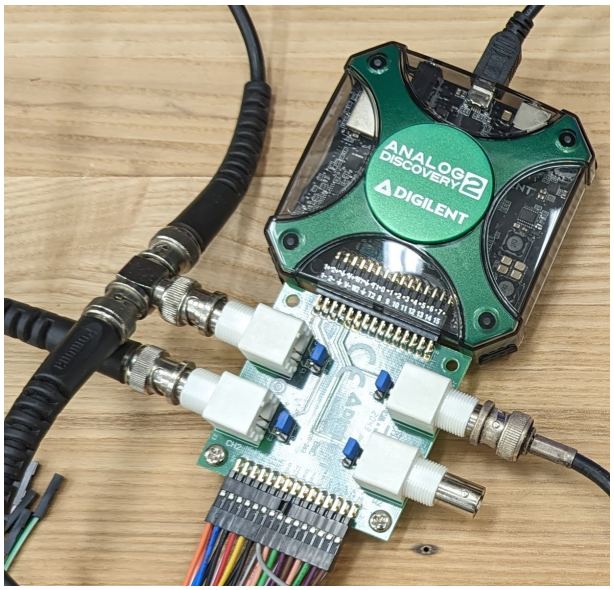

Figure 7.4: Analog Discovery 2 used as the USB-based data acquisition and waveform generation device

The onboard 2-channel oscilloscope has a resolution of 14-bits and is capable of sample rate of up to 100 MS/s, a 10 MHz bandwidth, 1 MΩ input impedance and a voltage range of $\pm 25V$. The USB device also includes a 2-channel, 14-bit waveform gener-

ator capable of up to 100 MS/s and a voltage range of $\pm 5V$. Unlike conventional and dedicated oscilloscopes and arbitrary waveform generators, USB DAQs are capable of logging extended signal files and also "playing out" much longer waveforms, respectively. In conjunction with Digilent's own Waveforms application and the included Software Development Kit (SDK) [23], a custom data acquisition and waveform generation configuration is used to automate the sequential data collection and processing steps required for the iterative DFID process. More details on the specific data acquisition and waveform generation configuration is discussed in section 7.2.3.

7.2.2 Experimental layout for acoustic SER testing

In the setting of an anechoic chamber where external disturbances and reflections from walls have been significantly minimized, the primary path dynamics are primarily defined by the distances between the speakers and the microphones. In this study, it is the objective to validate performance of the novel DFID algorithm in various configurations for service environment replication. The speakers and microphones are arranged in the anechoic chamber as shown in Figure 7.5. This configuration is the initial setting for the tests conducted and allows modularity for the different experiments.

A 3-dimensional schematic of the anechoic chamber and the relevant equipment is shown in Figure 7.6a, which details the locations of the speakers and microphones with reference to the walls of the chamber. With the choice of two speakers and microphones each, the nature of acoustical signals and the directional nature of the sound field and the free-field microphones as shown in Figure 7.6b and the nature of SER testing, the following test conditions are considered:

Number of inputs and outputs With the ability to turn on and off each of the speakers

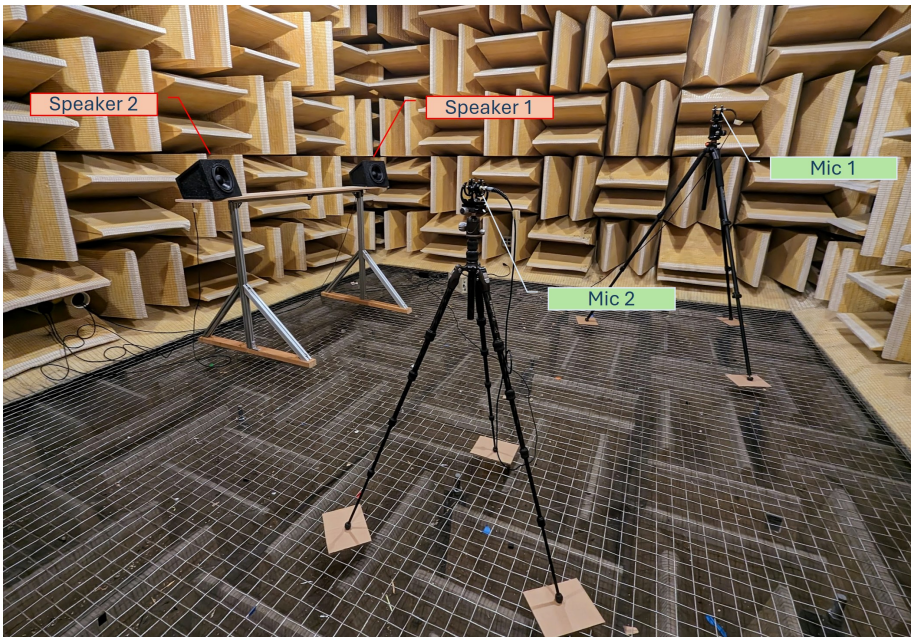

Figure 7.5: Initial arrangement of the speakers and microphones in the anechoic chamber

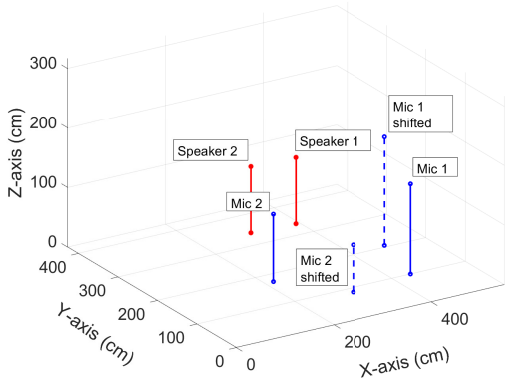

(a) 3-dimensional view of the arrangement of speakers and microphones in the anechoic chamber for the initial (solid lines) and shifted (dashed lines) layouts

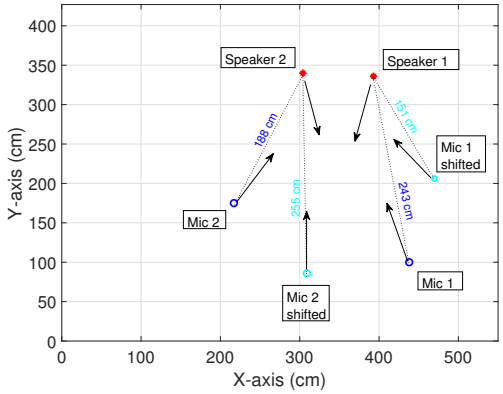

(b) Top view of the equipment layout in the anechoic chamber with arrows to show directions in which the equipment are pointing

Figure 7.6: Schematic of the initial and shifted setups of the speakers and microphones in the anechoic chamber

and microphones, four different configurations are chosen for this experimental study:

- SISO (Single Input Single Output) - Speaker 1 and Mic 1
- SIMO (Single Input Multiple Output) - Speaker 1 and both microphones
- MISO (Multiple Input Single Output) - Both speakers and Mic 1
- MIMO (Multiple Input Multiple Output) - Both speakers and both microphones

Known and unknown ground truths Experiments are conducted with the initial setup as shown in Figure 7.6a where at first the designed speaker inputs are played, and the target waveforms are measured at the microphones. Following this, the DFID algorithm identifies the path dynamics and DFID algorithm is used to generate the control sequence that replicates the measurements at the speakers. In such an experiment, the ground truth control sequence is known, even if not explicitly used but makes for a convenient method to validate the derived speaker inputs.

In an alternate experiment, after the target waveforms are measured, the microphones are slightly shifted, as shown in Figure 7.6. Relating to the motivational application presented in previous chapters, this change of dynamics between the input-output pairings is representative of a vehicle being mounted on a test rig for waveform replication compared to when the target waveforms were measured on the vehicle in its service environment. In this acoustical experiment, the shift in dynamics is primarily because of the change in distance between the speaker and microphones and also the directional nature of the microphones.

Target waveforms In order to simplify the signal processing and analysis of the DFID process, single-tone sinusoidal waveforms are first considered. This allows for easier alignment of signals in the time-domain, which is required for the iterative algorithm, since the error sequence between the desired and measured waveforms is used to drive the Pulse Train Filtered-x LMS algorithm.

The second and more challenging case for time-alignment and signal processing is a sample speech signal. The considered speech signal is an 8-second sound clip of the commentary from Manchester United's iconic winning moment at the 1999 Champions League Final. The target waveform is pre-processed and filtered to have a cutoff frequency of 4000 Hz, in order to limit the number of samples in the sound signal and make the most efficient use of the computational resources available. The spectrum of this target speech signal in dBV is given in Figure 7.7. For reference, this recorded signal is approximately 48 dB SPL, or 33 dB SPL above the noise floor of the anechoic chamber and the single tone sinusoidal signal has a recorded sound pressure level of 54 dB SPL, in this case the measurements given for the SISO case.

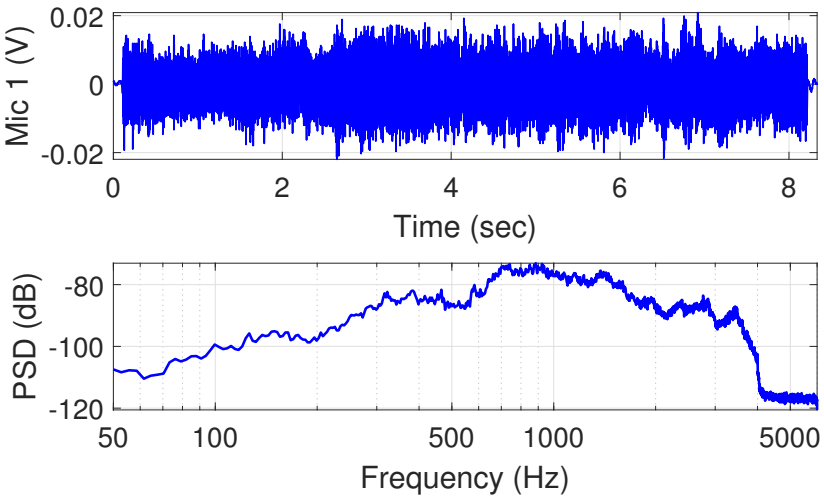

Figure 7.7: Sound signal and spectrum of speech sample used for SER validation experiment

The test matrix can hence be given as shown in Table 7.1. In the case of single tone sinusoidal waveforms played to the speakers, a single tone is played on one or both speakers and in the case of speech signals, one of the speakers plays the speech signal and the other speaker plays a single tone sinusoid to distinguish the signals in the sound measurements, visually.

Table 7.1: Test matrix for acoustical experimental validation of novel DFID algorithm

System	Unshifted configuration	Shifted configuration
SISO (1×1)	Single sine input Speech input	Single sine input Speech input
SIMO (2×1)	Single sine input Speech input	Single sine input Speech input
MISO (1×2)	Single sine input on each speaker Single sine and speech inputs	Single sine input on each speaker Single sine and speech inputs
MIMO (2×2)	Single sine input on each speaker Single sine and speech inputs	Single sine input on each speaker Single sine and speech inputs

7.2.3 Data Acquisition methods and signal processing considerations

Time-domain adaptive filtering methods are not often used for high frequency audio signals considering large number of data samples and because for most audio applications, real time processing requirements constrains the typical signal processing methods to block frequency-domain algorithms. Considering that the speech signal is filtered to suppress all frequencies beyond 4 kHz and the limited computational resources available to process large number of data samples in an iterative algorithm, the data acquisition has a sampling rate f_s of 12 kS/s, unlike typical audio applications that sample at 44 kS/s. While this acoustic experiment is still capable of demonstrating the effectiveness of the proposed DFID algorithms, data processing workloads are significantly lower in other applications of interest such as suspension shaker rigs, vibration shake tables or powertrain dynamometers, where the sampling requirements are much more relaxed. The target signals are 8.33 s long, and hence 100,000 samples are recorded for each microphone during the test.

The DFID procedure described in previous chapters is similarly followed in this experiment with batch collection of the system responses, offline processing of the measured data for system identification or iterative control synthesis and repeating these steps until

an appropriate drive file is identified. The Analog Discovery and Waveforms application based data acquisition system described in section 7.2.2 allows for synchronous, programmatic triggering of the waveform generator and scope channels. Considering the length of the acoustic signals and the turnover time of the computational steps in each iteration, test automation is a critical requirement in the data acquisition and processing scripts. While the WaveForms SDK provides significant documentation related to creating custom Python based scripts, better success in terms of predictable and reproducible triggering, playing and recording longer duration sound clips and modularity with channel and file selections was found with launching a JavaScript based data acquisition project directly on the dedicated WaveForms GUI application. As with previous simulated test benches, the initializations, computation algorithms and data processing are configured in a modular MATLAB environment that automates the data collection and processing steps but allows for configuring the different experimental test cases presented in Table 7.1 and making performance and stability based adjustments to the different parameters in the adaptive algorithms used in the DFID framework.

System identification of the primary paths between the speakers and microphones requires careful considerations. In all the tested configurations: shifted or unshifted, or the different number of inputs and outputs, each input to output path is individually identified to preserve the maximum possible signal-to-noise ratio and aid in faster convergence of the LMS algorithm. Through testing, it was found that in this configuration, better coherence in identification was obtained with a swept-sine or chirp signal instead of a broadband white Gaussian noise signal. This identification drive is shown in Figure 7.8 with the relevant spectrogram that shows the linear frequency sweep from 60 Hz to 4000 Hz over 40 seconds.

In the DFID procedure of all the test cases, the filter bank is initialized at zero, the iteration step-size is initialized as in the case studies in Chapter 6 and equation 6.1. Addi-

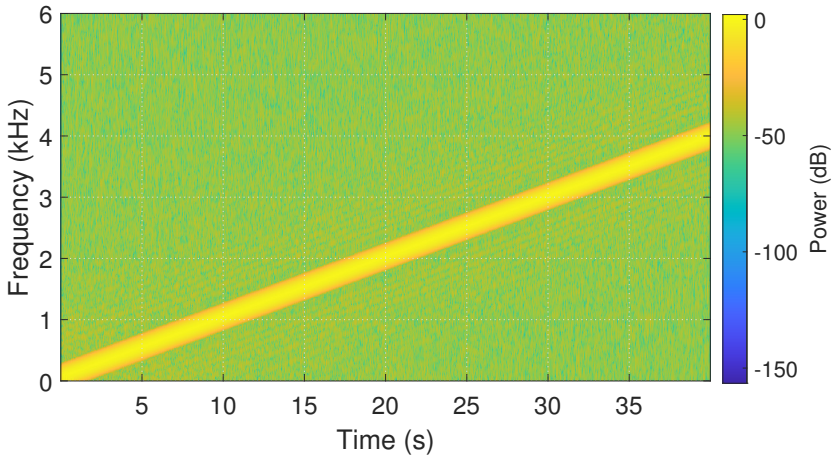

Figure 7.8: Spectrogram of the reference identification chirp signal with a linear sweep from 60 Hz to 4000 Hz

tionally, considering that the test turnover time is critical and instability in the convergence process based on an initial estimate of the factor-of-safety for the iteration constant often leads to repeated calibration of the iterative process, a step-size relaxation scheme is applied where the step size is halved and the particular batch iteration repeated if the overall MSE diverges. This brute force methodology can be inefficient for performance optimization in the case of poorly identified models, but always ensures a stable adaptation curve.

Comparative studies are not conducted in these validation experiments for multiple reasons. For the presented comparative ILC methods in previous chapters, the derivation of the inverse model was found to be extremely challenging considering the low damping in the system, sensitivity to path delays and the modeling quality required for the derivation of usable inverse models. Alongside other challenges related to the experimental apparatus and data processing considerations, the quality of the sound field produced using the conventional ILC methods were deemed unusable for this study.

The final consideration with signal processing techniques for experimental validation is the challenge presented with using a time-domain based algorithm in combination with lim-

ited quality of the data acquisition apparatus and requirement of time-alignment of the passively measured signal to the reference target waveform. Conventional alignment algorithms using peak matching or using the cross-correlation to determine relative delay in signals are insufficient for audio waveforms with large bandwidths and deficient data acquisition systems with large jitter errors. Accounting for the frequency-dependent phase delays requires the development of a zero-phase error tracking controller to derive the inverse model. This experimental demonstration steers away from deriving inverse models for control synthesis. Instead, performance characterization is simplified and appropriate using power spectrum, where a Normalized Spectrum Error Energy is used to track adaptation progress. Since a time-aligned error signal is still needed to drive the iterative algorithm, for most of the test cases discussed in section 7.3, the experimental recordings are only used for validation and the control synthesis is performed with the Model-in-Loop. This architecture is equivalent to the first sequence of batch iterations as presented in the Estimation-Based PT-Fx-LMS DFID method in Chapter 5.

7.3 Results and discussions

7.3.1 System Identification results

Given the layouts presented in section 7.2.2 and the identification drive for each channel given in Figure 7.8, the LMS system identification method is used to characterize the FIR model between each actuator and sensor in this experimental setup. The control signal and mic data used for this identification step is attached in Figure D.1. The identified transfer function model for the initial unshifted configuration in which the reference target waveforms are measured is shown in Figure 7.9, which also presents the coherence function

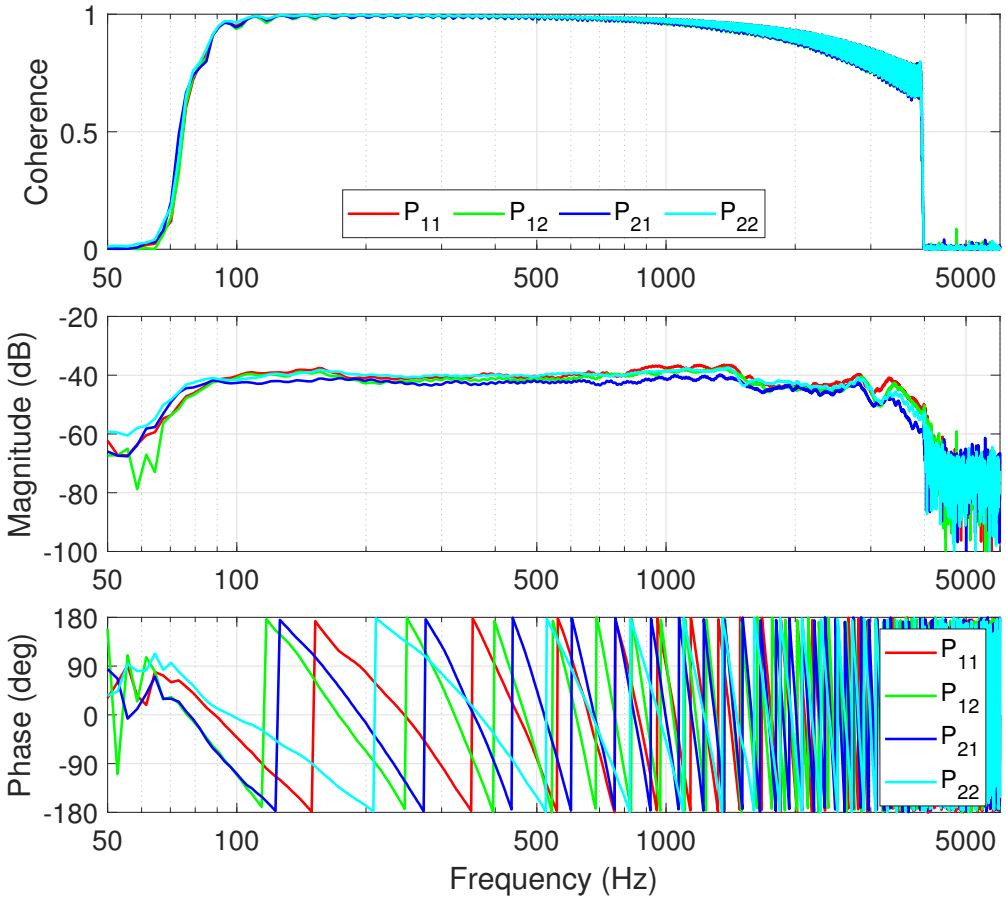

Figure 7.9: Frequency response transfer function estimate of the initial unshifted experimental layout for the 2×2 MIMO acoustical setup

of the transfer function estimate. The identified frequency response function matches very well with the manufacturer presented response of the speakers [17].

It can be seen that the speaker indeed produces a very flat response in the acoustical range of interest for speech signals in the 100-500 Hz range. The identification drive used also guarantees high coherence in the identified model in this bandwidth. Since these woofer drivers are not designed for flat response fidelity at the higher frequencies of the audio bandwidth. This is also seen in the fact the coherence drops below 0.75. The actual FIR models that are used for the adaptive time-domain based algorithms for DFID is shown in Figure 7.10 which also includes the identified FIR models of the shifted configuration to

illustrate the changes in proximity of the microphones to the speakers.

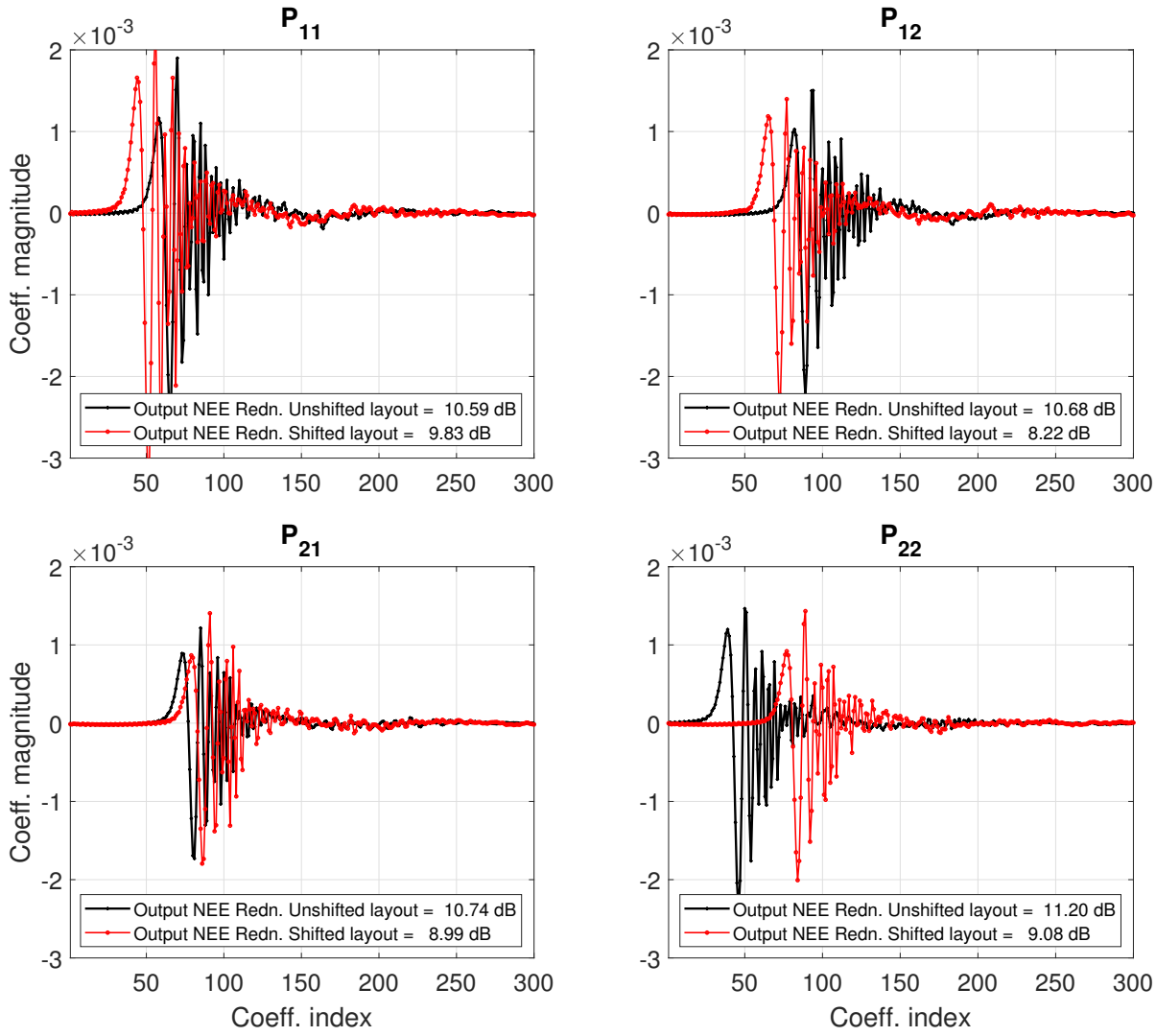

Figure 7.10: FIR models of the initial unshifted and shifted layouts of the acoustical experiment setup

It can be seen in all the FIR models that the propagation delay of the sound pressure waves from the speakers to the respective microphone is clearly identified and changes in the layout is also clearly observed in the models, for example, this is most obvious for the P_{22} model, i.e., the transfer function mapping the second microphone output from the second speaker input is clearly seen to moved farther away from the speaker, considering

no amplifier level changes have been made between experiments. The slight magnitude and shape differences seen in the impulse response models and the equivalent frequency response models are attributed to the shifted layouts changing the distance between the actuators and sensors and also the angle at which these free-field microphones are pointed at the sound source.

It is also to be noted that all the NEE reduction curves have converged for the results shown in Figure 7.10, and while only 8–11 dB of NEE reduction has been achieved across all paths, in a clean, low noise-level environment such as the anechoic chamber, the model quality is usable for the applications considered as will be shown in the next sections. The presented FIR models are also used for the other layouts with fewer actuators or sensors and the FIR matrix model would be a subset of the above results.

7.3.2 SISO experiment configuration

7.3.2.1 Initial unshifted layout

In the simplest form of the experimental configuration, the reference input is a 200 Hz monotonic sinusoidal input. It is seen in the measured target signal that despite attempts to reduce rattles, vibrations and harmonics in the spectrum of the signal, the waveform generator introduces harmonics in the signal, which are much smaller ($>$ 45 dB) in magnitude. The PT-Fx-LMS algorithm is driven by the time-aligned processed measured signal. In the simple case of a single sinusoid, the signal alignment algorithm based on the cross-correlation shows a constant deviation from the reference signal and hence can be used directly to compute the time-domain error signal based NEE performance evaluation metrics as shown in Figure 7.11.

This test routine using actual measured response to drive the DFID algorithm is further

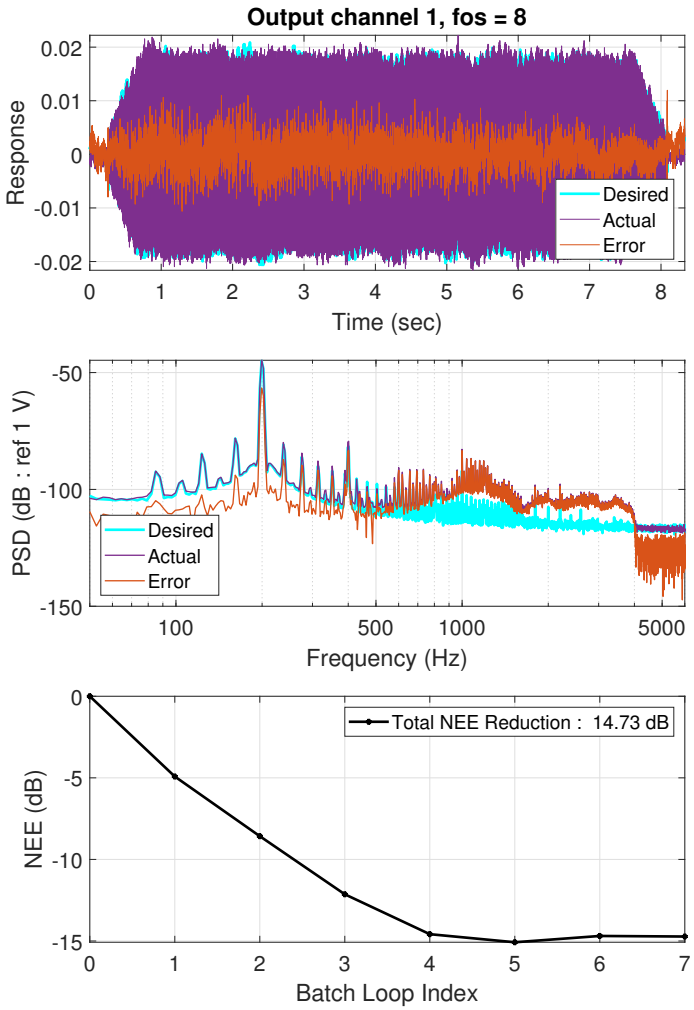

Figure 7.11: Experimental result of PT-Fx-LMS DFID algorithm for the unshifted SISO configuration with a single sinusoid target output

validated by comparing the wavelet coherence plot of the final measured microphone response against that of the simulated model output trace. The wavelet coherence [58] plot in Figure 7.12 is used to analyze signals in a time-frequency domain and allows for the observation of the phase vector shifts (shown with black arrows) in zones of high coherence between the signals. In the case of the single sinusoid input, it is clearly seen that both the measured and modeled output shows high coherence and no relative phase-delay with the reference target signal in the frequency bandwidth of interest for this test. In this experimental study,

the wavelet coherence is found to be a useful tool to recognize the nonlinear effects of the waveform generation and data acquisition pipeline.

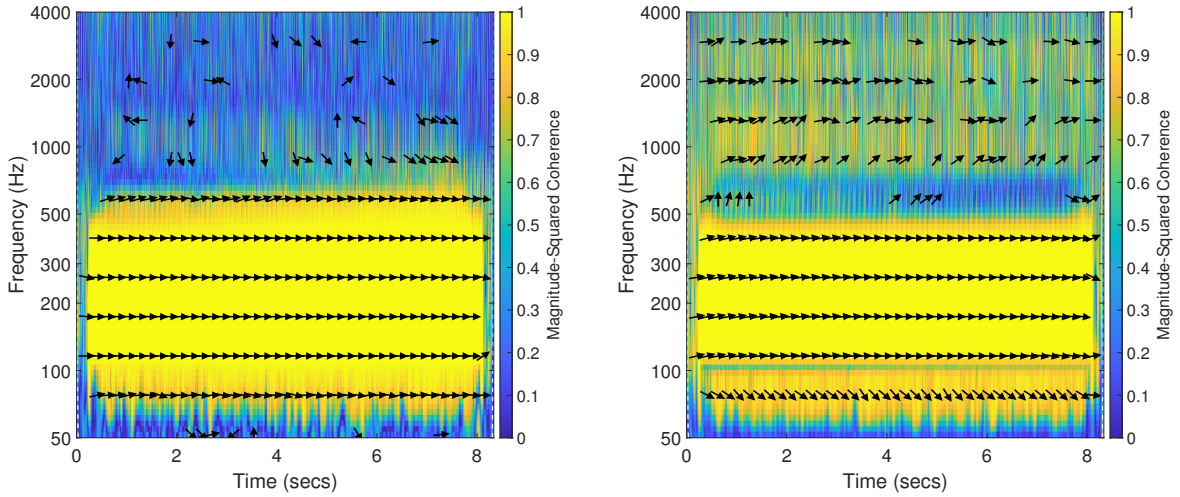

(a) Wavelet coherence between final measured and target response

(b) Wavelet coherence between final model output and target response

Figure 7.12: Comparison of the wavelet coherence plots of the measured and modeled output for the unshifted SISO configuration with a single sine 200 Hz target response

For the speech sample target reference signal shown in Figure 7.7, the test routine is set up to use the simulated model output to drive the DFID algorithm because conventional time alignment algorithms fail to capture the frequency-dependent phase delays and would require more advanced synchronization techniques like Dynamic Time Warping which stretches the signal to minimize the distance between the measured and reference signals, which is not appropriate for speech signals. The results for the experiment presented in Figure 7.13 show more clearly the effect of time synchronization of signals being a critical factor in analyzing the effectiveness of the time-domain DFID algorithm, with the left column of plots illustrating the large errors seen purely as a consequence of lack of proper time-alignment using standard techniques. This misalignment in the time history of the signal prevents its use directly in time-domain based adaptive filtering methods for iterative control synthesis. Such behavior is not observed in the power spectrum that shows a 15 dB reduction in the

Normalized Spectral Error energy in the frequency band of interest. The results on the right column show much lower misadjustment when only tracking the performance metrics of the modeled outputs that drives the adaptive algorithm, which are not corrupted by nonlinear time-synchronization noise factors.

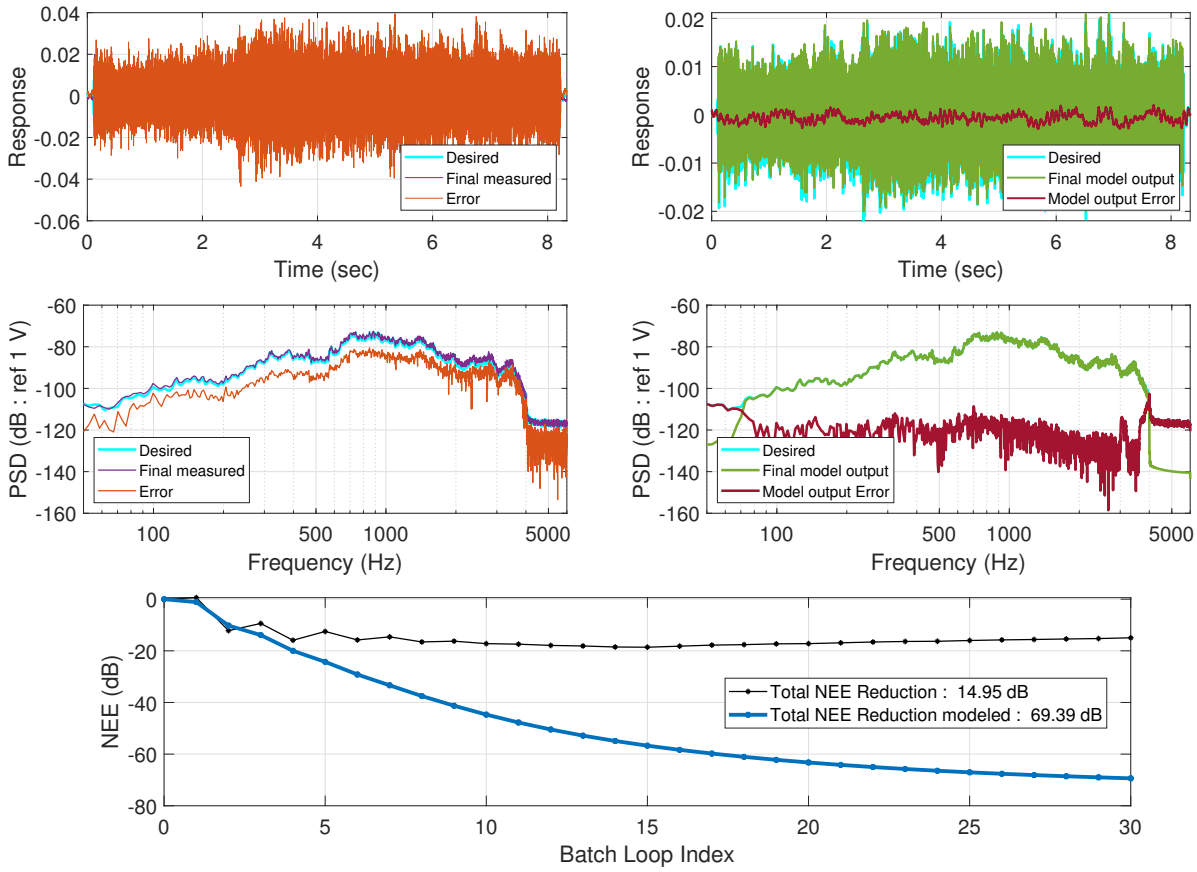

Figure 7.13: Experimental result of PT-Fx-LMS DFID algorithm for the unshifted SISO configuration with the speech sample target output. Left column: Measured response; Right column: Modeled output

As a contrast to the wavelet coherence plots for the single tone sinusoidal inputs, the need for a Model-in-Loop implementation of the DFID algorithm for speech signals is reinforced by its respective wavelet coherence plots shown in Figure 7.14 where it can be much more clearly seen that the phase vectors of the measured signal with reference to the target response varies

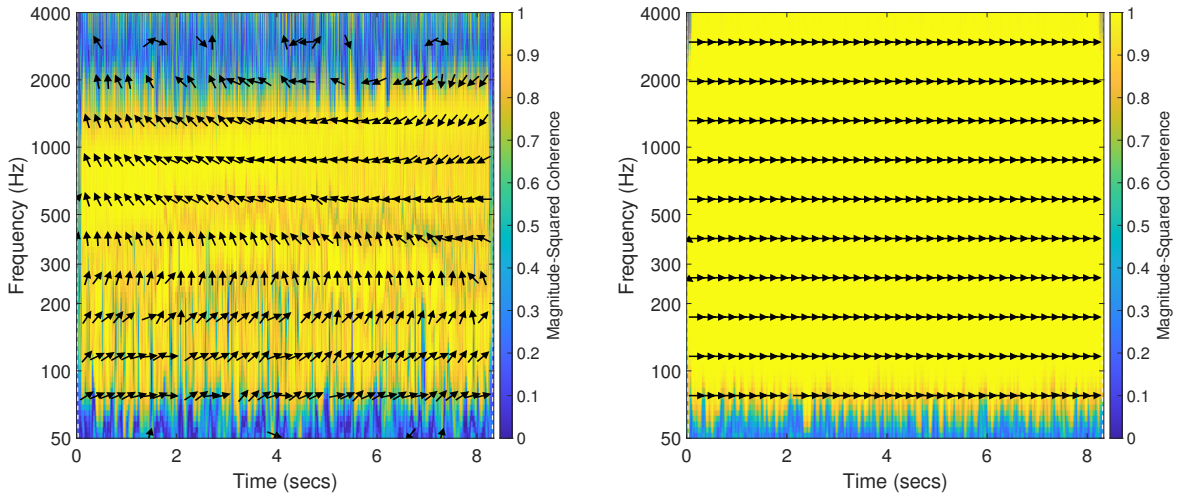

(a) Wavelet coherence between final measured and target response

(b) Wavelet coherence between final model output and target response

Figure 7.14: Comparison of the wavelet coherence plots of the measured and modeled output for the unshifted SISO configuration with a speech sample target response

nonlinearly across both frequency and time axes which needs to be time-aligned before direct use for control synthesis. On the other hand, the wavelet coherence of the model output with reference to the target shows perfect alignment and high coherence across the frequency bandwidth of interest in Figure 7.14b.

While the performance metrics of the studies above show a global error energy reduction, the adaptive algorithm always attempts to ”attack” the peak prominences in the spectrum in order to maximize the global error convergence to the minima under the restrictions of measurement noise and iteration step-sizes. This is hence used for a final sanity check on the converged control sequence and the final measured output response by using sound engineering judgment by listening to the actual target and measured sound signals, where sample delays are inconsequential for the SER application being evaluated. This is best illustrated by plotting the progression of the response spectra through the multiple batch iterations in Figure D.2, which shows clearly that the peak prominences in the spectrum

are adapted very quickly, and the algorithm works on finer adjustments through many more iteration sequence to minimize the misadjustment in less-dominant bandwidths.

7.3.2.2 Shifted layout

In the case of a single speaker used as an actuator, the major difference when the layout is shifted as in Figure 7.6, is directly correlated to the change in dynamics of the primary path between the speaker and the single target microphone as in Figure 7.10. Considering that the amplifier gain settings remain unchanged, the derived input sequence that minimizes the output response error shows a clear change in the magnitude of the signal, in comparison to the known control sequence used when measuring the target response. The derived control sequences for both the single sinusoid and speech sample target response tests are given in Figure 7.15 with reference to their respective initial known ground truths.

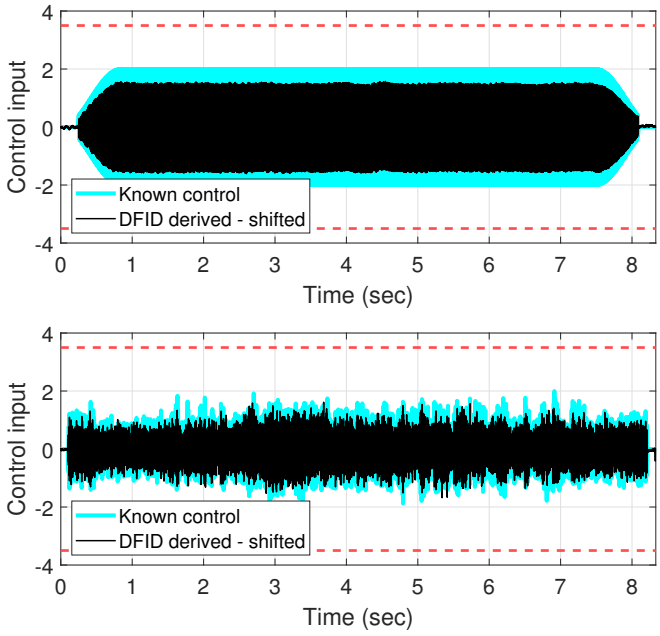

Figure 7.15: Experimental result of PT-Fx-LMS DFID algorithm derived control sequences for the shifted SISO configuration with a single sinusoid (top) and speech sample (bottom) target outputs

7.3.3 SIMO and MISO experiment configurations

7.3.3.1 SIMO experiment configuration

The experimental results for the Single Input Multiple Output configuration with Speaker 1 stimulated and both microphone channels being measured with its respective target responses follows similar trends as the SISO configuration results in section 7.3.2. The derived control sequence matches the known ground truth very accurately in the unshifted layout with the adaptive algorithm being driven by the model output and the performance metrics being characterized using the Normalized Error Energy of the power spectrum, in order to not consider the previously described time-synchronization issues with the data acquisition system. For concision, only the model output time-histories and power spectrums are shown in Figures 7.16 and 7.17 for the single sinusoid and speech sample target responses.

Note that in Figure 7.17, the error reduction at the lower frequency range is much more significant than at frequencies over 1500 Hz, which aligns with the coherence of the model identification being lower at these higher frequencies for a woofer driver designed for more accurate bass and mid-range, compared to the higher treble frequencies. While the actual spectrum-based NEE reduction of the measured signals show similar misadjustment levels as the SISO tests, the modeled output is much more consistent with the measured responses in the SIMO configuration. In these tests, after each batch iteration, the control sequence derived using the model output error is played to the actual system and the NEE reduction for the actual measured responses are calculated. If there exists confidence in the model quality, extensive batch iterations can be run in a simulated domain before playing the control sequence to the actual unit-under-test saving significant experiment turnover time, as laid out in the EB-PT-Fx-LMS architecture of Chapter 5.

Other results related to derived control traces, time-domain versus spectrum-based NEE

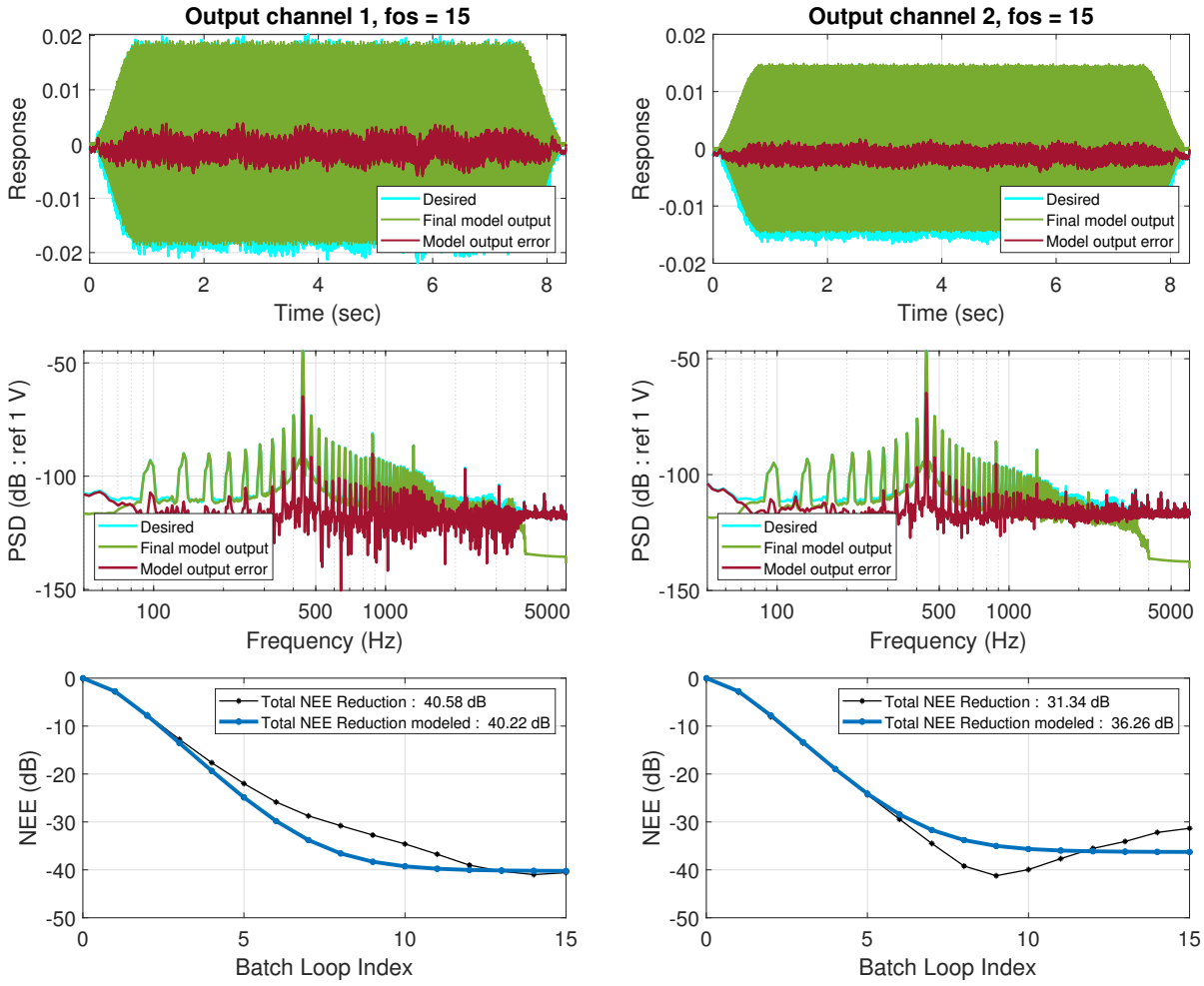

Figure 7.16: Experimental result of PT-Fx-LMS DFID algorithm for the unshifted SIMO configuration with the single sinusoid target output.

performance metrics, the wavelet coherence plots of the measured and model-output responses with respect to the target response for the unshifted SIMO configuration follows similar trends as the SISO experiment and are attached in Appendix D.3.

While Figure 7.17 shows good tracking of the target response spectrum at the end of the iterative algorithm for the unshifted layout, upon moving the two microphones to their new locations as given in Figure 7.6, anti-resonance harmonics are introduced in the measured signal spectra that severely limits the minimum misadjustment that can be achieved as

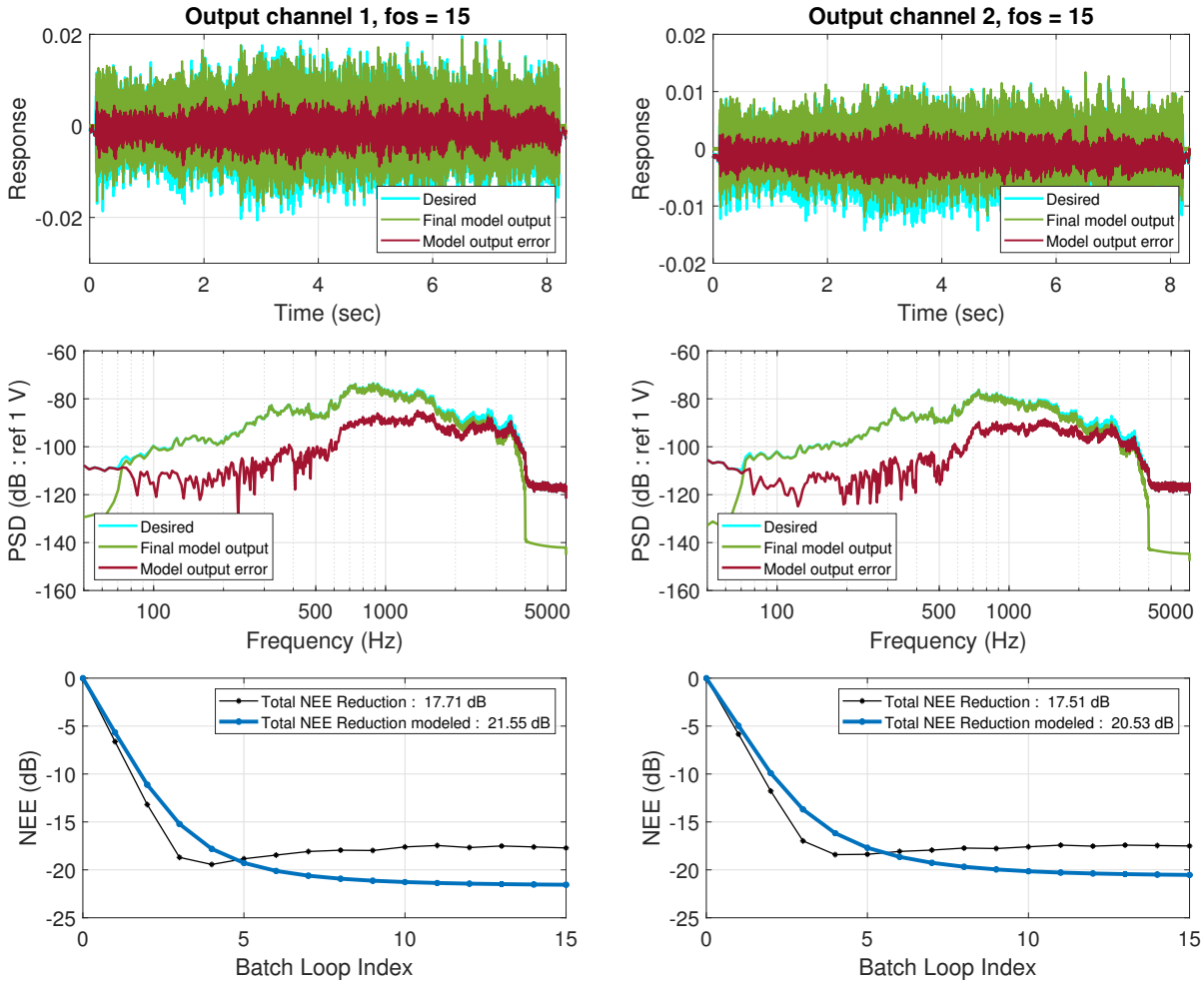

Figure 7.17: Experimental result of PT-Fx-LMS DFID algorithm for the unshifted SIMO configuration with the speech sample target output.

shown in Figure 7.18. While these notches in the spectrum were not observed in any other measurements, including in the system identification procedure for the SIMO configuration, such limitations are expected with fewer degrees of freedom and hardware modifications including relocation of actuators and sensors could be necessary to continue performance evaluation and SER testing. Such deficiencies were similarly observed for the shifted SIMO configuration with the single sinusoid target response.

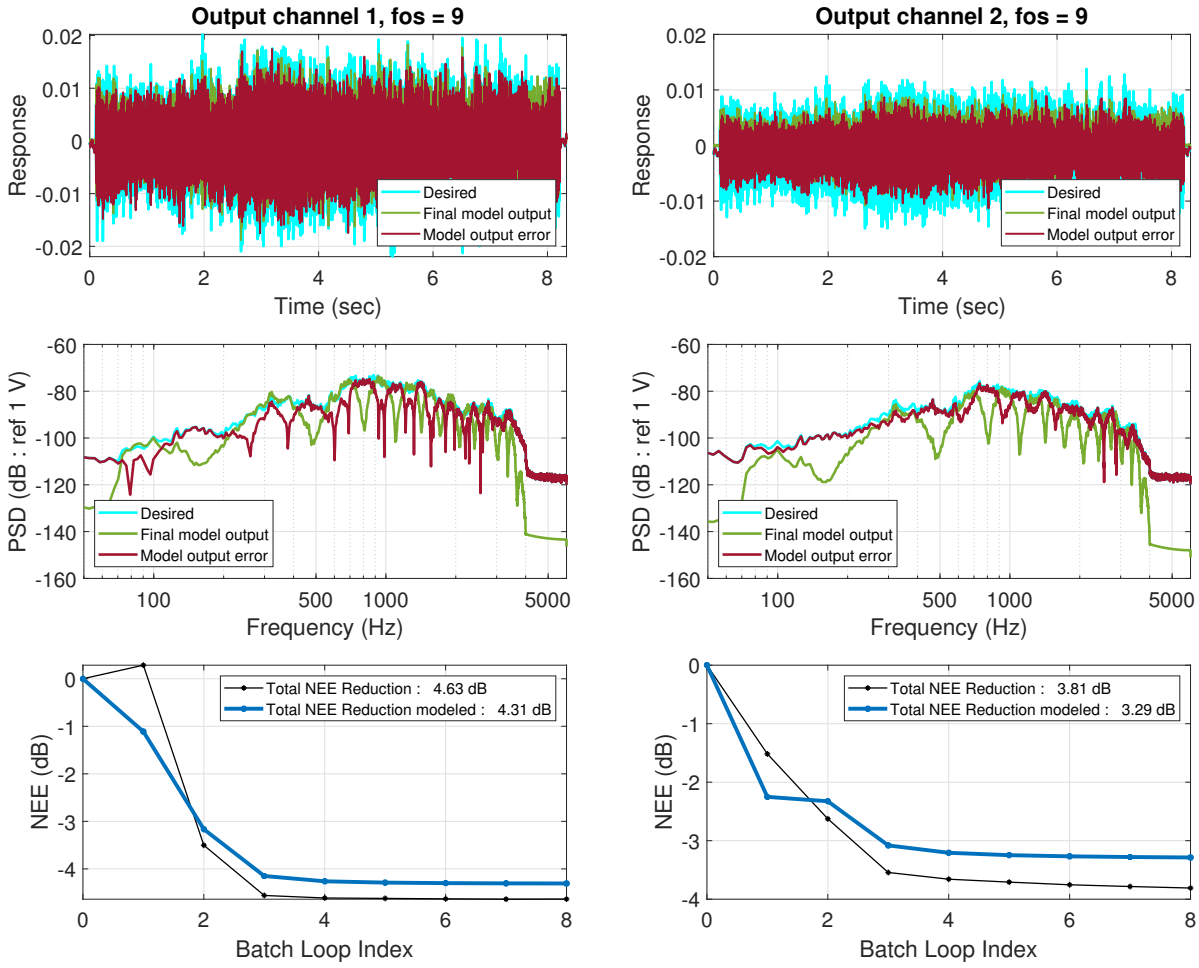

Figure 7.18: Experimental result of PT-Fx-LMS DFID algorithm for the shifted SIMO configuration with the speech sample target output.

7.3.3.2 MISO experiment configuration

For the under-determined case with two actuators and one sensor, the primary focus is observing the uniqueness of solutions obtained and how they correlate to known ground truths for the control sequences. As planned in Table 7.1, for the MISO configuration, the target response is measured on the single microphone with the speakers stimulated with either a single sinusoid of different amplitude and frequency to aid analysis on each speaker or the speech sample on one speaker and a single sinusoid on the other.

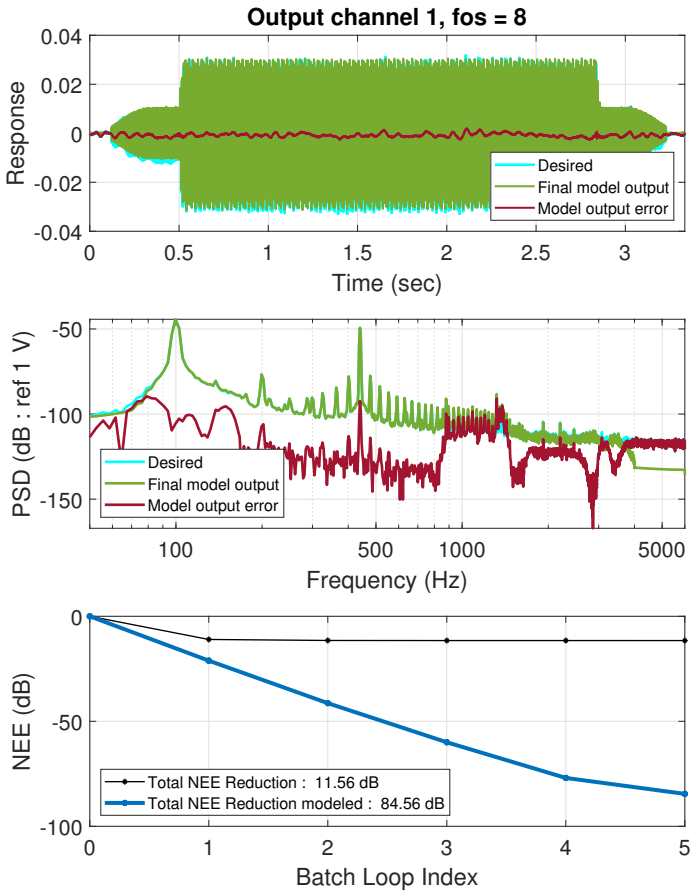

Figure 7.19: Experimental result of PT-Fx-LMS DFID algorithm for the unshifted MISO configuration with the dual sinusoid target response

The modeled response in Figure 7.19 shows the designed target response, where the measured response due to distinct frequency and amplitude sinusoids being played on the speakers. The modeled response which drives the DFID algorithm also shows very low final misadjustment and good performance on the actual measured response using the derived control sequences. Figure 7.20 shows the control sequences that have been derived for this test case. Despite the known ground truths having distinct sinusoids on each speaker, i.e. a 100 Hz monotone on the first speaker and a 440 Hz monotone on the second, the iterative algorithm does not make such distinction and distributes the required energy across the available actuators to simply produce the required target waveform. It should hence be

expected in the case of under-determined systems to converge to non-unique solutions while producing the same desired outputs at the sensors.

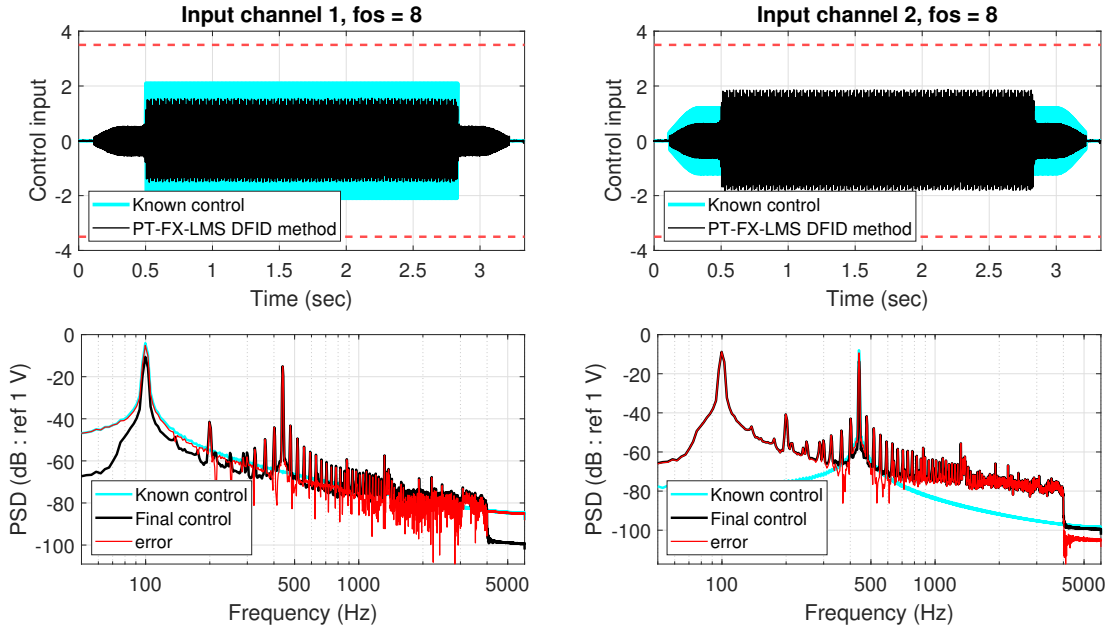

Figure 7.20: Experimental result of PT-Fx-LMS DFID algorithm derived control sequences for the unshifted MISO configuration comapring the derived control with the known ground truth for the sinusoid input test case

For the shifted experimental layout with sinusoid inputs, the results are consistent with previous test cases and the derived control inputs are attenuated again to account for the change in path dynamics. The time-frequency analysis is also consistent with previous results for simple sinusoid target responses where the measured response only shows good coherence around the monotone frequencies of interest and conventional time-alignment methods are sufficient to significantly reduce time-shift errors in the output response.

When considering separate inputs to the speakers when recording the target responses, the sample speech signal input is played on the first speaker and a 440 Hz single sinusoid is played to the second. As in the test cases above, the derived control sequences shown in Figure D.6 do not distinguish between the sources and the energy required to replicate

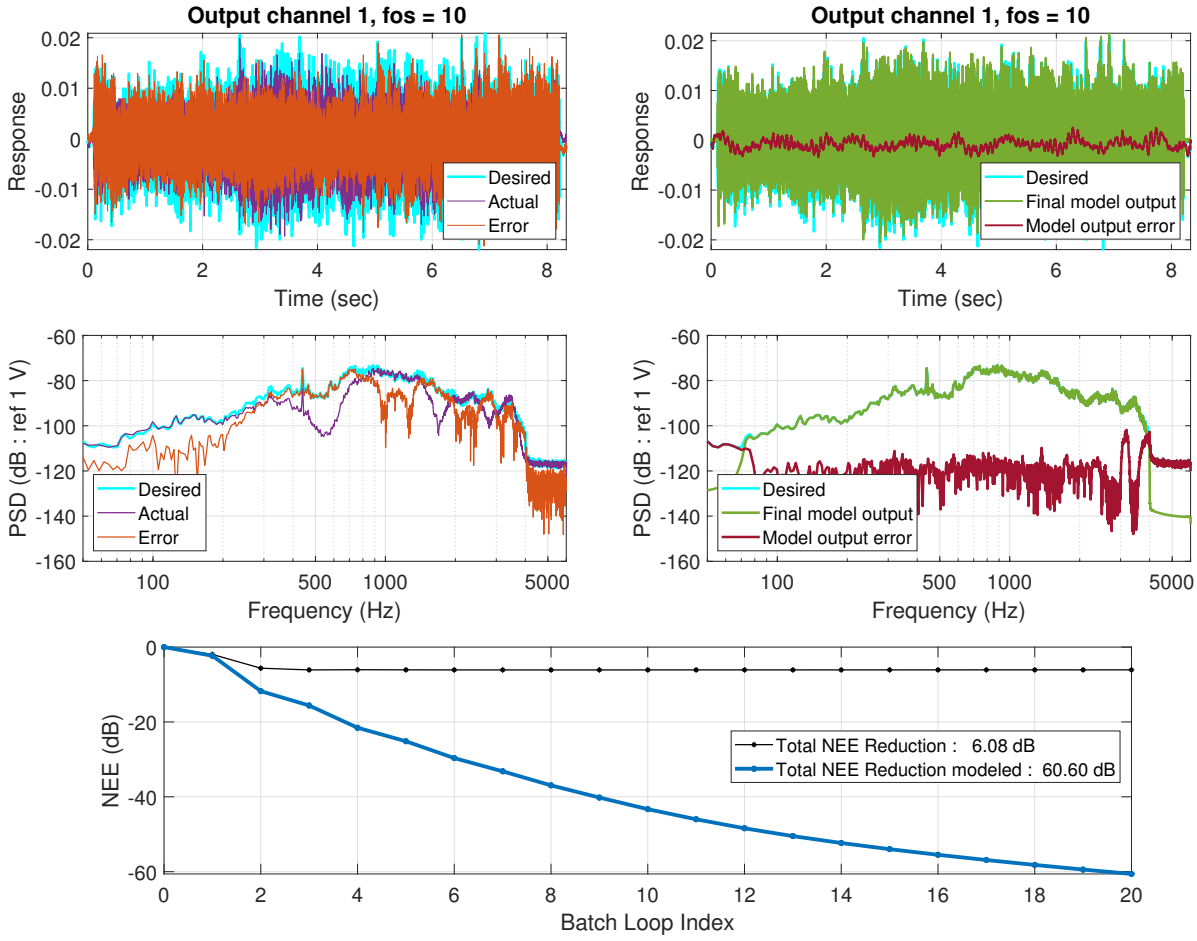

Figure 7.21: Experimental result of PT-Fx-LMS DFID algorithm for the unshifted MISO configuration with the speech sample and sinusoid combined target output. Left column: Measured response; Right column: Modeled output

the target waveform is distributed between both the actuators. With the initial unshifted layout, it can be seen in the spectrum of the final measured output in Figure 7.21 that the adaptive algorithm targets the peaks in the spectrum through the batch iterations, but there exists larger errors in the measured output at specific frequencies (543 Hz, 1693 Hz and 2795 Hz) that are not captured in the model output. This is hypothesized to be because of the layout of the speakers and microphones leading to destructive interferences at these specific frequencies.

While the modeled output keeps achieving a lower misadjustment level and has not yet converged in the 20 batch iterations conducted in this test, it can clearly be seen that running more iterations does not improve the actual measured response which converges within just 4 iterations. This is more clearly observed in Figure 7.22 which tracks the progression of the measured output spectrum through the batch iterations. The peaks in the response quickly converge to their final values and the later batch iterations target the response in the 1600–3500 Hz frequency range that is known to have poorer coherence in the identified model. The poor response replication in the 350–750 Hz range is also clearly seen in the drop in wavelet coherence in this bandwidth with the measured output as seen in Figure D.7a. Considering the convergence of the actual measured output at a higher misadjustment level and earlier than the modeled output, a termination criterion, similar to the development in section 5.3.2 can be considered to further reduce testing turnover time.

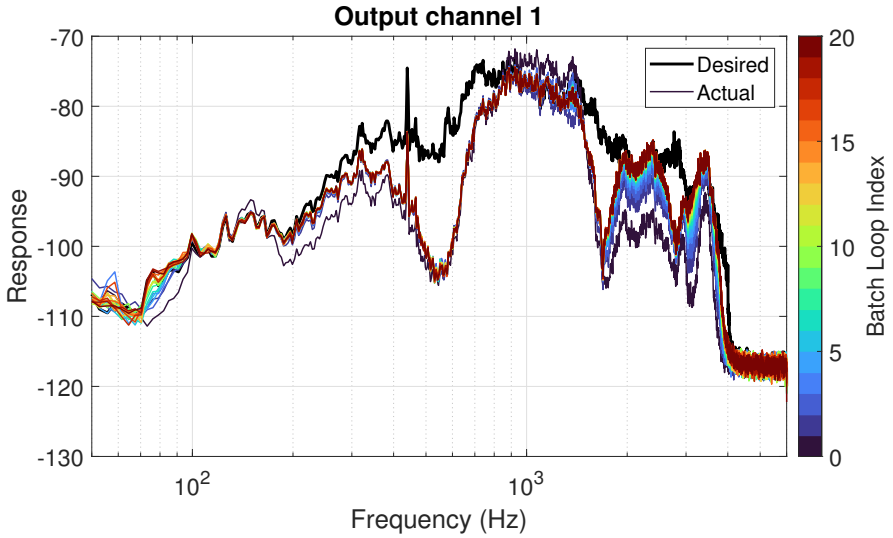

Figure 7.22: Progression of the output response through the batch loop iterations for the MISO unshifted configuration experiment

When the sensors have been moved to their new shifted positions, the troughs in the spectrum are no longer observed in the measured output as shown in Figure 7.23. On the other hand, the model output does not show the same level of performance which can be

attributed to model deficiency for the shifted configuration and poorer woofer performance beyond the 1500 Hz bandwidth that these woofers have not been primarily designed for. Additional plots for this test case have been attached in Appendix D.4.

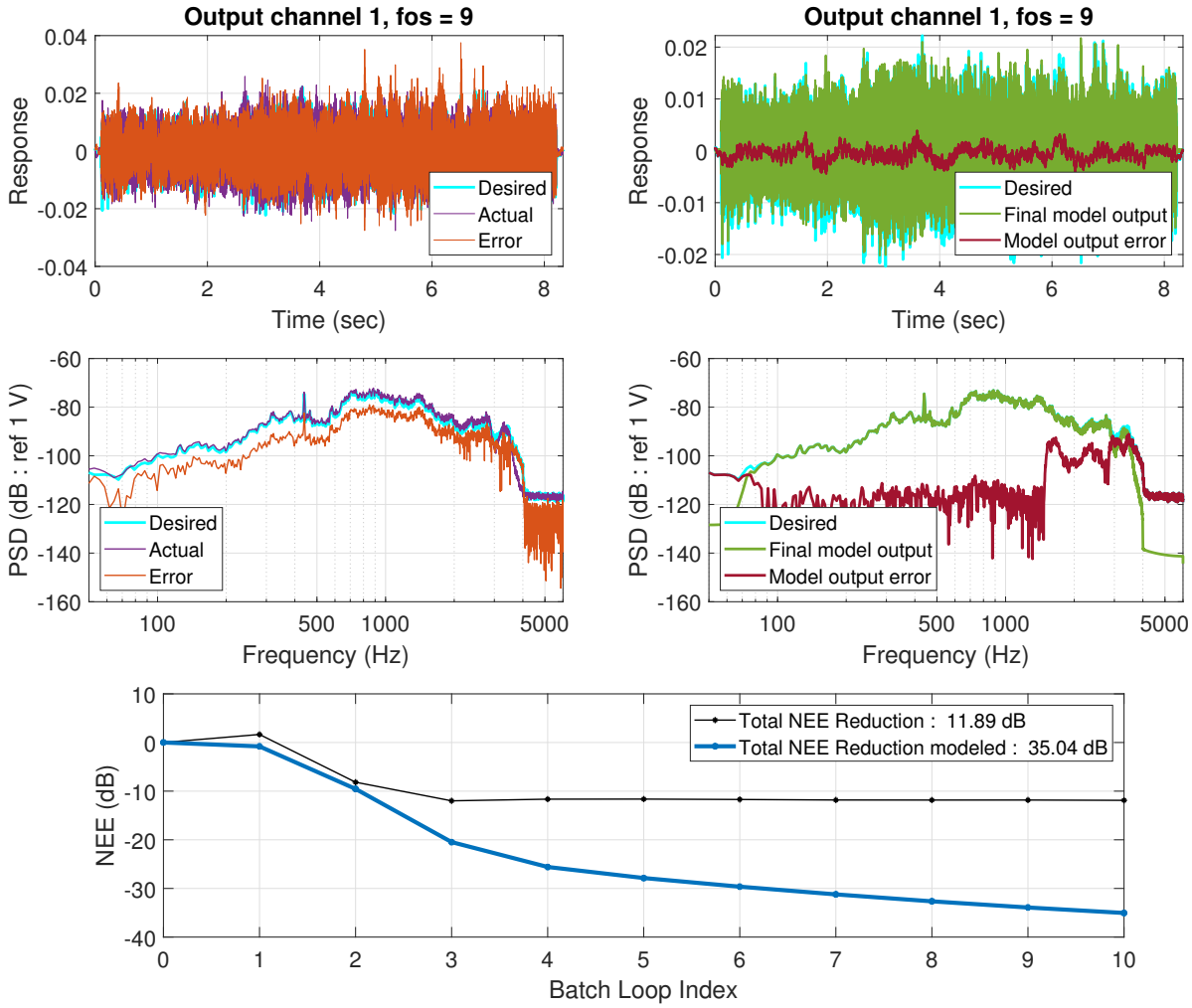

Figure 7.23: Experimental result of PT-Fx-LMS DFID algorithm for the shifted MISO configuration with the speech sample and sinusoid combined target output. Left column: Measured response; Right column: Modeled output

7.3.4 MIMO experiment configuration

As an extension of the SIMO and MISO tests conducted in section 7.3.3, in the MIMO configuration, both the speakers inputs are stimulated in order to replicate the target responses on both the speakers. Similar to the results in section 7.3.3.2 for the MISO configuration, it is seen that the shifted layout allows for better replication of the sound field, most likely because the microphones are closer to the speakers or the free-field microphones are pointing directly at them. Figure 7.24 presents the model output response results for the shifted configuration with dual sinusoid target response and Figure 7.25 presents the model output results for the unshifted configuration with the combined speech sample and sinusoid inputs. These two results show the best to worst results obtained for the test cases considered. Additional validation results are presented in Appendix D.5.

While harmonics have been observed in all the other test cases with pure sinusoids, in this MIMO test case, the derived control sequence is also close to the defined soft limits in control voltage of 3.5 V built in to protect clipping on the amplifiers, as seen in Figure D.10. Saturation controls are always built into actuators and can lead to nonlinear effects in the measured response.

The response progression of the measured response in Figure D.11 shows clearly that the adaptive algorithm again tracks the dominant peak in the target spectrum. Much of the attenuation with subsequent batch iterations involves corrections in response to the harmonics around the 1000 Hz range. It is hypothesized that the slight peaks in the frequency response of the model shown in Figure 7.9 in this bandwidth affects the initial estimates of the drive files derived. Further analysis of this behavior with specific target responses that dominate this bandwidth could provide more insights.

In the case of the dual sinusoid target response, the model output also does not achieve a

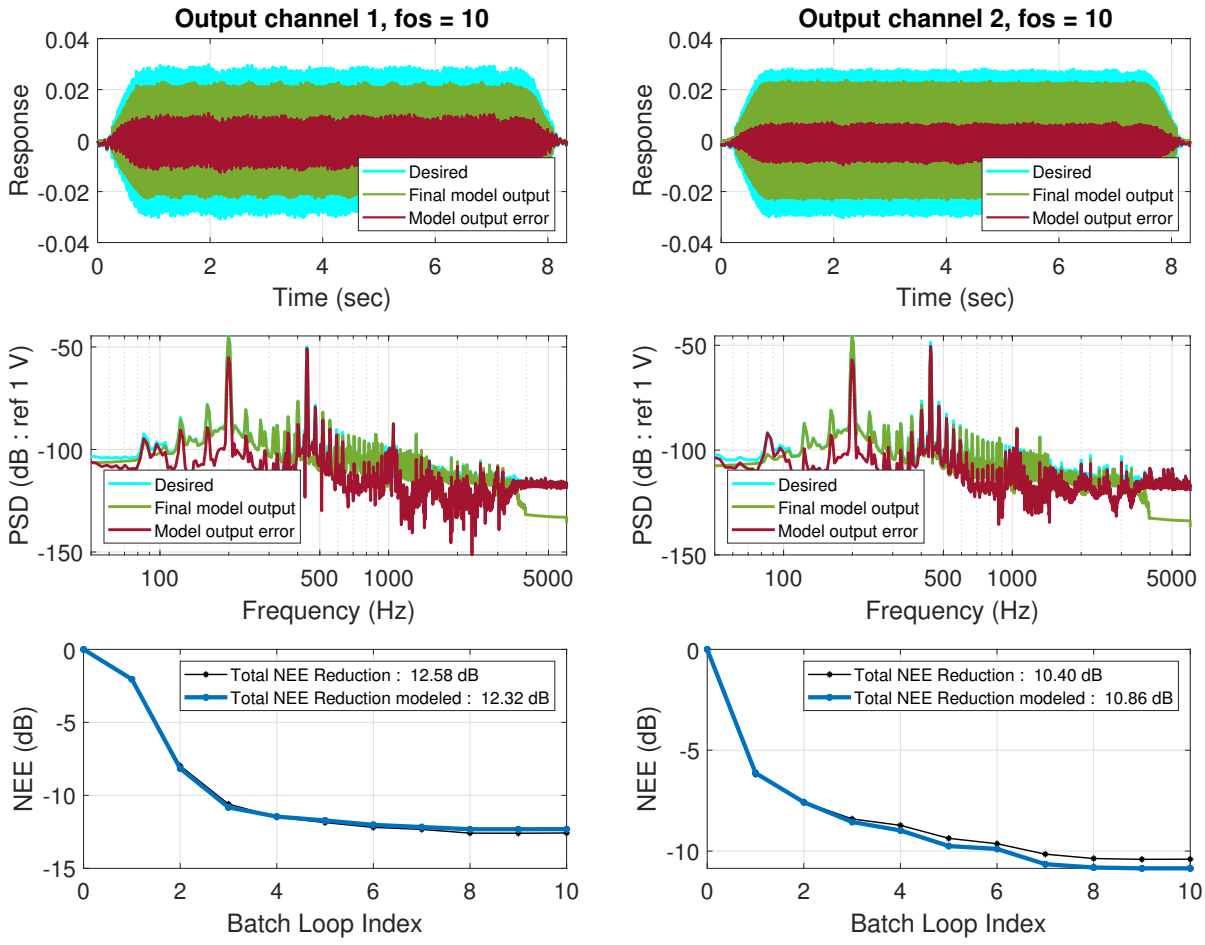

Figure 7.24: Experimental result of PT-Fx-LMS DFID algorithm for the shifted MIMO configuration with the dual sinusoid target output.

very low misadjustment as in the previous test cases because the cross-correlation based time-alignment method only captures and aligns the phase-delay associated with the dominant sinusoid at 200 Hz and the second sinusoid at 440 Hz remains misaligned, as can be seen in Figure D.12.

While anti-resonances were observed in the case of the shifted SIMO configuration, the sound field produced by the unshifted MIMO configuration shows similar anti-resonances even in the modeled output as shown in Figure 7.25. This affects the final misadjustment that is achieved by the adaptive algorithm which produces a stable NEE reduction curve

only because of the global step-size relaxation strategy that repeats the batch iteration with a reduced iteration constant.

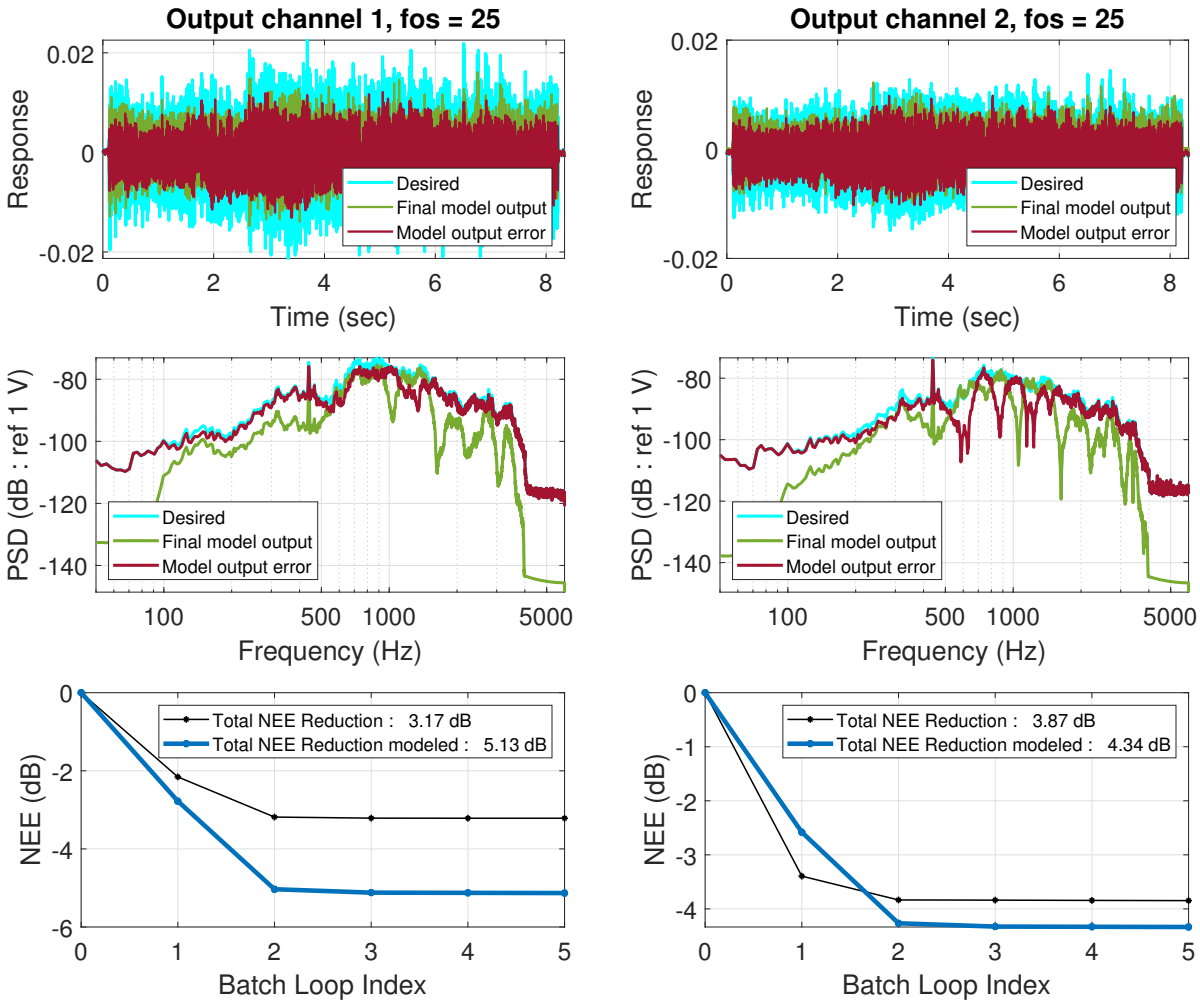

Figure 7.25: Experimental result of PT-Fx-LMS DFID algorithm for the unshifted MIMO configuration with the combined speech and sinusoid target output.

These anti-resonance troughs are also seen distinctly in the spectrum of the derived control sequences in Figure D.13 that also do not match the known ground truth. The wavelet coherence plots in Figure D.14 also show that there exist phase delays across the time-frequency axes even for the modeled output. Compared to the other presented wavelet coherence analysis, this test case presents the worst-case scenario, which is often best tackled

in practice by changing the paths of energy transfer. A complete analysis of the environment to map out the locations of maximum destructive interference as a function of frequency will better provide insight into allowable configurations or indicate the primary path dynamics that might be difficult to replicate.

7.4 Summary of results and conclusion

This chapter validates the developed novel PT-Fx-LMS algorithm for Drive File identification in an acoustic experiment to replicate the sound field generated by either one or two speaker drivers in multiple configurations. The performance of the algorithm is analyzed for a simple SISO system, over-determined SIMO and under-determined MISO systems and a MIMO configuration by choosing the number of active speakers and microphones. The experiment layout is described in detail and designed to reduce external noise factors, with the available resources. The experiments are conducted with two different types of target responses, with monotone sinusoid signals chosen to aid in time-alignment of signals for the offline batch iterative algorithms and a sample speech signal to test a more real-world relevant and challenging application. In the initial configuration, the microphones are left in the same locations as when the target responses are measured so that the derived control sequences can be directly compared against the known ground truths. When the layout is shifted, the primary paths are re-identified before the DFID process and the speaker inputs required to replicate the sound field consequently do not match the reference control waveforms, as expected. In cases where there are multiple inputs (MISO and MIMO), the derived drive files also do not match the reference because the required sound output energy is shared across the speakers. The adaptive algorithm in all the test cases are model driven in order to simplify data processing and while this is not an ideal case for real-world applications,

Table 7.2: Summary of spectrum-based NEE (in dB) results for the series of model-based DFID experiments conducted with the acoustical setup

System	**Sinusoid Target**†		**Speech sample target**††	
	Unshifted Layout	Shifted Layout	Unshifted Layout	Shifted Layout
SISO (1×1)	17.97	46.43	14.95	16.19
SIMO (2×1)	[40.58, 31.34]	[2.06, 0.85]	[17.71, 17.51]	[4.63, 3.81]
MISO (1×2)	11.56	20.72	6.08	11.89
MIMO (2×2)	[5.28, 1.33]	[12.58, 10.40]	[3.17, 3.87]	[10.35, 9.93]

† Single sinusoid in the case of single input, two separate sinusoids for multiple inputs
†† Single Speech sample in the case of single input, the speech sample and a single sinusoid for multiple inputs

the use of Model-in-the-Loop control architectures is widespread in various industries to still make this a relevant test case.

Performance of the algorithm is characterized by tracking the Normalized Error Energy of the spectrum of the signals instead of the time-domain error sequences and are summarized in Table 7.2. Subjective interpretation of the results is also detailed through analysis of the progression of the measured output spectrums, the wavelet coherence plots and physically listening to the final output responses.

Many improvements to this experimental workflow are possible, the most important of which is running the tests in a Hardware-in-the-Loop configuration as is most desired for SER applications. With the ability to accurately time-align signals and use data acquisition systems that are more robust to jitter and do not introduce phase delays across time and frequency, measured signals instead of a model output can be used to drive the adaptive algorithm. The experimental layout can also be designed with injection of various non-linearities to further validate the applicability of the time-domain based DFID algorithm for such dynamical systems. Development of a functioning comparative ILC scheme for DFID could allow for further insights into the performance of the proposed novel algorithm.

Chapter 8

Conclusions and Future Work

The main research objective of this dissertation was the development of a time-domain based Drive File identification algorithm using adaptive filtering techniques for direct synthesis of control sequences to achieve accurate tracking of responses for Service Environment replication. This objective was achieved by reformulation of the adaptive filtering architecture used for vibration and noise cancellation of primary path disturbances using the Filtered-x LMS algorithm. By choosing a pulse-train reference input, direct synthesis of the control sequences is possible, without the need for the derivation of inverse models that pose challenges in various applications.

Through various case studies, the novel method for DFID is validated on simulated test-benches for different classes of nonlinearities in the dynamics of the unit-under-test and demonstrate the performance of the algorithm in comparison to conventional Iterative Learning Control schemes using frequency domain techniques and adaptive inverse models. Case studies related to replicating target waveforms in certain intervals of time without interfering in the already adapted sections outside of such time slices. The novel algorithm shows better performance than the considered conventional methods in these relevant practical requirements. Improvements to the DFID workflow using a model estimation based iterative algorithm by leveraging computational resources to iterate many more times in a simulation domain using the identified plant model before adding the corrections to the target using the actual measured responses. A termination criterion is also introduced to further reduce

the number of batch iterations required to reach the threshold accuracy desired.

The Pulse Train Fx-LMS architecture is expanded to MIMO applications and validated for both square and non-square systems with a randomly generated dynamic system with considerations for stability, controllability and minimum-phase dynamics. It has been shown in the case studies demonstrating the proposed novel methods of DFID that the presence of nonlinearities in the dynamic system test benches, as is generally found in most real-world systems, makes the identification of their estimated models and consequently the derived drive files to be deficient in performance compared to linear dynamic systems. In order to align the test benches to more real-world applications, a simulation study considering a quarter-car model of an automotive system that more closely represents the SER testing requirements in the automotive industry is demonstrated. These empirical case studies show significant improvement in response replication using the workflow presented for the proposed algorithm.

While the proposed DFID methods have been previously validated on simulated test benches, with the resources available for this project, an acoustic experimental demonstration for this method of waveform replication is conducted. With the use of two speakers and microphones and the data acquisition system used, different configurations are tested. The novel algorithm achieves acceptable signal replication, characterized by the spectrum errors for acoustic signals.

8.1 Future work

The following research and investigative studies are proposed for the future:

- Nonlinear system dynamics, as were considered for a SISO mass-spring-damper system

in section 3.2.3 can be considered for the quarter-car suspension test bench. This expands the applicability for a broader class of applications and the consideration of other external noise factors.

- For the main application of interest in this thesis, real-world experiments should be conducted on quarter-car test setups with the required system identification steps instead of using black-box simulated dynamic systems with apriori knowledge of system parameters. Fidelity of the identified system models used for the adaptive filtering based DFID methods has been shown to be critical and hence the logical extension for validation requires implementation on actual hardware where the effects of nonlinear dynamics, noise factors, real-time data acquisition and processing pose significant challenges to this practical problem.

- Inclusion of real-time control methods can allow for online adaptation of the drive file, instead of offline batch processing as presented in this thesis. Appropriate resources for such implementation can also reduce issues with time-synchronization of the target and measured signals that forms a critical noise factor for time-domain implementation and performance characterization.

- Further investigation of the Drive File Identification procedure for MIMO systems is proposed by considering a wider array of generated dynamic systems of various dimensions previously mentioned in section 4.2.2, different FIR filter lengths, minimum and non-minimum phase systems, full-rank or rank deficient systems in order to further understand the existence and uniqueness questions related to DFID solutions. The conventional time-domain DFID method using adaptive inverse models and the novel PT-Fx-LMS method should be utilized to develop a set of guidelines based on the estimated dynamics of the system and the desired target responses to inform the user about the best-practices for the DFID procedure for SER applications. Hence, evalu-

ating the proposed test matrix involves a large number of empirical experiments. Such a survey was conducted but a discernible pattern was missing and specific guidelines for predicting if a solution exists was not arrived at. A more fundamental mathematical formulation of the problem, combining with research in other scientific fields, is required.

Bibliography

[1] *ART SLA-4 four channel Studio Linear Aplifier Users Guide*. Applied Research and Technology, 10 2023. URL https://www.artproaudio.com/framework/uploads/2018/06/om_sla4.pdf.

[2] Andrew J Barber. Generating a nonlinear model and generating drive signals for simulation testing using the same, Sept 2001. URL http://patft.uspto.gov/netacgi/nph-Parser?patentnumber=6,285,972.

[3] J. S. Bendat and A. G. Piersol. *Engineering applications of correlation and spectral analysis*. 1980. URL https://ui.adsabs.harvard.edu/abs/1980wi...book.....B. Provided by the SAO/NASA Astrophysics Data System.

[4] C Berger, K.-G Eulitz, P Heuler, K.-L Kotte, H Naundorf, W Schuetz, C.M Sonsino, A Wimmer, and H Zenner. Betriebsfestigkeit in Germany – an overview. *International Journal of Fatigue*, 24(6):603–625, 2002. ISSN 0142-1123. doi: https://doi.org/10.1016/S0142-1123(01)00180-3. URL https://www.sciencedirect.com/science/article/pii/S0142112301001803.

[5] Chris Boggs, Mehdi Ahmadian, and Steve Southward. Application of System Identification for Efficient Suspension Tuning in High-Performance Vehicles: Full-Car Model Study. *SAE International Journal of Passenger Cars - Mechanical Systems*, 2(1): 622–635, 2009. ISSN 1946-3995. doi: https://doi.org/10.4271/2009-01-0433. URL https://doi.org/10.4271/2009-01-0433.

[6] J.A. Butterworth, L.Y. Pao, and D.Y. Abramovitch. Analysis and comparison of three discrete-time feedforward model-inverse control techniques for nonminimum-

phase systems. *Mechatronics*, 22(5):577–587, 2012. ISSN 0957-4158. doi: 10.1016/j.mechatronics.2011.12.006. URL https://www.sciencedirect.com/science/article/pii/S0957415812000311. Special Issue on Distributed Intelligent MEMS: from hardware to software.

[7] Denis Byrne, Harvey Dillon, Khanh Tran, Stig Arlinger, Keith Wilbraham, Robyn Cox, Bjorn Hagerman, Raymond Hetu, Joseph Kei, C. Lui, Jurgen Kiessling, M. Nasser Kotby, Nasser H. A. Nasser, Wafaa A. H. El Kholy, Yasuko Nakanishi, Herbert Oyer, Richard Powell, Dafydd Stephens, Rhys Meredith, Tony Sirimanna, George Tavartkiladze, Gregory I. Frolenkov, Soren Westerman, and Carl Ludvigsen. An international comparison of long term average speech spectra. *The Journal of the Acoustical Society of America*, 96(4):2108–2120, 10 1994. ISSN 0001-4966. doi: 10.1121/1.410152. URL https://doi.org/10.1121/1.410152.

[8] Danilo Cambiaghi, Marco Gadola, and David Vetturi. Suspension System Testing and Tuning with the Use of a Four-Post Rig. In *Motorsports Engineering Conference & Exposition*. SAE International, Nov 1998. doi: https://doi.org/10.4271/983023. URL https://doi.org/10.4271/983023.

[9] Daniel Chindamo, Marco Gadola, and Felipe P Marchesin. Reproduction of real-world road profiles on a four-poster rig for indoor vehicle chassis and suspension durability testing. *Advances in Mechanical Engineering*, 9(8), 2017. doi: 10.1177/1687814017726004. URL https://doi.org/10.1177/1687814017726004.

[10] AJ Clark. Dynamic characteristics of large multiple degree of freedom shaking tables. In *Proceedings of the 10th World Conference on Earthquake Engineering*, pages 2823–2828. Madrid, Spain, 1992.

[11] Robert L Clark, William R Saunders, Gary P Gibbs, et al. *Adaptive structures: dynamics and control*, volume 28. Wiley New York, 1998.

[12] Bram Cornelis, Alessandro Toso, Wouter Verpoest, and Bart Peeters. Adaptive modelling for improved control in durability test rigs. In *Proceedings of the 20th International Congress on Sound and Vibration*, pages 507–16, 2013.

[13] B. W. Cryer, P. E. Nawrocki, and R. A. Lund. A Road Simulation System for Heavy Duty Vehicles. In *1976 Automotive Engineering Congress and Exposition*, volume 85, pages 1322–1334. SAE International, 1976. doi: 10.4271/760361.

[14] J. De Cuyper and M. Verhaegen. State space modeling and stable dynamic inversion for trajectory tracking on an industrial seat test rig. *Journal of Vibration and Control*, 8(7):1033–1050, 2002. doi: 10.1177/107754602029580. URL https://doi.org/10.1177/107754602029580.

[15] J. De Cuyper, D. Coppens, Christophe Liefooghe, Jan Swevers, and Michel Verhaegen. Advanced drive file development methods for improved service load simulation on multi axial durability test rigs. 1998.

[16] Joris De Cuyper, Michel Verhaegen, and Jan Swevers. Off-line feed-forward and H_∞ feedback control on a vibration rig. *Control Engineering Practice*, 11(2):129–140, 2003. ISSN 0967-0661. doi: https://doi.org/10.1016/S0967-0661(02)00103-X. URL https://www.sciencedirect.com/science/article/pii/S096706610200103X. Automotive Systems.

[17] *DC160S-8 6.5in Classic Shielded Woofer 8 Ohm.* Dayton Audio, 10 2023. URL https://www.daytonaudio.com/images/resources/295-306-dayton-audio-dc160s-8-specifications-46147.pdf.

[18] J De Cuyper, D Coopens, C Liefooghe, and J Debille. Advanced system identification methods for improved service load simulation on multi axial test rigs. *European journal of mechanical and environmental engineering*, 44(1):27–39, 1999. ISSN 1371-6980.

[19] Joris De Cuyper. *Linear feedback control for durability test rigs in the automotive industry*. PhD thesis, Katholieke Universiteit Leuven, Department of Mechanical Engineering, 2006.

[20] Vasilis K Dertimanis, Harris P Mouzakis, and Ioannis N Psycharis. On the acceleration-based adaptive inverse control of shaking tables. *Earthquake Engineering & Structural Dynamics*, 44(9):1329–1350, 2015.

[21] S. Devasia, Degang Chen, and B. Paden. Nonlinear inversion-based output tracking. *IEEE Transactions on Automatic Control*, 41(7):930–942, 1996. doi: 10.1109/9.508898.

[22] Digilent. Analog discovery 2 reference manual, 2016. URL https://digilent.com/reference/test-and-measurement/analog-discovery-2/reference-manual.

[23] Digilent. Waveforms reference manual, 2016. URL https://digilent.com/reference/software/waveforms/waveforms-3/reference-manual.

[24] C.J. Dodds and A.R. Plummer. Laboratory Road Simulation for Full Vehicle Testing: A Review. In *SIAT 2001*. The Automotive Research Association of India, Jan 2001. doi: 10.4271/2001-26-0047. URL https://doi.org/10.4271/2001-26-0047.

[25] Coan J Dodds. A computer system for multi-channel remote parameter control of a test specimen. *MTS publication*, 1977.

[26] Colin J Dodds. *The Response of Vehicle Components to Random Road Surface Undulations*. PhD thesis, University of Glasgow, 1972.

[27] Stephen J. Elliott. *Signal Processing for Active Control*. Signal processing and its applications. Academic, San Diego, CA, 2001. ISBN 0122370856 9780122370854.

[28] Stephen J. Elliott and Philip A. Darlington. Adaptive cancellation of periodic, synchronously sampled interference. *IEEE Transactions on Acoustics, Speech, and Signal Processing*, 33(3):715–717, 1985. doi: 10.1109/TASSP.1985.1164596.

[29] Stephen J. Elliott, I. Stothers, and Philip A. Nelson. A multiple error lms algorithm and its application to the active control of sound and vibration. *IEEE Transactions on Acoustics, Speech, and Signal Processing*, 35(10):1423–1434, 1987. ISSN 0096-3518. doi: 10.1109/TASSP.1987.1165044.

[30] Guang feng Guan, Hai tao Wang, and Wei Xiong. Multi-input multi-output random vibration control of a multi-axis electro-hydraulic shaking table. *Journal of Vibration and Control*, 21(16):3292–3304, 2015. doi: 10.1177/1077546314521444. URL https://doi.org/10.1177/1077546314521444.

[31] David M Fricke, Mark D Hansen, and Rakan C Chabaan. Effective road profile control method for a spindle-coupled road simulator, mar 1997. URL http://patft.uspto.gov/netacgi/nph-Parser?patentnumber=5,610,330.

[32] Christopher C Fuller, Stephen J Elliott, and Philip A Nelson. *Active control of vibration*. Academic press, 1996.

[33] S. T. Furr. Development of a new laboratory test method for spring steels. *Journal of Basic Engineering*, 94(1):223–227, 03 1972. ISSN 0021-9223. doi: 10.1115/1.3425371.

[34] Shen Gang, Zhu Zhen-Cai, Zhang Lei, Tang Yu, Yang Chi-fu, Zhao Jin-song, Liu Guang-da, and Han Jun-Wei. Adaptive feed-forward compensation for hybrid control with acceleration time waveform replication on electro-hydraulic shaking table.

Control Engineering Practice, 21(8):1128–1142, 2013. ISSN 0967-0661. doi: https://doi.org/10.1016/j.conengprac.2013.03.007. URL https://www.sciencedirect.com/science/article/pii/S0967066113000531.

[35] K George, M Verhaegen, and JMA Scherpen. A systematic and numerically efficient procedure for stable dynamic model inversion of lti systems. In *Proceedings of the 38th IEEE Conference on Decision and Control (Cat. No. 99CH36304)*, volume 2, pages 1881–1886. IEEE, 1999.

[36] Ali G. Goktan and Argun Yetkin. Road Load Data Estimation on Multiaxial Test Rigs for Exhaust System Vibrations. *SAE Transactions*, 111:1194–1201, 2002. ISSN 0096736X, 25771531. URL http://www.jstor.org/stable/44719294.

[37] Bernhard Gründer and Michael Speckert. Design of Durability Sequences Based on Rainflow Matrix Optimization. In *International Congress & Exposition*. SAE International, Feb 1998. doi: 10.4271/980690. URL https://doi.org/10.4271/980690.

[38] ID Gupta. The state of the art in seismic hazard analysis. *From Seismic source to structural response: Contributions of Professor Mihalio D. Trifunac*, pages 146–147, 2004.

[39] Colin Hansen, Scott Snyder, Xiaojun Qiu, Laura Brooks, and Danielle Moreau. *Active control of noise and vibration*. CRC press, 2012.

[40] Gemma Hatton. Seven-post rigs: Shaking down the best in suspension testing tech. *Racecar Engineering*, 2018. URL https://www.servotestsystems.com/media/attachments/2020/04/17/reprint_-_racecar_engineering_june_july_2018.pdf.

[41] Y. Inouye and Ruey-Wen Liu. Critera for direct blind deconvolution of mimo fir

systems driven by white source signals. In *Proceedings of the Acoustics, Speech, and Signal Processing, 1999. on 1999 IEEE International Conference - Volume 05*, ICASSP 99, page 2889–2892, USA, 1999. IEEE Computer Society. ISBN 0780350413. doi: 10.1109/ICASSP.1999.761366. URL https://doi.org/10.1109/ICASSP.1999.761366.

[42] Dominic Jordan and Peter Smith. *Nonlinear ordinary differential equations: an introduction for scientists and engineers*. OUP Oxford, 2007.

[43] Jer-Nan Juang and Richard S. Pappa. An eigensystem realization algorithm for modal parameter identification and model reduction. *Journal of Guidance, Control, and Dynamics*, 8(5):620–627, 1985. doi: 10.2514/3.20031. URL https://doi.org/10.2514/3.20031.

[44] Yoshinobu Kajikawa, Woon-Seng Gan, and Sen M. Kuo. Recent advances on active noise control: open issues and innovative applications. *APSIPA Transactions on Signal and Information Processing*, 1(1):–, 2012. ISSN 2048-7703. doi: 10.1017/ATSIP.2012.4. URL http://dx.doi.org/10.1017/ATSIP.2012.4.

[45] AM Karshenas, MW Dunnigan, and BW Williams. Adaptive inverse control algorithm for shock testing. *IEE Proceedings-Control Theory and Applications*, 147(3):267–276, 2000.

[46] Steven M Kay. *Modern spectral estimation : theory and application*. Prentice Hall, Englewood Cliffs, N.J. SE - xv, 539 pages : illustrations ; 24 cm., 1988. ISBN 0130151599 9780130151599.

[47] Hassan K Khalil. *Nonlinear control*, volume 406. Pearson New York, 2015.

[48] Henri Kowalczyk. Damper Tuning with the use of a Seven Post Shaker Rig. *SAE*

Transactions, 111:1182–1193, 2002. ISSN 0096736X, 25771531. URL http://www.jstor.org/stable/44719293.

[49] V A Kulagin and A I Bokarev. Modern approaches of vehicle suspension durability evaluation at early stages of development. *IOP Conference Series: Materials Science and Engineering*, 941(1):012072, Dec 2020. doi: 10.1088/1757-899X/941/1/012072. URL https://dx.doi.org/10.1088/1757-899X/941/1/012072.

[50] Kuo. *Active Noise Control Systems: Algorithms and DSP Implementations*. Wiley, 1996.

[51] Sen M. Kuo and Dennis R. Morgan. Active noise control: a tutorial review. *Proceedings of the IEEE*, 87(6):943–973, 1999. ISSN 00189219. doi: 10.1109/5.763310.

[52] Justin David Langdon. Design and Adaptive Control of a Lab-based, Tire-coupled, Quarter-car Suspension Test Rig for the Accurate Re-creation of Vehicle Response. Master's thesis, Virginia Tech, 2007.

[53] R. Lopez-Valcarce and S. Dasgupta. On blind equalization of rank deficient nonlinear channels. In *Proceedings of the 11th IEEE Signal Processing Workshop on Statistical Signal Processing (Cat. No.01TH8563)*, pages 269–272, 2001. doi: 10.1109/SSP.2001.955274.

[54] Richard A. Lund. Method and apparatus for generating input signals in a physical system, apr 2006. URL http://patft.uspto.gov/netacgi/nph-Parser?patentnumber=7,031,949.

[55] F. Löcken and M. Welsch. The dynamic characteristic and hysteresis effect of an air spring. *International Journal of Applied Mechanics and Engineering*, 20(1):127–

145, 2015. doi: doi:10.1515/ijame-2015-0009. URL https://doi.org/10.1515/ijame-2015-0009.

[56] A. Maleki-Tehrani, B. Hassibi, and J.M. Cioffi. Adaptive equalization of multiple-input multiple-output (mimo) frequency selective channels. In *Conference Record of the Thirty-Third Asilomar Conference on Signals, Systems, and Computers (Cat. No.CH37020)*, volume 1, pages 547–551 vol.1, 1999. doi: 10.1109/ACSSC.1999.832390.

[57] Tetsuya Manabe and Fumio Miyazaki. Learning control based on local linearization by using DFT. *Journal of Robotic Systems*, 11(2):129–141, 1994. doi: https://doi.org/10.1002/rob.4620110206. URL https://onlinelibrary.wiley.com/doi/abs/10.1002/rob.4620110206.

[58] D. Maraun, J. Kurths, and M. Holschneider. Nonstationary gaussian processes in wavelet domain: Synthesis, estimation, and significance testing. *Phys. Rev. E*, 75: 016707, Jan 2007. doi: 10.1103/PhysRevE.75.016707. URL https://link.aps.org/doi/10.1103/PhysRevE.75.016707.

[59] Philip James Meymand. *Shaking table scale model tests of nonlinear soil-pile-superstructure interaction in soft clay*. University of California, Berkeley, 1998.

[60] L. Mianzo, D. Fricke, and R. Chabaan. Road profile control methods for laboratory vehicle road simulators. In *1998 IEEE AUTOTESTCON Proceedings. IEEE Systems Readiness Technology Conference. Test Technology for the 21st Century (Cat. No.98CH36179)*, pages 222–228, 1998. doi: 10.1109/AUTEST.1998.713448.

[61] Tino Müller and Christian Endisch. An estimation based iterative learning control approach for cross-coupled vehicle test systems. In *2017 IEEE International Conference on Advanced Intelligent Mechatronics (AIM)*, pages 1375–1381, 2017. doi: 10.1109/AIM.2017.8014210.

[62] P.A. Nelson and S.J. Elliott. *Active control of sound*. Academic Press, August 1991. URL https://eprints.soton.ac.uk/354428/.

[63] *Model 130D20 ICP Electret array microphone with integral preamplifier, 45mV/Pa, BNC connector. Installation and Operatic manual*. PCB piezotronics, 10 2023. URL https://www.pcb.com/contentstore/docs/PCB_Corporate/Vibration/products/Manuals/130D20.pdf.

[64] *Model 482A22 4 channel, line-powered ICP Sensor signal conditioner, unity gain, BNC. Installation and Operatic manual*. PCB piezotronics, 10 2023. URL https://www.pcb.com/contentstore/docs/PCB_Corporate/Electronics/products/Manuals/482A22.pdf.

[65] Bart Peeters, Wim Hendricx, Jan Debille, and Hé Climent. Modern Solutions for Ground Vibration Testing of Large Aircraft. *Sound and Vibration*, 43(1):8–15,6, 01 2009. URL https://www.proquest.com/trade-journals/modern-solutions-ground-vibration-testing-large/docview/194545624/se-2.

[66] Rik Pintelon and Johan Schoukens. *System identification: a frequency domain approach*. John Wiley & Sons, 2012.

[67] Andrew R Plummer. Control techniques for structural testing: a review. *Proceedings of the Institution of Mechanical Engineers, Part I: Journal of Systems and Control Engineering*, 221(2):139–169, 2007.

[68] A.D. Raath and C.C.Van Waveren. A time domain approach to load reconstruction for durability testing. *Engineering Failure Analysis*, 5(2):113–119, 1998. ISSN 1350-6307. doi: https://doi.org/10.1016/S1350-6307(98)00008-9. URL https://www.sciencedirect.com/science/article/pii/S1350630798000089.

[69] Kevin Reichel and Martin Meywerk. Acceleration signal simulation induced by single obstacle crossings by means of nonlinear, block-oriented models for an automotive comfort simulator. *Proceedings of the Institution of Mechanical Engineers, Part D: Journal of Automobile Engineering*, 0(0), 2022. doi: 10.1177/09544070221124716. URL https://doi.org/10.1177/09544070221124716.

[70] Jörnsen Reimpell, Helmut Stoll, and Jürgen W. Betzler. Springing. In *The Automotive Chassis*, pages 307–385, Oxford, UK, 2001. Butterworth-Heinemann. ISBN 978-0-7506-5054-0. doi: https://doi.org/10.1016/B978-075065054-0/50005-5. URL https://www.sciencedirect.com/science/article/pii/B9780750650540500055.

[71] Brian P. Rigney, Lucy Y. Pao, and Dale A. Lawrence. Nonminimum phase dynamic inversion for settle time applications. *IEEE Transactions on Control Systems Technology*, 17(5):989–1005, 2009. doi: 10.1109/TCST.2008.2002035.

[72] D.E. Roberts and N.C. Hay. Dynamic response simulation for a nonlinear system. *Journal of Sound and Vibration*, 281(3):783–798, 2005. ISSN 0022-460X. doi: https://doi.org/10.1016/j.jsv.2004.02.016. URL https://www.sciencedirect.com/science/article/pii/S0022460X04001725.

[73] Gary Savage. Six- and 12-axis servo-hydraulic actuators were developed for durability testing of suspensions for Honda Racing Formula 1 cars. *Advanced Materials & Processes, Volume 165, Issue 5, May 2007 (ASM International)*, pages 35–37, 2007. URL https://www.asminternational.org/en/news/magazines/am-p/-/journal_content/56/10192/AMP16505P035/PERIODICAL-ARTICLE.

[74] Maarten Schoukens and Koen Tiels. Identification of block-oriented nonlinear systems starting from linear approximations: A survey. *Automatica*, 85:272–292, 2017. ISSN

0005-1098. doi: https://doi.org/10.1016/j.automatica.2017.06.044. URL https://www.sciencedirect.com/science/article/pii/S0005109817303990.

[75] Walter Schütz. A history of fatigue. *Engineering Fracture Mechanics*, 54(2):263–300, 1996. ISSN 0013-7944. doi: https://doi.org/10.1016/0013-7944(95)00178-6. URL https://www.sciencedirect.com/science/article/pii/0013794495001786.

[76] G Shen, S T Zheng, Z M Ye, Z D Yang, Y Zhao, and J W Han. Tracking control of an electro-hydraulic shaking table system using a combined feedforward inverse model and adaptive inverse control for real-time testing. *Proceedings of the Institution of Mechanical Engineers, Part I: Journal of Systems and Control Engineering*, 225(5): 647–666, 2011. doi: 10.1177/2041304110394529. URL https://doi.org/10.1177/2041304110394529.

[77] Gang Shen, Shu-Tao Zheng, Zheng-Mao Ye, Qi-Tao Huang, Da-Cheng Cong, and Jun-Wei Han. Adaptive inverse control of time waveform replication for electrohydraulic shaking table. *Journal of Vibration and Control*, 17(11):1611–1633, 2011.

[78] Gang Shen, Zhencai Zhu, Xiang Li, Ge Li, Yu Tang, and Shanzeng Liu. Experimental evaluation of acceleration waveform replication on electrohydraulic shaking tables: A review. *International Journal of Advanced Robotic Systems*, 13(5): 1729881416662537, 2016. doi: 10.1177/1729881416662537. URL https://doi.org/10.1177/1729881416662537.

[79] Sigurd Skogestad and Ian Postlethwaite. *Multivariable feedback control: analysis and design*. john Wiley & sons, 2005.

[80] Suzanne W. Smith, Charles S. Pack, and Theodore J. Bartkowicz. *Understanding Dynamic Challenges of In-Space Modular Assembly and Reconfiguration of Flexible*

Structures from Early Efforts. 2021. doi: 10.2514/6.2022-2374. URL https://arc.aiaa.org/doi/abs/10.2514/6.2022-2374.

[81] Steve Soderling, Malcolm Sharp, and Christoph Leser. Servo controller compensation methods selection of the correct technique for test applications. 1999.

[82] Steve C Southward and Christopher M Boggs. Comparison of the Performance of 7-Post and 8-Post Dynamic Shaker Rigs for Vehicle Dynamics Studies. *SAE International Journal of Passenger Cars-Mechanical Systems*, 1(2008-01-2966):1319–1324, 2008.

[83] Lucas D. Staab, James P. Winkel, Vicente J. Suárez, Trevor M. Jones, and Kevin L. Napolitano. Fixed Base Modal Testing Using the NASA GRC Mechanical Vibration Facility. In Evro Wee Sit, editor, *Sensors and Instrumentation, Volume 5*, pages 143–161. Springer International Publishing, 2016. ISBN 978-3-319-29859-7.

[84] J. Stoppel and M. Degener. Investigations of Helicopter Structural Dynamics and a Comparison with Ground Vibration Tests. *Journal of the American Helicopter Society*, 27(2):34–42, 1982. ISSN 2161-6027. doi: 10.4050/JAHS.27.34. URL https://www.ingentaconnect.com/content/ahs/jahs/1982/00000027/00000002/art00005.

[85] DP Stoten and H Benchoubane. Empirical studies of an mrac algorithm with minimal controller synthesis. *International Journal of Control*, 51(4):823–849, 1990.

[86] Donald A Streit, BT Kulakowski, PE Sebaaly, and RJ Wollyung. Road simulator study of heavy-vehicle wheel forces. Technical Report FHWA-RD-98-019, 1998.

[87] MTS Systems. Model 329 Spindle-Coupled Road Simulators, . URL https://www.mts.com/en/products/automotive/full-vehicle-test-systems/model-329-spindle-coupled-road-simulator#technical.

[88] MTS Systems. Kinematic & Compliance (K&C) Deflection Measurement Systems, . URL https://www.mts.com/en/products/automotive/full-vehicle-test-systems/kinematic-compliance-systems#technical.

[89] MTS Systems. Model 320 Tire-coupled Road Simulators, . URL https://www.mts.com/en/products/automotive/full-vehicle-test-systems/model-320-tire-coupled-road-simulator.

[90] MTS Systems. Multi-Axial Simulation Table (MAST) Systems, 2021. URL https://www.mts.com/en/products/automotive/subsystem-component-test-systems/multi-axial-simulation-table-systems#technical.

[91] Yu Tang, Gang Shen, Zhen-Cai Zhu, Xiang Li, and Chi-Fu Yang. Time waveform replication for electro-hydraulic shaking table incorporating off-line iterative learning control and modified internal model control. *Proceedings of the Institution of Mechanical Engineers, Part I: Journal of Systems and Control Engineering*, 228(9): 722–733, 2014. doi: 10.1177/0959651814536553. URL https://doi.org/10.1177/0959651814536553.

[92] Yu Tang, Zhencai Zhu, and Gang Shen. Design and experimental evaluation of feedforward controller integrating filtered-x lms algorithm with applications to electro-hydraulic force control systems. *Proceedings of the Institution of Mechanical Engineers, Part C: Journal of Mechanical Engineering Science*, 230(12):1951–1967, 2016. doi: 10.1177/0954406215584810. URL https://doi.org/10.1177/0954406215584810.

[93] Technical Committee ISO/TC 108/SC 2 Measurement and evaluation of mechanical vibration and shock as applied to machines vehicles and structures. Mechanical vibration - Road surface profiles - Reporting of measured data. Technical report,

International Organization for Standardization, Geneva, Switzerland, 2016. URL https://www.iso.org/standard/71202.html.

[94] Brad Thoen. Optimum Sample Rate for Servohydraulic systems. URL https://www.mts.com/en/articles/automotive/optimum-sample-rate.

[95] Masayoshi Tomizuka. Zero Phase Error Tracking Algorithm for Digital Control. *Journal of Dynamic Systems, Measurement, and Control*, 109(1):65–68, 03 1987. ISSN 0022-0434. doi: 10.1115/1.3143822. URL https://doi.org/10.1115/1.3143822.

[96] Toyota Higashifuji Technical Center. Driving Simulator - Toyota Motor Corporation Official Global Website, 2016. URL https://global.toyota/en/download/14221137.

[97] J.K. Tugnait. Fir inverses to mimo rational transfer functions with application to blind equalization. In *Conference Record of The Thirtieth Asilomar Conference on Signals, Systems and Computers*, volume 1, pages 295–299 vol.1, 1996. doi: 10.1109/ACSSC.1996.600876.

[98] Y Uchiyama, M Mukai, and M Fujita. Robust control of electrodynamic shaker with 2dof control using H_∞ filter. *Journal of Sound and Vibration*, 326(1-2):75–87, 2009.

[99] Marcos A Underwood and Tony Keller. Recent system developments for multi-actuator vibration control. *Sound and Vibration*, 35(10):16–23, 2001.

[100] Pieter Van den Braembussche. *Robust motion control of high-performance machine tools with linear motors.* PhD thesis, Katholieke Universiteit Leuven, Department of Mechanical Engineering, 1999.

[101] Michel Verhaegen. Identification of the deterministic part of mimo state space models given in innovations form from input-output data. *Automatica*, 30(1):61–74, 1994.

[102] David Vetturi and Andrea Magalini. Road profile excitation on a vehicle measurement and indoor testing using a four-post rig. *Dipartimento di Ingengeria Meccanica–Universita degli Studi di Brescia*, 2002.

[103] Mathukumalli Vidyasagar. *Nonlinear systems analysis*. SIAM, 2002.

[104] Paul Weal, Christophe Liefooghe, and Klaus Dressler. Product durability engineering: Improving the process. *SV Sound and vibration*, 31(1):68–79, 1997.

[105] Bernard Widrow and Samuel D Stearns. *Adaptive Signal Processing*. Prentice Hall, Upper Saddle River, NJ, USA, 1985. ISBN 0-13-004029-0.

[106] Bernard Widrow and Eugene Walach. *Adaptive Inverse Control*. Prentice Hall, Upper Saddle River, N.J., 1996. ISBN 9780130059680.

[107] Bernard Widrow and Eugene Walach. *Adaptive inverse control: a signal processing approach*. John Wiley & Sons, 2008.

[108] Zhifei WU, Yuxia Xiang, and Chenggui Liu. Influence of suspension hysteresis characteristics on vehicle vibration performance. *Proceedings of the Institution of Mechanical Engineers, Part D: Journal of Automobile Engineering*, 235(5):1211–1224, 2021. doi: 10.1177/0954407020970839. URL https://doi.org/10.1177/0954407020970839.

Appendices

Appendix A

Simulation test bench identification results

A.1 Inverse model identification using the frequency domain ZMETC method

This section presents a compilation of the results of the frequency domain based ZMETC inverse model identification for all four dynamic plants under consideration in this thesis. The pole-zero maps of the identified frequency domain forward model which contains NMP zeroes and the stabilized inverse model are presented as was provided for the purely linear plant in the main text in Figure 3.9. Additionally, the identified inverse model is used to derive an initial estimate of the drive file considering the target response shown in Figure 3.4a and the simulated plant response is presented here for all four dynamic plants considered which were listed in Table 3.4.

A.1.1 Purely linear plant

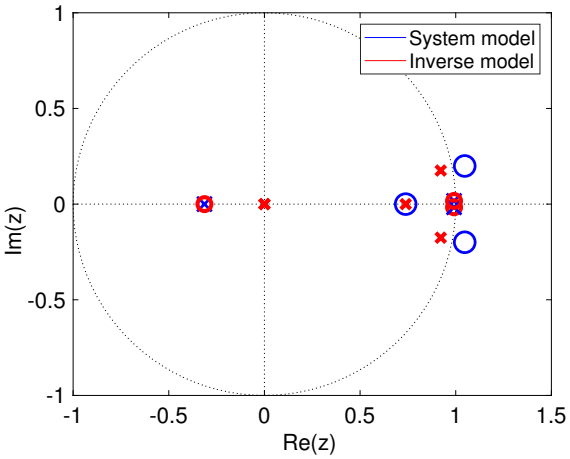

(a) Pole-Zero map for the system model and identified inverse model for the purely linear plant

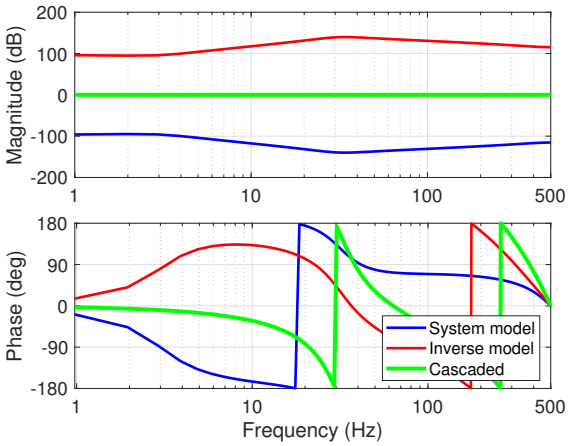

(b) Bode plot for the system model, identified inverse model and the cascaded models for the purely linear plant

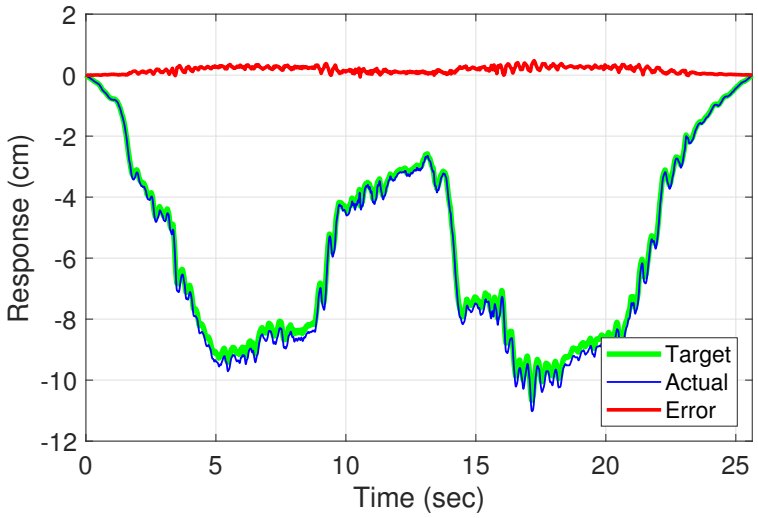

(c) Output response obtained from the initial estimate of the derived drive file based on the ZMETC inverse model

Figure A.1: Frequency domain based identification of the inverse model for the purely linear plant

A.1.2 Piece-wise linear plant

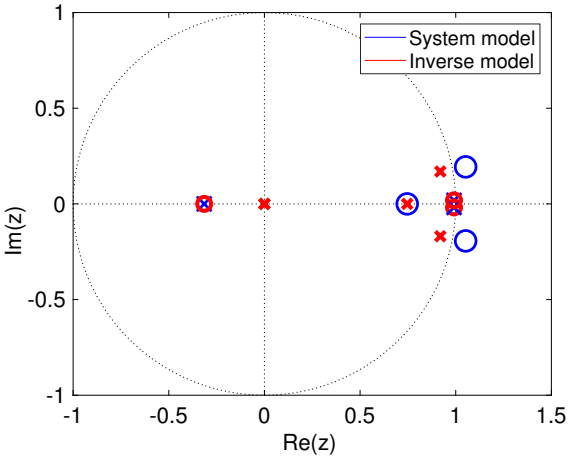

(a) Pole-Zero map for the system model and identified inverse model for the piece-wise linear plant

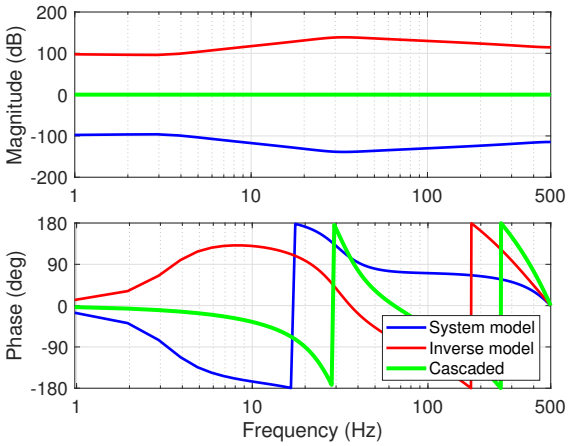

(b) Bode plot for the system model, identified inverse model and the cascaded models for the piece-wise linear plant

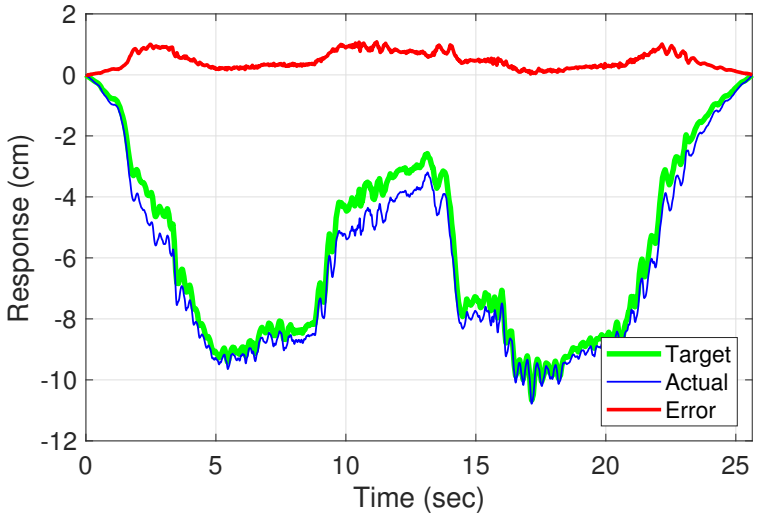

(c) Output response obtained from the initial estimate of the derived drive file based on the ZMETC inverse model

Figure A.2: Frequency domain based identification of the inverse model for the piece-wise linear plant

A.1.3 Mild cubic nonlinear plant

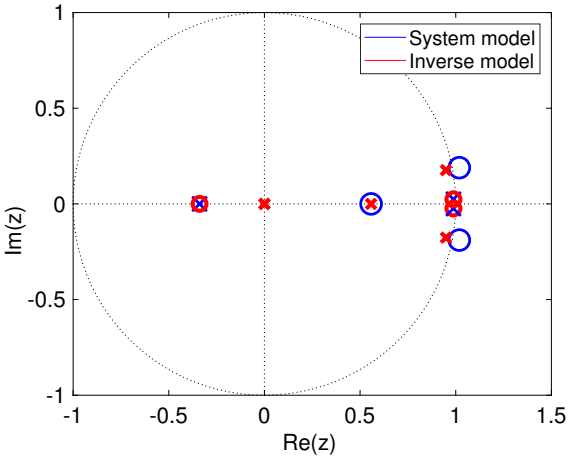

(a) Pole-Zero map for the system model and identified inverse model for the mild cubic nonlinear plant

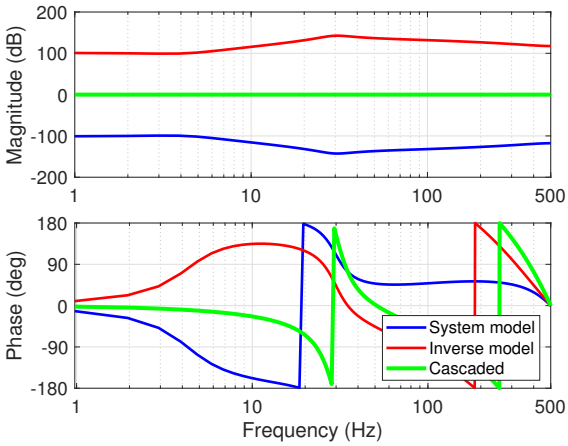

(b) Bode plot for the system model, identified inverse model and the cascaded models for the mild cubic nonlinear plant

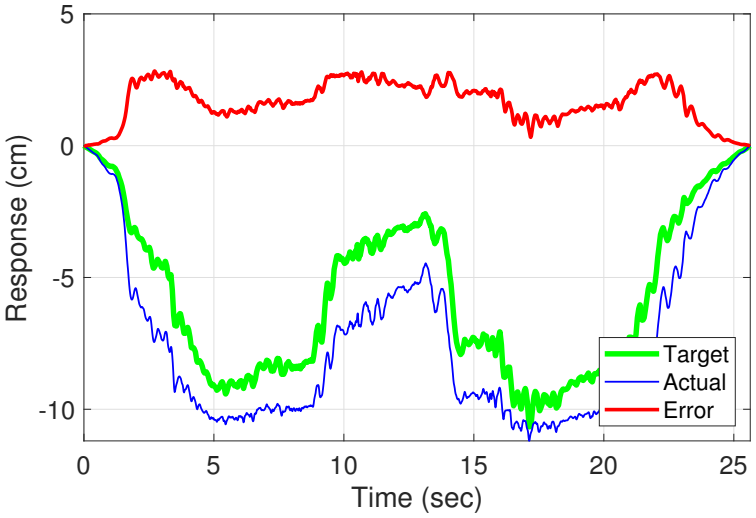

(c) Output response obtained from the initial estimate of the derived drive file based on the ZMETC inverse model

Figure A.3: Frequency domain based identification of the inverse model for the mild cubic nonlinear plant

A.1.4 Harsh cubic nonlinear plant

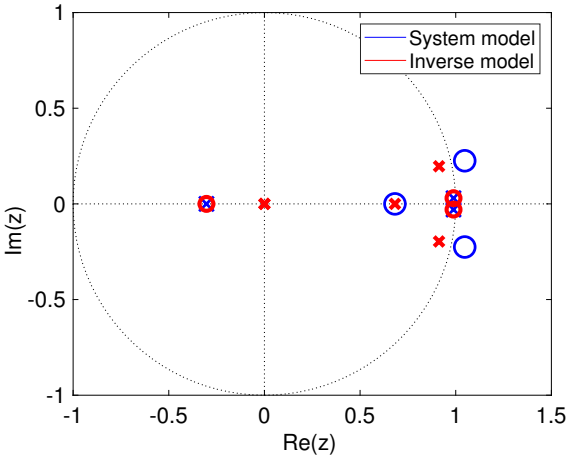

(a) Pole-Zero map for the system model and identified inverse model for the harsh cubic nonlinear plant

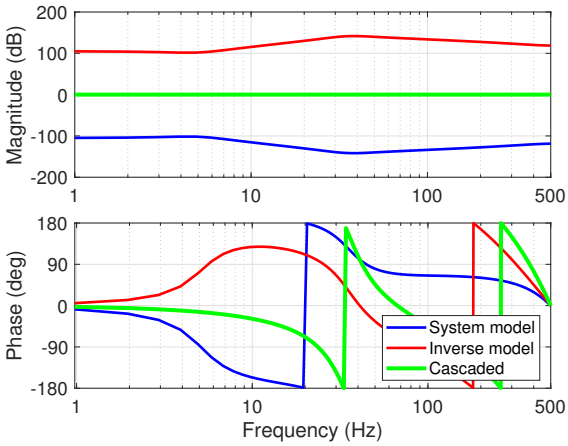

(b) Bode plot for the system model, identified inverse model and the cascaded models for the harsh cubic nonlinear plant

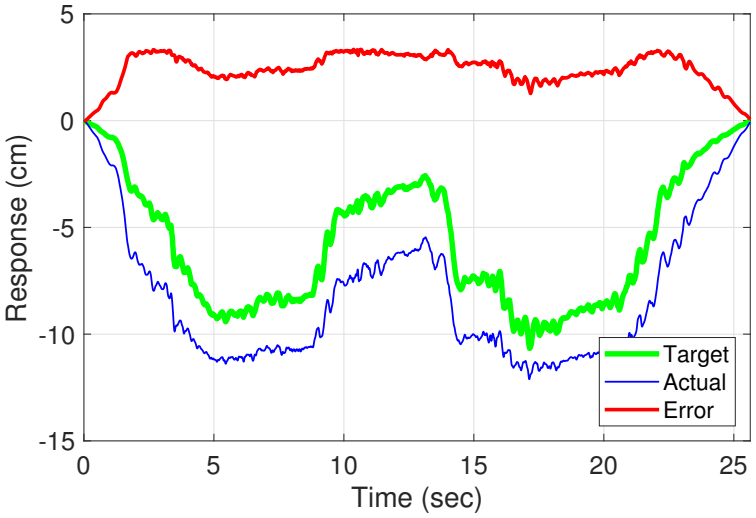

(c) Output response obtained from the initial estimate of the derived drive file based on the ZMETC inverse model

Figure A.4: Frequency domain based identification of the inverse model for the harsh cubic nonlinear plant

A.2 Inverse model identification using the Filtered-x LMS method

This section presents a compilation of the results of the Filtered-x LMS based adaptive inverse model identification for all four dynamic plants under consideration in this thesis. The identified FIR filters for the delayed inverse models are presented, which is consequently used to derive an initial estimate of the drive file considering the target response shown in Figure 3.4a and the simulated plant response is presented here for all four dynamic plants considered, the results of which were listed in Table 3.5.

A.2.1 Purely linear plant

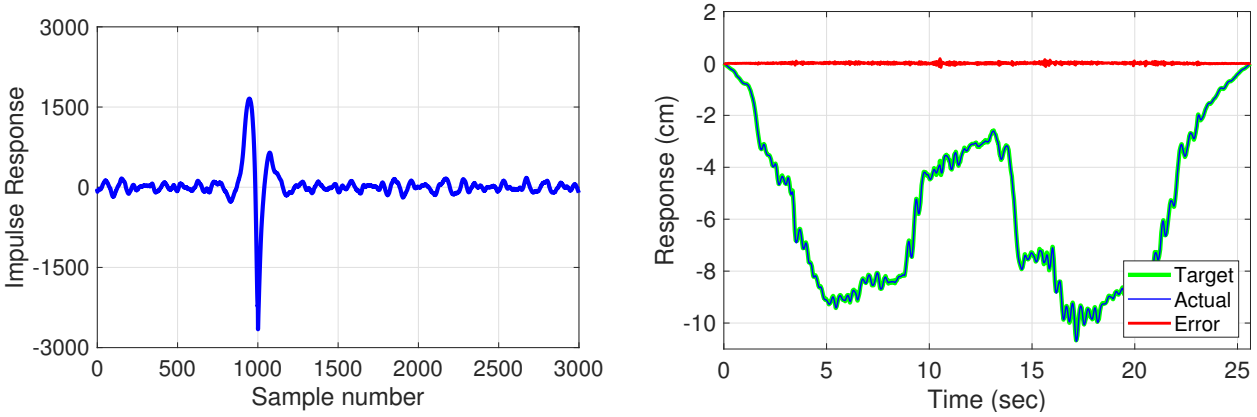

(a) FIR filter of the delayed inverse model for the purely linear plant, $L_{inv} = 3000$, $\Delta = 1000$

(b) Output response obtained from the initial estimate of the derived drive file based on the Filtered-x LMS adaptive inverse model

Figure A.5: Filtered-x LMS based identification of the delayed inverse model for the purely linear plant

A.2.2 Piece-wise linear plant

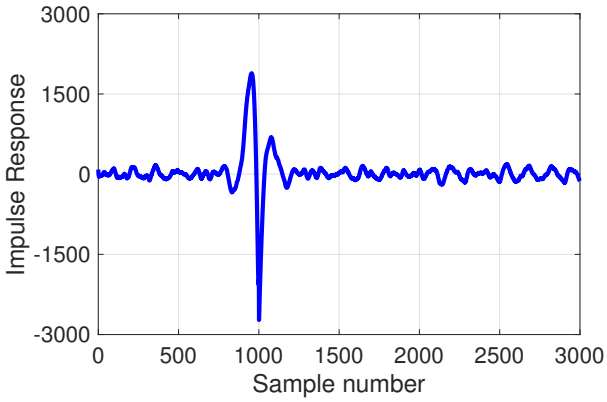

(a) FIR filter of the delayed inverse model for the piece-wise linear plant, $L_{inv} = 3000$, $\Delta = 1000$

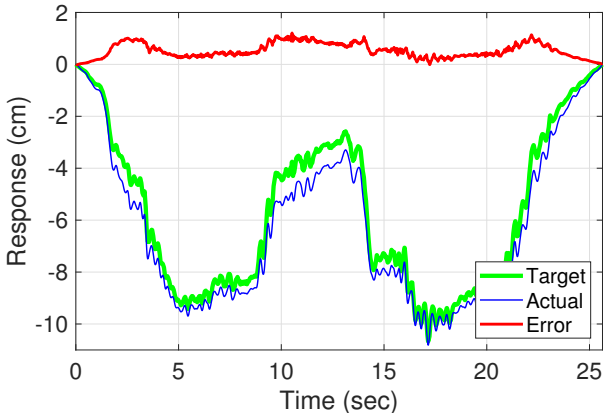

(b) Output response obtained from the initial estimate of the derived drive file based on the Filtered-x LMS adaptive inverse model

Figure A.6: Filtered-x LMS based identification of the delayed inverse model for the piece-wise linear plant

A.2.3 Mild cubic nonlinear plant

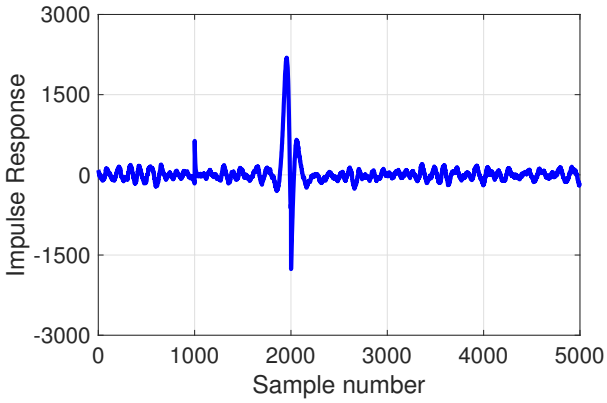

(a) FIR filter of the delayed inverse model for the mild cubic nonlinear plant, $L_{inv} = 5000$, $\Delta = 2000$

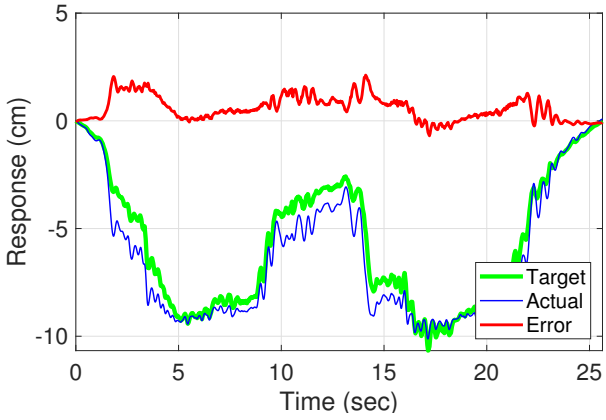

(b) Output response obtained from the initial estimate of the derived drive file based on the Filtered-x LMS adaptive inverse model

Figure A.7: Filtered-x LMS based identification of the delayed inverse model for the mild cubic nonlinear plant

A.2.4 Harsh cubic nonlinear plant

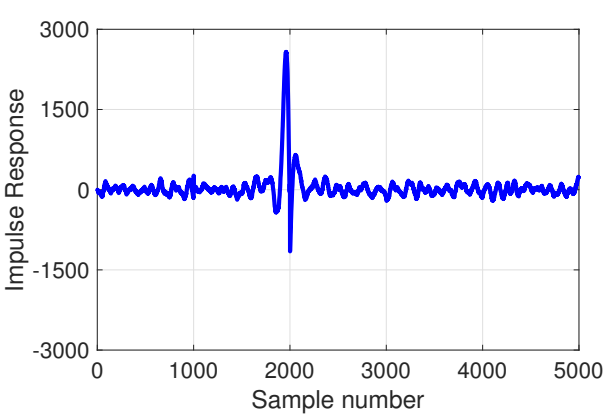

(a) FIR filter of the delayed inverse model for the harsh cubic nonlinear plant, $L_{inv} = 5000$, $\Delta = 2000$

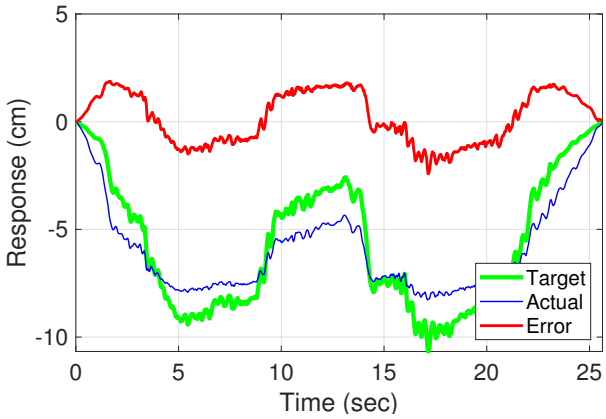

(b) Output response obtained from the initial estimate of the derived drive file based on the Filtered-x LMS adaptive inverse model

Figure A.8: Filtered-x LMS based identification of the delayed inverse model for the harsh cubic nonlinear plant

Appendix B

Performance evaluation case studies for the PT-Fx-LMS algorithm

B.1 Case Study 1: Drive files initialized at zero

This section presents a compilation of the results for the simulation Case study 1 presented in section 4.4.1 for the different test benches using the three DFID methods presented: (1) the conventional frequency-domain ILC method which uses the inverse plant model using the ZMETC method, (2) the conventional time-domain ILC method using the delayed FIR inverse models and, (3) the proposed PT-Fx-LMS method for DFID. These plots additionally show the time series final drive files, the final response errors obtained from the simulated test benches using the above-mentioned DFID methods and the final actuator force (the drive files) PSD for all the test benches as previously shown in Figure 4.8 for the mild cubic nonlinear plant.

B.1.1 Purely linear plant

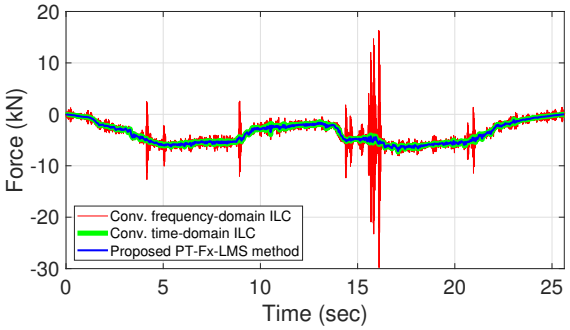

(a) Time series of the final drive file

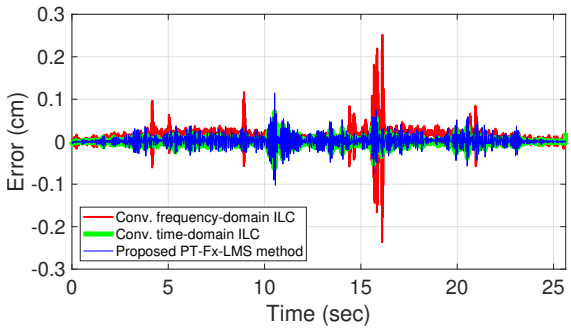

(b) Time series of the final output error

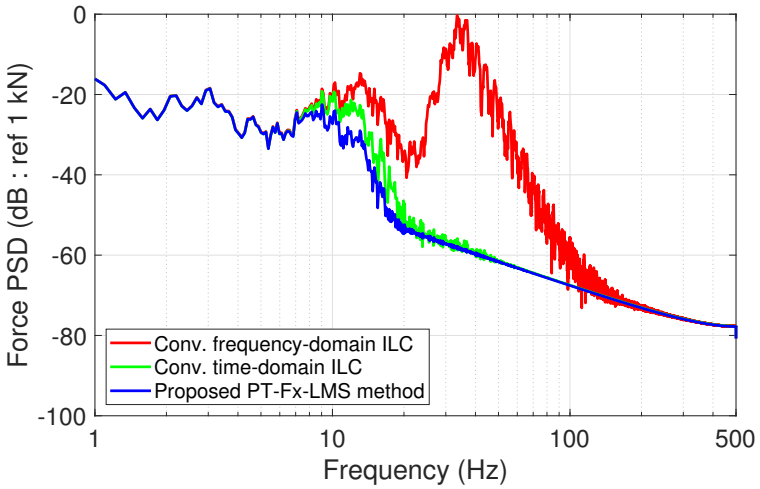

(c) PSD of the final drive file for Case Study 1

Figure B.1: Additional plots for the Case Study 1 simulation for the purely linear model test bench

B.1.2 Piece-wise linear plant

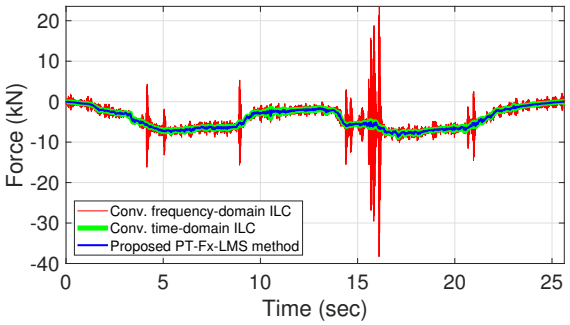

(a) Time series of the final drive file

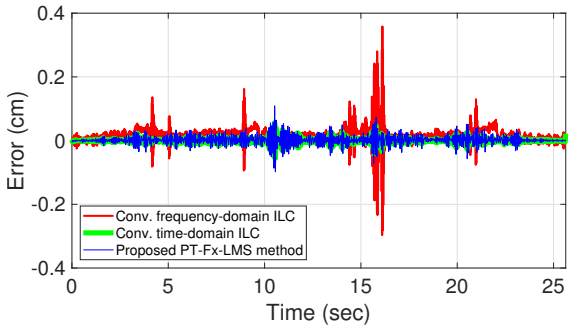

(b) Time series of the final output error

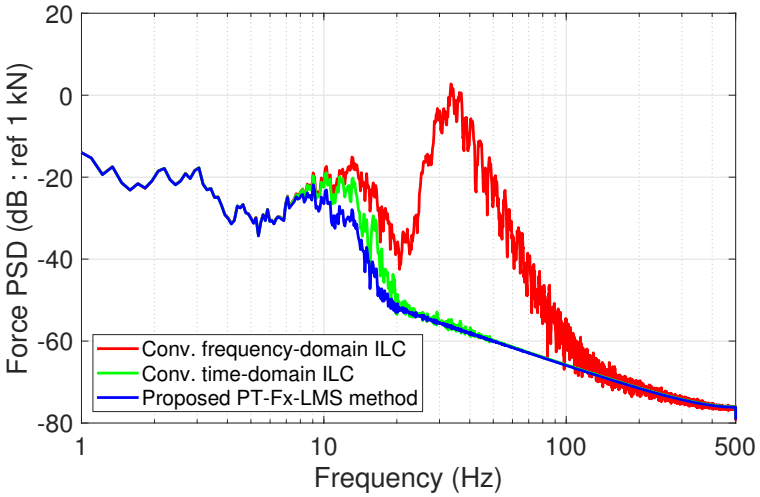

(c) PSD of the final drive file for Case Study 1

Figure B.2: Additional plots for the Case Study 1 simulation for the piece-wise linear model test bench

B.1.3 Mild cubic nonlinear plant

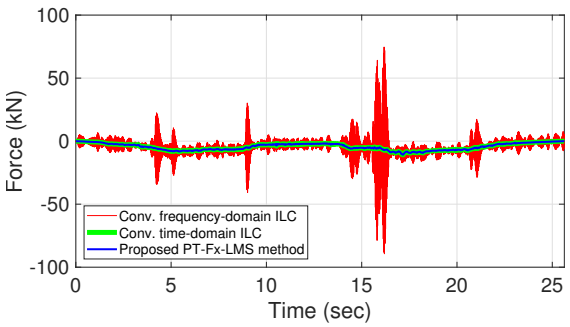

(a) Time series of the final drive file

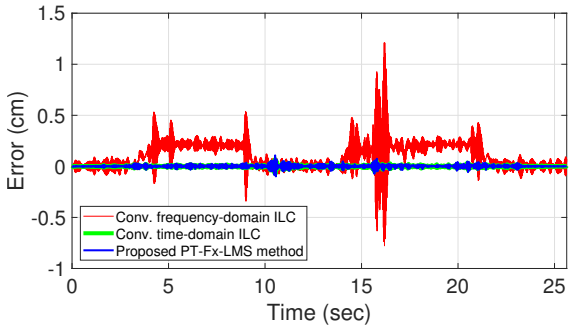

(b) Time series of the final output error

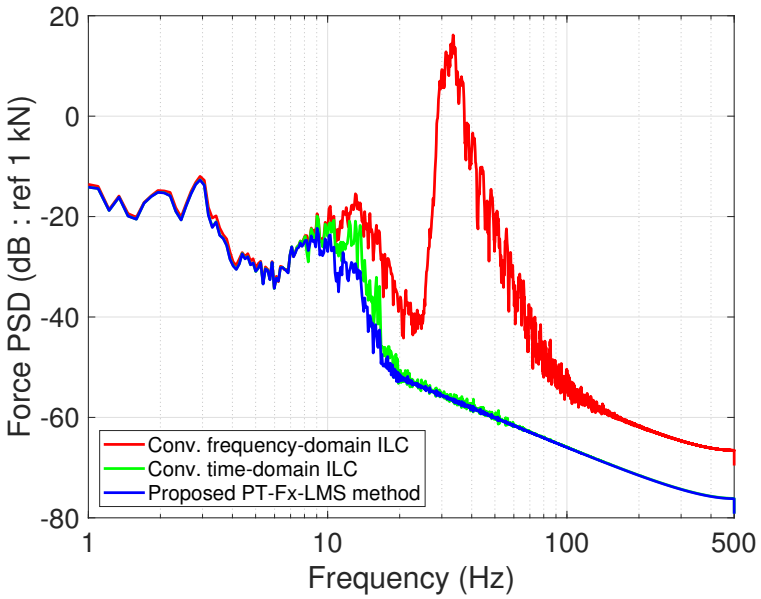

(c) PSD of the final drive file for Case Study 1

Figure B.3: Additional plots for the Case Study 1 simulation for the mild cubic nonlinear model test bench

B.1.4 Harsh cubic nonlinear plant

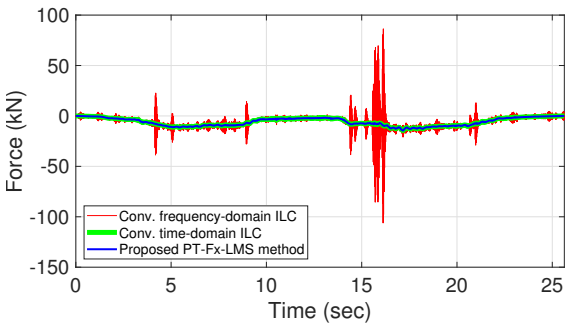

(a) Time series of the final drive file

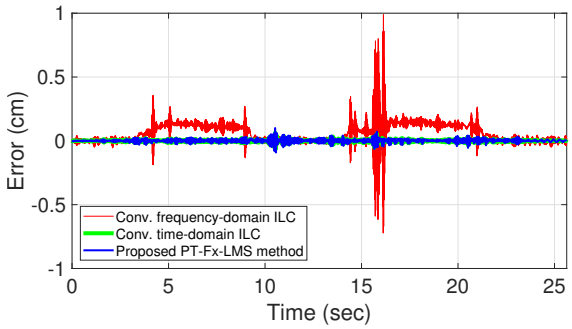

(b) Time series of the final output error

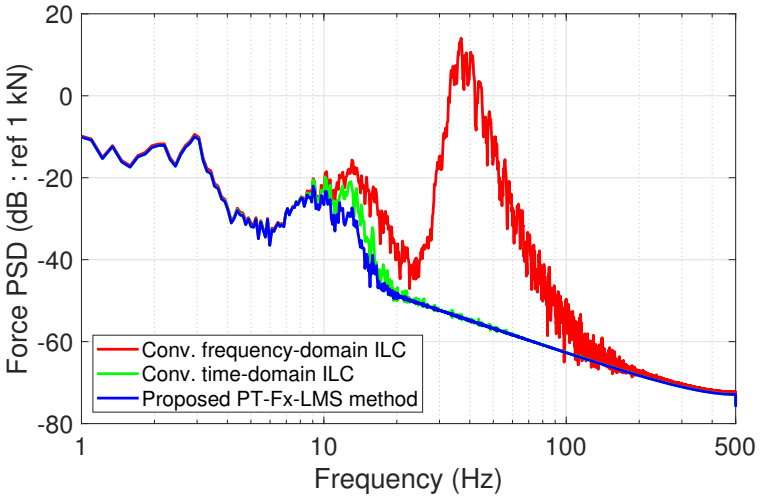

(c) PSD of the final drive file for Case Study 1

Figure B.4: Additional plots for the Case Study 1 simulation for the harsh cubic nonlinear model test bench

Appendix C

MIMO Simulation test bench details

C.1 Plant dynamics and case studies

This section presents a compilation of additional characteristics of the plant dynamics and results of the DFID methods considered in this thesis.

C.1.1 Case Study 1: MIMO 2×2 dynamic system

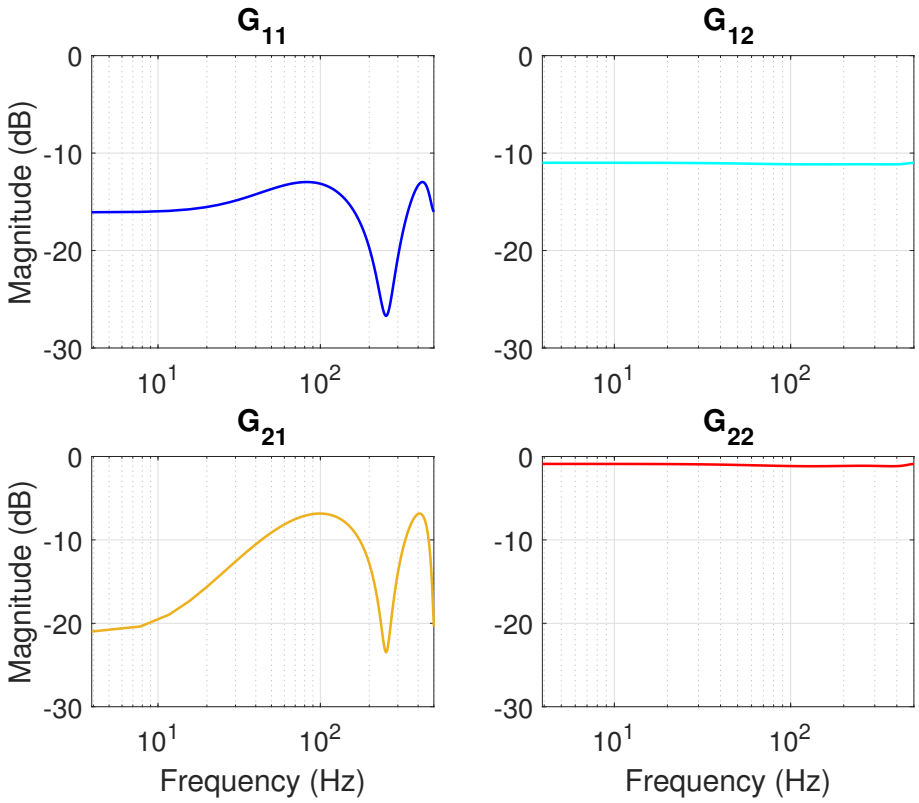

Figure C.1: Frequency response function of the considered 2×2 dynamic plant model, illustrating the difference in the magnitude of the plant dynamics along each path.

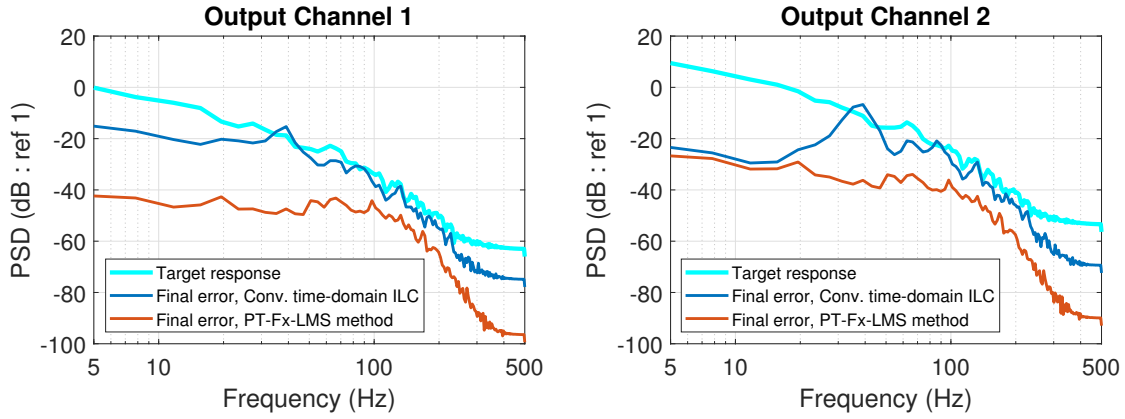

Figure C.2: Spectral comparison of the target response and final response errors using the two considered DFID methods for the MIMO 2×2 dynamic system

C.1.2 Case Study 2: MIMO 3×2 quarter-car dynamic system

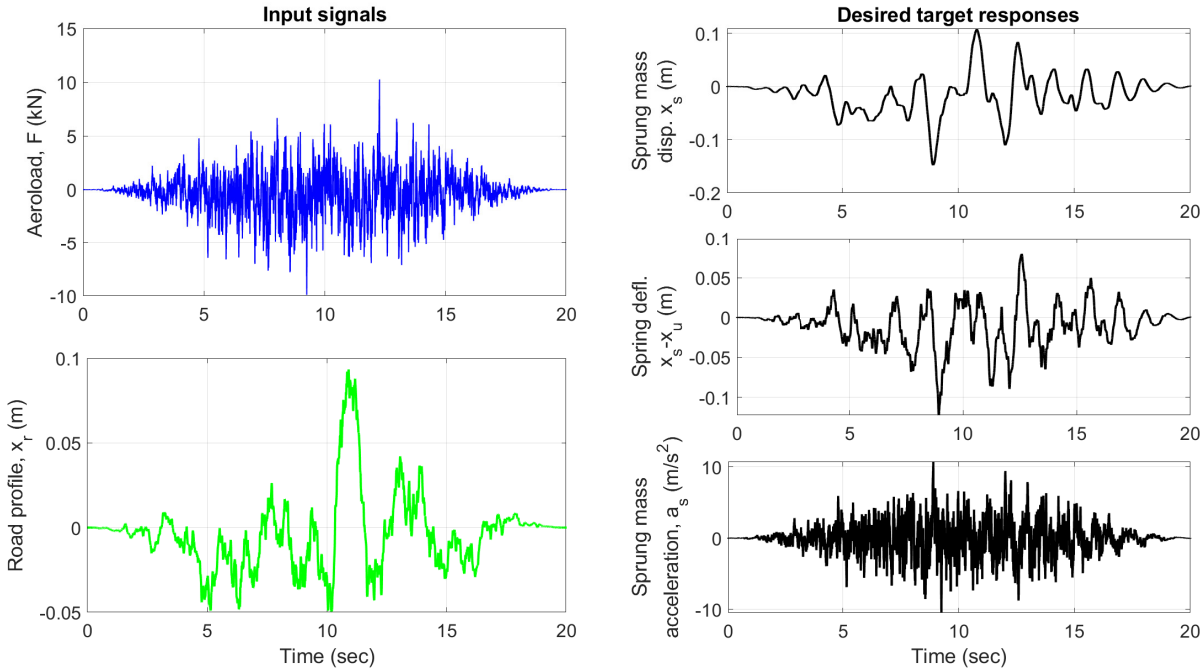

Figure C.3: Time history of the designed ground truth input signals and target output responses for the 3×2 quarter-car system.

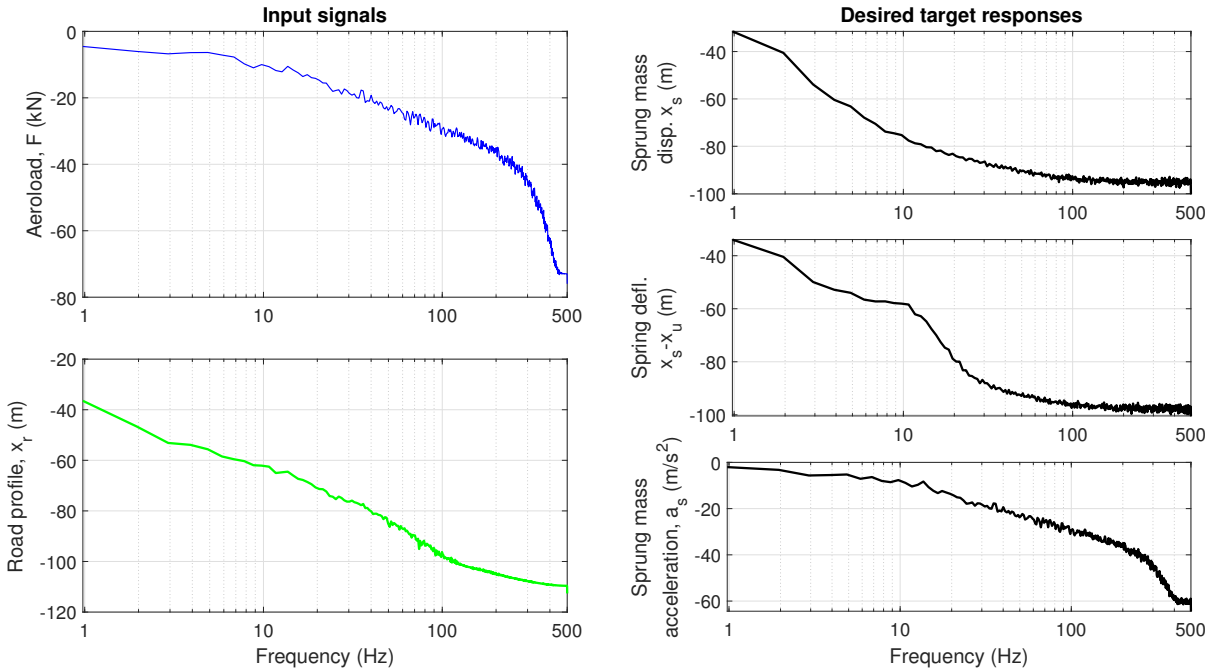

Figure C.4: Spectrum of the designed ground truth input signals and target output responses for the 3×2 quarter-car system.

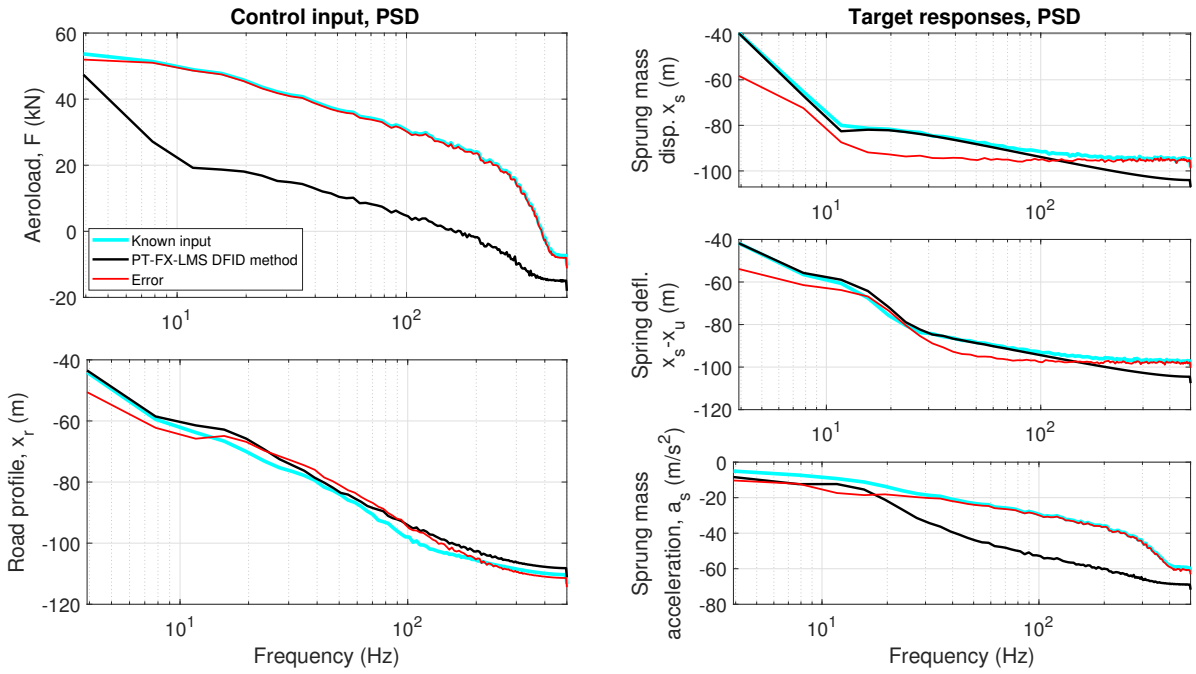

Figure C.5: Spectrum of the input and output signals for the 3×2 quarter-car system at the end of the 200 batch iterations of the PT-Fx-LMS method for DFID.

C.2 Eigen Realization Algorithm implementation

Please refer to Juang and Pappa for more formulation details. This section only describes the implementation for this thesis study.

For the discrete-time state space formulation, with states $x \in \mathbb{R}^P$, inputs $u \in \mathbb{R}^M$ and outputs $y \in \mathbb{R}^N$,

$$\mathbf{x}_{k+1} = \mathbf{A}\mathbf{x}_k + \mathbf{B}\mathbf{u}_k \tag{C.1}$$

$$\mathbf{y}_k = \mathbf{C}\mathbf{x}_k + \mathbf{D}\mathbf{u}_k \tag{C.2}$$

For the impulse response of the system

$$u_i(0) = 1 \; \forall i = 1, \cdots, m \tag{C.3}$$

$$u_i(k) = 0 \; \forall k > 0, i = 1, \cdots, m \tag{C.4}$$

The Markov parameters $Y \in \mathbb{R}^{N \times M}$ of the Pulse response matrix is given by:

$$\begin{aligned} Y_0 &= D \\ Y_1 &= CB \\ Y_2 &= CAB \\ &\vdots \\ Y_k &= CA^{k-1}B \end{aligned} \tag{C.5}$$

The objective of the realization is the computation of the A, B, C matrices from the Markov parameters. The minimum realization with the smallest state-space dimension among all realizable systems is desired. The system realization begins with the construction of the

Hankel matrix from the Markov parameters

$$H(k-1) = \begin{bmatrix} Y_k & Y_{k+1} & \cdots & Y_{k+\beta-1} \\ Y_{k+1} & Y_{k+2} & \cdots & Y_{k+\beta} \\ \vdots & \vdots & \ddots & \vdots \\ Y_{k+\alpha-1} & Y_{k+\alpha} & \cdots & Y_{k+\alpha+\beta-2} \end{bmatrix} \tag{C.6}$$

If $\alpha \geq P, \beta \geq P$

$$H(k-1) = P_\alpha A^{k-1} Q_\beta \tag{C.7}$$

where the observability matrix P_α and controllability matrix Q_β are given as

$$P_\alpha = \begin{bmatrix} C \\ CA \\ CA^2 \\ \vdots \\ CA^{\alpha-1} \end{bmatrix} \quad Q_\beta = \begin{bmatrix} B & AB & A^2B \cdots A^{\beta-1}B \end{bmatrix} \tag{C.8}$$

For an observable and controllable system, the rank of the P_α and Q_β matrices are P and the minimum dimension of the state matrix is $P \times P$ and hence the rank of the $H(k-1)$ matrix is also P if $\alpha \geq P, \beta \geq P$.

Assuming that $H^\dagger$ exists satisfying

$$Q_\beta H^\dagger P_\alpha = I_P \tag{C.9}$$

$$H(0)H^\dagger H(0) = P_\alpha Q_\beta H^\dagger P_\alpha Q_\beta = P_\alpha Q_\beta = H(0) \tag{C.10}$$

Hence, $H^{\dagger}$ is the pseudo-inverse of $H(0)$.

To derive the shifted Generalized Hankel matrix $H(1)$, first perform a singular value decomposition of the $H(0)$ Hankel matrix.

$$H(0) = R\Sigma S^T = P_\alpha Q_\beta \tag{C.11}$$

where columns of R and S are orthonormal and Σ is the rectangular matrix:

$$\Sigma = \begin{bmatrix} \Sigma_P & 0 \\ 0 & 0 \end{bmatrix} \tag{C.12}$$

$\Sigma_P = diag(\sigma_1, \sigma_2, \cdots, \sigma_P)$ is the diagonal matrix of monotonically increasing singular values. Let R_P and S_P be the matrices formed by the first P-columns of R and S respectively.

$$H(0) = R_P \Sigma_P S_P^T, \quad R_P^T R = I_P = S_P^T S_P \tag{C.13}$$

Since, $H^{\dagger}$ is the pseudo-inverse of $H(0)$.

$$H^{\dagger} = (S_P \Sigma_P^{-1} R_P^T R_P \Sigma_P S_P^T)^{-1} (S_P \Sigma_P^{-1} R_P^T) = S_P \Sigma_P^{-1} R_P^T \tag{C.14}$$

Model reduction can be achieved by setting tolerance on the singular values to reduce the dimension of P. The shifted Hankel matrix is hence given by

$$H(1) = P_\alpha A Q_\beta = R_P \Sigma_P^{1/2} A \Sigma_P^{1/2} S_P^T \tag{C.15}$$

The realized state matrix is hence given as a function of the Markov parameters as

$$\widehat{A} = \Sigma_P^{-1/2} R_P^T H(1) S_P \Sigma_P^{-1/2} \tag{C.16}$$

Define the pair of matrices E_N and E_M such that

$$E_N = \begin{bmatrix} I_N & \mathbf{0}_N \end{bmatrix}^T \in \mathbb{R}^{\alpha N \times N} \quad E_M = \begin{bmatrix} I_M & \mathbf{0}_M \end{bmatrix}^T \in \mathbb{R}^{\beta M \times M} \tag{C.17}$$

Since $Y_k = CA^{k-1}B$ and also $Y_k = E_N^T H(k-1) E_M$

$$\begin{aligned} Y_k &= E_N^T P_\alpha A^{k-1} Q_\beta E_M \\ &= E_N^T P_\alpha [Q_\beta H^\dagger P_\alpha] A^{k-1} [Q_\beta H^\dagger P_\alpha] Q_\beta E_M \\ &= E_N^T H(0) [S_P \Sigma_P^{-1} R_P^T R_P] P_\alpha A^{k-1} Q_\beta [S_P \Sigma_P^{-1} R_P^T R_P] H(0) E_M \end{aligned} \tag{C.18}$$

With the choice of $P_\alpha = R_P \Sigma_P^{1/2}$ and $Q_\beta = \Sigma_P^{1/2} S_P^T$ and simplifying Equation C.18

$$Y_k = (E_N^T R_P \Sigma_P^{1/2}) A^{k-1} (\Sigma_P^{1/2} S_P^T E_M) \tag{C.19}$$

Comparing with Equation C.5,

$$\widehat{B} = \Sigma_P^{1/2} S_P^T E_M \tag{C.20}$$

$$\widehat{C} = E_N^T R_P \Sigma_P^{1/2} \tag{C.21}$$

This hence completes the algorithm to derive the minimal state-space realization with $\widehat{A}, \widehat{B}, \widehat{C}$ matrices using the ERA.

Appendix D

Additional Experimental validation resources

D.1 System identification procedure for the MIMO experimental setup

The time history and spectrums of the identification drive and the measured mic data are given in Figure D.1. Note that for a 2×2 MIMO system, two separate identification runs are required where only one of the speakers are played during each test. During each of these runs, the microphone signal from both the sensors are simultaneously recorded to identify both the transmission paths. Stimulating the actuators one after the another ensures maximum signal-to-noise ratio and vastly speeds up the number of batch iterations required in the LMSID adaptive procedure. The test shown here is for the initial unshifted configuration of the experimental layout.

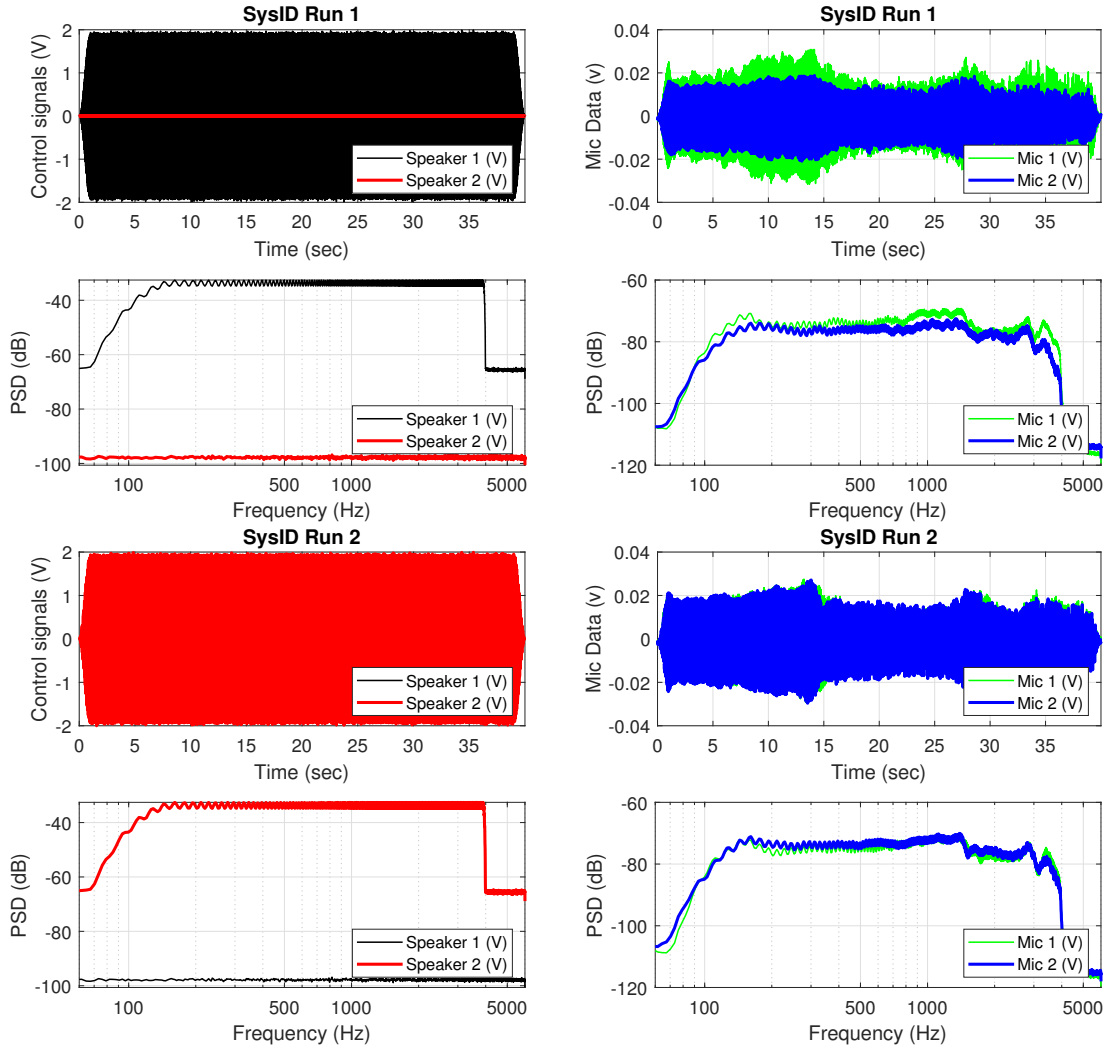

Figure D.1: Time history and spectrum of the control signals and measured responses for the MIMO identification procedure of the acoustical experiment for the initial unshifted configuration

D.2 Unshifted SISO experiment configuration

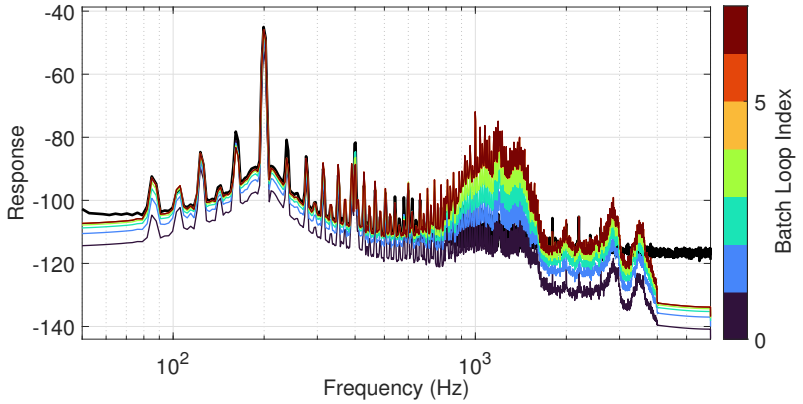

(a) Unshifted SISO configuration with single sinusoid target response

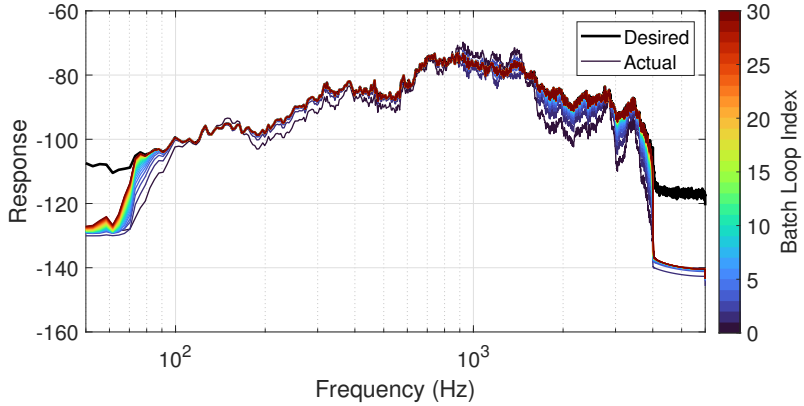

(b) Unshifted SISO configuration with speech sample target response

Figure D.2: Progression of the output response through the batch loop iterations for the SISO unshifted configuration experiments

D.3 SIMO experiment configuration

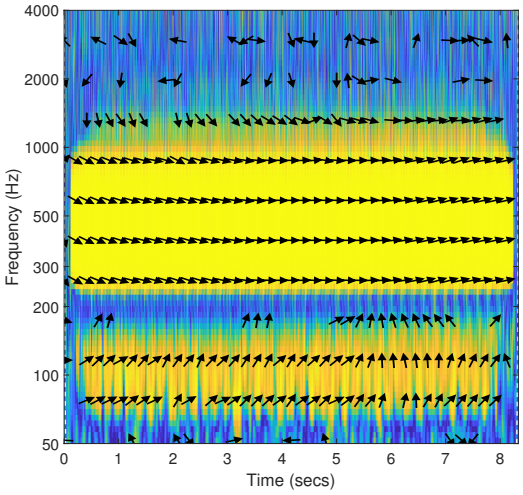

(a) Output channel 1 Measured response

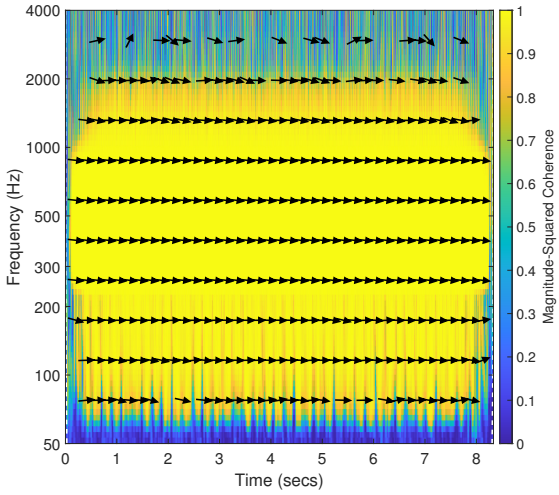

(b) Output channel 1 Modeled response

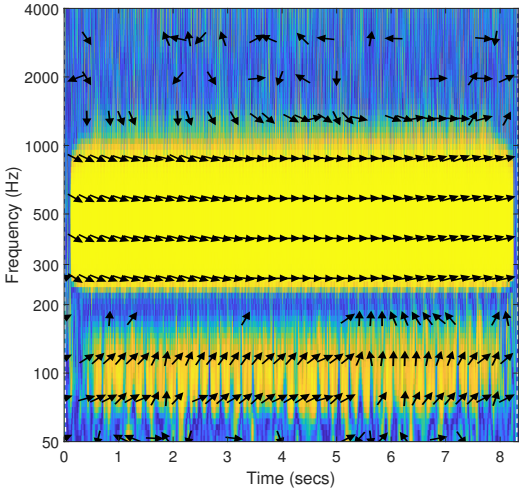

(c) Output channel 2 Measured response

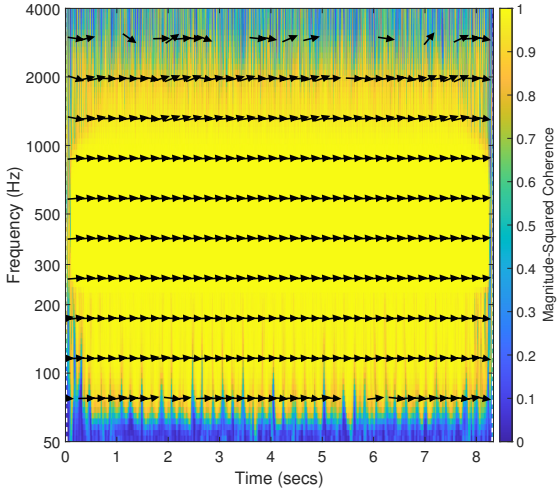

(d) Output channel 2 Modeled response

Figure D.3: Comparison of the wavelet coherence plots of the measured and modeled output for the unshifted SIMO configuration with a single sinusoid target response

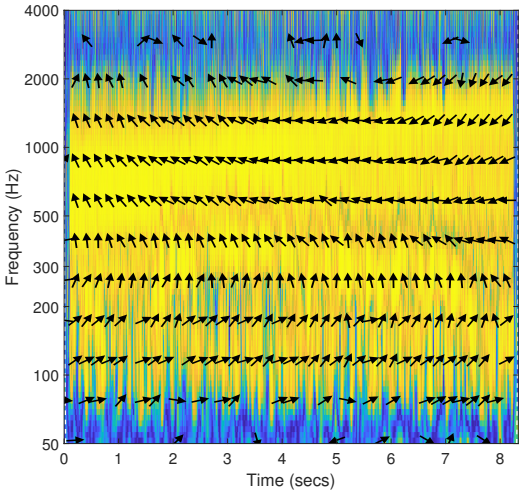

(a) Output channel 1 Measured response

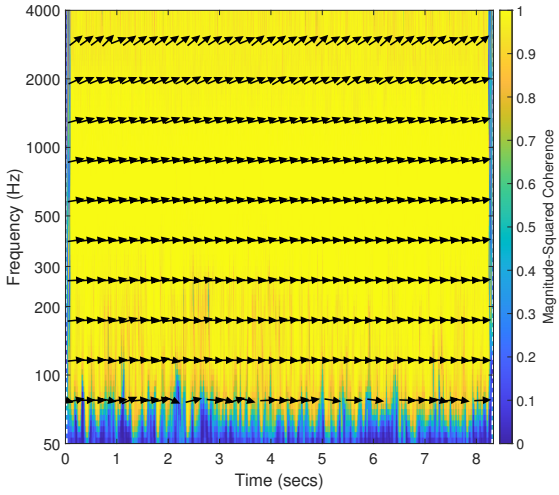

(b) Output channel 1 Modeled response

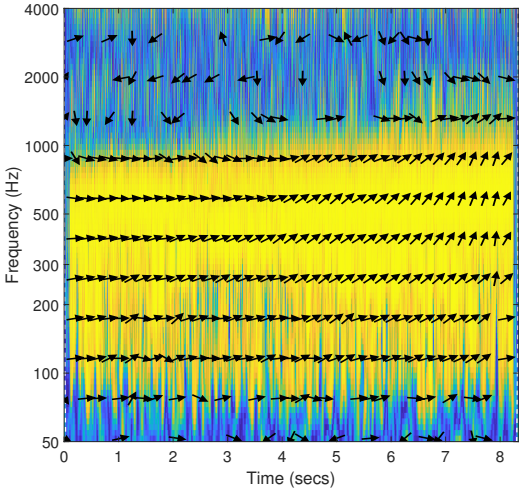

(c) Output channel 2 Measured response

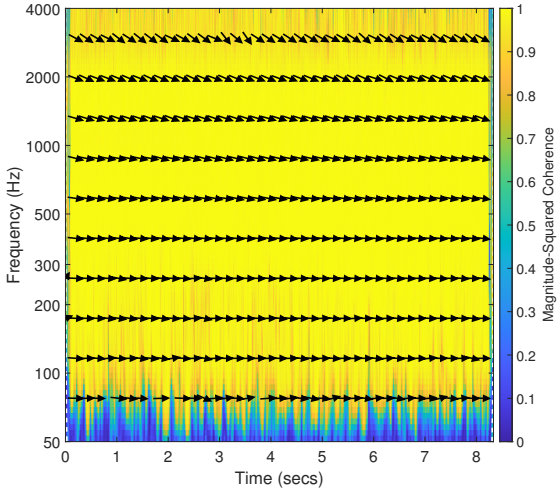

(d) Output channel 2 Modeled response

Figure D.4: Comparison of the wavelet coherence plots of the measured and modeled output for the unshifted SIMO configuration with the sample speech target response

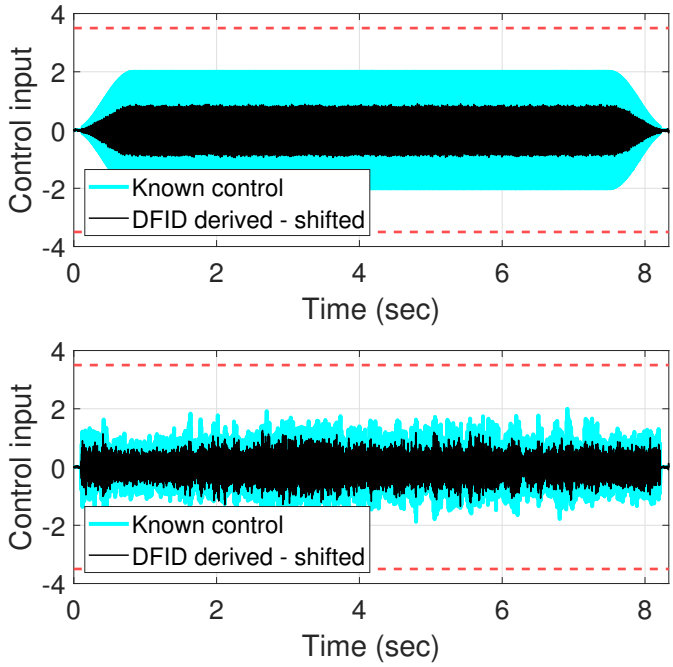

Figure D.5: Experimental result of PT-Fx-LMS DFID algorithm derived control sequences for the shifted SIMO configuration with a single sinusoid (top) and speech sample (bottom) target outputs

D.4 MISO experiment configuration

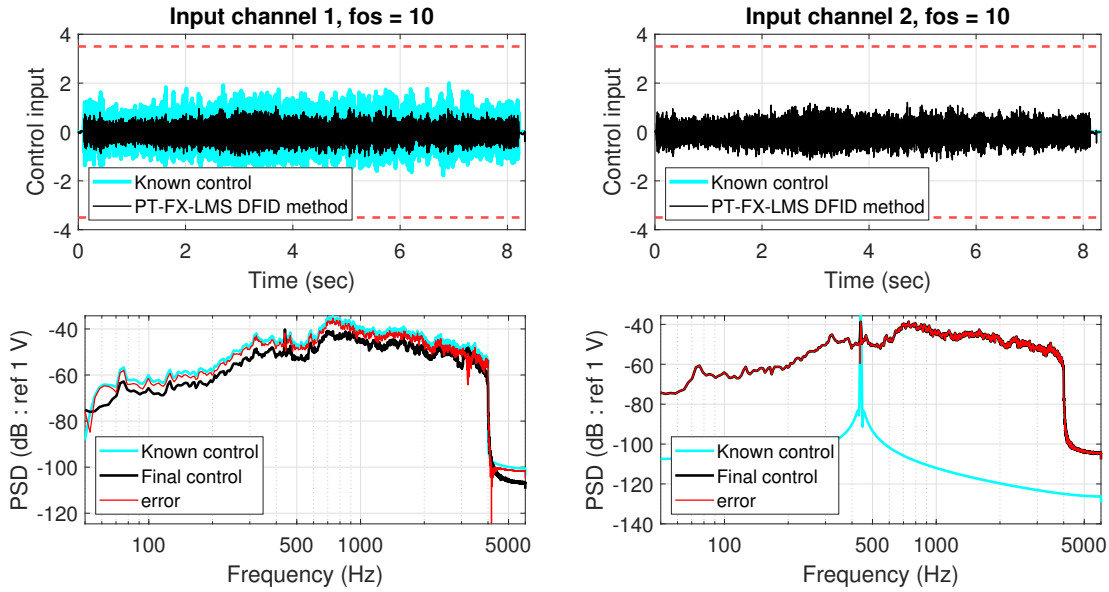

Figure D.6: Experimental result of PT-Fx-LMS DFID algorithm derived control sequences for the unshifted MISO configuration comparing the derived control with the known ground truth for the combined speech and sinusoid input test case

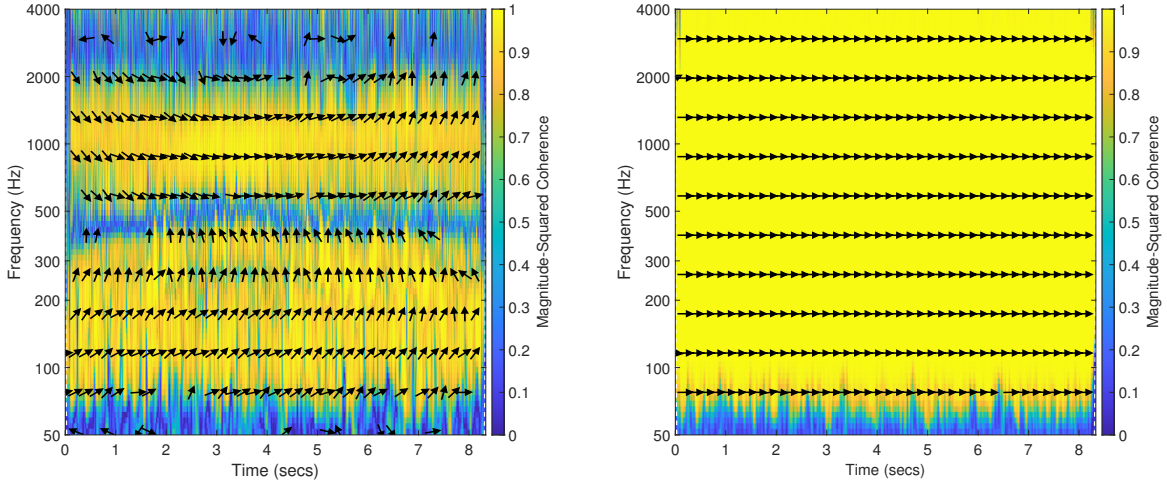

(a) Wavelet coherence between final measured and target response

(b) Wavelet coherence between final model output and target response

Figure D.7: Comparison of the wavelet coherence plots of the measured and modeled output for the unshifted MISO configuration with the speech and sine combined target response

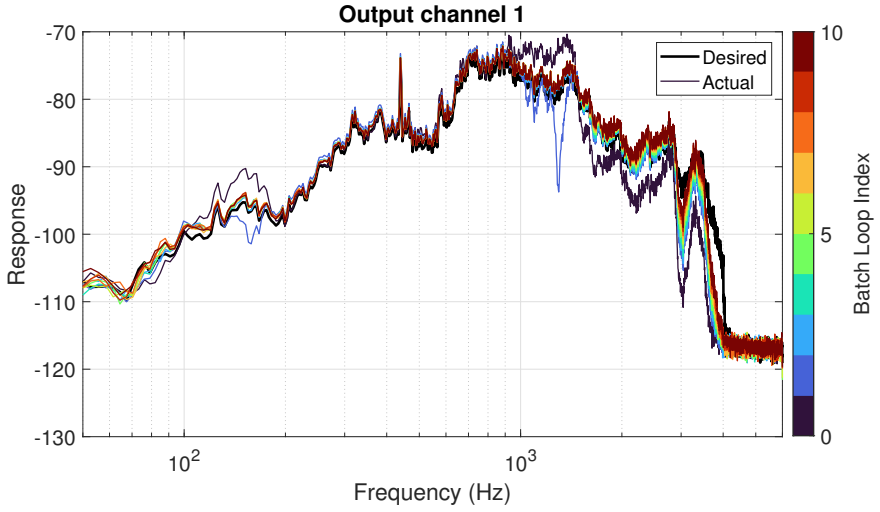

Figure D.8: Progression of the output response through the batch loop iterations for the MISO shifted configuration experiment

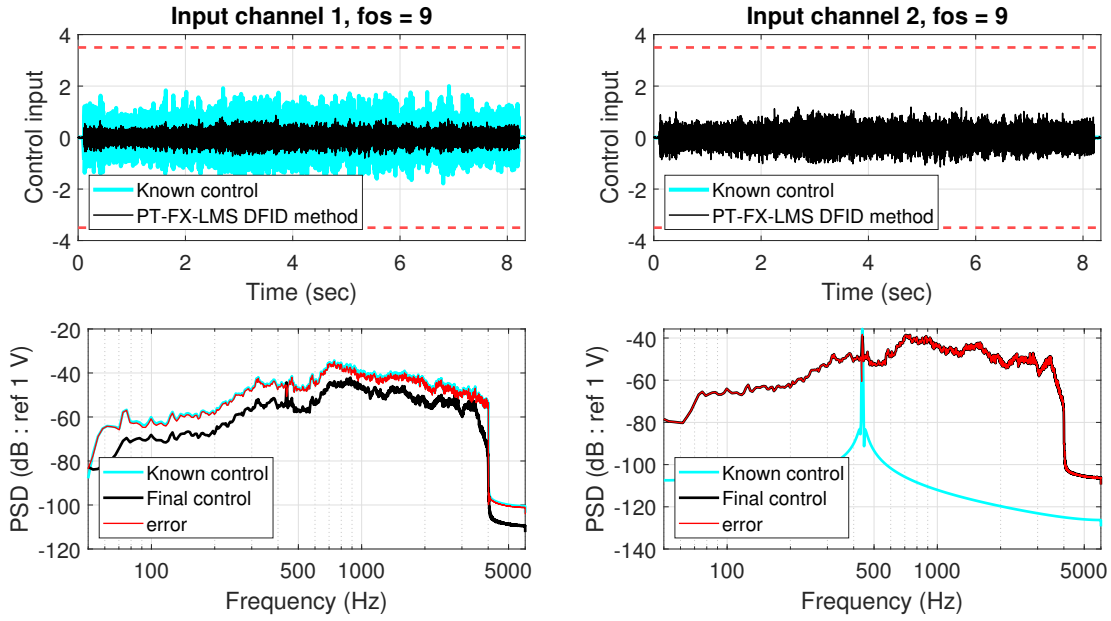

Figure D.9: Experimental result of PT-Fx-LMS DFID algorithm derived control sequences for the shifted MISO configuration comparing the derived control with the known ground truth for the combined speech and sinusoid input test case

D.5 MIMO experiment configuration

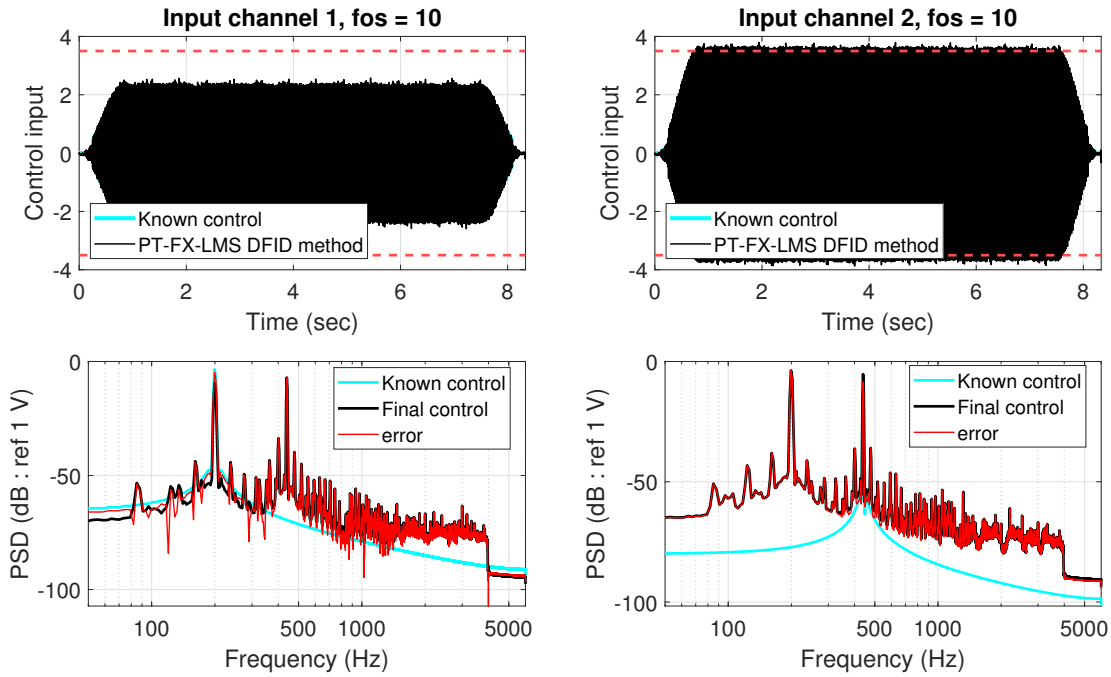

Figure D.10: Experimental result of PT-Fx-LMS DFID algorithm derived control sequences for the shifted MIMO configuration comparing the derived control with the known ground truth for the dual sinusoid target test case

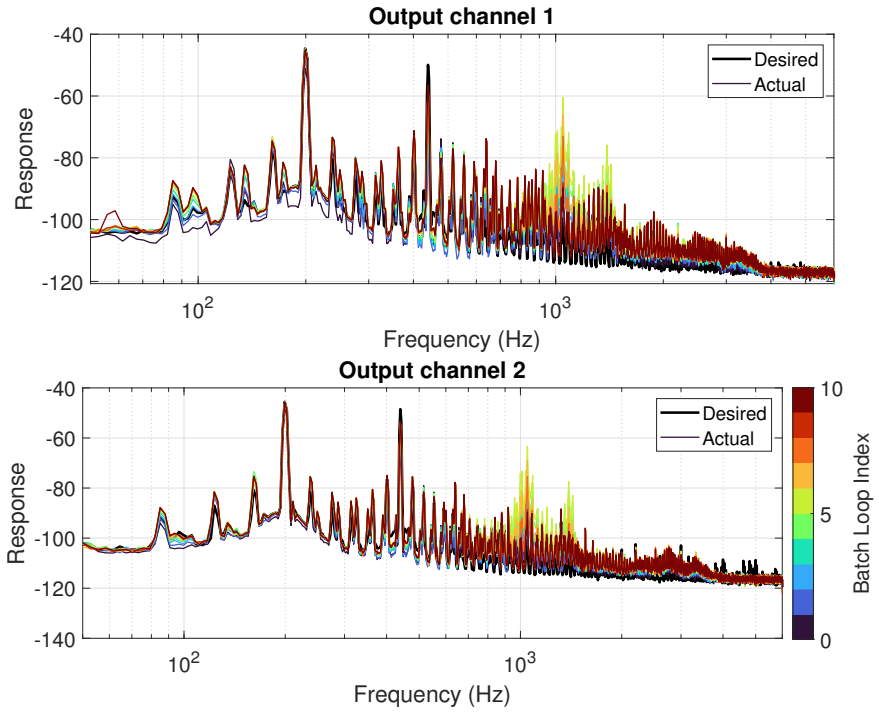

Figure D.11: Progression of the output response through the batch loop iterations for the shifted MIMO configuration experiment with the dual sinusoid target response

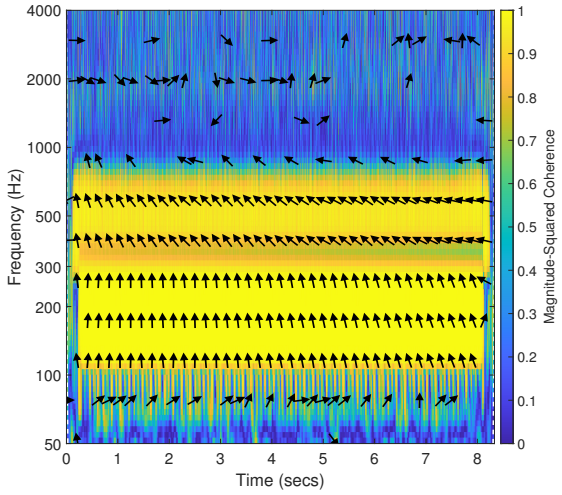

(a) Output channel 1 Measured response

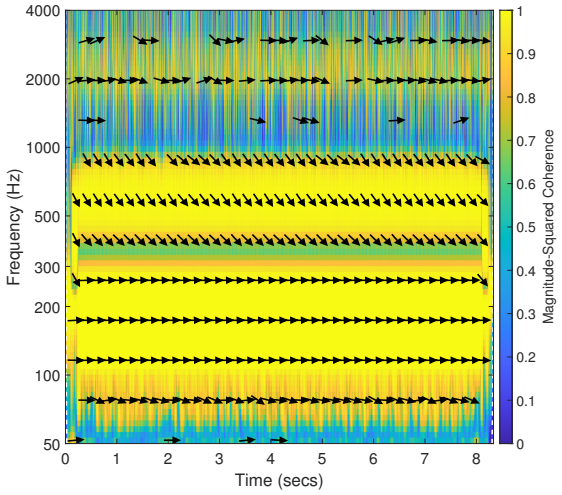

(b) Output channel 1 Modeled response

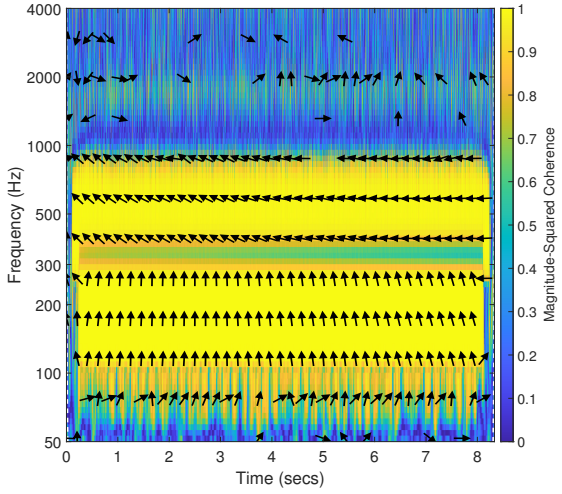

(c) Output channel 2 Measured response

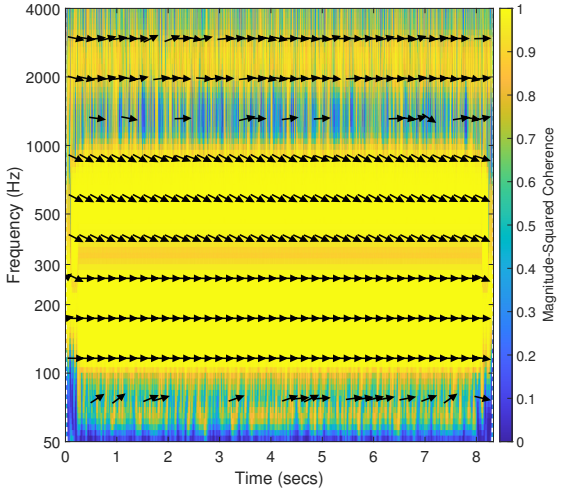

(d) Output channel 2 Modeled response

Figure D.12: Comparison of the wavelet coherence plots of the measured and modeled output for the shifted MIMO configuration with the dual sinusoid target response

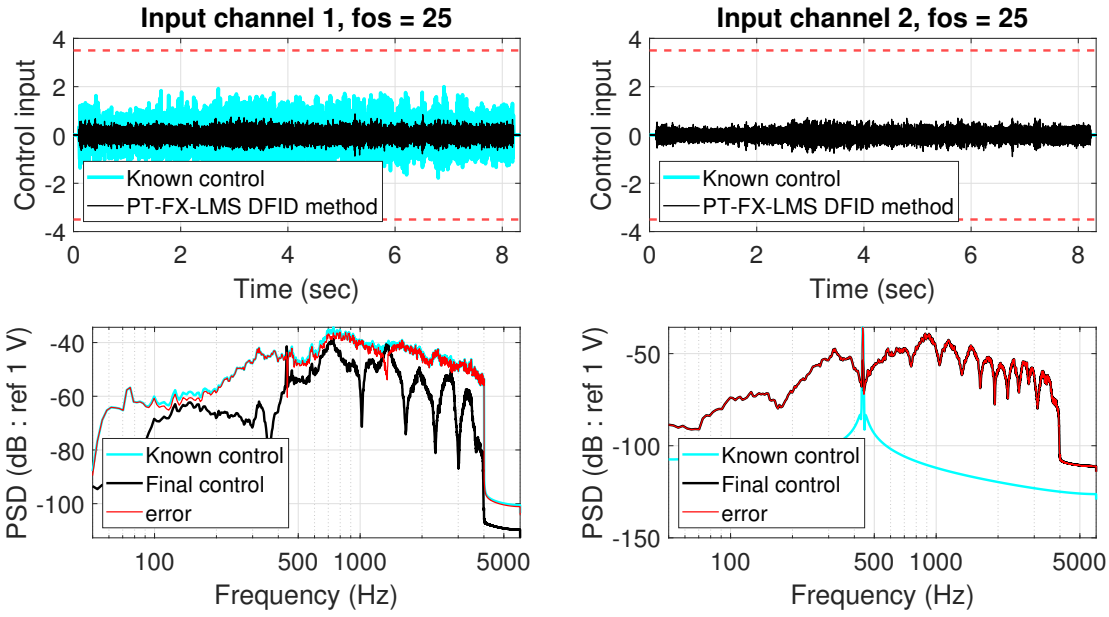

Figure D.13: Experimental result of PT-Fx-LMS DFID algorithm derived control sequences for the unshifted MIMO configuration comparing the derived control with the known ground truth for the combined sample speech and sinusoid target test case

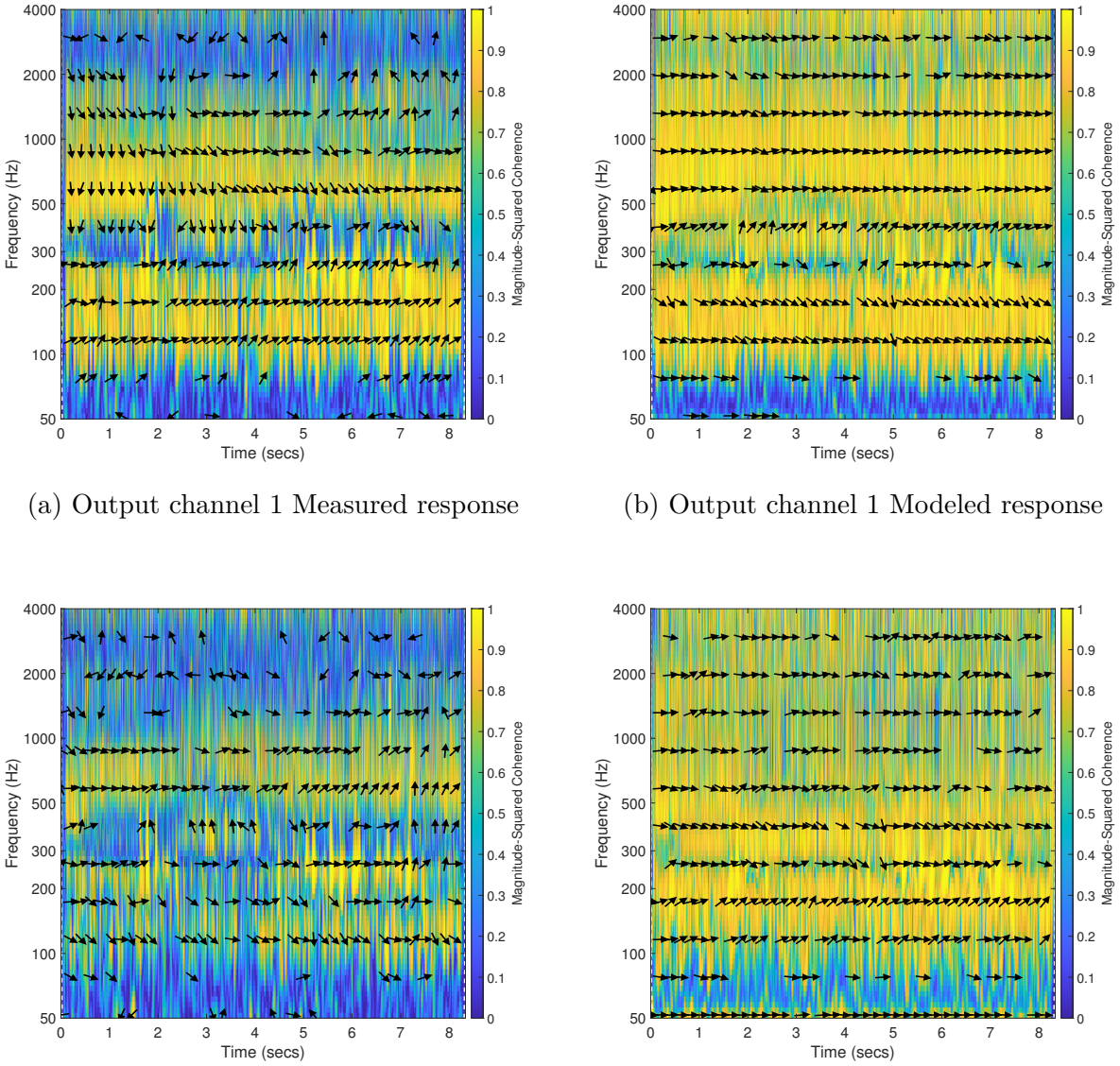

(a) Output channel 1 Measured response

(b) Output channel 1 Modeled response

(c) Output channel 2 Measured response

(d) Output channel 2 Modeled response

Figure D.14: Comparison of the wavelet coherence plots of the measured and modeled output for the unshifted MIMO configuration with the combined sample speech and sinusoid target test case